Volume 67C
Number 4
Oct.–Dec. 1963

Engineering and Instrumentation

U.S. DEPARTMENT OF COMMERCE

SECTION C

JOURNAL OF RESEARCH

NATIONAL BUREAU OF STANDARDS

Journal of Research
of the
National Bureau of Standards

C. Engineering and Instrumentation

OCT.-DEC. • 1963

VOLUME • 67C

NUMBER • 4

Editor: Martin Greenspan

Associate Editors: G. F. Montgomery, R. B. Jacobs

Publication dates:
Feb. 15, May 15, Aug. 15, Nov. 15, 1963

JOURNAL OF RESEARCH

The National Bureau of Standards Journal of Research reports research and development in the fields of activity shown at right. Also included from time to time are survey articles on topics closely related to the Bureau's scientific and technical program.

The Journal is published in four separate sections as follows:

A. Physics and Chemistry

Contains papers of interest primarily to scientists working in these fields. Issued six times a year. Annual subscription: domestic, $4.00; foreign, $4.75.

B. Mathematics and Mathematical Physics

Presents studies and compilations designed mainly for the mathematician and the theoretical physicist. Issued quarterly. Annual subscription: domestic, $2.25; foreign, $2.75.

C. Engineering and Instrumentation

Reports research and development results of interest chiefly to the engineer and the applied scientist. Issued quarterly. Annual subscription: domestic, $2.25; foreign, $2.75.

D. Radio Propagation

Reports work in radio propagation physics and upper atmospheric research. Issued six times a year. Annual subscription: domestic, $4.00; foreign, $4.75.

U.S. DEPARTMENT OF COMMERCE
Luther H. Hodges, Secretary
NATIONAL BUREAU OF STANDARDS
A. V. Astin, Director

Functions and Activities

The functions of the National Bureau of Standards are set forth in the Act of Congress, March 3, 1901, as amended. These include the development and maintenance of the national standards of measurement and the provision of means and methods for making measurements consistent with these standards; the determination of physical constants and properties of materials; the development of methods and instruments for testing materials devices, and structures; advisory services to government agencies on scientific and technical problems; invention and development of devices to serve special needs of the Government; and the development of standard practices codes and specifications. The work includes basic and applied research development engineering, instrumentation, testing, evaluation, calibration services, and various consultation and information services. The Bureau also serves as the Federal technical research center in a number of specialized fields. The scope of activities of the National Bureau of Standards is suggested in the following listing of the divisions and sections engaged in technical work.

WASHINGTON, D.C.

Electricity. Resistance and Reactance. Electrochemistry. Electrical Instruments. Magnetic Measurements. Dielectrics. High Voltage. Absolute Electrical Measurements.

Metrology. Photometry and Colorimetry. Refractometry. Photographic Research. Length. Engineering Metrology. Mass and Volume.

Heat. Temperature Physics. Heat Measurements. Cryogenic Physics. Equation of State. Statistical Physics.

Radiation Physics. X-ray. Radioactivity. Radiation Theory. High Energy Radiation. Radiological Equipment. Nucleonic Instrumentation. Neutron Physics.

Analytical and Inorganic Chemistry. Pure Substances. Spectrochemistry. Solution Chemistry. Standard Reference Materials. Applied Analytical Research. Crystal Chemistry.

Mechanics. Sound. Pressure and Vacuum. Fluid Mechanics. Engineering Mechanics. Rheology. Combustion Controls.

Polymers. Macromolecules: Synthesis and Structure. Polymer Chemistry. Polymer Physics. Polymer Characterization. Polymer Evaluation and Testing. Applied Polymer Standards and Research. Dental Research.

Metallurgy. Engineering Metallurgy. Metal Reactions. Metal Physics. Electrolysis and Metal Deposition.

Inorganic Solids. Engineering Ceramics. Glass. Solid State Chemistry. Crystal Growth. Physical Properties. Crystallography.

Building Research. Structural Engineering. Fire Research. Mechanical Systems. Organic Building Materials. Codes and Safety Standards. Heat Transfer. Inorganic Building Materials. Metallic Building Materials.

Applied Mathematics. Numerical Analysis. Computation. Statistical Engineering. Mathematical Physics. Operations Research.

Data Processing Systems. Components and Techniques. Computer Technology. Measurements Automation. Engineering Applications. Systems Analysis.

Atomic Physics. Spectroscopy. Infrared Spectroscopy. Far Ultraviolet Physics. Solid State Physics. Electron Physics. Atomic Physics. Plasma Spectroscopy.

Instrumentation. Engineering Electronics. Electron Devices. Electronic Instrumentation. Mechanical Instruments. Basic Instrumentation.

Physical Chemistry. Thermochemistry. Surface Chemistry. Organic Chemistry. Molecular Spectroscopy. Elementary Processes. Mass Spectrometry. Photochemistry and Radiation Chemistry.

Office of Weights and Measures.

BOULDER, COLO.

CRYOGENIC ENGINEERING LABORATORY

Cryogenic Processes. Cryogenic Properties of Solids. Cryogenic Technical Services. Properties of Cryogenic Fluids.

CENTRAL RADIO PROPAGATION LABORATORY

Ionosphere Research and Propagation. Low Frequency and Very Low Frequency Research. Ionosphere Research. Prediction Services. Sun-Earth Relationships. Field Engineering. Radio Warning Services. Vertical Soundings Research.

Troposphere and Space Telecommunications. Data Reduction Instrumentation. Radio Noise. Tropospheric Measurements. Tropospheric Analysis. Spectrum Utilization Research. Radio-Meteorology. Lower Atmosphere Physics.

Radio Systems. Applied Electromagnetic Theory. High Frequency and Very High Frequency Research. Frequency Utilization. Modulation Research. Antenna Research. Radiodetermination.

Upper Atmosphere and Space Physics. Upper Atmosphere and Plasma Physics. High Latitude Ionosphere Physics. Ionosphere and Exosphere Scatter. Airglow and Aurora. Ionospheric Radio Astronomy.

RADIO STANDARDS LABORATORY

Radio Standards Physics. Frequency and Time Disseminations. Radio and Microwave Materials. Atomic Frequency and Time-Interval Standards. Radio Plasma. Microwave Physics.

Radio Standards Engineering. High Frequency Electrical Standards. High Frequency Calibration Services. High Frequency Impedance Standards. Microwave Calibration Services. Microwave Circuit Standards. Low Frequency Calibration Services.

Joint Institute for Laboratory Astrophysics-NBS Group (Univ. of Colo.).

Order all publications from the Superintendent of Documents
U.S. Government Printing Office, Washington, D.C., 20402.

Use of funds for printing this publication approved by the Director of the Bureau of the Budget (June 19, 1961).

Journal of Research of the National Bureau of Standards—C. Engineering and Instrumentation
Vol. 67C, No. 4, October-December 1963

Limitations on Electron Beam Density of Unipotential Electron Guns at Low Voltages

J. Arol Simpson and C. E. Kuyatt

(Received April 1, 1963)

The problem of saturating a particular configuration of space with electrons is considered. It is shown that with unipotential guns of axial symmetry derived from space charge limited diodes there exist both a minimum energy and a maximum width-to-length ratio of the space that can be saturated. These limits are derived for the case of convergent flow between concentric spheres. Similar limits for partial saturation of the space are derived for cases of convergent, parallel, and divergent flow.

One of the constantly recurring problems in electron physics is the generation of low energy electron beams in free space. These beams are usually required to be circular in cross sections of some specified length and diameter and have some energy between 1 and 1,000 ev. The highest electron current possible within these specifications is usually desired. The authors recently gave [1] [1] a procedure for designing such guns using the multistaging principle, i.e., the use of an intermediate anode operated far above the final beam voltage. Since added complexity and practical difficulties, such as the increased probability of ionizing the residual gas and increased problems of interelectrode leakage, are inherent in such designs, it appears desirable to delineate the regions where the failure of unipotential guns makes multistaging essential.

It is essential to understand the basic physical limitations on achievable electron flow patterns for it is the nature of these limitations which determines the beam profile and density. These limitations are of two classes, one the result of space charge repulsion, the other essentially of thermodynamic nature. The resulting restrictions function both individually and most importantly in combination.

Let us consider the usual case figure 1. It is desired to irradiate a volume defined by a length l and a diameter $2r_0$. Alternately we may consider the space defined by l and the angle γ.

As is well known [2], the maximum current, I_{max}, that can be forced through such a space against the dispersive forces of space charge is

$$I_{max}=38.5\,E^{3/2}\frac{2r_0}{l}=38.5E^{3/2}\tan^2\gamma \qquad (1)$$

where current is in microamperes and energies E are in ev. It can be further shown that this results in a maximum current density at the point of minimum cross section (where the beam diameter is $2r_0/2.35$) of

$$J_{max}=\frac{211}{\pi r_0^2}E^{3/2}\tan^2\gamma \qquad (2)$$

where current density is in microamperes per square length unit used in measuring r_0.

To achieve this maximum the beam must be launched through a hole the same size as the diameter of the space and directed so that in the absence of space charge there would be a crossover in the center of the volume. We note that while the current depends only on the shape but not the size of the space this is not true of the density and moreover no absolute upper limit on density is predicted.

One solution to the problem of generating space charge limited beams and launching them at the proper angle was found by the design techniques developed by Pierce [3] and expanded by Samuel [4], Field [5] and other more recent workers [6, 7].

These solutions consist of a section of a spherical diode where the effects of the radial flow beyond the beam limits are simulated by proper electrode profiles or auxiliary electrodes. When proper account is taken of the lens formed by the hole in the inner sphere (anode lens) such guns can be designed for currents up to the point where the effect of the anode hole on the field at the cathode can no longer be compensated. For guns without an anode grid this point occurs when the hole size approaches the diode spacing or at a point where I (μ amp) approaches $E^{3/2}$ (v), i.e., a microperveance of unity. Particularly useful design curves for such guns may be found in Spangenberg's work [8].

Field [5] seems to have been the first to point out that the effects of the thermal energies of the electrons at the cathode spread the beam and may be an im-

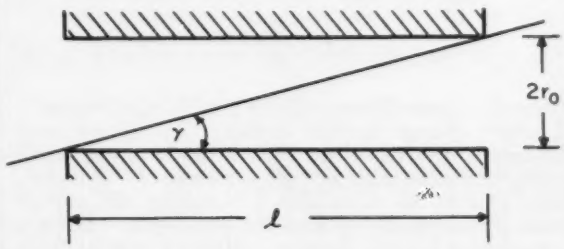

FIGURE 1. *Definition of space to be saturated and of defining angle* γ.

[1] Figures in brackets indicate the literature references at the end of this paper.

portant factor in limiting beam current and density. This beam spread is a consequence of a fundamental law of optics which in various forms carries the names of Helmholtz, Lagrange, Clausius, and Langmuir. This law, based upon general arguments of classical mechanics and derivable from Liouville's theorem, states, for electrons, that

$$E_1^{1/2} \sin \theta_1 d\theta_1 dx_1 = E_2^{1/2} \sin \theta_2 d\theta_2 dx_2.$$

In this case E_1 and E_2 are the energies of the electrons in planes 1 and 2, θ the convergence angles in these planes and dx_1 and dx_2 are the corresponding elements of length in these planes.

As written in differential form, this law applies to any system whether or not images are formed. It is generally not very useful since to determine the x's and θ's a complete trajectory calculation must be performed. If, however, planes 1 and 2 are conjugate object and image, or object and crossover then the equation may be integrated to give

$$E_1^{1/2} \sin \theta_1 = M E_2^{1/2} \sin \theta_2$$

when M is the Gaussian magnification.

If we specialize further to the case where plane 1 is a thermionic cathode and express E_1 in terms of the cathode temperature and M as a ratio of current densities we can obtain the Langmuir [9] form:

$$J_2 = J_1[1 + E/(T/11{,}600)] \sin^2\theta_2 \approx J_1(11{,}600E/T) \sin^2\theta_2. \tag{3}$$

The general consequences of these equations are well known and are treated at length in the standard texts [10].

If we compare eqs (2) and (3) we see that *a priori* there is no reason why the density required by eq (2) cannot be obtained subject to eq (3) since J_1 is not limited. In practice of course there are material limits on the cathode, but it can be shown that for energies below a few hundred volts modern cathodes are sufficiently "bright" to satisfy almost any demand.

However, there is a third restriction on unipotential guns which in certain voltage regions prohibits the densities required by eq (2) to saturate a given space. This restriction is the bound on obtainable J_1 which is set by space charge within the gun structure. Meltzer [11] has shown that a limitation of the form:

$$J = \frac{kE^{3/2}}{S^2} \tag{4}$$

where S a linear dimension is a general characteristic of space charge limited diodes [12]. If we now consider a gun based on such a diode r_0 can serve to determine the scale and play the role of S in eq (4). The value of the multiplier k is set by the overall geometry necessary to give the convergence angle γ in free space beyond the gun. Hence k is a function of γ. There are, of course, many conceivable guns which give an angle γ but for each general class k remains a function of γ. The result is a limitation on cathode current density of the form:

$$J_0 = \frac{f(\gamma)E^{3/2}}{r_0^2}. \tag{5}$$

Substitution of this value of J_0 for J_1 in eq (3) gives the maximum obtainable current density, J_2, in the space to be saturated. If J_2 is less than J_{max} from eq (2), the space cannot be saturated. Combining the equations shows that if

$$E < \frac{211}{\pi} \frac{T}{11{,}600} \frac{\tan^2\gamma}{f(\gamma) \sin^2\theta_2} \tag{6}$$

the space cannot be saturated. The connection between γ, the launching angle, and θ_2, the angle at minimum beam density, is somewhat subtle involving as it does the detailed nature of the trajectories between the anode and the point of minimum beam cross section as well as the angle and energy with which a given electron leaves the cathode. However, without this detailed knowledge one fact is clear: θ_2 cannot exceed γ without some electrons passing outside of the space to be saturated. Hence, we can set θ_2 equal to γ without violating the inequality.

There is moreover an upper limit on γ since the anode hole lens of a diode is always divergent. Hence electrons make a larger angle with the axis just before the lens than they do after the lens. Considering a class of guns which give saturation and taking 90° as a natural limit of the angle inside the lens we see that there is always a maximum value of γ for which the space can be saturated. Actually the limit is reached at smaller angles since a large γ requires a higher perveance which in most structures requires closer anode cathode spacing resulting in higher fields inside the anode and hence stronger divergence at the anode lens.

For guns based on radial flow between concentric spheres the quantity $f(\gamma)$ in eq (6) may be obtained from the well-known optics of Pierce guns [8]. Pierce [14] has calculated the values of the gun parameters where the space charge spread equals the thermal spread. In our notation this procedue. is equivalent to the assumption that γ equals θ_2. Danielson, Rosenfeld, and Saloom [6] have done careful numerical calculations on the trajectories in a series of Pierce guns and obtained the final size of the minimum beam cross section when both space charge and thermal spread are important. This procedure, of course, accounts fully for the detailed relationship between γ and θ_2. Over the range of gun parameters studied, there is no doubt that the latter is the more precise calculation and should be the final check on any proposed design. However, both calculations focus their attention on the gun and require the calculation of a series of guns each of which will saturate the space. It is more useful, especially in the early stages of design of an experiment, to concentrate on the space so that the feasibility of the experiment may be judged prior to detailed gun design.

To achieve this end we have evaluated eq (6) using an $f(\gamma)$ derived from the results of Pierce. We assumed a current efficiency of 0.9 and a corresponding intensity efficiency of 0.39. The anode lens was assumed to be of the Davisson [15] form, the ~10 percent correction of Danielson et al., not being significant for our purposes. We assumed γ equal to θ_2. Our calculations are hence much in the spirit of those of Pierce but extended to account more fully for the effect of the anode lens. They are somewhat less optimistic than his, but still must be considered outer bounds of possible operation.

The limits found are independent of the scale of the space, depending only on γ. If the scale is reduced beyond a critical minimum, it is possible that the cathode material limit may be reached. However, if a cathode-anode spacing of 1 mm is considered a practical lower limit 1 amp/cm² cannot be exceeded below 265 v.

The results of the calculation are shown in figure 2. On this plot lines of constant perveance, $I/V^{3/2}$, appear as straight lines sloping upward to the right. When the space is saturated, as in the upper portion of the graph, eq (1) gives the relation between the perveance and corresponding value of γ. In this portion of the graph the unity perveance line corresponds to a $\gamma=9.2°$. The area to the left of this line is generally not accessible to unipotential guns because of their limited perveance. In the area above the almost horizontal line $I/I_{max}=1$, spaces characterized by gammas up to 9.2 deg may be fully saturated. Below this $I/I_{max}=1$ line the spread of the beam due to thermal velocities dominates the situation and frustrates attempts to operate at lower voltages by reducing the current drastically below the value predicted by extending the lines of constant γ. It will be noted that there is no unipotential gun which will saturate a space below ~220v beam energy.

If one is prepared to relax the current requirement so that only 0.5 of the maximum possible current is passed, the guns need be less convergent and the area between the perveance=1.0 curves now marked $\gamma=12.8$ and $I/I_{max}=0.5$ is available. The entrance diameter (anode hole of the gun) instead of being equal to the space diameter is now found to equal 0.52 of this diameter.

If one still further reduces the current requirement to 0.25 I_{max} it is possible to use guns whose injection angle into the space is 0°. Under this circumstance the anode hole diameter should be 0.425 of the tube diameter. The details of the calculation are slightly different since now the maximum density lies within the gun structure but the results are of the same form. The minimum usable voltage is decreased to 10 ev and spaces up to $\gamma=17.85°$ may be one-quarter saturated.

A sort of natural limit to this process is reached at the dotted curves above and to the right of which the highly divergent parallel diode guns are usable. Although such guns can be used to a minimum of almost 1 ev and to space angles of $\gamma=74°$ (we assumed a unity spaced diode of microperveance

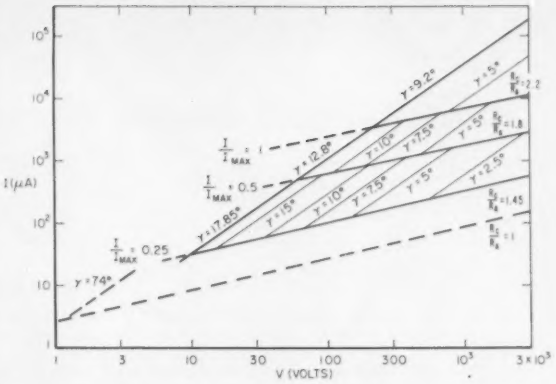

FIGURE 2. *Graph of current versus voltage showing regions accessible to guns capable of saturating a given space with I_{max}.*

Cases of subsaturation, 0.5 I_{max}, 0.25 I_{max} and 0.05 I_{max} are shown. The usable range lies to the right and above of all curves. On the right margin are given the ratio of cathode/anode radius of the optimum Pierce gun.

2.33 whose anode diameter is very much smaller than the tube diameter) the fact that they will only put 0.05 I_{max} through any given space makes them not very attractive.

The curves of figure 2 show clearly that the range of applicability of unipotential guns lies at comparatively high energy and wide angles. To operate outside these limits it is necessary to effectively decouple the thermal energy and space charge limit by adopting the multistaging principle and operating a diode or triode at comparatively high voltage and decelerating to the desired low energy.

References

[1] J. A. Simpson and C. E. Kuyatt, Rev. Sci. Instr. **34,** 265 (1963).
[2] E. E. Watson, Phil. Mag. **3,** 849 (1927).
[3] J. R. Pierce, J. Appl. Phys. **11,** 548 (1940).
[4] A. L. Samuel, Proc. IRE **33,** 233 (1945).
[5] L. M. Field, Rev. Mod. Phys. **18,** 353 (1946).
[6] W. E. Danielson, J. L. Rosenfeld, and J. A. Saloom, Bell Tech. Jour. **35,** 375 (1956).
[7] Müller, Arch. El. Übertr. **9,** 20 (1955).
[8] K. R. Spangenberg, Vacuum Tubes (McGraw-Hill Book Company, Inc., New York, N.Y., 1948).
[9] D. B. Langmuir, Proc. IRE **25,** 977 (1937).
[10] J. R. Pierce, Theory and Design of Electron Beams, 2d ed., ch. 8 (Van Nostrand Book Co., Inc., New York, N.Y., 1954).
[11] B. Meltzer, Proc. Phys. Soc. B**62,** 431 (1949).
[12] An example of this type of limitation is the well-known Langmuir-Blodgett [13] formula for the current density of a plane parallel diode of electrode spacing x, cm.

$$J_0=\frac{2.33}{x^2}E^{3/2}(\mu\text{amp/cm}^2)$$

[13] I. Langmuir and K. B. Blodgett, Phys. Rev. **24,** 49 (1924).
[14] J. R. Pierce, Theory and Design of Electron Beams, 2d ed., ch. 8 (Van Nostrand Book Co., Inc., New York, N.Y., 1954).
[15] C. J. Davisson and C. J. Calbick, Phys. Rev. **42,** 580 (1932).

(Paper 67C4–138)

JOURNAL OF RESEARCH of the National Bureau of Standards—C. Engineering and Instrumentation
Vol. 67C, No. 4, October–December 1963

New Radiofrequency Mass Spectrometer Having High Duty Cycle*

Robert M. Mills

(Received December 11, 1962)

A new type of time-of-flight mass spectrometer has been developed which, unlike most other such instruments, utilizes a large fraction of the nonpulsed stream of ions. The ions are accelerated through a d-c voltage and then pass into a drift tube. A radiofrequency voltage is applied at the exit and entrance gaps of the drift tube in such a way that the field at the entrance is the negative of that at the exit. The number of ions which pass through the drift tube with such a velocity that the energy change from the rf fields is a minimum, is measured by placing an electrical barrier in front of the collector and differentiating the cutoff curve. Velocity modulation of the beam resulting from the rf field at the first gap limits the instrument to moderate resolution. However, the instrument has a 60 percent duty cycle, a value significantly greater than that achieved by most other time-of-flight mass spectrometers. It also has the advantages of electrical and mechanical simplicity. Due to the nature of the instrument's output, it will be most useful in applications requiring the analysis of a simple mass spectrum and where high duty cycle is of real value. The instrument has resolved the isotopes of rubidium at masses 85 and 87, and has identified one component ion beams ranging in mass from helium to cesium.

1. Introduction

This paper describes a new type of time-of-flight spectrometer which has a large duty cycle along with moderate resolving power. It was developed for use in flame research investigations at the National Bureau of Standards. Two types of experiments have been planned. The first is that of measuring the appearance potential of certain halogenated compounds. In experiments of this type, one looks for the appearance of a single ion peak as the energy of the ionizing electron is increased. High sensitivity is important if the appearance potential is to be determined accurately. The second application is that of analyzing ions drawn directly from a flame. Other laboratories that have used flames as the ion source have experienced difficulty in drawing enough ions from the flame for analysis. The high duty cycle of the mass spectrometer described in this paper should make the instrument efficient in using the ions which are available in these two experiments.

Most of the previous efforts to increase the sensitivity of mass spectrometers have been directed at the collector end by using electron multipliers. An electron multiplier suffers from a changing gain over a period of time and was not used in the instrument described here. However, it would be possible to incorporate one if an even greater sensitivity were desired.

In general, time-of-flight (T.O.F.) mass spectrometers depend on the fact that, given equal energy, heavy ions take a longer time to traverse a given distance than do light ions. The velocity of any ion varies according to:

$$v=\sqrt{\frac{2qV}{m}} \tag{1}$$

where q is the charge of the ion, V is the total voltage through which the ion has been accelerated, and m is the mass of the ion. If a pulse of ions of various masses enters a field-free drift tube, after being accelerated, the ions will travel in bunches corresponding to their mass. The distance between bunches will increase the further the ions travel down the drift tube. The mass spectrum can then be measured by observing the ion current collected at the exit end of the drift tube as a function of time.

All instruments of this type have to be pulsed at the source and the time between pulses must be great enough to clear the drift tube of ions from the previous pulse. The pulsing greatly reduces the duty cycle of the mass spectrometer which thus lowers its time average collector current. The instrument of this type which is best known was reported by Wiley and McLaren in 1955 [1].[1] Ions are created by a 0.25 μsec electron pulse once every 100 μsec [2], giving a duty cycle of 0.25 percent.

Another type of T.O.F. instrument which is described in the literature [3, 4] distinguishes masses by the energies the ions receive from a series of rf fields. A continuous beam of ions passes through 10 or more electrodes which are perpendicular to the beam path. The geometry of these electrodes and frequency of the rf fields maintained between them are such that ions of one mass receive more energy than lighter or heavier ions. An electrical barrier is placed in front of the ion collector. Only ions which have received extra energy from the rf fields are able to overcome the barrier and reach the collector. This instrument gives good resolution,

* A portion of the funds for support of the work reported was provided by the Bureau of Ships, Department of the Navy.

[1] Figures in brackets indicate the literature references at the end of this paper

but has several drawbacks. The spacing between the electrodes is critical for proper operation which makes construction and modification difficult. The numerous electrodes through which the ions must travel reduce the transmission of the instrument. And, finally, this type of instrument collects pulses of ions even though a continuous beam of ions enters the analyzing region. This effect is due to the fact that an ion of correct mass must also have the correct initial phase with respect to the rf voltages as it enters the fields in order to gain the necessary amount of energy to reach the collector. Thus the sensitivity of the instrument is reduced in the same way as with the pulsed type of spectrometer. The duty cycle is given in reference [4] as $\frac{N}{R8\sqrt{3}}$, where N is the number of stages and R is the resolution. An instrument of this type having 20 stages thus has a duty cycle less than 3 percent at a resolving power of 50.

2. Theory of Operation

The mass spectrometer reported here resembles the last instrument described in that ions of different masses are distinguished by their energies rather than their spatial positions. It differs in that initial phase requirements are much less severe.

Consider a drift tube of length L which has rf electric fields applied at its ends as shown in figure 1. Tungsten screens, not shown in the figure, are attached to the ends of the drift tube and define the entrance and exit. It is seen that the grids near each end of the drift tube are at the same potential. Therefore, at a given instant, the rf fields between the drift tube and the grids are exactly equal and opposite at the entrance and exit ends of the tube. These rf fields are represented by the upper and lower curves in figure 2.

The operation of the instrument can be explained most easily if the flight time of a given mass through the drift tube is assumed to be constant. This is not entirely a valid assumption since the effects of the variation in flight time (velocity modulation)

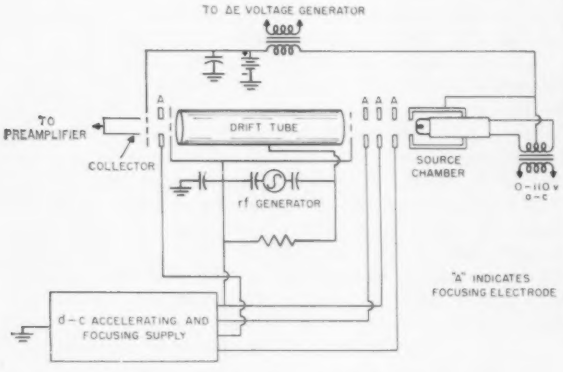

FIGURE 1. *Simplified diagram of the mass spectrometer.*

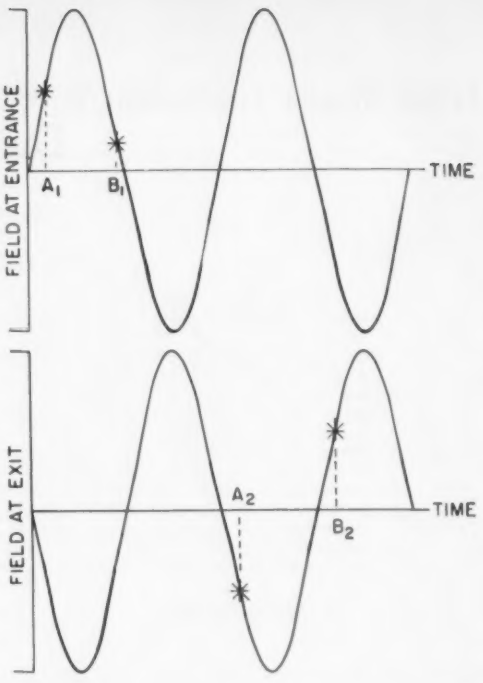

FIGURE 2. *Radiofrequency fields at the entrance and exit of drift tube.*

A resonant ion entering at time A_1 and leaving at time A_2 experiences no change in energy. A typical nonresonant ion entering at time B_1 and leaving at time B_2 experiences a net gain in energy.

resulting from the rf voltage at the entrance of the drift tube are quite noticeable. Nevertheless, velocity modulation will be neglected until the resolution and duty cycle of the instrument are discussed.

Suppose an ion enters the drift tube at some time A_1. If the frequency of the rf voltage and the velocity of the ion are such that the ion emerges at the other end of the drift tube after one period of the rf wave, the ion will pass through the second rf field at time A_2. It is seen that no matter what part of the cycle the ion enters the drift tube, the energy which it obtains at the first field is exactly balanced out by the energy it loses at the second. Consider now, a heavier ion which takes a longer time to traverse the drift tube. For example, if it enters the drift tube at time B_1, it might pass through the exit field at time B_2. Any ion which does not pass through the drift tube in an integral number of cycles will undergo an increase or decrease in energy, depending upon when it entered the drift tube. A beam of such ions which is homogeneous in energy at the entrance of the drift tube will emerge with a distribution of energies. However, a similar stream of ions which passes through the tube in an integral number of rf cycles will emerge with all the ions unchanged in energy. These are the ions which the detection system measures.

3. Detection System

As stated before, the detection system must identify the resonant ions by their energy. This measurement is made by the retarding field method [5, 6]. An electrical barrier is placed immediately in front of the Faraday cage collector. For a given barrier potential, E, measured with respect to the ion source, only ions with energies equal to E electron volts or greater can pass. Or

$$S(E)=\int_E^\infty N(e)de \tag{2}$$

where $S(E)$ is the number of ions per unit of time that penetrate a barrier of height E and $N(e)$ is the number of ions approaching the barrier per unit of time with energy e at the barrier. $N(e)$ is obtained from (2) by differentiating with respect to E

$$\frac{dS(E)}{dE}=-N(E). \tag{3}$$

Since the detection system must measure the number of ions which have had their energies unchanged by the rf fields, and, since these particular ions arrive at the barrier with the same energy that they had at the source, $N(0)$ is the quantity sought. Figure 3 is a set of cutoff curves showing collector current as a function of barrier height in volts, obtained with an x-y recorder. The center curve is the cutoff curve for a potassium beam which is in resonance with the rf voltage, taken with n equal to 12. Here, n is equal to the number of rf cycles which an ion takes to traverse the drift tube. The other curves were taken with n equal to 11.5, 11.7, 12.2, and 12.4.

The differentiation represented in eq (3) is performed in the instrument by introducing a variation in E about the point $E=0$ shown as ΔE in figure 3. The resulting a-c component in the collector current is proportional to $dS(E)$. And $dS(E)$ is proportional to $N(e)$ if dE is infinitely small. A square wave of magnitude ± 3.9 v was used to produce this variation and this value will be assumed in the remainder of the paper. Using a dE of finite size means that an average value of N is actually measured over the range $E=0\pm 3.9$ v. If the ion beam is composed of more than one mass, the resulting a-c signal is the sum of the contributions from the individual masses.

The variation in the ion current was amplified by a-c amplifiers and then fed to a synchronous detector, ΔE supplying the reference phase used in the detector. An x-y recorder was connected to the output of the detector. The masses were swept by changing the frequency of the rf voltage. A potentiometer was attached to the tuning knob of the rf generator. The voltage from the potentiometer was thus related to the rf frequency and was connected to the other input of the x-y recorder. The potentiometer and tuning knob were driven by a 1 rpm motor.

Figures 4, 6, 7a, 7b, and 8 were made using this

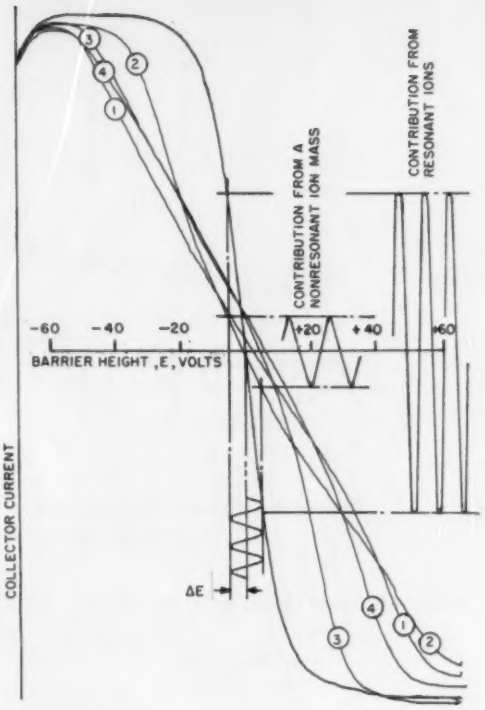

FIGURE 3. *Cutoff curves obtained from an* x-y *recorder for* n=*12.0 (central curve)* n=*11.5(1)*, n=*11.7(2)*, n=*12.2(3)*, *and* n=*12.4(4) showing the difference in output signals for resonant and nonresonant ions.*

A square wave was used for ΔE instead of the sine wave shown.

arrangement. The abscissa is not linear in frequency. No development work has been done to make this instrument a fast-sweep instrument, capable of displaying its output on an oscilloscope, but this seems feasible.

The advantage of picking out the ions with zero energy change should be noted. Instruments of the type in reference [4] must maintain a constant ratio of barrier height to rf voltage to obtain the desired resolution. However, if the number of ions with zero energy change is measured instead of the number with maximum energy change, the strong dependence on resolution no longer exists and less care need be taken in controlling the rf amplitude as the rf frequency is changed.

4. Harmonics

As has been mentioned before, ions may stay in the drift tube any whole number of cycles in order to be detected. Thus, as the frequency is varied, the mass peaks will repeat corresponding to various values of n as in figure 4. The two rf frequencies at which adjacent harmonics of a particular ion appear must be measured to determine the ion's mass. The ratio of these two frequencies is equal to

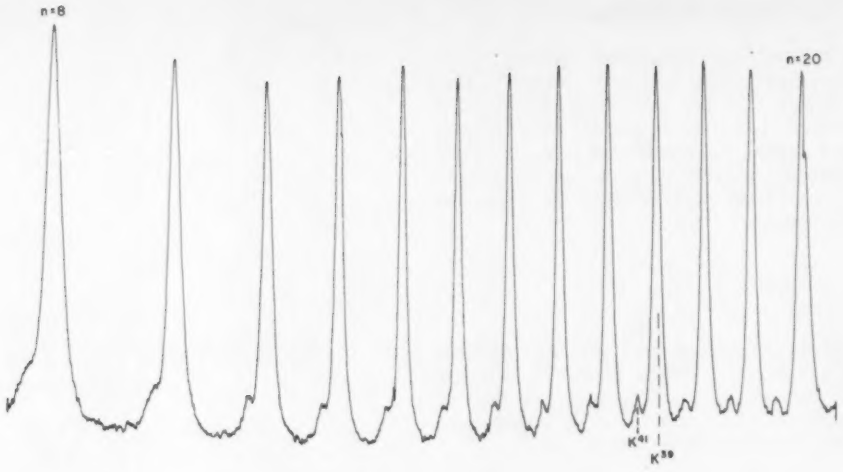

FIGURE 4. *The a-c collector current as a function of rf frequency as plotted by an x-y recorder.*
The eight through twentieth harmonics of K^{39} and K^{41} are shown.

the ratio of their harmonic numbers. That is:

$$\frac{f_n}{f_{n+1}}=\frac{n}{n+1}. \tag{4}$$

This equation can be solved for n, or n can be found conveniently on a slide rule. The procedure is to look for two consecutive integers which have the same ratio as f_n/f_{n+1}. Knowing n and the corresponding frequency, f_n (equal to $1/T_n$), the flight time of the ion, t, is found from $t=nT_n$. If the length of the drift tube is L, eq (1) can be solved for m, using $v=L/t$.

The determination of m becomes difficult if the beam contains ions of many masses. The harmonics of the mass peaks become too cluttered to pick out two adjacent harmonics. In applications requiring the study of complex beams, it would be desirable to eliminate all but one of the harmonics for each mass. Partial elimination of the harmonics has been achieved by applying two radiofrequencies, referred to as f_l and f_h, as in figure 5. Frequency f_l is generated from f_h by frequency division so that the ratio of f_h to f_l is a known whole number, say r.

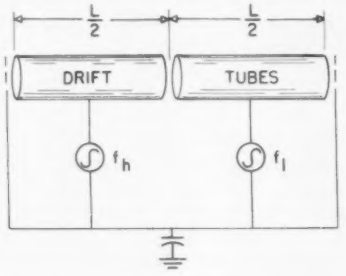

FIGURE 5. *Drift tube arrangement used to eliminate harmonics.*

With the present equipment, r can be chosen to be equal to 2, 4, 8, 16, or 32. In order for the ions to escape a change in energy, they must pass through two drift tubes emerging from each tube after an integral number of rf cycles. Let n_l be the number of rf cycles an ion takes to travel through the first drift tube, and n_h the number of rf cycles an ion takes to travel through the other tube. Since both tubes are of equal length, the transit times for both tubes must be equal. That is, $n_lT_l=n_hT_h$. By definition, $f_l=1/T_l$ and $f_h=1/T_h$.

Then

$$n_l=n_h\frac{T_h}{T_l}=\frac{n_h}{r}.$$

If n_l is equal to one, n_h must be equal to r. If n_l is equal to any integer, k, n_h must be equal to kr. In practice the possibility of k being greater than one for a particular mass is eliminated by sweeping over an rf frequency range of less than one to two. Thus, an ion which would pass through the second drift tube with $n_h \neq r$ does not pass through the first drift tube in a whole number of rf cycles. The voltage at frequency f_l discriminates against the unwanted harmonics while the voltage at frequency f_h resolves the masses as before. As is the case in using a single drift tube, each rf voltage can be increased until the improvement in resolution is balanced out by the adverse effects of velocity modulation.

Figure 6 was obtained by using this principle of harmonic elimination. It shows the frequency range where the 10th through 28th harmonics of potassium would normally appear. The largest peak at the center is the 16th harmonic of K^{39}. The two small peaks on either side are the 15th and 17th harmonics of K^{39}. Figure 6 was made using the maximum low frequency voltage which the equipment could generate.

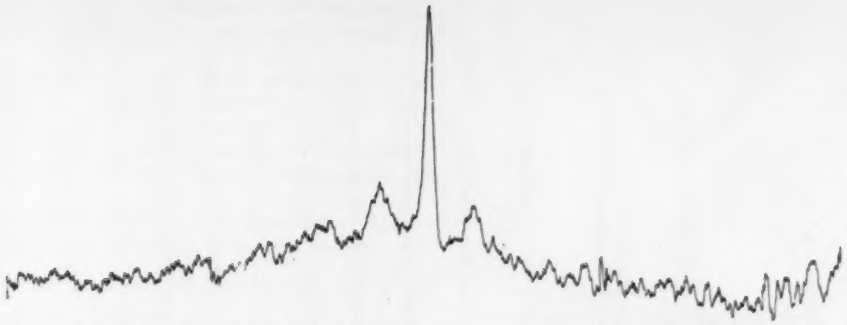

FIGURE 6. *An x-y recorder plot of the a-c collector current as a function of rf frequency using the harmonic elimination equipment.*

The large peak is the 16th harmonic of K^{39}. The smaller peaks on either side are the 15th and 17th harmonic of K^{39}.

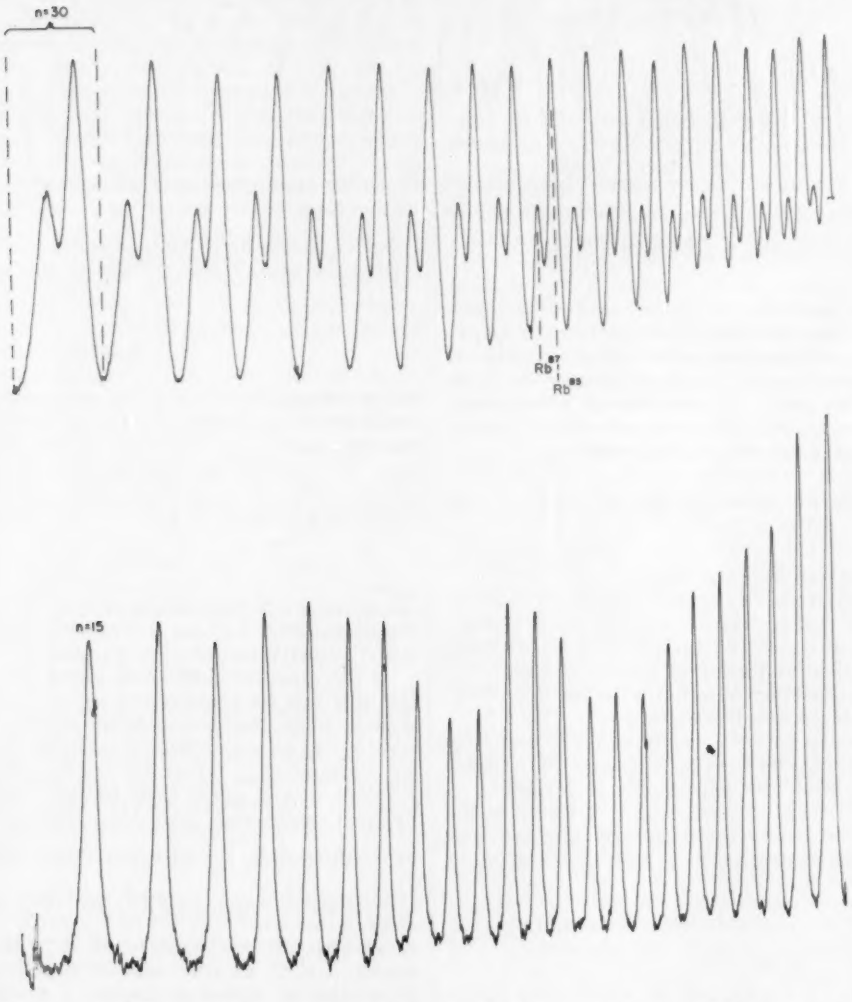

FIGURE 7. *The a-c collector current as a function of rf frequency showing the harmonics of* Rb^{85} *and* Rb^{87} *(a) and of cesium (b).*

The plots were obtained by using an *x-y* recorder.

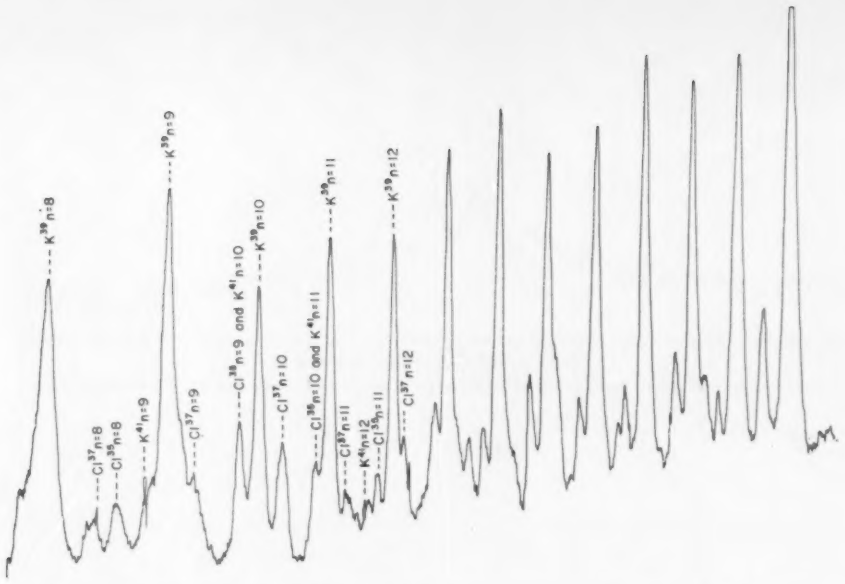

FIGURE 8. *An x-y recorder plot showing a-c collector current as a function of rf frequency.*
Shown are harmonics of K^{39}, K^{41}, Cl^{35} and Cl^{37}.

5. Resolution and Duty Cycle

In order to find the resolution and duty cycle which can be expected from this instrument (without harmonic elimination), the effect of the rf voltage at the entrance of the drift tube on the flight time of the ion must be considered. Neglecting initial energy, the energy of an ion after passing through both rf gaps can be expressed as:

$$e=q\{V_{dc}+V_{rf}F[\sin\omega\tau-\sin\omega(\tau+t)]\} \tag{6}$$

where

V_{dc} is the d-c accelerating voltage,
V_{rf} is the amplitude of the radiofrequency voltage,
t is the time of flight of the ion through the drift tube,
τ is the time at which the ion enters the drift tube,
ω is the angular frequency of the rf voltage,
F is the transit-time factor due to the fact that the gap widths are of finite size.

F can be shown to be very nearly equal to unity by a calculation similar to that in reference [7]. Under the conditions that the gap width is 2 mm, L is 1 m, $n=20$, and that $V_{rf}<<V_{dc}$, F is found to be 0.997. Since the above conditions are valid approximations for this instrument, F will be assumed to be unity.

By writing $v=\frac{L}{t}$ in eq (1):

$$t=t_0\left[1+\frac{V_{rf}}{V_{dc}}\sin\omega\tau\right]^{-\frac{1}{2}} \tag{7}$$

where t_0 is the flight time of an ion which enters the drift tube when the rf voltage is zero and is equal to

$$t_0=L\sqrt{\frac{m}{2qV_{dc}}}. \tag{8}$$

Substituting (7) in (6), the net energy in electron volts which the ion receives from the rf fields is seen to be:

$$e_{rf}=V_{rf}\left\{\sin\omega\tau-\sin\left[\omega\tau+\omega t_0\left(1+\frac{V_{rf}}{V_{dc}}\sin\omega\tau\right)^{-1}\right]\right\} \tag{9}$$

Thus e_{rf} is not zero under the condition that t_0 is a whole number of cycles as was assumed to be the case when velocity modulation was neglected.

If the magnitude of e_{rf} is larger than 3.9 ev, the ion will not be represented in the collector output signal. The theoretical peak shape was found by plotting e_{rf} as a function of $\omega\tau$ between zero and 2π for various ωt_0. Then for each value of ωt_0 the fraction of the cycle over which $-3.9<e_{rf}<+3.9$ ev was measured, and this fraction was plotted as a function of $\frac{\omega t_0}{2\pi}$ in figure 9 over the range $19.5<\frac{\omega t_0}{2\pi}<20.5$. Values of V_{rf} and V_{dc} used were the measured values when t_0 equaled 20 times T for potassium (K^{39}): 24 volts and 3000 volts, respectively. It is seen in figure 9 that as a result of velocity modulation (a) the maximum duty cycle does not actually occur when $\frac{\omega t_0}{2\pi}=\frac{t_0}{T}$ is a whole number as was

the case when velocity modulation was neglected, and (b) the duty cycle at its maximum is equal to 61 percent.

The duty cycle actually obtained under the above conditions was measured by presetting the rf frequency for maximum collector output signal. The ratio of the a-c collector current with rf voltage on to that with rf voltage off was found to be about 60 percent.

For a given radiofrequency, the abscissa of figure 9 may be converted to mass numbers by eq (8). With $\frac{\omega t_0}{2\pi}$ equal to 20 for mass number 39, $\frac{\omega t_0}{2\pi}=20.5$ corresponds to mass number 41.

Up to a point, the difference in e_{rf} between two ions slightly different in mass increases as the time rate of change of the rf voltage increases. The time rate of change can be increased by increasing the rf frequency or by increasing the magnitude of the rf voltage. However, increasing the rf voltage increases the amount of velocity modulation, and it can be seen in figure 9 that velocity modulation causes a broadening in the peak shape. Increasing the frequency of the rf voltage increases the adverse effect of whatever velocity modulation is present. It is thus reasonable to assume that there exist values of V_{rf} and ω which give a maximum resolution.

An analysis of the peak shape was made only for the values of V_{rf} and ωt_0 given above. These values were chosen because they produced good resolution between K^{39} and K^{41} (see fig. 4). It is possible that a further study might show that other values would result in better resolution.

It is assumed in figure 9 that (a) the ions are monoenergetic at the source, (b) they do not lose energy by collisons as they travel through the instrument, (c) they are in perfect focus at the barrier [7], and (d) ions with insufficient energy are cut off with perfect sharpness at the barrier.[2] The center curve in figure 3 indicates a final energy spread in the order of 30 electron volts, probably due mainly to the failures of assumption (a) and (d). Failure of any of the above assumptions results in a lower current efficiency, as well as a broadening of the peak shape. A careful study of these factors has not been made.

6. Results

The following positive ions have been detected with this instrument: K^{39}, K^{41}, Na^{23}, He^4, N_2^+, N^{++}, Cl^{35}, Cl^{37}, Rb^{85}, Rb^{87}, and Cs^{133}. All except the helium and nitrogen ions were obtained by placing salts on a hot tungsten wire filament [9]. Helium and nitrogen were ionized by heating a bare tungsten filament in the respective atmospheres at reduced pressures.

The d-c accelerating voltage was maintained at approximately 3,000 v, and the drift tube was roughly 1.12 m long (0.56 m long when used with the harmonic eliminator). In order to avoid the necessity of measuring V and L accurately, a calibration

[2] For sharp cutoff, the barrier must be such that no field can penetrate through it. The collector must be able to collect ions of large and small energy with equal efficiency and be able to prevent ions which have experienced elastic reflections from escaping the collector.

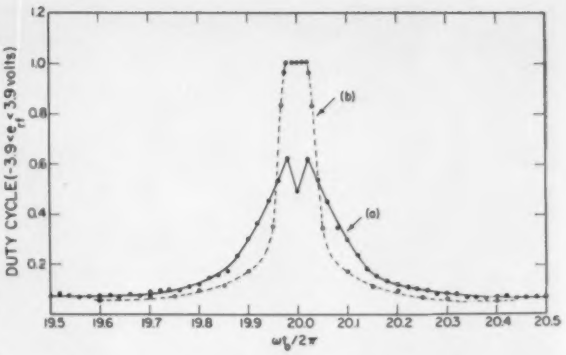

FIGURE 9. *Computed peak shape, (a) with velocity modulation, and (b) when velocity modulation is neglected.*

If ω is set so that $t_0=20T$ for K^{39}, $\omega t_0/2\pi=20.5$ corresponds to K^{41}.

actor d efined as $CF=\frac{1}{T_n}\frac{\sqrt{m}}{n}=\frac{\sqrt{2eV}}{L}$ was measured for each of the ions listed above. It was found to be equal to 0.678 ± 0.003 ($\simeq 0.4\%$) if m is expressed in atomic mass units ($O^{16}=16.00$) and $1/T$ in megacycles.

This figure was obtained by using known values of mass for the above ions. The frequencies at which the various harmonics appeared were measured with a timer-counter. The percent fluctuation of the calibration factor is an indication of the precision of which the instrument is capable. With the present source, it is necessary to apply a focusing field in the region where the filament is located. The proper focusing voltage changes each time the filament is removed to replace the salt. It has been found that this change in focusing voltage produces a slight change in the calibration factor, accounting for a portion of the 0.4 percent variation. For a fixed value of the focusing voltage, the calibration factor is found to vary about 0.1 percent. Figure 7a shows the 30th through 48th harmonics of Rb^{85} and Rb^{87}; figure 7b shows the 15th through 37th harmonics of Cs^{133}. Figure 8 is a mass spectrum showing K^{39}, K^{41}, Cl^{35}, and Cl^{37}. Some variation in the peak heights of the harmonics can be observed in figures 7b and 8. Duplicating these graphs shows that this fluctuation is due to the instability of the source. Little care has been taken, up to date, to ensure linearity in peak heights.

In figure 10, the ion source at the right, the tube containing the drift tube, the collector shielding box, and some of the electronic equipment are visible.

Because of the cluttering of the harmonic peaks, this instrument will be useful in experiments requiring the analysis of ion beams containing a small number of mass components such as those mentioned in the introduction. In experiments where the cluttering is not a serious limitation, the instrument offers important advantages. In addition to the high duty cycle, it has light weight, and electrical and mechanical simplicity. There are no critical alinements or spacings.

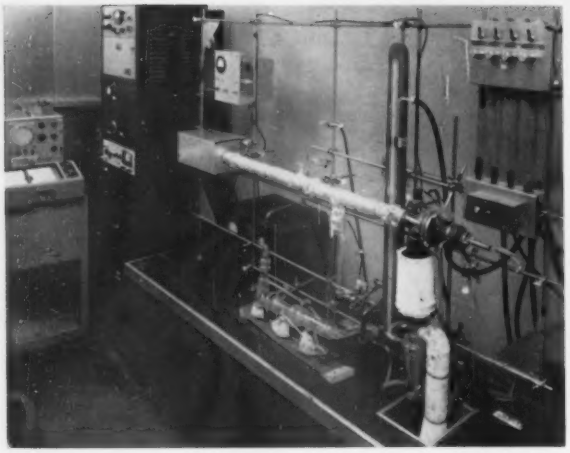

FIGURE 10. *The mass spectrometer.*

The author thanks E. Carroll Creitz for his help and interest, William H. Bailey for his shop work, Louis A. Marzetta and Malcom S. Morse for their work in developing the rf generators, Kenneth McCulloh for pointing out the importance of velocity modulation, and others who have made helpful suggestions.

7. References

[1] W. C. Wiley and I. H. McLaren, Time-of-flight mass spectrometer with improved resolution, Rev. Sci. Instr. **26,** 1150 (1955).
[2] D. B. Harrington, Advances in mass spectrometry, Edited by J. D. Waldron (Pergamon Press, New York, 1959).
[3] P. A. Redhead, A linear radio frequency mass spectrometer, Can. J. Phys. **30,** 1 (1952).
[4] P.A. Redhead and C. R. Crowell, Analysis of the linear r. f. mass spectrometer, J. Appl. Phys. **24,** 331 (1953).
[5] R. E. Fox, W. M. Hickam, D. J. Grove, and T. Kjeldass, Jr., Rev. Sci. Instr. **26,** 1101 (1955).
[6] L. B. Leder and J. A. Simpson, Rev. Sci. Instr. **29,** 571 (1958).
[7] J. J. Livingood, Principles of cyclic particle accelerators, p. 269 (D. Van Nostrand Co., Inc., Princeton, N.J., 1961).
[8] J. A. Simpson, Rev. Sci. Instr. **32,** 1283 (1961).
[9] Mark G. Inghram and Richard J Hayden, Mass spectroscopy, Nuclear Science Series Report No. 14, National Academy of Sciences-National Research Council, Washington, D.C. (1954).

(Paper 67C4–139

JOURNAL OF RESEARCH of the National Bureau of Standards—C. Engineering and Instrumentation
Vol. 67C, No. 4, October–December 1963

A Power-Series Buildup Factor Formulation. Application to Rectangular and Off-Axis Disk Source Problems*

J. H. Hubbell

(May 31, 1963)

The response (e.g., dose-rate) of an isotropic detector to primary radiation from a finite plane source may, for points less than a mean-free-path distant, be evaluated as the sum over an infinite series, This series is derived by expanding the exponential dependence $\exp(-\mu_0 r)$ as a power series in $\mu_0 r$ and integrating, numerically or analytically, each term over the source array. If the medium is effectively infinite and homogeneous, the scattering properties of this medium can be characterized by a point isotropic source buildup factor. Buildup factor data are often approximated by formulas having simple analytic dependences on $\mu_0 r$ and numerical parameters independent of $\mu_0 r$. Any such set of parameters can be used to generate a set of weight functions b_n for an infinite series buildup factor representation

$$\exp(+\mu_0 r) \sum_{n=0}^{\infty} b_n \cdot (-\mu_0 r)^n / n!$$

which can be used with the above primary radiation series solution to give, instead, a series solution including both primary and scattered radiation. Tables of b_n's (*air-dose* buildup only) derived from coefficients of cubic polynomials fitted to the Goldstein-Wilkins data (NYO–3075) are given for $0 \leq n \leq 13$ at primary photon energies of 0.5, 0.7, 1.0, 1.5, 2.0, 3.5, 5.5, 7.5, and 9.5 Mev in water, Al, Fe, Sn, W, Pb, and U. The method is applied to give: (1) a comparison with dose-rates measured by a detector separated from a Co-60 rectangular plaque food irradiator by a layer of steel and a layer of water and (2) dose-rate profiles at constant heights across a cleared circular area in a Co-60 infinite plane source in air.

1. Introduction

A number of methods for evaluating radiation fields from distributed sources have been developed as part of a general program at the National Bureau of Standards [1, 2][1] and other agencies. Some of these methods, which provide easy and rapid solutions to radiation shielding problems, rely on the approximate proportionality between dose-rate and the solid angle subtended by a uniformly radiating surface. This approximation has been shown to be quite good if the material interposed between source and detector is of the order of a mean free path in thickness [3].

For situations involving much less than a mean free path of interposed material, as in the case of a detector separated from a surface deposition of radioactive material by only a thin roof or a few feet of air [4, 5], the power-series method developed by Sievert [6] for circular disk sources has been extended [7, 8] to include rectangular sources and to take into account point-source buildup factor data in polynomial form [9].

In addition, it has been reported [10] that buildup data from a number of other analytic formulations [11–15] can also readily be transformed for direct use in a Sievert-type power-series solution. The present work constitutes a published account of the material reported in [10] and includes a quantitative comparison of the buildup data formulations considered [9, 11–15] for Co-60 gamma rays in aluminum for zero to ten mean-free-path penetrations, a table of buildup data transformations, a sample table of transformed buildup data, and sample calculations and results.

Besides fallout radiation studies [5], the power series method is applicable, or has already been applied [16] to such diverse distributed source studies as:

(a) Tracer studies involving an elongated rectangle as the initial distribution of radioisotope-tagged sand in a beach-erosion sand-drift experiment [16],

(b) food irradiator design studies involving plaque sources [3, 17, 18], and

(c) calculation of the dose distribution in tissue adjacent to disk or other shaped radioactive applicators for treatment of malignancies [6, 19]. Also, buildup data in the form of the series coefficients presented here are directly applicable to a method

*Work supported jointly by the Office of Civil Defense (DOD), the Navy Bureau of Yards and Docks, and the Defense Atomic Support Agency.

[1] Figures in brackets indicate the literature references at the end of this paper.

of barrier shape optimization described by Jain and Sharma [20] who use, in effect, the first three terms of this series for their analysis.

2. Buildup Factor: Definition and Discussion

As in references [9] through [15], the source and detector environment is idealized throughout this paper as a homogeneous infinite medium, shown schematically in figure 1. In such an idealized situation the scattered radiation reaching the detector can be taken into account by means of a point isotropic (PTI) source buildup factor [21]

$$B_{\mathrm{PTI}}(E_0, Z, r)=(D^0+D^s)/D^0 \qquad (1)$$

which depends on the effective atomic number Z characterizing the medium and the distance r between the detector and a monoenergetic point source of photons of energy [2] E_0.

The quantities D^0 and D^s in (1) refer to the unscattered and the scattered components, respectively, of the radiation received by the detector. For a given physical situation, D^0 and D^s (and hence $B_{\mathrm{PTI}}(E_0, Z, r)$) can assume a variety of numerical values depending on what kind of detector response (e.g., photon number flux [22], energy current [22] at an interface, energy dissipation in a medium- or air-equivalent detector, etc.) is used to describe the radiation field. The buildup factor data in this work correspond to a detector which measures radiation *flux* in terms of *energy dissipation in air*. In this case $B_{\mathrm{PTI}}(E_0, Z, r)$, D^0 and D^s in (1) are the same as the quantities B_d, $I_d^{(0)}$ and $I_d^{(s)}$ defined in [21].

[2] Here, and in what follows, the source is considered to be either monoenergetic or an effectively monoenergetic component of a photon energy distribution over which the final results must be summed.

The total detector response D to a point isotropic source is

$$D=D^0+D^s=D^0B_{\mathrm{PTI}}(E_0, Z, r)$$
$$=(k/4\pi)[\exp(-\mu_0 r)/r^2]B_{\mathrm{PTI}}(E_0, Z, r) \qquad (2)$$

in which $\mu_0[=\mu(E_0, Z)]$ is the narrow-beam attenuation coefficient [23] at photon energy E_0 for the *medium*. The source strength factor k, for the detector response-type ($D=I_d$) specified above is

$$k=n\times E_0\times\mu_{en}(E_0, Z)\times(\text{dimensional factors}) \qquad (3)$$

where n is the total number of photons of energy E_0 emitted per second by the source, $\mu_{en}(E_0, Z)$ is the energy absorption coefficient [24] for *air*,[3] and the "dimensional factors" provide the units [e.g., (rads/hr)/curie] desired in the final answer.

3. Analytic Formulations for $B_{\mathrm{PTI}}(E_0, Z, r)$

For applying buildup data to distributed source problems, the dependence of $B_{\mathrm{PTI}}(E_0, Z, r)$ on r is usually approximated by some analytic function. This not only provides some economy in data tabulation, but the function can be so chosen that its presence entails little or no additional complication in the integration

$$D=(\sigma/4\pi)\int_S[\exp(-\mu_0 r)/r^2]B_{\mathrm{PTI}}(E_0, Z, r)dS \qquad (4)$$

of (2) over a distributed source S with differential elements dS, as schematized in figure 2. The constant factor in (4)

$$\sigma=dk/dS \qquad (5)$$

[3] Note, however, that example 1 in section 7 requires an answer in terms of energy dissipation in *water* ($D=I_{\mathrm{D}}$) rather than in *air* ($D=I_d$), so, that $\mu_{en}(E_0, \mathrm{H_2O})$ is used in the computation in 7.1, rather than $\mu_{en}(E_0, \text{air})$ corresponding to the data in table 3 in section 5.

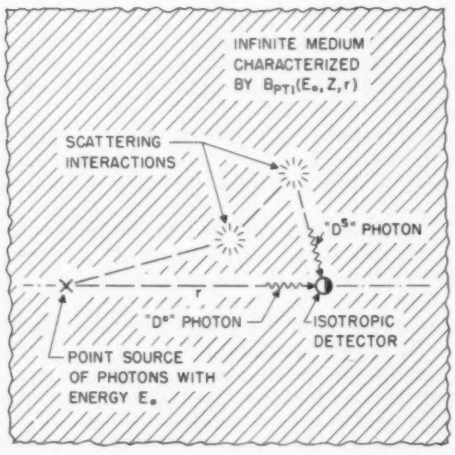

FIGURE 1. *Point isotropic source geometry.*

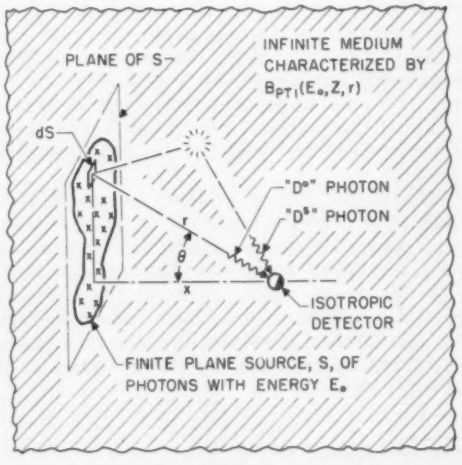

FIGURE 2. *Finite plane isotropic source geometry.*

is the source strength per unit of source area or volume, with k defined as in (3).

The following functions (a) to (f) have been used to represent point isotropic source $B_{\mathrm{PTI}}(E_0, Z, r)$ data in order to obtain analytic solutions to (4).

(a) Linear approximation [11] (one parameter):

$$B_{\mathrm{PTI}}(E_0, Z, r)=1+a\mu_0 r \tag{6}$$

where

$$a=(\mu_0-\mu_{en})/\mu_{en}. \tag{7}$$

(b) Exponential-linear empirical fit [12] (two parameters):

$$B_{\mathrm{PTI}}(E_0, Z, r)=1+a\mu_0 r \exp(-b\mu_0 r). \tag{8}$$

(c) Exponential-polynomial fit [13] (one or three parameters):

$$B_{\mathrm{PTI}}(E_0, Z, r)=\exp(+\mu_0 r)(br+1) \tag{9a}$$

or, for larger thicknesses:

$$B_{\mathrm{PTI}}(E_0, Z, r)=\exp(+\mu_0 r)(ar^2+br+c). \tag{9b}$$

(d) Low order polynomial fit [9, 25] (three parameters):

$$B_{\mathrm{PTI}}(E_0, Z, r)=1+\beta_1\mu_0 r+\beta_2(\mu_0 r)^2+\beta_3(\mu_0 r)^3. \tag{10}$$

(e) Sum-of-exponentials fit [14] (three parameters):

$$B_{\mathrm{PTI}}(E_0, Z, r)=A \exp(-a_1\mu_0 r)+(1-A) \exp(-a_2\mu_0 r) \tag{11}$$

(f) Exponential-linear moments calculation result [15] (four parameters):

$$B_{\mathrm{PTI}}(E_0, Z, r)=1+\mu_0 r\{A_1B_1 \exp[(1-B_1)\mu_0 r]+A_2B_2 \exp[(1-B_2)\mu_0 r]\}. \tag{12}$$

Table 1 contains data calculated at $\mu_0 r=1, 2, 4, 7$, and 10 mean free paths according to approximation (a) above, empirical fits (b) to (e) and direct-result parameters (f), in addition to earlier calculated results from NYO-3075, [26] (g), all for "exposure dose" (air-equivalent detector) in aluminum and interpolated to 1.25 Mev.

The column headed ϵ_f beside each column of calculated data contains percent deviations from the recent Berger-Spencer [15] results (f),

$$\epsilon_f=\frac{B-B\ (\text{Berger-Spencer})}{B\ (\text{Berger-Spencer})}\times 100\% \tag{13}$$

and the column headed ϵ_g contains percent deviations from the Goldstein-Wilkins results (g) to which (b), (d), and (e) were fitted,

$$\epsilon_g=\frac{B-B\ (\text{Goldstein-Wilkins})}{B\ (\text{Goldstein-Wilkins})}\times 100\%. \tag{14}$$

As seen in table 1, the Goldstein [11] linear approximation (a), above, involves neither fitting nor transport theory calculations. It is very useful for penetrations up to one or two mean free paths, and gives results within a factor of two up to ten mean free paths in aluminum.

TABLE 1. *The point isotropic source buildup factor ("exposure dose": air-equivalent detector), $B_{\mathrm{PTI}}(E_0, Z)$, for 1.25-Mev gamma rays in aluminum evaluated from five different analytic approximations (a to e) at 0, 1, 2, 4, 7, and 10 mfp, compared with the corresponding moments-calculated analytic (f) and numerical (g) results*

	(a) Goldstein [11] 1-parameter linear approximation (6)			(b) Chilton et al. [12] 2-parameter exponential-linear fit (8)			(c) Leshchinskii [13] 1-parameter exponential-linear fit (9a)		
$\mu_0 r$	B_{PTI}	ϵ_f*	ϵ_g**	B_{PTI}	ϵ_f	ϵ_g	B_{PTI}	ϵ_f	ϵ_g
		%	%		%	%		%	%
0	1.00	0	0	1.00	0	0	1.00	0	0
1	2.06	7.9	7.3	1.97	3.1	2.6	1.80	−5.8	−6.3
2	3.01	−1.0	−2.0	3.06	0.7	−0.3	2.41	−21	−21
4	5.04	−13	−13	5.69	−2.2	−2.2	−18.9	----------	----------
7	8.04	−27	−29	11.0	0	−3.5	−1490	----------	----------
10	11.0	−36	−37	18.3	6.4	4.6	−52100	----------	----------

	(d) Capo [9] 3-parameter polynomial (cubic) fit (10)			(e) Taylor [14] 3-parameter sum-of-exponnetials fit (11); Lakey [28] data			(f) Berger-Spencer [15] 4-parameter exponential-linear moments calculation results (12)	(g) Goldstein-Wilkins [26] moments calculation results; Al data in tabulated form only
$\mu_0 r$	B_{PTI}	ϵ_f	ϵ_g	B_{PTI}	ϵ_f	ϵ_g	B_{PTI}	B_{PTI}
		%	%		%	%		
0	0.997	−0.3	−0.3	1.00	0	0	1.00	1.00
1	1.93	1.0	0.5	2.10	9.0	9.4	1.91	1.92
2	3.05	0.3	−0.7	3.26	7.2	6.2	3.04	3.07
4	5.81	−0.2	−0.2	5.76	−1.0	−1.0	5.82	5.82
7	11.1	0.9	−2.6	10.2	−7.3	−11	11.0	11.4
10	17.6	2.3	0.6	15.7	−8.7	−10	17.2	17.5

* $\epsilon_f=[(B_{\mathrm{PTI}}-B_{\mathrm{PTI}}(\text{Berger-Spencer}))/B_{\mathrm{PTI}}(\text{Berger-Spencer})]\times 100\%$.
** $\epsilon_g=[(B_{\mathrm{PTI}}-B_{\mathrm{PTI}}(\text{Goldstein-Wilkins}))/B_{\mathrm{PTI}}(\text{Goldstein-Wilkins})]\times 100\%$.

The two-parameter exponential-linear empirical fit (b) of Chilton, Holoviak, and Donovan [12] is surprisingly good for penetrations up to ten mean free paths. This formulation, similar in form to the calculated result (f) of Berger and Spencer [15], can thus provide economical storage and easy application of buildup data over a wider range of penetration thicknesses. Reference [12] contains parametric data for aluminum only, which was the deciding factor in selecting this as the reference substance for table 1.

Leshchinskii [13] supplied data, for the reference situation of Co–60 gammas in aluminum, only for the one-parameter exponential-linear fit (9a), intended for penetrations of 0 to 10 cm (0 to 1.49 mean free paths), although for Co–60 gammas in water he *did* use the three-parameter fit (9b) for penetrations of 2 to 70 cm (0.127 to 4.44 mean free paths). In each case the fit is within about 5 percent up to the specified upper limit and then departs wildly. However, this formulation does have the advantage that the exponential dependence exp $(-\mu_0 r)$ is canceled out of the distributed source integral (4), and it will be seen that the power-series solution of (4) [8, 10] is, in effect, a generalization of the Leshchinskii result.

The slight departure of the Capo data (d) from the condition $B_{\mathrm{PTI}}(E_0, Z, r)=1$ at $\mu_0 r=0$ results from additional cross fitting as a polynomial in energy or reciprocal energy, in which it is difficult to preserve this normalization. This discrepancy is not large enough to detract from the usefulness of the data, however, and in this specific comparison (1.25 Mev photons in Al) the departures ϵ_f and ϵ_g from calculated data (f) and (g) are seen to be less, over the given range of $\mu_0 r$ values, than corresponding departures of (a), (b), (c), and (e).

In addition to the empirically fitted Capo tabulation, β_i polynomial coefficients for Co–60 and Cs–137 gamma rays in concrete and water were directly calculated by Spencer [1] using the moments method and were punched on IBM cards for use in further calculations. In [1] the A_j coefficients in (A1), page 80, are identical with β_i coefficients if (a) A_j refers to the zeroth Legendre harmonic ($l=0$), and (b) A_j refers to integral dose data rather than to the differential energy data indicated by the dependence on E_i in (A1).

The sum-of-exponentials three-parameter fit (4) of Taylor [14] is perhaps the most well-known and widely used buildup factor formulation in current use [27]. The only published parametric data for aluminum seem to be those of Lakey [28], and these were used for the comparison in table 1.

The exponential-linear four-parameter formula (f) of Berger and Spencer [15] represents direct calculated results by the moment method [21]. Parametric data in [15] are tabulated for 0.0341- to 10.22-Mev gamma-rays in aluminum and concrete, and additional formulas are supplied for applying these buildup parameters to such geometries as the isotropic disk source (on-axis) and the isotropic spherical surface source. The buildup data in table 1, obtained by evaluating (12) using parameters interpolated to 1.25 Mev, agree within 4 percent with the earlier moments calculation [21] results of Goldstein and Wilkins [26], (g), to which the formulas (b), (d), and (e) were fitted.

4. Power-Series Solution for Unscattered Radiation From a Distributed Source

It has been shown [6, 7] that for finite plane sources of simple shape, a solution of (4) for D^0 (i.e., omitting the factor $B_{\mathrm{PTI}}(E_0, Z, r)$ within the integrand) may be obtained in the form of an infinite series

$$D^0=(\sigma/4\pi)\sum_{n=0}^{\infty} q_n(\mathrm{geom})\cdot(\mu_0 x)^n \qquad (15)$$

which converges quickly when the detector is less than a mean free path from the source. The dimensionless q_n(geom) coefficients in (15) depend only on the *shape* of the detector-source geometry, and are derived from a power series expansion of the exponential in (4)

$$\exp\,(-\mu_0 r)=\sum_{n=0}^{\infty}(-\mu_0 r)^n/n! \qquad (16)$$

such that

$$q_n(\mathrm{geom})=\int_S (-r/x)^n dS/(r^2\cdot n!). \qquad (17)$$

The quantity $\mu_0 x$, also dimensionless, is the mean-free-path thickness of material between source and detector.

Formulas and tables of q_n(geom) coefficients (tables include values for $0\leq n\leq 9$) have been generated for a rectangular source [7] and for a circular disk source with detector off-axis [8]. As a check, it was noted [8] that for a detector on-axis over a circular disk source the series (15) reduces to the familiar exponential-integral solution, in which the exponential integrals $E_1(x)$ are replaced by power series in x.

5. Adaptation of Analytic $B_{\mathrm{PTI}}(E_0, Z, r)$ Formulations to the Distributed Source Power-Series Solution

In the series solution (15) for the unscattered component D^0 in section 4, the material between source and detector can either be distributed throughout the intervening space, or can be arranged as one or more uniform slabs or sheets lying parallel to the source-plane. In this section, on the other hand, the source and detector are assumed embedded, as discussed in section 2, in an infinite homogeneous medium.

Replacing the polynomial in the Leshchinskii formula (9b) by a power series we obtain the buildup factor formulation

$$B_{\mathrm{PTI}}(E_0, Z, r)=\exp\,(+\mu_0 r)\sum_{n=0}^{\infty} b_n(E_0, Z)\cdot(-\mu_0 r)^n/n! \tag{18}$$

reported in [10], from which the coefficients[4] $b_n(E_0, Z)$ can be used with the series solution (15). The only change in (15) is the multiplication of each series term $q_n(\mathrm{geom})\cdot(\mu_0 x)^n$ by the additional factor $b_n(E_0, Z)$ to give the *total* dose-rate solution

$$D=D^p+D^s=(\sigma/4\pi)\sum_{n=0}^{\infty} b_n(E_0, Z)\cdot q_n(\mathrm{geom})\cdot(\mu_0 x)^n. \tag{19}$$

Equations (18) and (19) are, of course, of little practical value if an infinite number of $b_n(E_0, Z)$ coefficients must be fitted and tabulated. However, by expanding as power-series all exponentials appearing in the analytic formulations (a) to (f) in section 3, then equating coefficients of like powers of $\mu_0 r$, a transformation for generating $b_n(E_0, Z)$ coefficients from the parameters of any of these formulations may be obtained. Table 2 presents these "parasite" transformations, and includes (18) for comparison.

[4] The simpler notation $b_n(E_0, Z)$, used throughout this work, is equivalent to $B'_n(E_0, Z)$ used in [8] and [10].

The surprisingly simple transformation (e) of Taylor [14] and Lakey [28] parametric data results because inclusion of a $B_{\mathrm{PTI}}(E_0, Z, r)$ of this form into (4) produces no change in the analytic form of the integrand. It can also be seen in table 2 that the Goldstein [11] linear approximation (a) is a special case of the polynomial fit (d) used by Capo [9], and that the four-parameter calculated result (f) of Berger and Spencer [15] is identical in analytic form with the two-parameter empirical fit (b) of Chilton et al. [12]. The similarities are reflected in the respective transformations in the last column.

To illustrate the use of table 2, transformation (d) was used to generate the $b_n(E_0, Z)$ values for $0\leq n\leq 13$ in table 3 from "dose" (air-equivalent detector) buildup data for water, Al, Fe, Sn, Pb, W, and U in the form of $\beta_i(E_0, Z)$ polynomial coefficients. The input $\beta_i(E_0, Z)$'s were taken from reference [9], tables 1B, 4B, 7B, 10C, 13B, 16C, and 18B which in turn were fitted by least squares to data calculated by Goldstein and Wilkins [26] using the moments method. Of the 15 gamma-ray energies from 0.4 to 9.5 Mev presented in [9] for reactor "operating" and "shutdown" shielding calculations, the 10 energies $E_0=0.5$, 0.7, 1.0, 1.5, 2.0, 2.5, 3.5, 5.5, 7.5, and 9.5 Mev were arbitrarily selected.

The appearance in table 3 of $b_0(E_0, Z)$ $\{=\beta_0(E_0, Z)=B(E_0, Z, r)$ at $\mu_0 r=0\}$ values which are not unity follows from the discussion of the Capo data in section 3.

TABLE 2.—*Summary of analytic formulations (a to f) for the point isotropic source buildup factor* $B_{\mathrm{PTI}}(E_0, Z)$ *(column 4)*

The power-series formulation, in which the "∞" for number of parameters (column 3) may be replaced by 1, 2, 3, 4, or N, depending on which of the formulations (a to f) is used for generating the $b_n(E_0, Z)$ coefficients, has been added for comparison. The last column contains the "parasite" transformations, of which (d) was used to generate the sample $b_n(E_0, Z)$'s in table 3 from the Capo [9] tables of β_i polynomial coefficients

Formulation	Reference	Number of parameters	$B_{\mathrm{PTI}}(E_0, Z, r)$, point isotropic source	Eq No.	$b_n(E_0, Z)$; $n=0, 1, 2, \ldots$
(a)	Goldstein [11]	1	$1+a\mu_0 r$	(6)	$1-na$
(b)	Chilton, Holoviak, Donovan [12]	2	$1+a\mu_0 r\exp(-b\mu_0 r)$	(8)	$1-a\sum_{i=1}^{n} i\binom{n}{i}b^{i-1}$
(c)	Leshchinskii [13]	1	$\exp(+\mu_0 r)(br+1)$	(9a)	$b_0=1;\ b_1=-b/\mu_0;\ b_{n\geq 2}=0$
		3	$\exp(+\mu_0 r)(ar^2+br+c)$	(9b)	$b_0=c;\ b_1=-b/\mu_0;\ b_2=2a/\mu_0^2;\ b_{n\geq 3}=0$
(d)	Capo [9]	3 or N	$\sum_{i=0}^{N}\beta_i(E_0, Z)(\mu_0 r)^i$	(10)	$\sum_{i=0}^{n\leq N}(-1)^i\{n!/(n-i)!\}\beta_i(E_0, Z)$
(e)	Taylor, [14] Lakey [28]	3	$A\exp(-a_1\mu_0 r)+(1-A)\exp(-a_2\mu_0 r)$	(11)	$A(1+a_1)^n+(1-A)(1+a_2)^n$
(f)	Berger, Spencer [15]	4	$1+\mu_0 r[A_1B_1\exp[-(B_1-1)\mu_0 r]+A_2B_2\exp[-(B_2-1)\mu_0 r]]$	(12)	$1-\sum_{i=1}^{n} i\binom{n}{i}[A_1B_1(B_1-1)^{i-1}+A_2B_2(B_2-1)^{i-1}]$
Power series	This work	∞	$\exp(+\mu_0 r)\sum_{n=0}^{\infty} b_n(E_0, Z)\cdot(-\mu_0 r)^n/n!$	(18)	$b_n(E_0, Z)$

TABLE 3. *Coefficients $b_n(E_0, Z)$ of the power-series buildup factor formulation (18) derived from the Capo [9] β_i polynomial coefficients according to transformation (d), table 2.*

These b_n (E_0, Z) coefficients may be used directly in the distributed source series solution (19) with geometry coefficeints g_n (geom) (17) such as are given in references [7] and [8] for rectangular or off-axis disk sources.

$b_n(E_0, H_2O)$

n \ E_0(Mev)	0.5	0.7	1.0	1.5	2.0
0	1.0011 (0)	1.0008 (0)	9.9678 (−1)	9.9480 (−1)	9.9542 (−1)
1	6.4656 (−2)	5.0643 (−2)	9.7950 (−3)	6.6752 (−2)	1.5973 (−1)
2	2.3708 (−1)	−2.4382 (−1)	−6.3441 (−1)	−7.1188 (−1)	−5.9935 (−1)
3	1.4491 (0)	1.0713 (−1)	−9.2998 (−1)	−1.3348 (0)	−1.2776 (0)
4	3.6313 (0)	1.0932 (0)	−8.7106 (−1)	−1.7959 (0)	−1.8709 (0)
5	6.7143 (0)	2.7040 (0)	−4.5177 (−1)	−2.0887 (0)	−2.3751 (0)
6	1.0629 (1)	4.9293 (0)	1.3372 (−1)	−2.2071 (0)	−2.7859 (0)
7	1.5306 (1)	7.7588 (0)	3.4913 (0)	−2.1448 (0)	−3.0992 (0)
8	2.0675 (1)	1.1182 (1)	3.0268 (0)	−1.8955 (0)	−3.3109 (0)
9	2.6668 (1)	1.5189 (1)	4.9461 (0)	−1.4529 (0)	−3.4167 (0)
10	3.3216 (1)	1.9769 (1)	7.2551 (0)	−8.1092 (−1)	−3.4124 (0)
11	4.0248 (1)	2.4912 (1)	9.9595 (0)	3.6838 (−2)	−3.2940 (0)
12	4.7695 (1)	3.0608 (1)	1.3065 (1)	1.0966 (0)	−3.0571 (1)
13	5.5489 (1)	3.6846 (1)	1.6578 (1)	2.3746 (0)	−2.6977 (0)

n \ E_0(Mev)	2.5	3.5	5.5	7.5	9.5
0	9.9663 (−1)	9.9899 (−1)	1.0022 (0)	1.0042 (0)	1.0054 (0)
1	2.4502 (−1)	3.7542 (−1)	5.2925 (−1)	6.1392 (−1)	6.6696 (−1)
2	−4.6449 (−1)	−2.3628 (−1)	4.9890 (−2)	2.1199 (−1)	3.1471 (−1)
3	−1.1293 (0)	−8.3515 (−1)	−4.3613 (−1)	−2.0236 (−1)	−5.2252 (−2)
4	−1.7467 (0)	−1.4203 (0)	−9.2912 (−1)	−6.2983 (−1)	−4.3481 (−1)
5	−2.3140 (0)	−1.9906 (0)	−1.4294 (0)	−1.0711 (0)	−8.3385 (−1)
6	−2.8287 (0)	−2.5453 (0)	−1.9372 (0)	−1.5270 (0)	−1.2503 (0)
7	−3.2881 (0)	−3.0834 (0)	−2.4529 (0)	−1.9981 (0)	−1.6849 (0)
8	−3.6895 (0)	−3.6040 (0)	−2.9767 (0)	−2.4851 (0)	−2.1387 (0)
9	−4.0302 (0)	−4.1060 (0)	−3.5090 (0)	−2.9888 (0)	−2.6124 (0)
10	−4.3077 (0)	−4.5885 (0)	−4.0501 (0)	−3.5099 (0)	−3.1071 (0)
11	−4.5193 (0)	−5.0506 (0)	−4.5980 (0)	−4.0491 (0)	−3.6235 (0)
12	−4.6623 (0)	−5.4914 (0)	−5.1597 (0)	−4.6071 (0)	−4.1626 (0)
13	−4.7340 (0)	−5.9099 (0)	−5.7288 (0)	−5.1846 (0)	−4.7253 (0)

$b_n(E_0, Al)$ $Z=13$

n \ E_0(Mev)	0.5	0.7	1.0	1.5	2.0
0	1.0001 (0)	9.9999 (−1)	9.9819 (−1)	9.9641 (−1)	9.9640 (−1)
1	−1.3070 (−1)	−2.5215 (−1)	9.0059 (−2)	2.1928 (−1)	2.7129 (−1)
2	−7.8756 (−1)	−1.2030 (0)	−5.6633 (−1)	−4.0565 (−1)	−3.6339 (−1)
3	−9.8747 (−1)	−1.8585 (0)	−9.6259 (−1)	−8.6972 (−1)	−9.0190 (−1)
4	−7.4740 (−1)	−2.2242 (0)	−1.0904 (0)	−1.1643 (0)	−1.3385 (0)
5	−8.4323 (−2)	−2.3060 (0)	−9.4128 (−1)	−1.2806 (0)	−1.6674 (0)
6	1.1545 (0)	−2.1097 (0)	−5.0695 (−1)	−1.2101 (0)	−1.8828 (0)
7	2.4430 (0)	−1.6409 (0)	2.2099 (−1)	−9.4414 (−1)	−1.9791 (0)
8	4.2732 (0)	−9.0553 (−1)	1.2509 (0)	−4.7400 (−1)	−1.9505 (0)
9	6.4586 (0)	9.0729 (−2)	2.5912 (0)	2.0895 (−1)	−1.7912 (0)
10	8.9821 (0)	1.3421 (0)	4.2502 (0)	1.1134 (0)	−1.4954 (0)
11	1.1827 (1)	2.8321 (0)	6.2364 (0)	2.2479 (0)	−1.0575 (0)
12	1.4976 (1)	4.5870 (0)	8.5580 (0)	3.6213 (0)	−4.7163 (−1)
13	1.8412 (1)	6.5691 (0)	1.1224 (1)	5.2421 (0)	2.6792 (−1)

n \ E_0(Mev)	2.5	3.5	5.5	7.5	9.5
0	9.9700 (−1)	9.9849 (−1)	1.0008 (0)	1.0022 (0)	1.0032 (0)
1	3.2250 (−1)	4.2042 (−1)	5.6586 (−1)	6.5832 (−1)	7.2035 (−1)
2	−2.9618 (−1)	−1.3354 (−1)	1.3872 (−1)	3.7355 (−1)	4.4436 (−1)
3	−8.5539 (−1)	−6.6191 (−1)	−2.8031 (−1)	−1.1564 (−2)	1.7550 (−1)
4	−1.3515 (0)	−1.1632 (0)	−6.9091 (−1)	−3.3714 (−1)	−8.5906 (−2)
5	−1.7808 (0)	−1.6359 (0)	−1.0928 (0)	−6.5622 (−1)	−3.3960 (−1)
6	−2.1397 (0)	−2.0785 (0)	−1.4856 (0)	−9.6859 (−1)	−5.8528 (−1)
7	−2.4251 (0)	−2.4896 (0)	−1.8690 (0)	−1.2741 (0)	−8.2266 (−1)
8	−2.6316 (0)	−2.8676 (0)	−1.2427 (0)	−1.5724 (0)	−1.0515 (0)
9	−2.7573 (0)	−3.2110 (0)	−2.6069 (0)	−1.8635 (0)	−1.2714 (0)
10	−2.7981 (0)	−3.5183 (0)	−2.9598 (0)	−2.1471 (0)	−1.4821 (0)
11	−2.7501 (0)	−3.7882 (0)	−3.3026 (0)	−2.4230 (0)	−1.6834 (0)
12	−2.6098 (0)	−4.0189 (0)	−3.6343 (0)	−2.6910 (0)	−1.8749 (0)
13	−2.3736 (0)	−4.2092 (0)	−3.9548 (0)	−2.9510 (0)	−2.0563 (0)

* See footnote at end of table.

TABLE 3. *Coefficients $b_n(E_0, Z)$ of the power-series buildup factor formulation (18) derived from the Capo [9] β_i polynomial coefficients according to transformation (d), table 2.—Continued

$b_n(E_0, Fe)$ $Z=26$

n \ E_0(Mev)	0.5	0.7	1.0	1.5	2.0
0	1.0025 (0)	9.3280 (−1)	1.0002 (0)	1.0162 (0)	1.0100 (0)
1	1.4156 (−1)	9.3980 (−3)	2.1196 (−1)	3.0483 (−1)	3.6092 (−1)
2	−5.2529 (−1)	−6.6107 (−1)	−4.1423 (−1)	−3.0932 (−1)	−2.1516 (−1)
3	−9.9713 (−1)	−1.0661 (0)	−8.7359 (−1)	−8.2351 (−1)	−7.1552 (−1)
4	−1.2730 (0)	−1.1932 (0)	−1.1632 (0)	−1.2350 (0)	−1.1374 (0)
5	−1.3520 (0)	−1.0298 (0)	−1.2726 (0)	−1.5412 (0)	−1.4781 (0)
6	−1.2332 (0)	−5.6333 (−1)	−1.2028 (0)	−1.7393 (0)	−1.7348 (0)
7	−9.1560 (−1)	2.1860 (−1)	−9.4685 (−1)	−1.8266 (0)	−1.9048 (0)
8	−3.9830 (−1)	1.3286 (0)	−5.0014 (−1)	−1.8004 (0)	−1.9854 (0)
9	3.1965 (−1)	2.7791 (0)	1.4217 (−1)	−1.6581 (0)	−1.9738 (0)
10	1.2392 (0)	4.5827 (0)	9.8487 (−1)	−1.3968 (0)	−1.8672 (0)
11	2.3612 (0)	6.7518 (0)	2.0328 (0)	−1.0139 (0)	−1.6629 (0)
12	3.6868 (0)	9.2991 (0)	3.2907 (0)	−5.0678 (−1)	−1.3582 (0)
13	5.2167 (0)	1.2237 (1)	4.7633 (0)	1.2739 (−1)	−9.5027 (−1)

n \ E_0(Mev)	2.5	3.5	5.5	7.5	9.5
0	1.0043 (0)	9.9882 (−1)	9.9768 (−1)	9.9931 (−1)	1.0011 (0)
1	4.1631 (−1)	5.1544 (−1)	6.5356 (−1)	7.3825 (−1)	7.9417 (−1)
2	−1.1129 (−1)	7.8643 (−2)	3.4281 (−1)	5.0375 (−1)	6.0957 (−1)
3	−5.7593 (−1)	−3.0975 (−1)	6.5479 (−2)	2.9451 (−1)	4.4503 (−1)
4	−9.7500 (−1)	−6.4792 (−1)	−1.7841 (−1)	1.0922 (−1)	2.9831 (−1)
5	−1.3059 (0)	−9.3405 (−1)	−3.8883 (−1)	−5.3419 (−2)	1.6714 (−1)
6	−1.5660 (0)	−1.1663 (0)	−5.6575 (−1)	−1.9471 (−1)	4.9286 (−2)
7	−1.7526 (0)	−1.3429 (0)	−7.0913 (−1)	−3.1596 (−1)	−5.7516 (−2)
8	−1.8633 (0)	−1.4620 (0)	−8.1896 (−1)	−4.1847 (−1)	−1.5552 (−1)
9	−1.8953 (0)	−1.5218 (0)	−8.9519 (−1)	−5.0353 (−1)	−2.4696 (−1)
10	−1.8461 (0)	−1.5205 (0)	−9.3780 (−1)	−5.7246 (−1)	−3.3411 (−1)
11	−1.7131 (0)	−1.4562 (0)	−9.4676 (−1)	−6.2656 (−1)	−4.1921 (−1)
12	−1.4935 (0)	−1.3272 (0)	−9.2203 (−1)	−6.6712 (−1)	−5.0452 (−1)
13	−1.1850 (0)	−1.1316 (0)	−8.6360 (−1)	−6.9545 (−1)	−5.9228 (−1)

$b_n(E_0, Sn)$ $Z=50$

n \ E_0(Mev)	0.5	0.7	1.0	1.5	2.0
0	1.0021 (0)	1.0023 (0)	1.0014 (0)	1.0008 (0)	1.0007 (0)
1	4.4293 (−1)	4.7107 (−1)	3.8940 (−1)	3.9964 (−1)	4.5973 (−1)
2	−1.3701 (−1)	−3.7218 (−2)	−1.8271 (−1)	−1.5486 (−1)	−3.2606 (−2)
3	−7.4062 (−1)	−5.2449 (−1)	−7.1325 (−1)	−6.5999 (0)	−4.7447 (−1)
4	−1.3707 (0)	−9.9267 (−1)	−1.2005 (0)	−1.1130 (0)	−8.6409 (−1)
5	−2.0301 (0)	−1.4437 (0)	−1.6428 (0)	−1.5113 (0)	−1.1997 (0)
6	−2.7218 (0)	−1.8796 (0)	−2.0384 (0)	−1.8520 (0)	−1.4794 (0)
7	−3.4484 (0)	−2.3022 (0)	−2.3856 (0)	−2.1326 (0)	−1.7015 (0)
8	−4.2129 (0)	−2.7134 (0)	−2.6827 (0)	−2.3503 (0)	−1.8642 (0)
9	−5.0181 (0)	−3.1153 (0)	−2.9280 (0)	−2.5023 (0)	−1.9657 (0)
10	−5.8668 (0)	−3.5097 (0)	−3.1199 (0)	−2.5861 (0)	−2.0042 (0)
11	−6.7620 (0)	−3.8986 (0)	−3.2566 (0)	−2.5988 (0)	−1.9779 (0)
12	−7.7063 (0)	−4.2839 (0)	−3.3363 (0)	−2.5378 (0)	−1.8850 (0)
13	−8.7028 (0)	−4.6676 (0)	−3.3576 (0)	−2.4004 (0)	−1.7237 (0)

n \ E_0(Mev)	2.5	3.5	5.5	7.5	9.5
0	1.0008 (0)	1.0010 (0)	9.9781 (−1)	9.9514 (−1)	9.9484 (−1)
1	5.1974 (−1)	6.1402 (−1)	7.1884 (−1)	7.8769 (−1)	8.3584 (−1)
2	8.8252 (−2)	2.7747 (−1)	4.7050 (−1)	5.9132 (−1)	6.7805 (−1)
3	−2.9304 (−1)	−1.0061 (−2)	2.4198 (−1)	3.8887 (−1)	5.0414 (−1)
4	−6.2353 (−1)	−2.4997 (−1)	1.8862 (−2)	1.6318 (−1)	2.9679 (−1)
5	−9.0259 (−1)	−4.4365 (−1)	−1.9888 (−1)	−1.0291 (−1)	3.8674 (−2)
6	−1.1296 (0)	−5.9248 (−1)	−4.3285 (−1)	−4.2656 (−1)	−2.8753 (−1)
7	−1.3039 (0)	−6.9785 (−1)	−6.9027 (−1)	−8.2495 (−1)	−6.9916 (−1)
8	−1.4250 (0)	−7.6116 (−1)	−9.8197 (−1)	−1.3152 (0)	−1.2135 (0)
9	−1.4921 (0)	−7.8379 (−1)	−1.3188 (0)	−1.9146 (0)	−1.8480 (0)
10	−1.5048 (0)	−7.6713 (−1)	−1.7204 (0)	−2.6401 (0)	−2.6198 (0)
11	−1.4622 (0)	−7.1256 (−1)	−2.1708 (0)	−3.5090 (0)	−3.5463 (0)
12	−1.3639 (0)	−6.2149 (−1)	−2.7078 (0)	−4.5385 (0)	−4.6449 (0)
13	−1.2093 (0)	−4.9529 (−1)	−3.3331 (0)	−5.7457 (0)	−5.9328 (0)

*See footnote at end of table.

TABLE 3. *Coefficients $b_n(E_0, Z)$ of the power-series buildup factor formulation (18) derived from the Capo [9] β_1 polynomial coefficients according to transformation (d), table 2.—Continued

$b_n(E_0, W)$ $Z=74$

n \ E_0(Mev)	0.5	0.7	1.0	1.5	2.0
0	1.0086 (0)	1.0089 (0)	1.0032 (0)	9.9925 (−1)	9.9840 (−1)
1	7.3645 (−1)	7.1129 (−1)	5.6840 (−1)	5.2793 (−1)	5.6382 (−1)
2	4.3004 (−1)	3.9926 (−1)	−1.1129 (−1)	3.9821 (−2)	1.2485 (−1)
3	8.5826 (−2)	6.7224 (−2)	−3.7041 (−1)	−4.6593 (−1)	−3.2002 (−1)
4	−2.9946 (−1)	−2.9038 (−1)	−8.7895 (−1)	−9.9020 (−1)	−7.7231 (−1)
5	−7.2925 (−1)	−6.7911 (−1)	−1.4166 (0)	−1.5338 (0)	−1.2335 (0)
6	−1.2069 (0)	−1.1880 (0)	−1.9855 (0)	−2.0977 (0)	−1.7052 (0)
7	−1.7358 (0)	−1.5723 (0)	−2.5880 (0)	−2.6827 (0)	−2.1888 (0)
8	−2.3194 (0)	−2.0878 (0)	−3.2264 (0)	−3.2897 (0)	−2.6859 (0)
9	−2.9610 (0)	−2.6567 (0)	−3.9028 (0)	−3.9195 (0)	−3.1979 (0)
10	−3.6640 (0)	−3.2846 (0)	−4.6195 (0)	−4.5729 (0)	−3.7265 (0)
11	−4.4317 (0)	−3.9770 (0)	−5.3788 (0)	−5.2510 (0)	−4.2740 (0)
12	−5.2677 (0)	−4.7396 (0)	−6.1829 (0)	−5.9545 (0)	−4.8390 (0)
13	−6.1752 (0)	−5.5767 (0)	−7.0341 (0)	−6.6842 (0)	−5.4261 (0)

n \ E_0(Mev)	2.5	3.5	5.5	7.5	9.5
0	9.9844 (−1)	9.9910 (−1)	9.9375 (−1)	9.8630 (−1)	9.8003 (−1)
1	6.1013 (−1)	6.8979 (−1)	7.6125 (−1)	7.8912 (−1)	7.9744 (−1)
2	2.2914 (−1)	4.0578 (−1)	5.3024 (−1)	5.6254 (−1)	5.6596 (−1)
3	−1.4706 (−1)	1.4271 (−1)	2.8324 (−1)	2.8069 (−1)	2.5718 (−1)
4	−5.2100 (−1)	−1.0380 (−1)	2.7784 (−3)	−8.4723 (−2)	−1.5728 (−1)
5	−8.9521 (−1)	−3.3811 (−1)	−3.2861 (−1)	−5.5836 (−1)	−7.0582 (−1)
6	−1.2722 (0)	−5.6459 (−1)	−7.2839 (−1)	−1.1673 (0)	−1.4168 (0)
7	−1.6545 (0)	−7.8762 (−1)	−1.2140 (0)	−1.9381 (0)	−2.3187 (0)
8	−2.0446 (0)	−1.0116 (0)	−1.8030 (0)	−2.8071 (0)	−3.4398 (0)
9	−2.4452 (0)	−1.2408 (0)	−2.5128 (0)	−4.0708 (0)	−4.8086 (0)
10	−2.8585 (0)	−1.4797 (0)	−3.3608 (0)	−5.4858 (0)	−6.4533 (0)
11	−3.2873 (0)	−1.7326 (0)	−4.3646 (0)	−7.1685 (0)	−8.4026 (0)
12	−3.7341 (0)	−2.0039 (0)	−5.5416 (0)	−9.1453 (0)	−1.0685 (1)
13	−4.2013 (0)	−2.2979 (0)	−6.9093 (0)	−1.1443 (1)	−1.3328 (1)

$b_n(E_0, Pb)$ $Z=82$

n \ E_0(Mev)	0.5	0.7	1.0	1.5	2.0
0	9.9993 (−1)	1.0087 (0)	1.0159 (0)	1.0171 (0)	1.0109 (0)
1	7.5580 (−1)	7.1782 (−1)	6.7548 (−1)	6.3718 (−1)	6.2940 (−1)
2	4.7600 (−1)	3.9601 (−1)	3.1164 (−1)	2.4664 (−1)	2.4906 (−1)
3	1.5697 (−1)	4.0094 (−2)	−7.5640 (−2)	−1.5563 (−1)	−1.3025 (−1)
4	−2.0485 (−1)	−3.5310 (−1)	−4.9597 (−1)	−5.7075 (−1)	−5.0870 (−1)
5	−6.1301 (−1)	−7.8073 (−1)	−9.4455 (−1)	−9.9981 (−1)	−8.8049 (−1)
6	−1.0711 (0)	−1.2939 (0)	−1.4262 (0)	−1.4439 (0)	−1.2638 (0)
7	−1.5826 (0)	−1.7879 (0)	−1.9433 (0)	−1.9042 (0)	−1.6407 (0)
8	−2.1512 (0)	−2.3618 (0)	−2.4982 (0)	−2.3818 (0)	−2.0175 (0)
9	−2.7804 (0)	−2.9887 (0)	−3.0934 (0)	−2.8777 (0)	−2.3944 (0)
10	−3.4737 (0)	−3.6718 (0)	−3.7314 (0)	−3.3931 (0)	−2.7714 (0)
11	−4.2347 (0)	−4.4144 (0)	−4.4144 (0)	−3.9291 (0)	−3.1488 (0)
12	−5.0669 (0)	−5.2194 (0)	−5.1449 (0)	−4.4869 (0)	−3.5267 (0)
13	−5.9709 (0)	−6.0301 (0)	−5.9253 (0)	−5.0674 (0)	−3.9054 (0)

n \ E_0(Mev)	2.5	3.5	5.5	7.5	9.5
0	1.0026 (0)	9.9132 (−1)	1.0012 (0)	9.9279 (−1)	9.6581 (−1)
1	6.4235 (−1)	6.9948 (−1)	8.0216 (−1)	8.0445 (−1)	8.0326 (−1)
2	2.9304 (−1)	4.2933 (−1)	6.1069 (−1)	5.8826 (−1)	5.9791 (−1)
3	−4.5410 (−2)	1.7884 (−1)	4.1282 (−1)	3.2014 (−1)	3.2578 (−1)
4	−3.7250 (−1)	−5.4018 (−2)	1.9459 (−1)	−2.4004 (−2)	−3.7126 (−2)
5	−6.8858 (−1)	−2.7128 (−1)	−5.7996 (−2)	−4.6826 (−1)	−5.1480 (−1)
6	−9.9345 (−1)	−4.5468 (−1)	−3.5890 (−1)	−1.0367 (0)	−1.1312 (0)
7	−1.2870 (0)	−6.6715 (−1)	−7.2210 (−1)	−1.7535 (0)	−1.9104 (0)
8	−1.5693 (0)	−8.4981 (−1)	−1.1616 (0)	−2.6426 (0)	−2.8763 (0)
9	−1.8401 (0)	−1.0250 (0)	−1.6913 (0)	−3.7282 (0)	−4.0529 (0)
10	−2.0994 (0)	−1.1947 (0)	−2.3252 (0)	−5.0344 (0)	−5.4642 (0)
11	−2.3472 (0)	−1.3611 (0)	−3.0774 (0)	−6.5832 (0)	−7.1342 (0)
12	−2.5833 (0)	−1.5260 (0)	−3.9617 (0)	−8.4047 (0)	−9.0869 (0)
13	−2.8077 (0)	−1.6916 (0)	−4.9921 (0)	−1.0517 (1)	−1.1346 (1)

*See footnote at end of table.

TABLE 3. *Coefficients $b_n(E_0, Z)$ of the power-series buildup factor formulation (18) derived from the Capo [9] β_1 polynomial coefficients according to transformation (d), table 2.—Continued

$b_n(E_0, U)$ $Z=92$

n \ E_0(Mev)	0.5	0.7	1.0	1.5	2.0
0	1.0107 (0)	1.0087 (0)	1.0061 (0)	1.0033 (0)	1.0017 (0)
1	8.3176 (−1)	7.8986 (−1)	7.4124 (−1)	6.9250 (−1)	6.7550 (−1)
2	6.2417 (−1)	5.4367 (−1)	4.5187 (−1)	3.6412 (−1)	3.3996 (−1)
3	3.8503 (−1)	2.6744 (−1)	1.3578 (−1)	1.6510 (−2)	−6.1238 (−3)
4	1.1141 (−1)	−4.1481 (−2)	−2.0028 (−1)	−3.5196 (−1)	−3.6398 (−1)
5	−1.9961 (−1)	−3.8575 (−1)	−5.8553 (−1)	−7.4292 (−1)	−8.4503 (−1)
6	−5.5096 (−1)	−7.6800 (−1)	−9.9522 (−1)	−1.1580 (0)	−1.1199 (0)
7	−9.4557 (−1)	−1.1909 (0)	−1.4406 (0)	−1.5989 (0)	−1.5204 (0)
8	−1.3864 (0)	−1.6571 (0)	−1.9239 (0)	−2.0671 (0)	−1.9376 (0)
9	−1.8763 (0)	−2.1692 (0)	−2.4473 (0)	−2.5644 (0)	−2.3726 (0)
10	−2.4182 (0)	−2.7299 (0)	−3.0131 (0)	−3.0923 (0)	−2.8268 (0)
11	−3.0151 (0)	−3.3419 (0)	−3.6236 (0)	−3.6526 (0)	−3.3013 (0)
12	−3.6699 (0)	−4.0078 (0)	4.2809 (0)	−4.2467 (0)	−3.7974 (0)
13	−4.3854 (0)	−4.7301 (0)	−4.9874 (0)	−4.8764 (0)	−4.3163 (0)

n \ E_0(Mev)	2.5	3.5	5.5	7.5	9.5
0	1.0010 (0)	1.0006 (0)	9.9775 (−1)	9.8835 (−1)	9.8163 (−1)
1	6.8131 (−1)	7.3122 (−1)	8.3551 (−1)	8.2590 (−1)	8.0789 (−1)
2	3.6080 (−1)	4.7491 (−1)	6.8739 (−1)	6.4374 (−1)	5.9135 (−1)
3	3.8355 (−2)	2.2977 (−1)	5.4509 (−1)	4.2402 (−1)	3.1040 (−1)
4	−2.8712 (−1)	−6.1556 (−3)	4.0033 (−1)	1.4889 (−1)	−5.6604 (−2)
5	−6.1672 (−1)	−2.3480 (−1)	2.4481 (−1)	−1.9951 (−1)	−5.3128 (−1)
6	−9.5156 (−1)	−4.5812 (−1)	7.0266 (−2)	−6.3902 (−1)	−1.1353 (0)
7	−1.2927 (0)	−6.7804 (−1)	−1.3165 (−1)	−1.1875 (0)	−1.8902 (0)
8	−1.6413 (0)	−8.9653 (−1)	−3.6916 (−1)	−1.8628 (0)	−2.8176 (0)
9	−1.9985 (0)	−1.1153 (0)	−6.5058 (−1)	−2.6828 (0)	−3.9393 (0)
10	−2.3653 (0)	−1.3369 (0)	−9.8419 (−1)	−3.6653 (0)	−5.2767 (0)
11	−2.7428 (0)	−1.5628 (0)	−1.3783 (0)	−4.8282 (0)	−6.8516 (0)
12	−3.1321 (0)	−1.7949 (0)	−1.8412 (0)	−6.1893 (0)	−8.6856 (0)
13	−3.5344 (0)	−2.0353 (0)	−2.3811 (0)	−7.7665 (0)	−1.0800 (1)

* The figures in parentheses in tables 3, 4, and 5 indicate the power of 10 by which the adjacent entry is to be multiplied; e.g., 6.4656 (−2) = 0.064656.

6. Utility and Limitations of the Power-Series Method

With respect to use of the infinite series (19), gamma-ray distributed source problems fall into three classes:

(a) In the region $0 \leq \mu_0 x \lesssim 0.01$, as is often the case in an air medium [29], all terms in (19) may be neglected except for the zeroth term $(\sigma/4\pi)\, q_0(\text{geom})$. This term is the complete solution for pure inverse square law attenuation as assumed by Meredith [29], and depends only on relative rather than absolute dimensions of the detector-source geometry.

(b) In the region $0.01 \lesssim \mu_0 x \lesssim 1.0$ the series (19) has its greatest usefulness, either with or without inclusion of scattered radiation by $b_n(E_0, Z)$ coefficients. This will be demonstrated in the numerical examples in section 7.

(c) In the region $1.0 \lesssim \mu_0 x < \infty$, as is the case in fallout shelter calculations, the series (19) is usually *not* useful, and recourse must be made to other available methods [1, 2].

It is interesting to note that the speed of convergence of (19) is usually *enhanced* over that for (15), rather than the converse. A possible explanation for this enhancement (with no attempt at a proof) is offered as follows:

In an absorbing and scattering medium the point-source buildup factor $B_{\text{PTI}}(E_0, Z, r)$ is bounded, roughly, by the limits

$$1 \leq B_{\text{PTI}}(E_0, Z, r) \lesssim \exp(+\mu_0 r). \tag{20}$$

The lower bound, $B_{\text{PTI}}(E_0, Z, r)=1$, corresponding to *pure absorption* ($D^s=0$ in eq (1)), would lead to buildup coefficients all equal to unity, i.e.,

$$b_n(E_0, Z)=1, \qquad n=0, 1, 2, \ldots \tag{21}$$

in which case (19) would be identical with (15). The upper *approximate* bound, $B_{\text{PTI}}(E_0, Z, r) = \exp(+\mu_0 r)$, corresponding to a *pure scatterer* (photons may be scattered, but never absorbed or degraded in energy) is the same as simple inverse-square-law attenuation, such that the point-source eq (2) would reduce to

$$D=(k/4\pi)/r^2. \tag{22}$$

This buildup-factor behavior can be applied to (19) by setting all except the zeroth buildup coefficient equal to zero, i.e.,

$$b_0(E_0, Z)=1$$

$$b_{n\geq 1}(E_0, Z)=0, \qquad n=1, 2, 3, \ldots . \tag{23}$$

Hence, in the intermediate region indicated in (20) we might expect the observed enhancement.

7. Numerical Examples

7.1. Example 1. Rectangular Co–60 Source, Stratified Barrier of Steel and Water. Comparison With Experiment

There exist little experimental data in the moderate-penetration region $0.01\lesssim\mu_0 x\lesssim 1.0$, discussed in (b) of the preceding section, for simple geometries amenable to direct analysis using (19). However, in connection with food irradiator design studies [17] data have been published for the more complicated situation of a two-layer barrier. Here, Donovan [30] measured the dose-rate received by a detector separated from a rectangular Co–60 source by a 3-in. layer of water and varying thicknesses of steel cladding as shown in figure 3. These results are over the range $0.589\leq\mu_0 x(\text{water}+\text{steel})\leq 1.225$, hence they provide an excellent check on (19) up to the upper limit of its usefulness as discussed in (b) of the preceding section.

The agreement between theory (infinite homogeneous medium) and experiment (layered inhomogeneous medium) in the following example must be considered somewhat fortuitous, although the position of the detector *within* the water phantom tends to minimize boundary effects. Since interest has been expressed in adapting eq (19) for use in nuclear engineering curricula, this example is presented in great detail, particularly in the steps involving dimensional analysis.

a. Situation

A 6-in. thick water-equivalent slab phantom is separated by an airgap of 2.5 in. from a 50-in. wide by 57-in. long rectangular plaque Co–60 source. This source, with a uniform activity of 1 curie per cm² of area, is encased in steel cladding of uniform thickness.

b. Problem

Find the dose-rate (rads [31] in H_2O) in the center of the phantom as the thickness of steel cladding is varied from 0.097 in. to 0.679 in. Use the simplifying approximations:

(1) To take into account the finite thickness of the source (Co, $Z=27$), include half the source thickness in the thickness of steel (Fe, $Z=26$) representing "cladding thickness" in the calculation, as was done in an alternative analytical study of this problem [3].

(2) Assume that the Co–60 nuclides emit two 1.25-Mev photons per disintegration, rather than a 1.17 Mev and a 1.33 Mev photon as is actually the case.

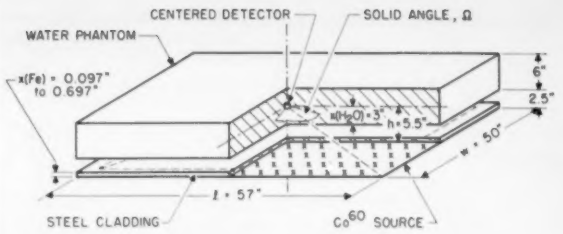

FIGURE 3. *Donovan [30] food irradiator rectangular source geometry treated in example 1.*

(3) Kalos ([21], page 796) has shown that for a composite barrier consisting of a layer of high-Z material followed by a layer of low-Z material, the resulting buildup factor shows a smooth rise from the value for pure high-Z material toward that for pure low-Z material, the rate of approach depending on the source energy. Indeed, substitution of the linear approximation (6) for $B_{\text{PTI}}(E_0, Z, r)$ in Kalos' empirical eq [21], (26.4) gives the linear connecting form

$$B_{\text{PTI}}(E_0, Z_1, Z_2, r_1+r_2) = \frac{\mu_0(Z_1)r_1}{\mu_0(Z_1)r_1+\mu_0(Z_2)r_2} B_{\text{PTI}}(E_0, Z_1, r_1) + \frac{\mu_0(Z_2)r_2}{\mu_0(Z_1)r_1+\mu_0(Z_2)r_2} B_{\text{PTI}}(E_0, Z_2, r_2) \tag{24}$$

in which Z_1, r_1 refer to one layer of the barrier and Z_2, r_2 refer to the other layer of the barrier. Since the buildup for iron and for water are not greatly different [32] over the penetration range in this problem, the approximate combinatorial form (24) will be used.

c. Plan of Attack

Evaluate the dose rate (rads in H_2O/hr) using (19) assuming the medium (a) to be all water:

$$D(\text{H}_2\text{O})=(\sigma/4\pi)\sum_{n=0}^{\infty} b_n(1.25\,\text{Mev}, \text{H}_2\text{O})\cdot q_n(\text{geom})\cdot(\mu_0 x)^n \tag{19a}$$

and (b) to be all steel:

$$D(\text{Fe})=(\sigma/4\pi)\sum_{n=0}^{\infty} b_n(1.25\ \text{Mev}, \text{Fe})\cdot q_n(\text{geom})\cdot(\mu_0 x)^n \tag{19b}$$

in which (19a) and (19b) differ only in the values of the buildup factor coefficients $b_n(E_0, Z)$. Then use (24) to obtain a dose rate between these upper and lower bounds by weighting the results from (19a) and (19b) by the fractions of mean-free-path distance traversed by the primary photons in each material:

$$D=\{(\mu_0 x)_{\text{H}_2\text{O}}/(\mu_0 x)_{\text{total}}\}D(\text{H}_2\text{O}) + \{(\mu_0 x)_{\text{Fe}}/(\mu_0 x)_{\text{total}}\}D(\text{Fe}). \tag{25}$$

d. Source Strength Constant $(\sigma/4\pi)$

For an answer from (19) in units of rads/hr per curie/cm^2 of source strength, the factor $(\sigma/4\pi)$ is

$$(\sigma/4\pi)=\mathbf{1.7005}\times\mathbf{10^5}\times N(\text{photons of energy } E_0/\text{disintegration})\times E_0\,(\text{Mev/photon})\times\{\mu_{en}(E_0, Z)/\rho\}\,(\text{cm}^2/\text{g}) \quad (26)$$

in which the numerical constant $\mathbf{1.7005}\times\mathbf{10^5}$ is obtained from the dimensional factors

$$\mathbf{1.7005}\times\mathbf{10^5}=(1/4\pi)\ (\text{steradians}^{-1})\times 3.71\times 10^{10}\ \{(\text{disintegrations/sec})/\text{curie}\}\times 1.6\times 10^{-8}\{\text{rads/(Mev/g)}\}\times 3.6\times 10^3\ (\text{sec/hr}) \quad (27)$$

For the problem stated above the numerical values of the other constants in (26) are

$N=\mathbf{2}$ photons/disintegration

$E_0=\mathbf{1.25}$ Mev/photon, and

$$\mu_{en}(1.25\text{ Mev, }H_2O)/\rho=\mathbf{0.0296}\text{ cm}^2/\text{g}.^5$$

Substitution of these values in (26) gives a source strength constant $(\sigma/4\pi)$ of

$$(\sigma/4\pi)=\mathbf{1.258}\times\mathbf{10^4}$$

for values of $D(H_2O)$ and $D(Fe)$ from (19a) and (19b) in units of $\{\text{rads }(H_2O)/\text{hr}\}/\{\text{curies/cm}^2\}$.

e. Buildup Factor Coefficients $b_n\,(E_0, Z)$

Since reference [9] and hence table 3 of this work do not contain data at 1.25 Mev, some interpolation is required to obtain the $b_n(E_0, Z)$ series coefficients needed in (19a) and (19b). This interpolation is conveniently performed on the "untransformed" $\beta_i(E_0, Z)$ *polynomial* coefficients, from which any number of $b_n(E_0, Z)$ *series* coefficients may be generated using (d), table 2. Table 4 contains polynomial coefficients:

(a) β_i(1.25 Mev, H_2O) interpolated from [25],[6] table 2, and

(b) β_i(1.25 Mev, Fe) interpolated from [9], table 7B

[5] Interpolated from [24], table 2.
[6] The coefficients in [25] as in [9] were fitted to the calculated results in NYO-3075[26].

TABLE 4. *Polynomial buildup factor coefficients* $\beta_i(E_0, Z)$ *used as input data in examples 1 and 2*

i	β_i(1.25 Mev, H_2O)*	β_i(1.25 Mev, Fe)**
0	1.00 (0)	1.013 (0)
1	9.00 (−1)	7.455 (−1)
2	1.40 (−1)	6.055 (−2)
3	−3.90 (−3)	−5.320 (−4)

*Interpolated from reference [25], table 2.
**Interpolated from reference [9], table 7B.

Corresponding values of b_n(1.25 Mev, H_2O) and b_n(1.25 Mev, Fe), computed using the numbers in table 4 as input values for formula (d), table 2, are given in table 5 for $0\leq n\leq 30$ and are ready for use in (19a) and (19b).

TABLE 5. *Buildup factor and geometry data used in example 1, series solutions (19a) and (19b).*

The $b_n(E_0, Z)$ coefficients, of which b_n(1.25 Mev, H_2O) were also used in example 2, eq (19c), were derived from table 4 using transformation (d), table 2. The q_n(geom) geometry coefficients were obtained from [7], table 3 (and unpublished higher coefficients from formulas (57) and (58), as

$$q_n(\text{Donovan geom})=4q_n(a,b)$$

using $a=(w/2)/h=5$, $b=(l/2)/h=5$ and the factor of four to apply the detector-over-corner data to Donovan's centered-detector geometry. For $h=5.5$ in., these a and b values imply plaque dimensions of 55 by 55 in., rather than Donovan's 50 by 57 in. However, the solid angles subtended in each case differ by less than 1 percent.

n	b_n(1.25 Mev, H_2O)	b_n(1.25 Mev, Fe)	q_n(geom)
0	1.000 (0)	1.013 (0)	1.090 (1)
1	1.000 (−1)	2.670 (−1)	−2.953 (1)
2	−5.200 (−1)	−3.574 (−1)	5.000 (2)
3	−8.366 (−1)	−8.575 (−1)	−6.638 (1)
4	−8.264 (−1)	−1.230 (0)	7.361 (1)
5	−4.660 (−1)	−1.472 (0)	−7.022 (1)
6	2.680 (−1)	−1.580 (0)	5.878 (1)
7	1.399 (0)	−1.551 (0)	−4.388 (1)
8	2.950 (0)	−1.382 (0)	2.959 (1)
9	4.946 (0)	−1.069 (0)	−1.822 (1)
10	7.408 (0)	−6.100 (−1)	1.032 (1)
11	1.036 (1)	−8.200 (−4)	−5.424 (0)
12	1.383 (1)	7.613 (−1)	2.658 (0)
13	1.783 (1)	1.680 (0)	−1.220 (0)
14	2.240 (1)	2.757 (0)	5.274 (−1)
15	2.755 (1)	3.998 (0)	−2.152 (−1)
16	3.330 (1)	5.404 (0)	8.322 (−2)
17	3.969 (1)	6.979 (0)	−3.057 (−2)
18	4.673 (1)	8.726 (0)	1.069 (−2)
19	5.445 (1)	1.065 (1)	−3.570 (−3)
20	6.288 (1)	1.275 (1)	1.140 (−3)
21	7.167 (1)	1.499 (1)	−3.488 (−4)
22	8.192 (1)	1.750 (1)	1.024 (−4)
23	9.258 (1)	2.016 (1)	−2.890 (−5)
24	1.040 (2)	2.300 (1)	7.852 (−6)
25	1.163 (2)	2.605 (1)	−2.056 (−6)
26	1.294 (2)	2.929 (1)	5.197 (−7)
27	1.434 (2)	3.273 (1)	−1.251 (−7)
28	1.583 (2)	3.577 (1)	2.998 (−8)
29	1.741 (2)	4.022 (1)	−6.857 (−9)
30	1.908 (2)	4.429 (1)	1.520 (−9)

f. Geometry Coefficients q_n(geom)

The parameters describing Donovan's experimental geometry, as shown in figure 3 are:

w=plaque width=**50 in.**

l=plaque length=**57 in.**

h=distance (height) of detector above plaque center

=2.5 in. airgap+3 in. water

=**5.5 in.**

In the notation of [7] the geometry coefficients for this centered-detector situation could be calculated exactly as

$$q_n(\text{Donovan geometry})=4q_n(a, b) \quad (28)$$

where $q_n(a, b)$ are corner-position rectangular-source geometry coefficients and

$$a=(w/2)/h=(50/2)/5.5=4.5\overline{454}$$

$$b=(l/2)/h=(57/2)/5.5=5.18\overline{18} \qquad (29)$$

However, $q_n(a, b)$ values for $a=5$, $b=5$ are already available in [7] for $0\leq n\leq 9$ and in unpublished form for $0\leq n\leq 35$. We can use these tabulated coefficients and avoid a two-way interpolation, or an exact calculation of q_n(geom) coefficients from formulas in [7], by the following argument:

It has been noted [1–3] that geometry effects scale approximately as the solid angle, Ω,[7] subtended by the source from the detector for barrier thicknesses of the order of one mean-free-path. Hence, since the solid angle corresponding to the already tabulated coefficients differs from the solid angle in Donovan's geometry by less than a percent, i.e.,

$$\Omega(a=5,\ b=5)/\Omega(a=4.5\overline{454},\ b=5.18\overline{18})$$

$$=4p_0(5, 5)/4p_0(4.5\overline{454},\ 5.18\overline{18})$$

$$=5.170 \text{ steradians}/5.132 \text{ steradians}$$

$$=\mathbf{1.007} \qquad (30)$$

the available coefficients for $a=5$, $b=5$ are used according to (19) and are given as the last column of table 5 for $0\leq n\leq 30$.

g. Penetration Thickness $\mu_0 x$

The last factor, $(\mu_0 x)^n$, in each series term of (19a) and (19b) is for this problem simply the n'th power of the barrier thickness in mean free paths (abbreviated mfp). If this thickness is given in inches, the thickness in mfp is

$$\mu_0 x(\text{mfp})=\mu(E_0, Z)(\text{cm}^2/\text{g})\times\rho(\text{g}/\text{cm}^3)$$
$$\times 2.54 \text{ (cm/in.)}\times x(\text{in.}) \qquad (31)$$

where $\mu(E_0, Z)$ is the narrow-beam attenuation coefficient [23] as used in (2) and ρ is the density of the medium.

For 1.25 Mev gammas in water we see that

$$\mu_0 x(\text{mfp})/x(\text{in.})=0.0634 \text{ (cm}^2/\text{g)}$$
$$\times 1.00 \text{ (g/cm}^3)\times 2.54 \text{ (cm/in.)}$$
$$=\mathbf{0.161} \text{ mfp/(in. of water)} \qquad (32)$$

and similarly for iron that

$$\mu_0 x(\text{mfp})/x(\text{in.})=0.0533 \text{ (cm}^2/\text{g)}$$
$$\times 7.83 \text{ (g/cm}^3)\times 2.54 \text{ (cm/in.)}$$
$$=\mathbf{1.06} \text{ mfp/(in. of steel)}. \qquad (33)$$

[7] This solid angle, Ω, is identical with the tabulated quantity p_0(geom) in [7] [i.e., $p_0(a, b)$] and [8] [i.e., $p_0(\rho, h)$].

Thus, for example,

$$3 \text{ in. water}=3 \text{ in.}\times 0.161 \text{ mfp/in.}=0.483 \text{ mfp},$$

and

$$0.097 \text{ in. steel}=0.097 \text{ in.}\times 1.06 \text{ mfp/in.}=0.103 \text{ mfp}.$$

h. Numerical Results, D^0 and D

Donovan's measured values of D for 3 in. of water preceded by various thicknesses of steel [30] are shown in figure 4, with his estimated ± 3 percent uncertainty indicated [33].

Before evaluating the total dose D according to (19a), (19b), and (25), it is of some interest to first evaluate the unscattered component D^0 according to (15). We can then note the effect of buildup as characterized by the $b_n(E_0, Z)$ coefficients. Inserting the data from the preceding sections (d), (f), and (g) in (15), sums for a variety of $\mu_0 x$ values yield D^0 (curve (a) in fig. 4) which is independent of the kind of medium and the photon energy except for the source strength factor $\sigma/4\pi$. Indeed, except for the factor $\sigma/4\pi$ the data for curve (a) are already tabulated in [7], table 4.

Next we can evaluate $D(H_2O)$ and D(Fe) from (19a) and (19b) using the same set of summations as for D^0 (curve (a), above) except that each series term is multiplied by the appropriate buildup factor coefficient $b_n(E_0, Z)$ from table 5. These sums $D(H_2O)$ and D(Fe) (for Donovan's geometry embedded in infinite media of water and steel, respectively) are displayed as curves (b) and (c) in figure 4. The circled numbers are a qualitative indication of the convergence rate of (19) and are, for the indicated calculated points, the number of the series term ($n+1$, including the zeroth term) beyond which the partial sum remains within 0.1 percent of the sum up to $n=30$.

Weighting $D(H_2O)$ and D(Fe) (curves (b) and (c)) according to (25) we obtain D, the hybrid curve (d), our desired result.

The calculated values of D in curve (d) can now be compared *absolutely* with Donovan's measured values, since the method is free of any arbitrary normalization. Agreement is seen to be within Donovan's 3 percent estimated uncertainty.

The results of a more approximate but simpler analysis by Moote [3] are shown as curve (e). In this analysis, which gives an excellent fit to the data in the neighborhood of $\mu_0 x=1$, the dose rate D is given as the simple product of:

(a) The source strength constant $\sigma/4\pi$,
(b) the solid angle Ω, indicated in figure 3, subtended by the source from the detector,
(c) the exponential integral $E_1(\mu_0 x)$ for the total barrier thickness $\mu_0 x$, and
(d) the *plane* isotropic source buildup factor, $B_{\text{PLI}}(E_0, H_2O, \mu_0 x)$, for the dose rate at a distance $\mu_0 x$ from an infinite plane source in water.

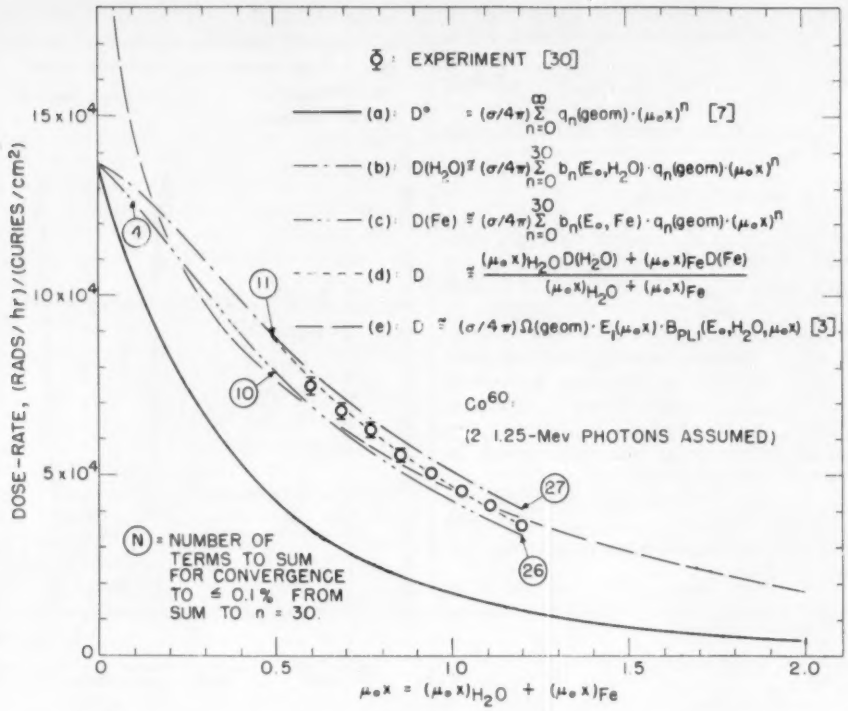

FIGURE 4. *Results for the Donovan food irradiator rectangular source geometry (example 1).*

Donovan's experimental points [30, 33] are compared with the theoretical results:
(a) The dose-rate component D° due to primaries (eq 15).
(b) The total dose-rate $D(H_2O)$ assuming an all-water medium (eq 19a).
(c) The total dose-rate $D(Fe)$ assuming an all-iron medium (eq 19b).
(d) A weighted average, D, of curves (b) and (c) according to (25).
(e) The total dose-rate, D, according to the solid-angle exponential-integral approximation used by Moote [3].

7.2. Example 2. Dose-Rate Profiles Across a Cleared Circular Area in a Co–60 Infinite Plane Source in Air

Along the *axis* of a circular disk source, analytic solutions for the flux in terms of exponential integrals and the buildup formulations [9, 11–15] are well known. However, *off-axis* solutions including buildup data have *not*, to the author's knowledge, yet appeared in the literature. The power-series solution (19) *does* apply to this situation, as will be illustrated in this example.

a. Situation

A circular area 600 ft in diameter has been cleared in an infinite plane isotropic source of 1 curie/ft² of Co–60. The surrounding medium is air (no ground-air interface is taken into account).

b. Problem

Find dose-rate profiles, relative to the undisturbed infinite plane source, at heights 3 ft (0.00626 mfp), 30 ft (0.0626 mfp) and 300 ft (0.626 mfp) above the plane of the source. Buildup data for air are not available in parametric form [9, 11–15], but water buildup data can be used to good approximation [1, 2].

c. Plan of Attack

Evaluate the dose-rates (rads/hr in air) at $h=3$, 30, and 300 ft above the infinite plane source [25, 34] using $\beta_i(E_0, Z)$ coefficients from the polynomial buildup formula (10) according to

$$D_{PLI}(h)=(\sigma/4\pi)2\pi[E_1(\mu_0 h) + \exp(-\mu_0 h)\{\beta_1+\beta_2+2\beta_3 + (\beta_2+2\beta_3)\mu_0 h+\beta_3(\mu_0 h)^2\}] \quad (34)$$

in which $E_1(\mu_0 h)$ is the ordinary exponential integral [35] and values $\beta_i(1.25$ Mev, $H_2O)$ are already given in table 4. Then, using the derived values $b_n(1.25$ Mev, $H_2O)$ from table 5, evaluate dose-rate profiles across a 600-ft diam disk source with the same source strength constant $(\sigma/4\pi)$ according to (19)

$$D_{DISK}(\rho,h)=(\sigma/4\pi)\sum_{n=0}^{\infty} b_n\,(1.25\text{ Mev, }H_2O) \cdot q_n(\rho,h)\cdot(\mu_0 h)^n \quad (19c)$$

where $q_n(\rho, h)$ geometry coefficients are available in [8] for $0 \leq \rho \leq 10$ disk radii and $0.1 \leq h \leq 10$ disk radii, and in unpublished form for $0.01 \leq h \leq 0.1$. In this problem, h assumes the values 0.01, 0.1, and 1.0 disk radii while the penetration thickness $\mu_0 h$ assumes the corresponding values 0.00626, 0.0626, and 0.626 mfp given in the problem.

d. Numerical Results

Evaluation of (34) using the source strength constant $\sigma/4\pi = 12.24$ (rads in air/hr)/(curies/ft^2)[8] gives infinite-plane dose-rates $D_{PLI}(h)$ of 423.7, 247.6, and 78.83 (rads in air/hr)/(curies/ft^2) for the heights 3, 30, and 300 ft, respectively, as indicated by the horizontal lines in figure 5. Summation of (19c) for these three heights and a number of ρ-values gives the dose-rate profiles $D_{DISK}(\rho, h)$ also shown in figure 5. The circled numbers, as in example 1, indicate the required number of series terms for convergence to within 0.1 percent of the stable value.

Subtraction of $D_{DISK}(\rho, h)$ from $D_{PLI}(h)$ gives the desired profiles shown in figure 6, normalized to 100 percent for each infinite plane source result $D_{PLI}(h)$, as specified in the problem.

[8] This value of $\sigma/4\pi$ is equivalent to the Clarke and Buchanan ([34], table 1) value of 14.0 (roentgens/hr)/(curies/ft^2) for Co–60.

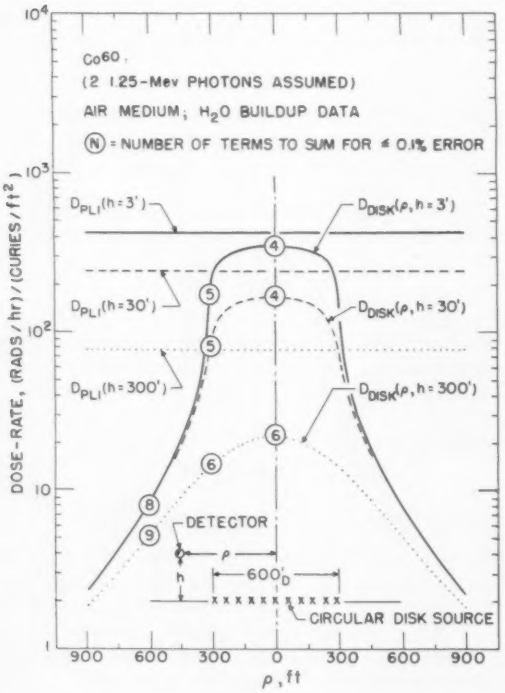

FIGURE 5. *Geometry and intermediate results for example 2.*

The solid, dashed and dotted horizontal lines are infinite-plane-source total dose-rates $D_{PLI}(h)$ calculated using (34) for detector heights h=3, 30, and 300 ft respectively. The corresponding total dose-rate profiles $D_{DISK}(\rho,h)$ over a 300-ft radius disk source were calculated using (19c).

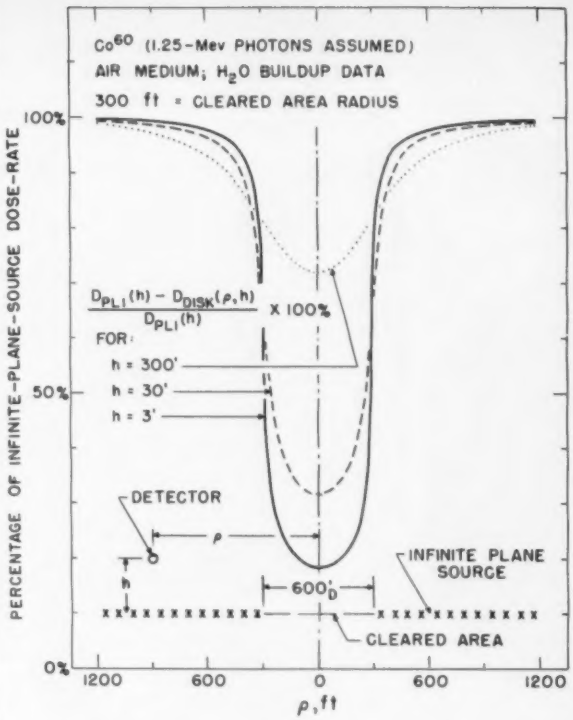

FIGURE 6. *Relative dose-rate profiles at heights 3, 30, and 300 ft above a 300-ft radius cleared circular area in an infinite plane Co–60 source in an infinite air medium (example 2).*

These profiles were obtained by subtracting the disk-source profiles $D_{DISK}(\rho,h)$ in figure 5 from the corresponding infinite plane source dose-rates $D_{PLI}(h)$, dividing by $D_{PLI}(h)$ and multiplying by 100 percent.

Caution must be taken in applying these results to the study of radiation fields from fallout deposition on the ground, since the ground-air interface has been shown by theoretical [36] and experimental [37, 38] studies to affect the scattered component by as much as a factor of three. Qualitatively, this would have the greatest effect on the h=3 ft profile in figure 5, "squaring the shoulders" of the curve and depressing the tails on either side. In figure 6 the 3-ft profile would more closely resemble a "square well," but the 30-ft and 300-ft profiles would not be appreciably changed.

8. Discussion

The power-series formulation for buildup data is seen to have two main limitations:

(a) Convergence of the primary-flux series (15), and hence the total-flux series (19), is poor for combinations of thick barriers ($\mu_0 x \gtrsim 1$) and detector-source separations much less than the source dimensions (i.e., $a, b >> 1$ or $h << 1$). In such cases the geometry closely resembles the infinite plane source geometry for which the series (15) for D° becomes, in the limit, the series representation ((5), [35]) for the exponential integral $E_1(\mu_0 x)$. The latter series converges absolutely for $0 < \mu_0 x < \infty$, but for $1 \lesssim$

$\mu_0 x < \infty$ the convergence rate is rather slow for practical use. In these situations it is more economical to revert to numerical integration, or to use an infinite plane source analytical formulation, such as (34) in example 2, as a close approximation.

(b) Boundary effects such as the density-interface effect [36–38] are neglected, but this limitation is inherent in any buildup factor formulation. Problems in which such effects are important are best treated by Monte Carlo techniques at present [36].

On the other hand, the series formulation provides some advantages:

(a) The three-way separation variables [(1) unique properties of the medium—$b_n(E_0,Z)$, (2) geometry—q_n (geom) and (3) barrier thickness—$\mu_0 x$] gives both economy of data tabulation and flexibility of application. A given set of buildup data can be applied to a variety of distributed source geometries, or vice versa, and at the same time the barrier thickness $\mu_0 x$ can be varied in a trivial fashion.

(b) In some simple idealized geometries the series (19) can provide exact answers, especially in the region of small barrier thickness ($\mu_0 x \lesssim 1$). These answers, in addition to available experimental data, can then be used to check the validity of simpler engineering-type approximate methods (e.g., [3]) in this region.

The author thanks R. L. Bach for computing table 3, R. J. Herbold for computing the additional q_n(geom) coefficients needed for example 2, and M. J. Berger for his interest and helpful criticisms regarding this effort.

9. References

[1] L. V. Spencer, Structure shielding against fallout radiation from nuclear weapons, NBS Mono. 42 (June 1, 1962).

[2] C. Eisenhauer, An engineering method for calculating protection afforded by structures against fallout radiation (unpublished).

[3] F. G. Moote, Dose rates from rectangular plaques, Nucleonics **19,** No. 7, 102 (1961).

[4] U. Ya. Margulis and A. V. Khrustalev, On the spatial distribution of the gamma-ray dose from a plane source (Experimental data for rectangular Co–60 source; analysis in terms of inscribed and circumscribed circular sectors), At. Energ. **3,** 338 (1957); transl. in Int. J. Appl. Rad. and Isotopes **4,** 109 (1958).

[5] J. A. Auxier, J. O. Buchanan, C. Eisenhauer, and H. E. Menker, Experimental evaluation of the radiation protection afforded by residential structures against distributed sources, CEX–58.1, ORNL (Jan. 19, 1959), and C. Eisenhauer, Analysis of experiments on light residential structures with distributed Co–60 sources (unpublished NBS Report 6539, Oct. 15, 1959).

[6] R. M. Sievert, Die Intensitätsverteilung der primaren γ–Strahlung in der Nähe medizinischer Radiumpräparate, Acta Radiol. (Stockholm) **1,** 89 (1921).

[7] J. H. Hubbell, R. L. Bach, and J. C. Lamkin, Radiation field from a rectangular source, NBS J. Res. **64C,** (Eng. and Instr.) No. 2, 121 (1960).

[8] J. H. Hubbell, R. L. Bach, and R. J. Herbold, Radiation field from a circular disk source, NBS J. Res. **65C,** (Eng and Instr.) No. 4, 249 (1961).

[9] M. A. Capo, Polynomial approximation of gamma ray buildup factors for a point isotropic source, APEX–510 (Nov. 1958).

[10] J. H. Hubbell, Dose distribution from finite plane sources using point source buildup data (abstract), Radiation Res. **16,** 598 (1962).

[11] H. Goldstein, The attenuation of gamma rays and neutrons in reactor shields, eq (98), p. 187, USAEC (May 1, 1957).

[12] A. B. Chilton, D. Holoviak, and L. K. Donovan, Determination of parameters in an empirical function for build-up factors for various photon energies, U.S. Naval Civil Engineering Laboratory, Tech. Note N–389 (Aug. 1960).

[13] N. I. Leshchinskii, Method of calculating dosage field of powerful isotopic units, At. Energ. **8,** 62 (1960); transl. in Soviet J. At. Energy **8,** 59 (1961).

[14] J. J. Taylor, Application of gamma ray build-up data to shield design, WAPD–RM–217 (Jan. 21. 1954).

[15] M. J. Berger and L. V. Spencer, Penetration of gamma rays from isotropic sources through aluminum and concrete, NBS Tech. Note 11 (May 11, 1959).

[16] N. E. Taney, Preliminary considerations of the use of radioisotopes for laboratory tracer techniques, Ann. Bull. of the Beach Erosion Board **14,** 16 (1960). [Note: The word "Legendre" on page 23 of this reference should be changed to read "power series."]

[17] D. C. Brunton (proj. mgr.), Final report on the high intensity food irradiator, HIFI Rep. No. 17 (May 1, 1960).

[18] B. Manowitz, O. A. Kuhl, L. Galanter, R. H. Bretton, and S. Zwickler, Experimental parametric study of large-scale Co–60, Na–24 and Cs–137 slab irradiators, p. 65–91 of Large Radiation Sources in Industry, International Atomic Energy Agency, Vienna, 1960.

[19] W. V. Mayneord, The distribution of radiation around simple radioactive sources, Brit. J. Radiol. **5,** 677 (1932).

[20] J. P. Jain and B. L. Sharma, Effect of building-up factor on the optimum shape for a shielding barrier, Reactor Sci. and Technology **16,** 375 (1962).

[21] U. Fano, L. V. Spencer, and M. J. Berger, Penetration and Diffusion of X-rays, Encyclopedia of Physics **38,** II, p. 813 (Springer-Verlag, 1959).

[22] For precise definitions of "flux" and "current" see, for example, G. N. Whyte, Principles of Radiation Dosimetry, p. 3. (John Wiley & Sons, New York, N.Y., 1959). Note, however, that Whyte introduces the designations "spherical intensity", I_s, and "plane intensity," I_p, for flux and current, respectively.

[23] G. White Grodstein, X-ray attenuation coefficients from 10 kev to 100 Mev, NBS Circ. 583 (1957).

[24] R. T. Berger, The x- or gamma-ray energy absorption or transfer coefficient: Tabulations and discussion, Rad. Res. **15,** 1 (1961).

[25] This polynomial formulation was also suggested by L. V. Spencer as the basis for an unpublished report (J. H. Hubbell, Dose due to distributed gamma-ray sources) which contains parametric data for 0.255- to 3-Mev gamma rays in water.

[26] H. Goldstein and J. E. Wilkins, Jr., Calculations of the penetration of gamma rays, AEC NYO–3075 (1954).

[27] See, for example, U. Fano, C. D. Zerby, and M. J. Berger, Gamma-ray attenuation, ch. 10 of Reactor Handbook. III B: Shielding, p. 115, E. P. Blizard and L. S. Abbott, editors, (John Wiley & Sons, New York, N.Y. 1962).

[28] B. T. Price, C. C. Horton and K. T. Spinney, Radiation Shielding (Pergamon Press, New York, 1957); parameters for Al were supplied by J. R. A. Lakey.

[29] J. L. Meredith, Method of evaluation of experimental radiation measurements over a rectangular source, NDL–TR–11, April 1961.

[30] J. L. Donovan, Three-plaque, two-pass irradiator, Nucleonics **19,** No. 7, 104 (1961).

[31] Recommendations of the International Commission on Radiological Units, Radiology **62,** No. 1, 106 (1954).

[32] H. Mochizuki, Y. Tanaka, Y. Higashihara, K. Nagato, and K. Yorihisa, Experimental study on the penetra-

tion of Co–60 γ-ray through finite heterogeneous media, J. At. Energy Soc. Japan **4,** 448 (Part 1), 703 (Part 2) (1962).
[33] J. L. Donovan, private communication.
[34] E. T. Clarke and J. O. Buchanan, Radiation shielding against fallout, Nucleonics **20,** No. 8, 143 (1962).
[35] G. Placzek, The functions $E_n(x)=\int_1^\infty e^{-xu}u^{-n}du$, MT–1, NRC No. 1547, Chalk River, Ont. (1946).
[36] M. J. Berger, Calculation of the energy dissipation by gamma radiation near the interface between two media, J. Appl. Phys. **28,** 1502 (1957).
[37] O. I. Leipunskii and V. N. Sakharov, Propagation of Co–60 radiation in the air above the earth. At. Energ. **6,** 585 (1959); transl. in Soviet J. At. Energy **6,** 440 (1960).
[38] C. E. Clifford, J. A. Carruthers and J. R. Cunningham, γ-radiation at air-ground interfaces with distributed Cs–137 sources, Can. J. Phys. **38,** 504 (1960).

(Paper 67C4–140)

JOURNAL OF RESEARCH of the National Bureau of Standards—C. Engineering and Instrumentation
Vol. 67C, No. 4, October–December 1963

An Alinement Interferometer

J. B. Saunders

(July 25, 1963)

This paper describes a diverging-beam type of alinement interferometer that permits the use of large apertures, provides ruggedness, high sensitivity, and is relatively compact. Since this interferometer is fully compensated, white light can be used.

The narrowness of the zero order fringe, relative to separation of fringes, in such a well compensated system permits settings to better than one twentieth of a fringe width. This corresponds to a lateral displacement of the light source of less than 1.5 mm at a distance of one mile for a one-inch aperture instrument and to less than 0.15 mm for a 10-inch aperture instrument.

The increase in dmands for higher accuracy in metrology includes that of pointing. The alinement interferometer described here is a precision device that is rugged and relatively easy to apply. Its performance,because of its high sensitivity, is severally affected by the homogeneity of the atmosphere or medium through which the light passes. However, this effect is also greatly reduced by the proximity of any two interfering rays of light.

There appears to be a growing need for an accurate method of alining objects over distances of several miles. The diffraction methods, described by Van Heel[1] and Dyson[2], appear to be inadequate for such distances. Other methods such as the axicon[3] and the telescope also have limited accuracy. The alinement interferometer described here is believed to be practical and more sensitive than previously described methods.

An arrangement of optical elements that form a precision alinement interferometer is shown in figure 1. It consists of two double-image prisms[4], P_1 and P_2, a beam divider, B, a lens, L, a source, S, and two pairs of quarter-wave plates, C_1 and C_2. Figure 2A shows the course of the light from B to the observer located either at F'_1 or F''_1 for measurements in the plane of figure 1, and figure 2B shows the same for measurement in the plane perpendicular to that of figure 1.

The alinement problem may consist of determining the position of the source, S, located a distance, d, from the optic axis of L, the precise adjustment of S on the axis of L, or the alinement of several sources along the axis of L. Obviously, if the problem is to determine the position of S relative to one plane only (the plane of fig. 1, for instance), then P_2 and B may be eliminated.

The optical sensitivity of this interferometer is proportional to the aperture. If the aperture of the prism is sufficient, the lens may be eliminated and the entrance face of the prism may be plane or spherical. A plane face prism, used without the aperture-increasing lens L, requires a collector lens as shown in figure 3. The 2d prism and beam divider are not shown in figure 3. They are, however, necessary for alinement in the plane perpendicular to this figure.

This prism is difficult to make in large sizes. Small prisms are relatively easy to construct and may be used with a lens to increase the aperture of the interferometer. Aperture sizes are limited only by the difficulty of producing large objectives (lenses or mirrors). A mirror objective is as easily used as a refractor and is free from chromatic aberration.

The equation of sensitivity is obtained from figure 4, in which the aperture is represented by the aperture of a lens, L. Consider two rays of light that emerge from the lens at points A_1 and A_2 that are equally

[1] Van Heel, A.C.S., Progress in optics **1**, 291 (1961).
[2] Dyson, J., Optics in metrology, p. 169 (Pergamon Press, Pol. Mollet Ed., 1960.
[3] McLeod, John H., The axicon., JOSA **44**, 592 (1954).
[4] J. B. Saunders, Construction of a Kösters double-image prism; J. Res. NBS **58**, 21–26 (1957).

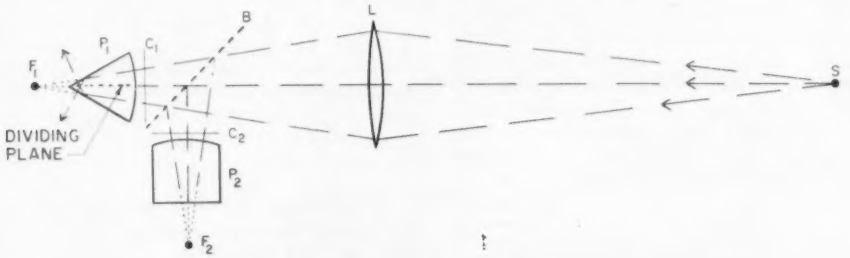

FIGURE 1. *Plane view of optical elements.*

The dividing plane of the double-image prism is a semi-reflecting optical film. It serves as the beam combiner in this interferometer.

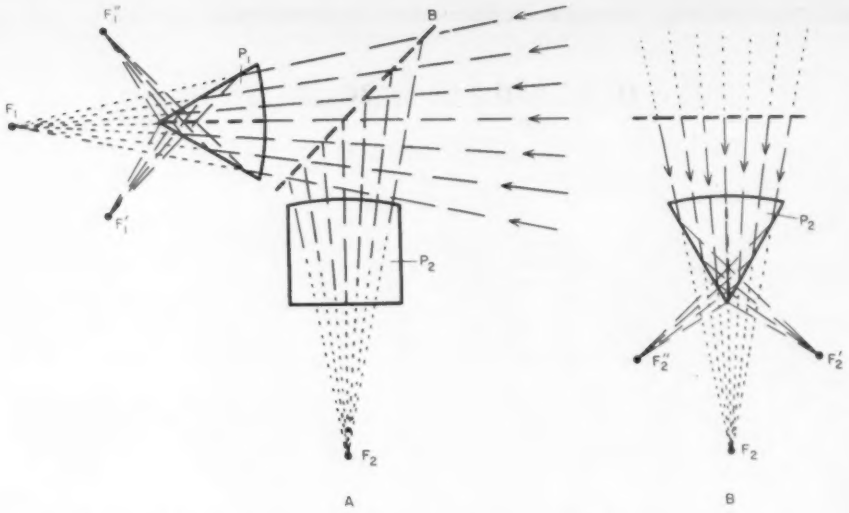

FIGURE 2. *Figure 2A represents the path of the light in the plane of figure 1. Figure 2B represents the same in a plane perpendicular to the plane of figure 1.*

The intersection of these two planes represent the straight line of interest.

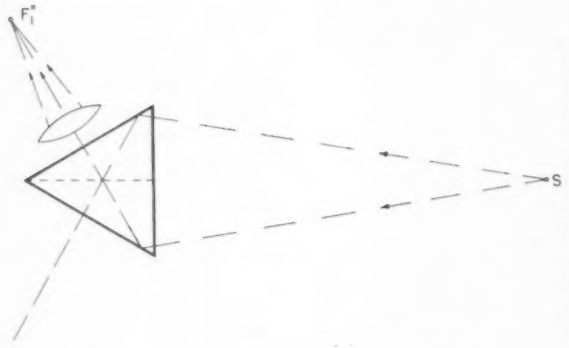

FIGURE 3. *Optics of an alinement interferometer.*

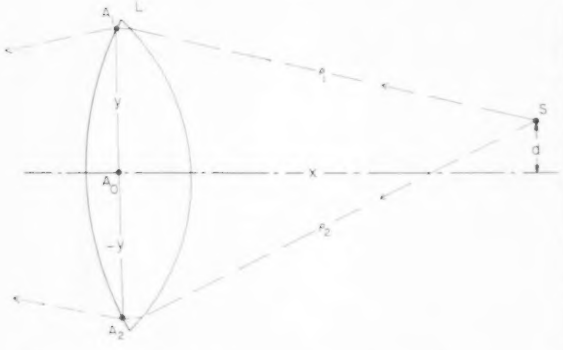

FIGURE 4. *Rays of light, ρ_1 and ρ_2, are combined in the prism. Consequently, points A_1 and A_2 appear to coincide at the reference points, indicated in figures 5 and 6.*

distant (y and $-y$) from A_0, which lie in the extension of the dividing plane of prism P_1. The distance X (approximating the distance from lens to source), shown in figure 4, is measured from A_0. The plane of figure 4 is assumed to include the optic axis of L. Let ρ_1 and ρ_2 equal the optical paths from the source to the observer (at F_1' or F_1'', fig. 2) through A_1 and A_2, respectively. The optical path from A_1 to the observer is identical to that from A_2, because of symmetry in the prism. The observer sees images of A_1 and A_2 superimposed, as shown in figure 5. The observed order of interference, N, at this pair of points, multiplied by the wavelength of the light, λ, is equal to $(\rho_1-\rho_2)$. Since X is assumed quite large relative to y and d, we can ignore the refractive index of the lens and obtain,

$$\rho_1^2=X^2+(y-d)^2, \tag{1}$$

$$\rho_2^2=X^2+(y+d)^2. \tag{2}$$

On subtracting eq (1) from (2), and expanding, we readily obtain

$$\rho_2^2-\rho_1^2=(\rho_2-\rho_1)(\rho_2+\rho_1)=4yd.$$

On putting $(\rho_2+\rho_1)=2X$ (which it approximates for large values of X) and solving for d we obtain

$$d=\frac{2X\cdot N\lambda}{4y}.$$

If A equals the aperture of the interferometer and the reference point is chosen at or near the margin then $y=\frac{1}{2}A$ and

$$d=\frac{XN\lambda}{A}. \tag{3}$$

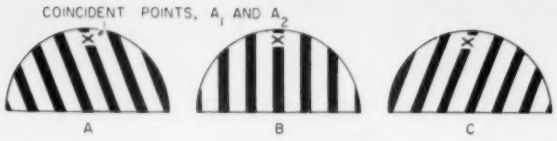

FIGURE 5. *The appearance of interference fringes when the point source is: A, above the line; B, on the line; and C, below the line of interest.*

If the problem is to adjust S on the axis, and the prism is adjusted to place the zero order of interference on the reference point where $d=0$, then the adjustment consists in moving S perpendicular to the axis until N equal zero. If white light is used with a reflecting objective (a parabolic mirror), the zero order of interference appears to have excellent contrast and an experienced observer can adjust the fringes to an accuracy of less than 0.05 fringe spacing. The corresponding error in N is 0.05 and for $\lambda=5.0\times10^{-5}$ cm (the approximate effective value for white light sources), the corresponding error in d is $X/A\times2.5\times10^{-6}$ cm. This corresponds to an error in d/X (the angular position of S) of $\frac{2.5}{A}\times10^{-6}$ (A expressed in cm). If A equals 6 in. and X equals 1 mile, the corresponding error in d is approximately 0.3 mm.

Two photomultiplier tubes placed in a differential arrangement can detect changes in the position of S to much less than this. Obviously, this principle can be used to guide an astronomical telescope when mounted on a satellite (above the atmosphere of the earth) to very high precision.

Visual observations are most easily made with a prism that has a "built-in-wedge" of convenient magnitude to produce interference fringes whose widths are most appropriate for precision of readings. Prisms may easily be adjusted to provide fringes that are neither too broad nor too narrow. When photoelectric recording is to be used for null settings the prism should be adjusted to have no built-in wedge. This permits the use of the entire beam for detection.

Figures 5A, 5B, and 5C respectively show the appearance of the fringes in a built-in wedge interferometer of 4 in. aperture when S is one second of arc above, on, and one second below, the dividing plane of the prism through which observation is made.

Because of differential polarization of light in the prism, unpolarized light cannot be used without properly oriented quarter-wave plates or a polarizer. Use of polarized light results in a loss of one-half the available light. The polarizer is used by placing it either between the prism and observer or near the source. If a polarizer is adjusted to transmit light vibrating parallel to the dividing plane of the prism, and if the observed fringe pattern is represented by figure 6A, then the pattern will change to that of figure 6B when the polarizer is rotated 90° (light vibrating perpendicular to the dividing plane of the prism). Therefore, unpolarized

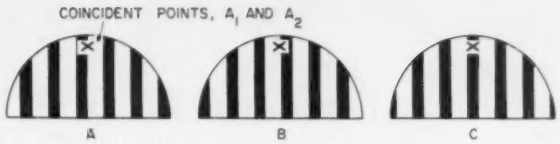

FIGURE 6. *The appearance of interference fringes when: A, the light is polarized parallel to the dividing plane of figure 1; B, the light is polarized perpendicular to the plane of figure 1; and C, when quarter-wave plates are used instead of a polarizer.*

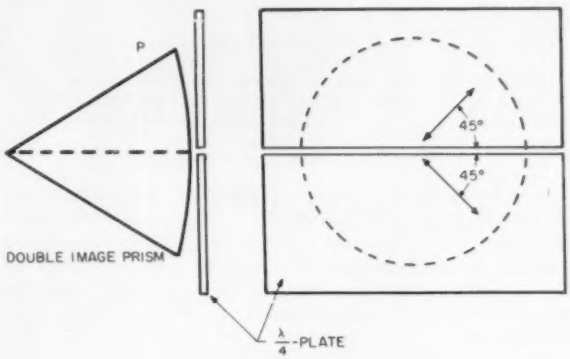

FIGURE 7. *Arrangement of quarter-wave plates to give good contrast with unpolarized light.*

light produces two sets of fringes with the maximum intensity areas of one set coinciding approximately, with the minimum intensity areas of the other set, thus eliminating contrast so that no fringes can be observed.

Dr. Charles J. Koester [5] suggested and demonstrated that by cutting a quarter-wave sheet [6] of mica at 45° to its optic axis and mounting it in front of the prism, in the manner shown in figure 7, the relative phase changes in the two polarized beams are practically equalized. The two sets of fringes produced by the two component beams (vibrating parallel and perpendicular to the dividing plane of the prism) will then coincide in phase. Good contrast is thereby obtained with little loss of light. The resultant fringe pattern (fig. 6C) indicates that the two sets of fringes, shown in figures 6A and 6B, are shifted in opposite directions by an amount that places them in coincidence.

Tests made in the laboratory showed that the sensitivity of the instrument, obtained from eq (3), agreed within the limits of observations. The theoretical accuracy claimed above requires that the medium through which the light travels be quite homogeneous. An evacuated light tube would probably be required to obtain the accuracy indicated by eq (3) when measurements are made over long distances.

[5] Working at NBS under a National Research Council Postdoctoral Research Associateship and now with American Optical Co., Southbridge, Mass.

[6] Subsequent tests showed that the relative retardation is not critical for obtaining good contrast.

(Paper 67C4–141)

JOURNAL OF RESEARCH of the National Bureau of Standards—C. Engineering and Instrumentation
Vol. 67C, No. 4, October–December 1963

Determination of Optical Path Difference for a Photographic Objective

Francis E. Washer and Walter R. Darling

(June 6, 1963)

A method of measuring longitudinal spherical aberration and optical path differences by a direct visual means is described. The method employs a nodal slide optical bench and a movable-slit system. The underlying theory of the method is presented together with a brief description of the apparatus used. The results of measurement on a typical lens and a procedure for checking the consistency of measurements are included.

1. Introduction

One of the criteria used in evaluating the potential image forming qualities of a photographic objective is the magnitude of the longitudinal spherical aberration which measures the variation in axial focus with radius of annular zone of the lens. It is sometimes desirable however to use a related quantity more meaningful in terms of physical optics, namely the optical path difference existing between the paraxial region of the lens and the various annular zones located between the axial and marginal regions of the lens. The optical path difference expressed in units of wavelength yields information on the manner in which light converging from a given annular zone of the lens to a specified focal point may be expected to contribute to image formation. In specifying the performance of a high quality telescope objective, a common requirement is that the optical path difference over the entire wave front emergent from a lens shall not depart by more than 0.25 wavelength from a true sphere.

A method has therefore been developed for the measurement of the departure of the emergent wave front from a true spherical surface in units of wavelength. The method is essentially a refinement of the method reported by Chalmers [1] and similar to the two slit method used by Väisälä.[2] The present method is well adapted for use with lenses having a wide range of focal lengths.

The accuracy of the final results compares favorably with that of results obtained by more elaborate interferometric methods. Moreover the results are in such a form as to simplify the computation of changes in optical path difference with shift of the focal plane.

2. Theory of the Method

2.1. Determination of Optical Path Difference, *P*

When a lens is affected by longitudinal spherical aberration, the position of best axial focus changes from zone to zone of the lens. The magnitude of this focal shift can be readily measured by a variety of methods, one of which is reported in an earlier paper.[3] The effect of longitudinal spherical aberration may also be described as a distortion of the wave front from a true spherical form by action of the lens. This distortion of the wave front produces variation in the optical path separating different portions of the wave front emerging from the lens and the focal point. It is possible to measure this variation using a technique similar to that reported by Chalmers (see footnote 1). In this method, two parallel slits, separated by distance h_0, are placed in front of a lens, the image of an infinitely distant bright line object formed by the lens then appears as a series of parallel interference fringes in the focal plane of the lens. The central fringe is the brightest of the group, the others growing fainter with increasing order of interference.

The separation of these fringes is given by the relation

$$S=\frac{\lambda f}{h_0} \tag{1}$$

where S is the measured separation of the central fringe and an adjacent fringe, h_0 is the slit separation, f the equivalent focal length of the lens, and λ the wavelength of the incident light.

If the slits are so placed that one is on the axis of the lens, the second slit will be at distance h_0 from the axis. A difference in focus between the paraxial zone and the annular zone of radius h_0, will shift the image of the central fringe laterally by amount δ_1 and the change in optical path, ΔP_1, is given by the relation

$$\Delta P_1=\frac{\delta_1 h_0}{f}. \tag{2}$$

[1] S. D. Chalmers: Proceedings of the Optical Convention **2**, 156 (1912).
[2] Y. Väisälä, Ann. Univ. Fenn. Abo. **1** 3 (1922).
[3] F. E. Washer and W. R. Darling, Optical T-bench method of measuring longitudinal spherical aberration, J. Research NBS **61**, 31 (1958) RP2880.

On moving the slits outward along a radius of the lens in such a manner that the first slit occupies the position formerly occupied by the second slit, a new value δ_2 will be found and the change in optical path difference ΔP_2 is given by the relation $\Delta P_2 = \frac{\delta_2 h_0}{f}$. This process is continued until the last setting is made with the second slit near the margin of the lens, and the corresponding value of ΔP is $\Delta P_m = \frac{\delta_m h_0}{f}$. The total optical path difference P between the center and a given zone designated by zone number $m (m = 1, 2, 3, \ldots)$ is given by the expression

$$P = \Sigma \Delta P = \frac{h_0}{f} \Sigma \delta. \tag{3}$$

This may be expressed in units of wavelength by dividing by λ giving the optical path difference in wavelengths, n_λ, which is

$$n_\lambda = \frac{P}{\lambda} = \frac{h_0}{\lambda f} \Sigma \delta. \tag{4}$$

With the aid of eq (4), the variation in n_λ, which may be interpreted as phase shift, can be determined for any point of the wave front with respect to any other point of the wave front located along the same diameter and for the particular image plane in which the measurements are made.

2.2. Effect of Focal Shift

The relation, shown in eq (4), is valid for any single position of the focal plane. For a focal plane separated by distance Δf from the initial position, a different set of values of n_λ will be found. The measured values of δ change by amount $\Delta\delta$ which changes are related to Δf as shown in the following equation

$$\frac{\Delta \delta}{h} = \frac{\Delta f}{f} \tag{5}$$

where h is the zone height. The change Δn_λ in n_λ is given by the relation

$$\Delta n_\lambda = \frac{h_0}{\lambda f} \cdot \frac{\Delta f}{f} \Sigma h. \tag{6}$$

For the case of one slit located initially on the lens axis, $h = h_0 (m - \frac{1}{2})$ and Δn_λ is given by the relation

$$\Delta n_\lambda = \frac{h_0^2}{\lambda f^2} \Delta f \Sigma \left(m - \frac{1}{2} \right) \tag{7}$$

For a specified value of the zone number m, eq (7) may be written

$$\Delta n_\lambda = \frac{h_0^2}{\lambda f^2} \cdot \Delta f \cdot \frac{m^2}{2}. \tag{8}$$

For the case of the lens axis located initially midway of the two slits, the zone height h is given by the relation

$$h = m h_0. \tag{9}$$

The value of Δn_λ is given by

$$\Delta n_\lambda = \frac{h_0^2}{\lambda f^2} \cdot \Delta f \Sigma m \tag{10}$$

which for a specified value of m becomes

$$\Delta n_\lambda = \frac{h_0^2 \Delta f}{\lambda f^2} \cdot \frac{m(m+1)}{2}. \tag{11}$$

2.3. Determination of the Longitudinal Spherical Aberration

The same initial observations δ from which the distortion of the wave front in units of wavelength are determined may also be used to derive the values of longitudinal spherical aberration $\Delta f'$, expressed as a focal shift. The values of $\Delta f'$, δ, and h the zone height are related as follows:

$$\Delta f' = \frac{\delta f}{h}. \tag{12}$$

For the case of one slit on the lens axis at the start of observations, eq (8) becomes

$$\Delta f' = \frac{\delta f}{(m - \frac{1}{2}) h_0} \tag{13}$$

and for the case of the zero point of observations occurring midway of two slits, eq (8) becomes

$$\Delta f' = \frac{\delta f}{m h_0}. \tag{14}$$

3. Method of Measurement

The optical bench, shown in figure 1, is used in making the measurements required for the determination of the distortion of the wave front, n_λ, and the longitudinal spherical aberration $\Delta f'$. Initially the lens under test is mounted in its holder on the nodal slide assembly and its optical axis alined with the optical axis of the collimator. The reticle, located in the focal plane of the collimator, consists of a luminous cross composed of intersecting vertical and horizontal lines. The collimated beam is incident upon the lens under test and forms an image of the luminous reticle in the focal plane of the lens. The viewing microscope is adjusted using the transverse and longitudinal motions provided until the microscope is focused on the image formed by the lens and the vertical line of the image coincides with the intersection of the crosshairs in the ocular of the viewing microscope.

A diaphragm containing two parallel slits is placed in front of the lens under test. This diaphragm is so mounted that the double slit may be moved transversely across the front of the lens by measured amounts. The slits are alined parallel to the vertical line of the target reticle and so positioned that the center of the slit system will lie in the plane determined by the horizontal front diameter of the lens and the center of the target reticle for all positions to be occupied by the slit system throughout its range of transverse movement. At the start of a run, the slit system is brought to a position as near the edge of the lens as feasible. Light from the collimator on passing through the double slit and lens forms a set of interference fringes in the focal plane of the lens. A photograph of the fringe system is shown in figure 2. The crosshair of the viewing microscope is brought into coincidence with the image of the central fringe using the transverse micrometer movement of the microscope to make the setting. This setting of the transverse micrometer is recorded. The slits are now moved transversely by an amount equal to the slit separation, h_0, and the new location of the central fringe is recorded. This process is repeated until the entire diameter of the lens is spanned. The microscope setting made when one of the slits lies on the lens axis is taken as the zero point of the displacement, δ, and the corresponding setting of the double slit is taken as the zero point of the zone number, m. From the series of observations made at the measured intervals across the lens diameter, the values of δ as a function of m are obtained for the particular focal setting. In addition, it is customary to determine the average fringe separation $\overline{S}_0$ in the vicinity of the lens axis as it can be used in eq (1) for the determination of f when λ is known or for the evaluation of $\Sigma\delta$ in units of wavelength in eq (4).

It is recognized that the use of a collimator with the illuminated reticle located in its focal plane instead of an object at infinite distance may introduce a systematic error in the determination of the longitudinal spherical aberration and the optical path difference in units of wavelength. However, such systematic errors may be minimized by using a collimator having negligible longitudinal spherical aberration. The measurements, reported in the following section, were made using an off-axis paraboloidal mirror to collimate the light from the target reticle. For the area of the emergent beam used in the measurements the error arising from this source does not exceed ± 0.01 wavelength in the determination of n_λ and hence may be regarded as negligible.

4. Results of Measurement

A series of measurements was made on a photographic objective of a type commonly used in aerial photography. The lens has a measured focal length of 210.4 mm and a maximum nominal f-number of f/6.8. The slit separation was 1.453 mm and the

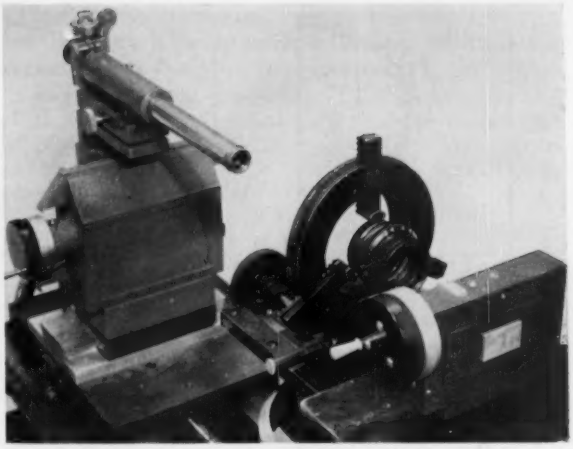

FIGURE 1. *Photograph showing optical bench with lens in position for test.*

The lens is mounted in the holder of the nodal slide. The double slit system is mounted in front of the lens on a transverse micrometer slide. Parallel light incident on the slit system passes through the lens and forms a fringe system in the focal plane of the lens under test. The fringe system is viewed with the microscope having a transverse micrometer movement.

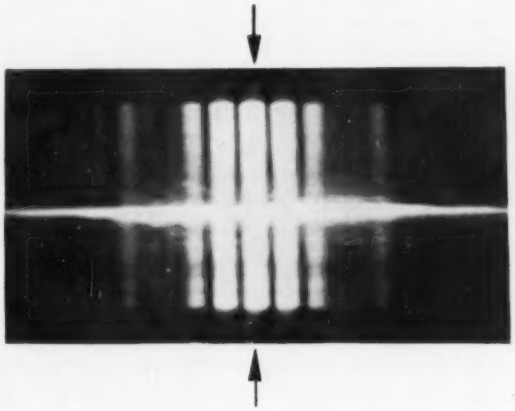

FIGURE 2. *Photograph of fringe system formed in the focal plane of the lens under test.*

In the photograph, the central fringe is indicated by the vertical arrows. The zero, first, and second order fringes are clearly visible; higher orders are present and may be seen through the microscope. The bright horizontal line is the image of the horizontal crossline in the collimator target.

effective wavelength of the light incident [4] on the lens was approximately 589.3 mμ. Observations of δ were made in the position of best focus and for two positions on either side of best focus. Values of δ for these three runs are listed in tables 1 to 3. Ten observations were made on either side of the optical axis and are designated by zone number m ranging from -10 to $+10$. Actual values of the zone height h are shown under the column headed $(m-\frac{1}{2})h_0$.

The observed values of the displacement δ of the central fringe with transverse displacement of the slit systems are shown graphically in the left hand frame of figure 3 which shows the variation of δ as a function of the zone height h for three positions of the image plane.

[4] The wavelength of the incident light is controlled by a narrow band interference filter whose peak transmittance is at $\lambda = 589.3$.

696-713—63——4

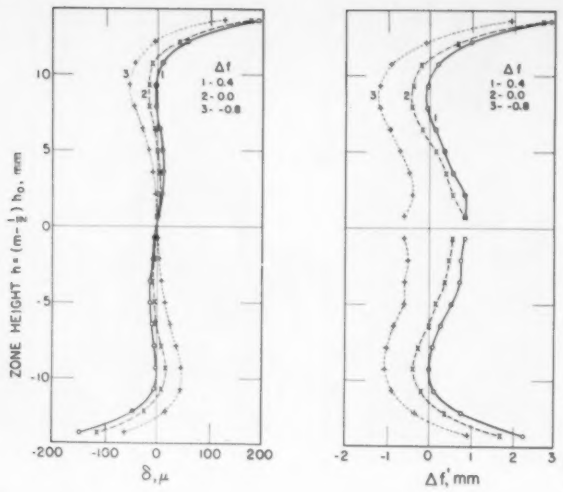

FIGURE 3. *Variation of transverse displacement, δ, of central fringe and computed value of longitudinal spherical aberration with zone height* h.

The left-hand frame shows the variation of δ with h for three positions of the focal plane. Curve 1 shows the results for a focal plane 0.4 farther from the lens than the position of best visual focus; curve 2 shows the results for the plane of best visual focus; and curve 3 the results for a plane 0.8 mm nearer to the lens than the plane of best visual focus. The right hand frame shows the values of the longitudinal spherical aberration $\Delta f'$ derived from the measured values of δ for the conditions described for the left hand frame.

TABLE 1. *Displacement δ in the image plane of central fringe as a function of zone height,* $h=(m-\frac{1}{2})h_0$

These values were obtained for a focal plane 0.4 mm farther from the lens than the plane of best focus of a lens having a focal length of 210.4 mm. The double slits are separated by h_0=1.453 mm. Wavelength of the incident light was 589.3 mm. Values of the longitudinal spherical aberration $\Delta f'$ and the distortion of the wave front, n_λ, in units of wavelength are also given.

m	$(m-\frac{1}{2})h_0$	δ	$\Delta f'$	$\Sigma\delta$	n_λ*
	mm	μ	mm	μ	
10	13.8	193	2.94	296	3.47
9	12.4	59	1.00	103	1.21
8	10.9	11	0.21	44	0.52
7	9.4	− 1	−.02	33	.39
6	8.0	− 2	−.05	34	.40
5	6.5	5	.16	36	.42
4	5.1	9	.37	31	.36
3	3.6	10	.58	22	.26
2	2.2	9	.87	12	.14
1	0.7	3	.87	3	.04
0	0	0			
−1	−0.7	− 3	0.87	− 3	0.04
−2	−2.2	− 8	.77	−11	.13
−3	−3.6	−13	.75	−24	.28
−4	−5.1	−13	.54	−37	.43
−5	−6.5	− 9	.29	−46	.54
−6	−8.0	− 4	−.10	−50	.59
−7	−9.4	− 1	.02	−51	.60
−8	−10.9	− 6	.12	−57	.67
−9	−12.4	−46	.78	−103	1.21
−10	−13.8	−148	2.26	−251	2.94

*$n_\lambda = \frac{(h_0)}{\lambda f}\Sigma\delta$.

4.1. Evaluation of Longitudinal Spherical Aberration $\Delta f'$

It is usually convenient to evaluate first the longitudinal spherical aberration $\Delta f'$ as it can be done readily using the observed values of δ and eq (13). The values of $\Delta f'$ are listed in tables 1 to 3 and are shown graphically in the right-hand frame of figure 3. It is clear that the form of the curves is essentially the same for the three focal positions but the curves are displaced with respect to each other by amounts closely approximating the nominal separations of planes in which the measurements were made.

TABLE 2. *Displacement δ in the image plane of central fringe as a function of zone height,* $h=(m-\frac{1}{2})h_0$

These values were obtained for the plane of best focus of a lens having a focal length of 210.4 mm. The double slits are separated by h_0=1.453 mm. Wavelength of the incident light was 589.3 mm. Values of the longitudinal spherical aberration $\Delta f'$ and the distortion of the wave front, n_λ, in units of wavelength are also given.

m	$(m-\frac{1}{2})h_0$	δ	$\Delta f'$	$\Sigma\delta$	n_λ*
	mm	μ	mm	μ	
10	13.8	178	2.71	192	2.25
9	12.4	41	0.70	14	0.16
8	10.9	−10	−.19	−27	−.32
7	9.4	−16	−.36	−17	−.20
6	8.0	−16	−.42	− 1	−.01
5	6.5	− 5	−.16	15	.18
4	5.1	4	.16	20	.23
3	3.6	7	.40	16	.19
2	2.2	6	.58	9	.10
1	0.7	3	.87	3	.04
0	0				
−1	−0.7	− 2	0.58	− 2	0.02
−2	−2.2	− 5	.48	− 7	.08
−3	−3.6	− 7	.49	−14	.16
−4	−5.1	− 4	.16	−18	.21
−5	−6.5	0	.00	−18	.21
−6	−8.0	9	−.24	− 9	.10
−7	−9.4	17	−.38	+ 8	− 09
−8	−10.9	9	−.17	17	−.20
−9	−12.4	−23	.39	− 6	.07
−10	−13.8	−114	1.74	−120	1.41

TABLE 3. *Displacement δ in the image plane of central fringe as a function of zone height,* $h=(m-\frac{1}{2})h_0$

These values were obtained for a focal plane 0.8 mm nearer to the lens than the plane of best focus of a lens having a focal length of 210.4 mm. The double slits are separated by h_0=1.453 mm. Wavelength of the incident light was 589.3 mm. Values of the longitudinal spherical aberration $\Delta f'$ and the distortion of the wave front, n_λ, in units of wavelength are also given.

m	$(m-\frac{1}{2})h_0$	δ	$\Delta f'$	$\Sigma\delta$	n_λ
	mm	μ	mm	μ	
10	13.8	130	1.98	−77	−0.90
9	12.4	− 4	− .07	−207	−2.42
8	10.9	−47	− .91	−203	−2.38
7	9.4	−53	−1.19	−156	−1.83
6	8.0	−44	−1.16	−103	−1.21
5	6.5	−29	−0.93	− 59	−0.69
4	5.1	−16	− .66	− 30	− .35
3	3.6	− 8	− .46	− 14	− .16
2	2.2	− 4	− .39	− 6	− .07
1	0.7	− 2	− .58	− 2	− .02
0	0				
−1	−0.7	2	−0.58	2	−0.02
−2	−2.2	5	− .48	7	− .08
−3	−3.6	10	− .58	17	− .20
−4	−5.1	14	− .58	31	− .36
−4	−6.5	26	− .84	57	− .67
−6	−8.0	38	−1.00	95	−1.11
−7	−9.4	47	−1.05	142	−1.66
−8	−10.9	46	− .89	188	−2.20
−9	−12.4	18	− .31	206	−2.41
−10	−13.8	−62	.94	144	−1.69

4.2. Check on Consistency of Observed Data

In work of this nature it is desirable to have and use check methods to ensure that errors are held to a minimum and to verify the selection of the form of equation used in the determination. This can be done by analysis of the variation $\bar{\delta}$, the average of δ,

for paired values of $+m$ and $-m$, for two focal positions. Consideration of eq (12) indicates that the difference $\Delta\bar{\delta}$ obtained from the differences in $\bar{\delta}$ for a given value of m at two different focal positions is a linear function of m. In table 4, values of $\Delta\bar{\delta}$ obtained by taking the differences between the corresponding values of $\bar{\delta}$ for focal positions $+0.4$ and -0.8 are listed under the caption, observed values of $\Delta\bar{\delta}$. When these values of $\Delta\bar{\delta}$ are plotted against zone number m as shown in curve 1 of figure 4, it is clear that a linear relation exists between $\Delta\bar{\delta}$ and $m-\frac{1}{2}$. This indicates that it was proper to use eq (13) in the evaluation of $\Delta f'$. The slope a of the best fitting line through the points on the graph is given by the expression

$$a=\frac{\Sigma\Delta\bar{\delta}}{\Sigma(m-\frac{1}{2})} \tag{15}$$

which in this instance gives a value

$$a=383/50=7.66\ \mu.$$

The equation of the best fitting line is

$$\Delta\bar{\delta}_c=a(m-\tfrac{1}{2}). \tag{16}$$

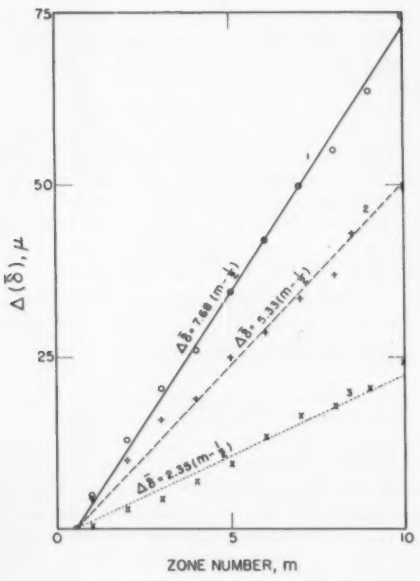

FIGURE 4. *Variation of the change in average transverse fringe displacement $\Delta\bar{\delta}$ between two specified focal planes with zone number,* m.

Curve 1 shows the variation in $\Delta\bar{\delta}$ for focal planes designated $\Delta f=0.4$ and $\Delta f=-0.8$; curve 2 shows the variation in $\Delta\delta$ for the focal planes designated $\Delta f=0.0$ and 0.8; and curve 3 shows the results for focal planes designated $\Delta f=0.4$ and $\Delta f=0.0$ mm. The equations of the best fitting straight line are shown adjacent to each curve.

Values of $\Delta\delta_c$ obtained with this equation for $a=7.66\ \mu$ are listed in table 4 together with the departures from the observed values of $\Delta\bar{\delta}$. It is clear that the agreement is excellent. Values of $\Delta\bar{\delta}$ for the other two combinations of focal position ($+0.4$ and 0.0, curve 3; 0.0 and -0.8, curve 2) are also shown in the graph and indicate that all three sets of data are reasonably consistent.

TABLE 4. *Comparison of values of $\Delta\bar{\delta}$ obtained for focal positions $+0.4$ and -0.8 as a function of* m *with values computed from relation $\Delta\bar{\delta}=7.66\ (m-\frac{1}{2})$*

m	$\Delta\bar{\delta}$ in microns		
	Observed	Comp	O−C
1	5	4	1
2	13	11	2
3	20	19	1
4	26	27	−1
5	34	34	0
6	42	42	0
7	50	50	0
8	55	57	−2
9	64	65	−1
10	74	73	1

From the values of the slope a, for the three combinations of $\Delta\delta$ versus m, it is possible to determine the average displacement of the focal plane for the three focal positions using the relation

$$\Delta(\overline{\Delta f})=\frac{af}{h_0}. \tag{17}$$

Values of $\Delta(\overline{\Delta f})$ derived from the analysis of $\overline{\Delta\delta}$ for the three combinations are given in table 5. The focal positions were known initially within ± 0.1. mm so it is clear that good agreement exists between the nominal values of $\Delta(\overline{\Delta f})$ and those derived from analysis of $\Delta\bar{\delta}$ as a function of m.

TABLE 5. *Comparison of nominal values of the relative separation $\Delta(\Delta f)$ of the three focal planes with that derived from the slopes of $\Delta\delta$ versus* $m-\frac{1}{2}$ *and with that derived from the slope of $\Delta\overline{n_\lambda}$ versus* m^2

Focal positions	Nominal	Value of $\Delta(\Delta f)$	
		From slope of $\Delta\delta$ vs $m-\frac{1}{2}$	From slope of Δn_λ vs m^2
	mm	*mm*	*mm*
0.0 and 0.4	0.4	0.34	0.32
0.0 and −0.8	.8	.77	.80
0.4 and −0.8	1.2	1.11	1.12

4.3. Evaluation of Optical Path Difference, n_λ

The values of the optical path difference, n_λ, are obtained with the aid of eq (4). Here the value of

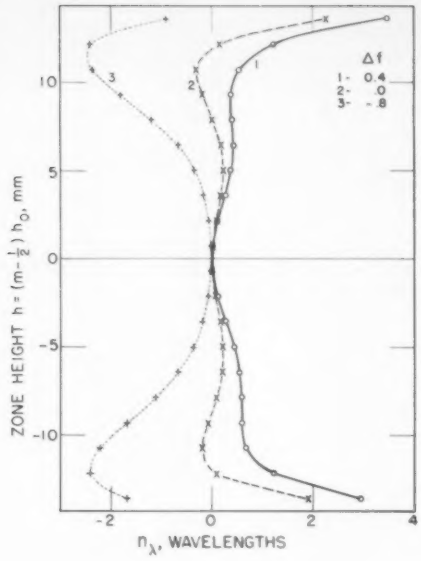

FIGURE 5. *Variation of the optical path difference expressed in number of wavelengths,* n_λ, *as a function of zone height* h.

Values of n_λ are shown for three focal positions. Curve 1 shows the results for $\Delta f=0.4$, curve 2 for $\Delta f=0.0$, and curve 3 for $\Delta f=-0.8$. These values of n_λ are derived from the values of δ shown in figure 2.

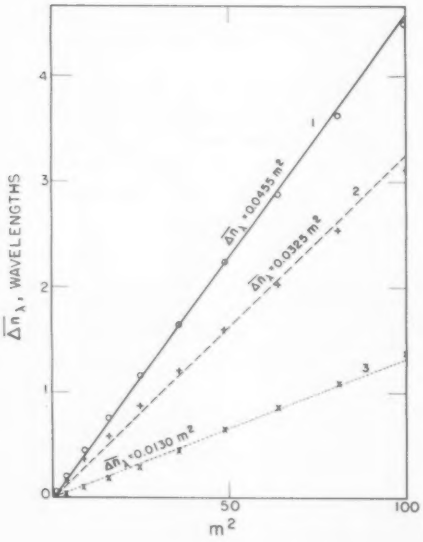

FIGURE 6. *Variation of the average change* $\Delta\bar{n}_\lambda$ *between two specified focal planes with* m^2, *where* m *is the zone number.*

Curve 1 shows the variation in $\Delta\bar{n}_\lambda$ for focal planes designated $\Delta f=0.4$ and $\Delta f=-0.8$ mm; curve 2 shows the variation for the focal planes designated $\Delta f=0.0$ and -0.8 mm; and curve 3 shows the variation for focal planes designated $\Delta f=0.0$ and 0.4 mm. The equations of the best fitting straight lines are shown adjacent to each curve.

the term $h_0/\lambda f$ is equal to 0.01172 wavelengths/micron. Values of $\Sigma\delta$ and n_λ for the three focal positions are shown in tables 1 to 3. The values of n_λ are also shown graphically in figure 5.

4.4. Check on Consistency of Values of n_λ

While it is possible to evaluate n_λ from data obtained for a single focal position, confidence in the results is increased by comparison with results for a different focal position. Hence it is desirable to check the inner consistency of results obtained for several focal positions to ensure that errors have been held to a minimum and to verify the form of equation to be used in determing the change in n_λ with shift of focus. This can be done by analysis of $\bar{n}_\lambda$, the average value of n_λ for paired values of $+m$ and $-m$ for two focal positions. Consideration of eq (8) indicates that the differences $\Delta\bar{n}_\lambda$ obtained from the differences in n_λ for a given value of m at two different focal positions is a linear function of m^2. In table 6, values of $\Delta\bar{n}_\lambda$ obtained by differencing the corresponding values of $\bar{n}_\lambda$ for focal positions $+0.4$ and -0.8 are listed under the caption, observed values of $\Delta\bar{n}_\lambda$. When these values of $\Delta\bar{n}_\lambda$ are plotted against m^2 as shown in curve 1 of figure 6, it is clear that a linear relation exists between $\Delta\bar{n}_\lambda$ and m^2. This also indicates that eq (8) was the proper choice for use in the interpretation of the relation between $\Delta\bar{n}_\lambda$ and m. The slope b of the best fitting line through the points on the graph is given by the expression

$$b=\frac{\Sigma\Delta\bar{n}\lambda}{\Sigma m^2} \tag{18}$$

which in this instance gives a value of

$$b=17.53/385=0.04553$$

The equation of the best fitting line is

$$\Delta\bar{n}_\lambda=bm^2. \tag{19}$$

Values of $\Delta\bar{n}_\lambda$ obtained with this equation for $b=0.04553$ are listed in table 6 under the caption, computed values of $\Delta\bar{n}_\lambda$ together with the departures from the observed values under the caption, $0-C$. It is clear that the agreement is excellent. Values of $\Delta\bar{n}_\lambda$ for the other two combinations of focal position (0.4 and 0.0, curve 3; 0.0 and -0.8, curve 2) are also shown in the graph and good consistency is indicated for the three sets of data although the values of $0-C$ are larger at $m=9$ and $m=10$.

From the values of the slope b for the three combinations it is possible to determine the average displacement of the focal plane for the three focal positions using the relation

$$\Delta(\overline{\Delta f}) = \frac{2\lambda f^2}{h_0^2} \cdot b. \qquad (20)$$

Values of $\Delta(\overline{\Delta f})$ derived from analysis of $\overline{\Delta n_\lambda}$ for the three combinations are also listed in table 5. It is clear that good agreement also exists between the nominal values of $\Delta(\overline{\Delta f})$ and those obtained in the foregoing manner.

TABLE 6. *Comparison of values of* $\overline{\Delta n_\lambda}$ *obtained for focal position* $+0.4$ *and* -0.8 *as a function of* m *with those computed from the relation* $\overline{\Delta n_\lambda} = 0.04553\text{m}^2$

m	Values of $\overline{\Delta n_\lambda}$		$O-C$
	Observed	Computed	
1	0.06	0.05	0.01
2	.21	.18	.03
3	.45	.41	.04
4	.76	.73	.03
5	1.16	1.14	.02
6	1.65	1.64	.01
7	2.24	2.23	.01
8	2.88	2.91	−.03
9	3.63	3.69	−.06
10	4.49	4.55	−.06

4.5. Effect of Focal Shift Δf on the Values of n_λ

One of the manifest advantages of this method of measuring optical path difference n_λ, is that it permits the evaluation of n_λ as a function of zone height h for any given focal position separated by Δf from the focal plane in which measurements were made. Hence it is not necessary to make the measurements of δ at the position of best axial focus. It is only necessary that the focal plane in which measurements are made is that of a reasonably good focus as the form of the curve can be computed for a selected focal plane if one has the measured values of n_λ as a function of m for a nearby plane. The suitability of such a procedure is illustrated by comparison of the 3 sets of values of n_0, the adjusted values of $\overline{n_\lambda}$, obtained from $\overline{n_0}$, the observed values of $\overline{n_\lambda}$ for the three focal positions for which results are given in tables 1, 2, and 3.

Values of n_0, the observed values of n_λ, as a function of zone number are given for the three focal positions in table 7. It is clear that the values differ by appreciable amounts. It is worthwhile to adjust these values by a focal shift of such amount that n_c, the adjusted values of n_λ, shall be zero at $m=7$. This may be done using the relation

$$n_0 - \Delta n_\lambda = n_c$$

where

$$\Delta n_\lambda = \left(\frac{n_0'}{49}\right) m^2 \qquad (21)$$

and n_0' is the observed value of n_λ for zone number $m=7$. Values of n_c obtained in this manner are also listed in table 7 together with $\overline{n_c}$, the average for the three focal planes. It is clear that there is good agreement among the three values of n_c although the determinations are based upon measurements made at markedly different focal positions. Consideration of the departures from the average $\overline{n_c}$ shows that the average error in n_λ does not exceed ± 0.02 for the range from $m=1$ to $m=8$ and does not exceed ± 0.05 for values of $m=9$ and $m=10$.

TABLE 7. *Values of* n_c *as a function of zone number* m *for three focal planes*

Values of n_c obtained from n_0, the observed values of n_λ, for three focal planes. Values of Δn_λ are so chosen that $n_c=0$ at $m=7$. The value of $\overline{n_c}$, the average of n_c for the three focal planes, for each value of m is also given.

m	$\Delta f=0.4$ mm			$\Delta f=0.0$ mm			$\Delta f=-0.8$ mm			$\overline{n_0}$
	n_0	Δn_λ	n_c	n_0	Δn_λ	n_c	n_0	Δn_λ	n_c	
1	0.04	0.01	0.03	0.03	0.00	0.03	−0.02	−0.04	0.02	0.02
2	.13	.04	.09	.09	−.01	.10	−.08	−.14	.06	.08
3	.27	.09	.18	.18	−.03	.21	−.18	−.32	.14	.18
4	.40	.16	.24	.22	−.05	.27	−.36	−.57	.21	.24
5	.48	.25	.23	.19	−.08	.27	−.68	−.89	.21	.24
6	.49	.36	.13	.05	−.11	.16	−1.16	−1.29	.13	.14
7	.49	.49	.00	−.15	−.15	.00	−1.75	−1.75	.00	.00
8	.59	.64	−.05	−.26	−.20	−.06	−2.29	−2.29	.00	−.04
9	1.21	.81	.40	.12	−.25	.37	−2.42	−2.89	.47	.41
10	3.20	1.00	2.20	1.83	−.31	2.14	−1.29	−3.57	2.28	2.21

The average value $\overline{n_c}$ versus zone height h is shown in figure 7. It is clear that for this particular focal position the optical path difference does not exceed ¼ wavelength for the range from $m=1$ to $m=8$. From this it may be inferred that the optical

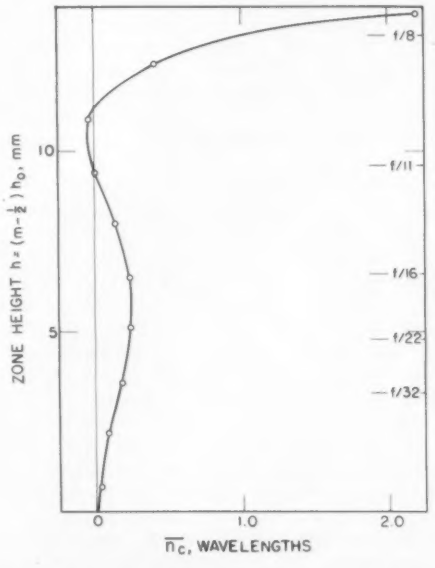

FIGURE 7. *Variation of the average adjusted value,* n_c *with zone height* $h=(m-\frac{1}{2})h_0$ *where* m *is the zone number and* h_0 *the slit separation.*

The value of $\overline{n_c}$ is the average value of $\overline{n_\lambda}$ for the three focal planes designated $\Delta f=0.4$, 0.0, and -0.8 following adjustment such that $n_c=0$ at $m=7$ in all three cases. The scale on the right-hand ordinate of the graph shows the value of the f/number corresponding to the indicated value of h, the zone height.

path difference will not exceed ¼ wavelength for one-half the effective area of the lens at maximum aperture. Moreover, it can be inferred that this lens should yield excellent imagery at f/11, good imagery at f/10, and that the quality of imagery can be expected to lessen appreciably at f/8 and smaller f/values.

5. Discussion

In this study, a visual method of determining longitudinal spherical aberration and departure of the wave front arriving at the image point from a true sphere is described. Results are reported for measurements made on a single lens for three positions of the focal plane. Tests for consistency of observations are described which permit an estimate of the reliability of the measurements.

The authors express their appreciation to other members of the staff for assistance during this work and particularly to Edgar C. Watts who designed the slit system and prepared the illustrations; and to George Cassiday and Peter Costello who performed many of the measurements.

(Paper 67C4–142)

JOURNAL OF RESEARCH of National Bureau of Standards—C. Engineering and Instrumentation
Vol. 67C, No. 4, October–December 1963

Development of Filters for a Thermoelectric Colorimeter

Sayeda H. Emara* and Ray P. Teele

(May 21, 1963)

Filters have been designed for use with photocells and phototubes in tristimulus colorimeters, but because of the variation in spectral response of these detectors from one to the other, it has not been worthwhile to attempt to achieve the best possible duplication of the CIE tristimulus functions. In the case of a thermoelectric detector, however, the response is so nonselective that the same filter designs can be used with any thermopile.

The new filters permit CIE tristimulus functions and chromaticity coordinates to be obtained directly with reasonable accuracy. Results obtained on a thermoelectric colorimeter for five standard filters are compared with tristimulus values obtained by computation from spectral transmittance data.

1. Introduction

Experience has shown that the results obtained in visual color measurements by a single observer are likely to differ from those of some other observer. For this reason, a number of observers must be used in order to obtain representative results. Furthermore, an observer using the equality-of-brightness method of photometry will change his criterion for photometric balance over a period of several days; some observers exhibit variation during a single day. If the properties of the normal average eye (CIE standard observer) can be reproduced in a completely physical instrument, these problems can be avoided. However, it is to be emphasized that physical color measurements must be made with high precision if they are to compare favorably with visual judgments of color, especially of small color difference. A colorimeter comparable to the eye of the standard observer in discrimination sensitivity must be capable of measuring tristimulus values, X, Y, Z, to at least one part in a thousand. For many years, the Bureau has been examining glasses and chemicals for possible use in physical colorimeters. It is more desirable to design tristimulus filters for use with a nonselective detector rather than a selective detector because such filters are not dependent on the useful life of an individual detector nor limited to a particular one.

No physical detector has been constructed which has the same relative response curve as the average human eye for radiant energy of different wavelengths. It is possible, however, to make a nonselective receiver, which indicates the amount of received energy per unit time independent of its wavelength throughout the visible spectrum. If we interpose between the source and such a receiver filters which duplicate the CIE tristimulus functions, we can then measure the tristimulus values and by computation obtain the chromaticity coordinates without reference to human observers. Such filters would permit CIE tristimulus functions and chromaticity coordinates to be obtained directly. The object of the present work was to determine if such filters could be realized closely enough to determine these quantities with reasonable accuracy.

Numerous instruments have been proposed and many constructed for direct color measurement over the years. Ives (1915) [1][1] described a thermopile tristimulus colorimeter in which he made use of a spectrum selectively projected through a series of carefully cut templates in place of the filters employed in the more recent devices. Twyman and Perry (1930) [2] suggested that three filters duplicating the then proposed standard observer could be used in a photoelectric instrument. Guild (1934) [3] described an experimental model of a photoelectric tristimulus colorimeter. A few years later Winch and Palmer (1937) [4], Dresler and Frühling (1938) [5], and Barnes (1939) [6] described devices for the same purpose. Gibson (1936) [7] and Van den Akker (1937) [8] have discussed the problem of obtaining source-filter-photocell combinations giving the closest equivalence to the standard observer. Hunter (1942) [9] described a three-filter method for photoelectric tristimulus colorimetry which was successfully applied to the Hunter multipurpose reflectometer [10] to measure surface color. Several new instruments have been designed in recent years. However, the photosensitive elements in these colorimeters have been barrier-layer photocells as in the instruments of Barnes (1939) [6] and Hunter (1942) [9], phototubes in the devices described by Glasser and Troy (1952) [11] and Hunter (1958) [12], and multiplier phototubes in the instruments designed by Sziklai (1951) [13], Bentley (1951) [14], and Nimeroff and Wilson (1954) [15]. Only in the instrument described by Ives (1915) [1] was a thermopile used.

*Guest Worker at the NBS—On leave from Ein-Shams University, Cairo, Egypt.

[1] Figures in brackets indicate the literature references at the end of this paper.

2. Filter Design

The only parts of a colorimeter over which the designer can exercise much control are the filters used to modify the detector response to obtain the $\bar{x}$, $\bar{y}$, and $\bar{z}$ functions of the CIE standard observer. The $\bar{x}$ function is bimodal and therefore two filters are used; one designated $\bar{x}$-short represents the $\bar{x}$ function from 380 to 500 nm and the other, $\bar{x}$-long, the $\bar{x}$ function from 510 to 760 nm. The components of these filters are usually absorbing solutions and glasses. Information on characteristics of various solutions and glass cells tested for photometric use is given in papers published by Ives and Kingsbury [16], [17], [18]. In this investigation, spectrophotometric curves of various solutions and glasses were made on a General Electric recording spectrophotometer. The data obtained on these filter components were used to compute the concentrations and thicknesses required to obtain a good fit for the spectral tristimulus values, $\bar{x}_\lambda$, $\bar{y}_\lambda$, $\bar{z}_\lambda$. Each of the filters designed contains as its components a solution, a cell, and two or more glasses.

2.1. Solutions

Chemicals used for preparation of solutions were labeled "analytical reagent quality" or "reagent quality." To prevent contamination from cork stoppers, glass-stoppered bottles were used as containers for all solutions.

The compositions of solutions used are as follows:

a. Solution I ($\bar{x}$-short and $\bar{z}$)

Cobalt ammonium sulphate ($CoSO_4 \cdot (NH_4)_2SO_4 \cdot 6H_2O$)	13.0 g
Nickelous sulphate ($NiSO_4 \cdot 6H_2O$)	19.5 g
Glacial acetic acid	60 ml
Distilled water to make one liter of solution.	

b. Solution II ($\bar{x}$-long)

Copper sulphate ($CuSO_4 \cdot 5H_2O$)	11.0 g
Ferric sulphate ($Fe_2(SO_4)_3 \cdot 9H_2O$)	11.5 g
Glacial acetic acid	60 ml
Distilled water to make one liter of solution.	

c. Solution III ($\bar{y}$)

Potassium dichromate ($K_2Cr_2O_7$)	0.140 g
Copper sulphate ($CuSO_4 \cdot 5H_2O$)	17.0 g
Cobalt ammonium sulphate ($CoSO_4 \cdot (NH_4)_2SO_4 \cdot 6H_2O$)	2.10 g
Sulphuric acid (1.835 sp gr)	10 ml
Distilled water to make one liter of solution.	

2.2. Cells

The filter accuracy obtained with solutions in cells depends in part on the spectral transmittance and uniformity of the cell. Cells having nonselective windows, closely parallel, and with close tolerances on window spacing are commercially available. Three identical cells with 1-mm thick windows and 50-mm spacing were selected. Spectrophotometric measurements indicated that the windows were nonselective in transmittance from 380 to 780 mm except for variations less than 1.5 percent. The solutions I, II, and III prepared as described above were placed in cells I, II, and III, respectively.

2.3. Glasses

The specifications of the glasses which were selected are shown in table 1.

TABLE 1. *Glass components of the four tristimulus filters*

No.	Mfgr.	Mfgr. No.	Name	Color spec. No.	Thickness
					mm
1	Corning	5433	Heat resistant projector blue	5-59	4.4
2	Corning	5543	Heat resistant lantern blue	5-60	0.84
3	Corning	9788	Colorimeter blue green light	4-97	.615
4	Corning	3780	Uranium yellow	3-80	.67
5	Kopp		Heat absorbing	K-48	[a]5

[a] (This thickness is about 5 mm as furnished by the manufacturer. This glass may no longer be obtainable from Kopp Glass Co., but it is similar to Corning filter No. 4600, color specification No. 1-69. The spectral transmittance of these heat-absorbing glasses from 560 to 780 mm is very similar to that of copper sulphate solution. Therefore, adjustment of concentration could be used to compensate for individual differences in spectral transmittance of the glass; however, glass samples obtained from three manufacturers were found to be sufficiently similar that no change in solution concentration was required.

2.4. Tristimulus

Solution-cells and the glasses listed in table 1 are combined to provide tristimulus filters as follows:

a. $\bar{x}$-short Filter

Solution-cell I and glasses numbered 1, 2, and 5

b. $\bar{x}$-long Filter

Solution-cell II and glasses numbered 3 and 5.

c. $\bar{y}$ Filter

Solution-cell III and glasses numbered 4 and 5. This filter design is a slight modification of the luminosity filter design by Gibson, Teele, and Keegan (1939) [19]. The use of heat-absorbing glass necessitated a reduction in copper sulphate and potassium dichromate and an increase in cobalt ammonium sulphate.

d. $\bar{z}$ Filter

Solution-cell I and glasses numbered 1 and 5.

3. Filter Characteristics

Spectral transmittance data for each of the four filters were obtained on a recording spectrophotometer [20], [21], [22]. Routine corrections for 100 percent, zero, and wave length scale were made [23] but additional corrections for inertia, slit width, and back reflectance were not made [24] since their total for these filters is less than the uncertainty of a single run on the spectrophotometer. The results

obtained are summarized in table 2. For each filter, the first column gives the spectral transmittance, the second column gives the relative transmittance adjusted to have the same area as the CIE curve, and the third column gives the CIE data. For ease of comparison the data from columns two and three for each filter are shown in figures 1, 2, 3, and 4. The transmittances less than 0.001 for the $\bar{z}$ colorimeter filter from 590 to 830 nm were found by remeasuring the three individual components of the filter on a wider range spectrophotometer after unexplained discrepancies turned up in the check of the performance of the colorimeter to be described presently.

For each colorimeter filter the sum of column three divided by the sum of column one gives the factor used to obtain the values in column two. These factors are also used to obtain the relative tristimulus values of any light source directly from the instrument readings, I.

$$X=2.560\ \ I_{\bar{x}\text{-short}} \quad +5.596 \quad I_{\bar{x}\text{-long}},$$
$$Y=2.033\ \ I_{\bar{y}},$$
$$Z=12.166\ \ I_{\bar{z}},$$

Where the subscript for I corresponds with the particular colorimeter filter being used.

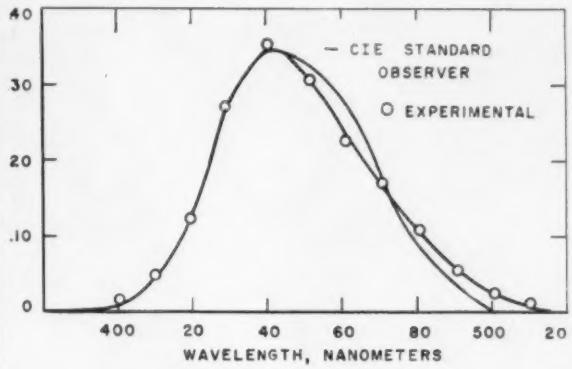

FIGURE 1. *Adjusted transmittance of* $\bar{x}$*-short filter compared to CIE tristimulus values* $\bar{x}_\lambda$.

TABLE 2. *Measured spectral transmittances, T, and adjusted spectral transmittances for each of the four filters compared to CIE spectral tristimulus values*

Wavelength	$\bar{x}$-short			$\bar{x}$-long			$\bar{y}$			$\bar{z}$		
	T	2.5605 T	CIE	T	5.5963 T	CIE	T	2.0327 T	CIE	T	12.166 T	CIE
nm												
380	0.0005	0.0013	0.0014				0.0000	0.0000	0.0000	0.0006	0.0073	0.0065
390	.0028	.0072	.0042				.0007	.0014	.0001	.0034	.0414	.0201
400	.0063	.0161	.0143				.0007	.0014	.0004	.0074	.0900	.0679
410	.0173	.0443	.0435				.0007	.0014	.0012	.0199	.2421	.2074
420	.0528	.1352	.1344				.0011	.0022	.0040	.0608	.7397	.6456
430	.1079	.2763	.2839				.0030	.0061	.0116	.1242	1.5111	1.3856
440	.1399	.3582	.3483				.0092	.0187	.0230	.1623	1.9746	1.7471
450	.1196	.3062	.3362				.0187	.0380	.0380	.1414	1.7203	1.7721
460	.0900	.2304	.2908				.0297	.0604	.0600	.1094	1.3310	1.6692
470	.0679	.1739	.1954				.0523	.1063	.0910	.0872	1.0609	1.2876
480	.0443	.1134	.0956	0.0000	0.0000		.0731	.1486	.1390	.0629	0.7652	0.8130
490	.0244	.0625	.0320	.0016	.0090		.1020	.2073	.2080	.0394	.4793	.4652
500	.0113	.0289	.0049	.0046	.0257		.1530	.3110	.3230	.0209	.2543	.2720
510	.0048	.0123		.0077	.0431	0.0093	.2437	.4954	.5030	.0106	.1289	.1582
520	.0019	.0049		.0121	.0677	.0633	.3545	.7206	.7100	.0053	.0645	.0782
530	.0007	.0018		.0212	.1186	.1655	.4250	.8639	.8620	.0026	.0316	.0422
540	.0005	.0013		.0414	.2317	.2904	.4671	.9495	.9540	.0021	.0255	.0203
550	.0010	.0026		.0716	.4007	.4334	.4925	1.0011	.9950	.0036	.0438	.0087
560	.0018	.0046		.1080	.6044	.5945	.4938	1.0037	.9950	.0058	.0706	.0039
570	.0013	.0033		.1493	.8355	.7621	.4692	0.9537	.9520	.0049	.0596	.0021
580	.0001	.0003		.1772	.9917	.9163	.4263	.8665	.8700	.00113	.0138	.0017
590	.0000	.0000		.1894	1.0599	1.0263	.3716	.7554	.7570	.00021	.0026	.0011
600				.1840	1.0297	1.0622	.3077	.6255	.6310	.00013	.0016	.0008
610				.1656	0.9267	1.0026	.2443	.4966	.5030	.00010	.0012	.0003
620				.1374	.7689	0.8544	.1832	.3724	.3810	.00007	.0008	.0002
630				.1078	.6033	.6424	.1297	.2636	.2650	.00003	.0004	.0000
640				.0778	.4354	.4479	.0853	.1734	.1750	.00001	.0001	
650				.0531	.2972	.2835	.0544	.1106	.1070	.00001	.0001	
660				.0338	.1892	.1649	.0316	.0642	.0610	.00001	.0001	
670				.0212	.1186	.0874	.0171	.0348	.0320	.00002	.0003	
680				.0121	.0677	.0468	.0090	.0183	.0170	.00005	.0006	
690				.0067	.0375	.0227	.0043	.0087	.0082	.00012	.0015	
700				.0035	.0196	.0114	.0013	.0026	.0041	.00019	.0023	
710				.0019	.0106	.0058	.0006	.0012	.0021	.00016	.0020	
720				.0010	.0056	.0029	.0003	.0006	.0010	.00013	.0016	
730				.0001	.0006	.0014	.0001	.0002	.0005	.00010	.0012	
740				.0000	.0000	.0007	.0001	.0002	.0003	.00008	.0010	
750						.0003	.0000	.0000	.0001	.00007	.0009	
760						.0002	.0000	.0000	.0001	.00006	.0007	
770–830						.0001				.00020	.0025	
Sums	0.6971	1.7850	1.7849	1.5901	8.8986	8.8987	5.2569	10.6855	10.6857	0.8751	10.6770	10.6770

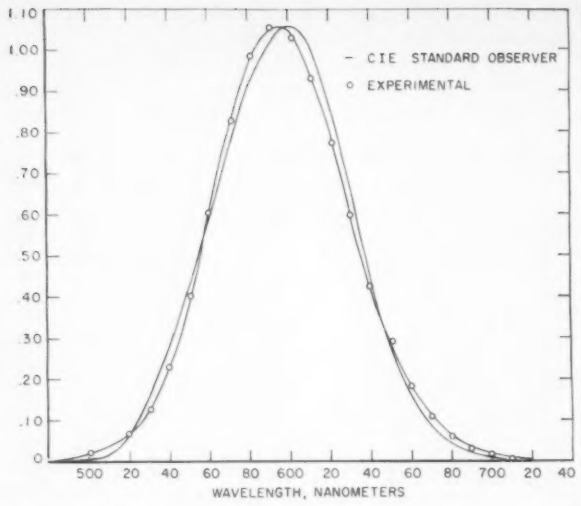

FIGURE 2. *Adjusted transmittance of $\bar{x}$-long filter compared to CIE tristimulus values $\bar{x}_\lambda$.*

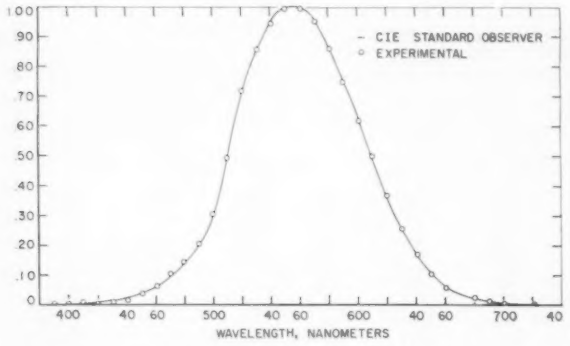

FIGURE 3. *Adjusted transmittance of $\bar{y}$ filter compared to CIE tristimulus values $\bar{y}_\lambda$.*

4. Performance

To check the performance of these four colorimeter filters, use was made of the instrument described by Teele [24] which consists essentially of a thermopile, potentiometer, and recorder.

The first check was a measurement of the chromaticity coordinates of an incandescent lamp at a color temperature of 2,854 °K (CIE source A). The tristimulus values obtained by reducing these data by the factors given above were divided by their sum in the usual way to obtain values of chromaticity coordinates as follows: $x=0.457$, $y=0.403$, $z=0.140$. These chromaticity coordinates differ from those obtained by computation from the spectral distribution of a Planckian radiator at a temperature of 2,854 °K by +0.009, −0.004, and −0.005, respectively. These differences correspond to a combination of errors from possible failure of the voltage assigned to the lamp to operate it at a color temperature of 2,854 °K, from failure of the lamp to yield spectral distributions characteristic of the Planckian radiator, from failure of the colorimeter filters to duplicate the CIE standard observer, and from the experimental errors of reading the thermopile.

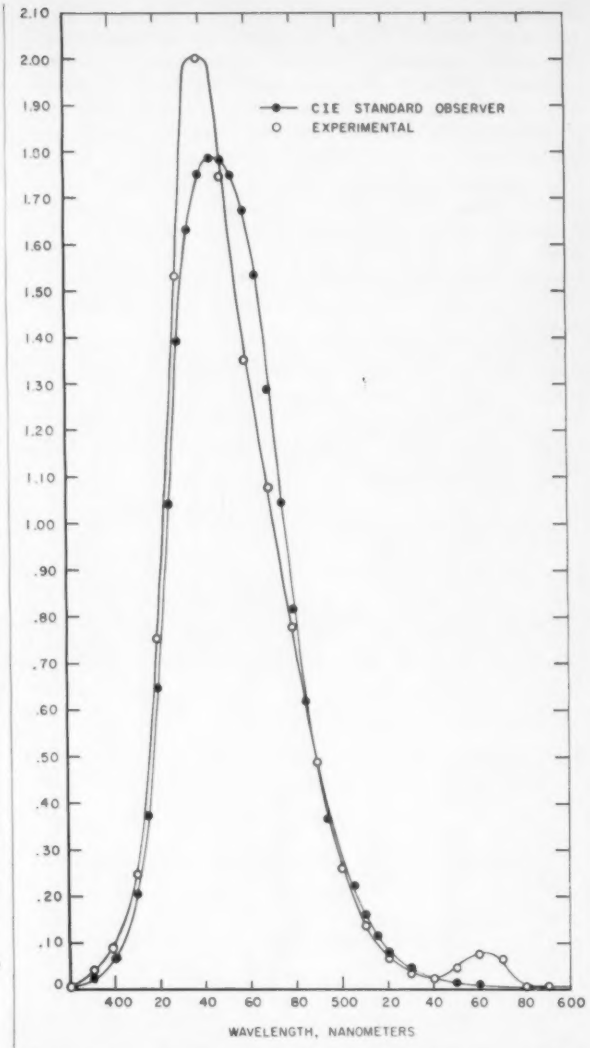

FIGURE 4. *Adjusted transmittance of $\bar{z}$ filter compared to CIE tristimulus values $\bar{z}_\lambda$.*

A more detailed check of the performance of the colorimeter filters was obtained by measuring five NBS standard spectrophotometer-integrator filters, NBS 2101 through 2105, master set number 1. These are glass filters described as selenium reddish orange, carbon yellow, sextant green, cobalt blue, and selective neutral.

They were originally calibrated to check the performance of spectrophotometers equipped with tristimulus integrators. [25] The five filters were measured on two spectrophotometers (Cary 14 and

GE); appropriate corrections (such as wavelength, zero, 100%, slit width, inertia, and back reflectance) were applied; spectral transmittances were adopted as weighted means; and uncertainties were estimated. The spectral transmittances of these filters are plotted in figure 5.

To provide a more detailed test of the performance of the colorimeter filters use was made of a device already devised by Teele, which consists essentially of a thermopile (nonselective receiver for radiant energy), potentiometer, and recorder, the incandescent lamp was operated at a color temperature of 2,854 °K as before. To eliminate back reflection effects, a concave-convex lens was positioned before and another after the filter to be measured as shown in figure 6. The colorimeter filter, say $\bar{x}$-short, was then introduced between the light source and thermopile, and the reading was recorded. The filter to be measured was placed in the beam between the concave-convex lenses, and a second reading was recorded. This procedure was repeated with each of the four colorimeter filters. The ratios, source through filter to source alone, of such readings through the four colorimeter filters, $\bar{x}$-short, $\bar{x}$-long, $\bar{y}$, and $\bar{z}$, gives the values: $R_{\bar{x}\text{-short}}$, $R_{\bar{x}\text{-long}}$, $R_{\bar{y}}$ and $R_{\bar{z}}$ respectively, which may in themselves serve as a colorimetric specification of the filter to be measured relative to the reference source. The CIE tristimulus values of the test filter with source A, adjusted to make Y_A equal to the luminous transmittance of the filter in percent, are computed as follows:

$$X_A = 5.37R_{\bar{x}\text{-short}} + 104.45R_{\bar{x}\text{-long}},$$

$$Y_A = 100.00R_{\bar{y}},$$

$$Z_A = 35.55R_{\bar{z}},$$

where the coefficients 5.37, 104.45, 100.00, and 35.55 are related to the source-A tristimulus values. The coefficients of $R_{\bar{y}}$ and $R_{\bar{z}}$, are the Y and Z tristimulus values for source A, respectively. The coefficients of $R_{\bar{x}\text{-short}}$ and $R_{\bar{x}\text{-long}}$ are the summations of the spectral tristimulus values for the $\bar{x}$ function and source A from 380 to 500 nm and from 510 to 770 nm, respectively.

The chromaticity coordinates, x, y, z, of the test filters are calculated from the tristimulus values, X, Y, Z, in the usual manner:

$$x = X/(X+Y+Z),\ y = Y/(X+Y+Z),\ z = Z/(X+Y+Z)$$

Table 3 compares the measured values of the five standard filters with their assigned values. Each measured value was computed from 10 independent determinations of the ratio R. The uncertainties of the assigned values shown in the table are those estimated by Keegan, Schleter, and Judd as the ranges of the values found by three different spectrophotometers [25]; see their table 11. The uncertainties shown for the measured values are based upon computations of huge error (4.9 times the probable error) of the mean of the ten settings of the ratios R. These computations showed that the huge error (uncertainty at the one-tenth of one percent level) of values of the ratio R was on the average equal to ± 0.0025, and these estimates of uncertainty are given directly for the values of Y in table 3. Propagation of these errors to chromaticity coordinates, x, y, z, leads to the estimates of uncertainties entered in table 3.

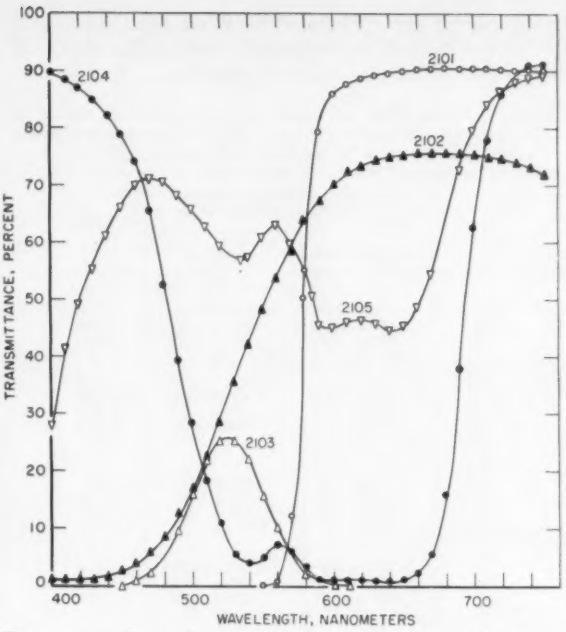

FIGURE 5. *Spectral transmittances of the five test filters.*

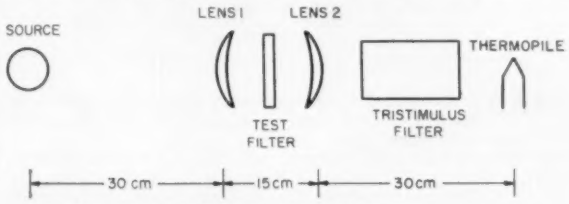

FIGURE 6. *Diagram of the optical arrangement.*

It will be noted from table 3 that the sum of the uncertainties listed fails in 11 cases out of 20 to exceed the difference between the measured and assigned values. Of course, since the colorimeter filters do not succeed precisely in duplicating the distribution functions of the 1931 CIE standard observer (see table 2), some discrepancy between measured and assigned values is to be expected. Table 4 gives in column 2 the differences ascribable to failure of the spectral transmittances of the colorimeter filters to have precisely the wavelength variation striven for. In column 3 are given the observed differences copied from the last column of table 3, and in column 4 are given the sums of the uncertainties listed in columns 2 and 3 of table 3. If the expected difference departs from the observed difference by less than the combined uncertainty, we may say that a reasonable basis for explaining the discrepancy has been found. Column 5 gives the amounts of the unexplained discrepancies. It is computed as the excess of the abso-

lute value of the difference between columns 2 and 3 over the sum of the uncertainties in column 4. If there is no excess, no entry is inserted.

TABLE 3. *Comparison of measured and assigned values of chromaticity coordinates, x, y, z, and luminous transmittance, Y, for CIE source A for the five NBS standard filters*

Filter No. and coordinate	CIE colorimetric coordinates for standard filters with source A		Difference
	Measured	Assigned	
2101			
x	0.6364±0.0018	0.6488±0.0009	−0.0124
y	.3577± .0018	.3509± .0009	+.0068
z	.0059± .0018	.0003± .0000	+.0056
Y	38.0 ± .25	37.6 ± .5	+.4
2102			
x	0.5443±0.0015	0.5497±0.0002	−0.0054
y	.4298± .0014	.4324± .0003	−.0026
z	.0260± .0007	.0179± .0001	+.0081
Y	55.1 ± .25	55.3 ± .02	−.2
2103			
x	0.253 ±0.016	0.236 ±0.005	+0.017
y	.654 ± .015	.668 ± .004	−.014
z	.093 ± .003	.096 ± .004	−.003
Y	8.56 ± .25	9.07 ± .13	−.51
2104			
x	0.1992±0.0060	0.1871±0.0019	+0.0121
y	.1609± .0059	.1630± .0034	−.0021
z	.6399± .0064	.6499± .0057	−.0100
Y	5.8 ± .25	5.9 ± .23	−.1
2105			
x	0.4211±0.0014	0.4163±0.0019	+0.0048
y	.4076± .0014	.4087± .0020	−.0011
z	.1712± .0005	.1750± .0016	−.0038
Y	53.3 ± .25	53.9 ± .2	−.6

TABLE 4. *Analysis of the discrepancies between the differences listed in table 3 and those to be expected from the actual colorimeter filters used.*

Filter No. and coordinate	Differences to be expected between measured and assigned values	Differences actually found (taken from last column of table 3)	Sum of the uncertainties in the assigned and measured values (from columns 2 and 3 of table 3)	Unexplained discrepancies. (If the absolute value of the difference between columns 2 and 3 exceeds the sum of the uncertainties in column 4, the amount of this excess is recorded below.)
(1)	(2)	(3)	(4)	(5)
2101				
x	−0.0023	−0.0124	0.0027	0.0074
y	−.0015	+.0068	.0027	.0056
z	+.0038	+.0056	.0008	.0010
Y	−.2	+.4	.75	
2102				
x	−0.0032	−0.0054	0.0017	0.0005
y	−.0042	−.0026	.0017	
z	+.0073	+.0081	.0008	
Y	−.1	−.2	.27	
2103				
x	−0.0009	+0.017	0.021	
y	−.0010	−.014	.019	
z	+.0020	−.003	.007	
Y	+.02	−.51	.38	0.15
2104				
x	+0.0096	+0.0121	0.0079	
y	+.0003	−.0021	.0093	
z	+.0099	−.0100	.0121	
Y	+.01	−.1	.48	
2105				
x	+0.0025	+0.0048	0.0033	
y	−.0017	−.0011	.0034	
z	−.0007	−.0038	.0021	0.0010
Y	.0	−.6	.45	.15

Table 4 shows that nearly all discrepancies are accounted for by the imperfection of the fit of the four filters to the respective CIE curves and that improvement in performance depends upon finding better constitutents for the solutions and different glasses (or different thicknesses of the same glasses that are now used).

It will be noted from table 4 that for four of the five filters the unexplained discrepancies (column 5) are few and small. For filter 2101, however, the discrepancies in chromaticity coordinates are large. Perhaps it is significant that this filter (selenium reddish orange) is the only one of the five which has a large temperature coefficient of spectral transmittance.

By comparing the uncertainties in the measured values (column 3, table 3) ascribable to the uncertainty of 2.5 on a scale of a thousand in the measured ratios with the differences (column 2, table 4) to be expected because the colorimeter filters do not have precisely the ideal spectral character striven for, it may be noted that those two sources of error are about equally important. The performance of the colorimeter could be significantly improved only by developing better $\bar{x}$ and $\bar{z}$ colorimeter filters and at the same time reducing the noise from the thermopile and amplifier. Significant improvement of the colorimeter filters might be accomplished by combining the components in parallel as well as in series as was originally suggested by Dresler [26], and used among others by Nimeroff and Wilson [15], Frühling and Krempel [27], Geutler [28], and Davies and Wyszecki [29].

The authors express their appreciation to the members of the staff who ran the numerous spectrophotometric curves required to develop the filters.

5. References

[1] H. E. Ives, A precision artificial eye, Phys. Rev. **6,** 334 (1915).

[2] F. Twyman and J. Perry, Improvements in or relating to colorimeters, Brit. Pat. Spec. No. 324, 351 (Jan. 20, 1930).

[3] J. Guild, The instrumental side of colorimetry, J. Sci. Instr. **11,** 68 (1934).

[4] G. T. Winch and E. H. Palmer, A direct reading photoelectric trichromatic colorimeter, Trans. Illum. Eng. Soc. London **2,** 137 (1937).

[5] A. Dresler and H. G. Frühling, A tristimulus photoelectric colorimeter (in German), Das Licht **8,** 238 (1938).

[6] B. T. Barnes, A four-filter photoelectric colorimeter, J Opt. Soc. Am. **29,** 448 (1939).

[7] K. S. Gibson, Photoelectric photometers and colorimeters, Instruments **9,** 309 and 335 (1936).

[8] J. A. Van den Akker, Chromaticity limitations of the best physically realizable three-filter photoelectric colorimeters, J. Opt. Soc. Am. **27,** 401 (1937).

[9] R. S. Hunter, Photoelectric tristimulus colorimetry with three filters, NBS Circ. C429 (1942).

[10] R. S. Hunter, A multipurpose photoelectric reflectometer, J. Res. NBS **25,** 581 (1940) RP1345; or J. Opt. Soc. Am. **30,** 536 (1940).

[11] L. G. Glasser and D. J. Troy, A new high sensitivity colorimeter, J. Opt. Soc. Am. **42,** 652 (1952).

[12] R. S. Hunter, Photoelectric color difference meter, J. Opt. Soc. Am. **48,** 985 (1958).

[13] C. G. Sziklai, A tristimulus photometer; J. Opt. Soc. Am. **41,** 321 (1951).
[14] G. P. Bentley, An industrial color matcher, Electronics **24,** 102 (1951).
[15] I. Nimeroff and S. W. Wilson, A colorimeter for pyrotechnic smokes, J. Res. NBS **52,** 195 (1954) RP2488.
[16] H. E. Ives and E. F. Kingsbury, Experiments with colored absorbing solutions for use in hetrochromatic photometry, Trans. Illum. Eng. Soc. **8,** 795 (1914).
[17] H. E. Ives and E. F. Kingsbury, Additional experiments on colored absorbing solutions for use in hetrochromatic photometry, Trans. Illum. Eng. Soc. **10,** 253 (1915).
[18] H. E. Ives, The photometric scale, J. of Franklin Inst. **188,** 217 (1919).
[19] K. S. Gibson, R. P. Teele, and H. J. Keegan, An improved luminosity filter, J. Opt. Soc. Am. **29,** 144 (1939).
[20] A. C. Hardy, A new recording spectrophotometer, J. Opt. Soc. Am. **25,** 305 (1935).
[21] K. S. Gibson and H. J. Keegan, Calibration and operation of the General Electric recording spectrophotometer of the National Bureau of Standards, J. Opt. Soc. Am. **28,** 372 (1938).
[22] H. J. Keegan and K. S. Gibson, On the use of working standards of didymium and vitrolite glasses for spectrophotometric measurements, J. Opt. Soc. Am. **34,** 770 (1944).
[23] K. S. Gibson, Spectrophotometry, NBS Circ. 484 (1949).
[24] R. P. Teele, A physical photometer, J. Res. NBS **27,** 217 (1941) RP 1415; also R. P. Teele, Measuring circuit for radiometers, J. Opt. Soc. Am. **44,** 860 (1954).
[25] H. J. Keegan, J. C. Schleter, and D. B. Judd, Glass filters for checking performance of spectrophotometer-integrator systems of color measurement, J. Res. NBS **66A** (Phys. and Chem.) No. 3, 203 (1962).
[26] A. Dresler, On a new kind of filter combination for exact adjustment of the spectral sensitivity of photocells to the eye-sensitivity curve (in German), Das Licht, **3,** 41 (1933).
[27] H. G. Frühling and F. Krempel, A photoelectric colorimeter constructed according to the Dresler principle (in German), Die Farbe, **3,** 1 (1955).
[28] G. Geutler, On the improvement and use of photoelectric colorimeters according to the Dresler principle, Die Farbe, **7,** 1953 (1958).
[29] W. E. R. Davies and G. Wyszecki, Physical approximation of color-mixture functions, J. Opt. Soc. Am. **52,** 679 (1962).

(Paper 67C4–143)

JOURNAL OF RESEARCH of the National Bureau of Standards—C. Engineering and Instrumentation
Vol. 67C, No. 4, October–December 1963

Application of Air Bearings to an Electrodynamic Vibration Standard

T. Dimoff and B. F. Payne

(July 3, 1963)

In an attempt to eliminate unwanted resonances and transverse motions in an electrodynamic exciter used as a vibration standard, the mechanical suspension-guide for the moving element was replaced with air bearings. The transverse motions of this exciter showed a distinct improvement over the transverse motions of the exciters with flexure plate and tensioned wire supports. The improved stability of the moving element of the air-bearing exciter made it possible to calibrate this exciter easily by an interferometer method. Agreement between three methods of calibration, reciprocity, interferometer, and optical target, was very good. The results of calibrations of two types of pickups on this modified standard are presented.

1. Introduction

The widespread use of vibration pickups to measure the amplitudes and frequencies of vibrations present in aircraft, rocket engines, ordnance systems, machinery, ships, etc., has led to the need for improved vibration standards. The feasibility of using certain kinds of electrodynamic vibration exciters as standards for the calibration of pickups was demonstrated by Levy and Bouche [1, 2] [1]. A limitation in the use of electrodynamic vibration exciters as calibrators has been the presence of undesirable transverse motions superimposed on the required sinusoidal axial motion of the moving element.

The present report describes the modifications made in a commercial electrodynamic exciter in which the mechanical suspension-guide for the moving element is replaced with air bearings. The methods used and the results of the calibration of this exciter are given and compared with exciters using flexure plate and tensioned wire supports. The results of calibrations of two types of vibration pickups using this exciter are also presented.

2. Description of the Electrodynamic Exciter

A rectilinear vibration exciter of the electrodynamic type was equipped with air-bearing support guides. The moving element includes a velocity sensing coil which, when calibrated, permits the exciter to be used as an electrodynamic vibration standard. The exciter is shown schematically in figure 1. The moving element consists of a mounting table, T, a velocity sensing coil, C_2, a driving coil, C_1, and a connecting shaft. The table is set in motion by applying alternating current to the driving coil which is in a steady magnetic field induced by the main magnet, M, when direct current is passed through the field coil, C_m. The motion of the table, T, is measured by the voltage output of the velocity sensing coil, C_2, in conjunction with the permanent magnet, M_2 since this voltage is proportional to the absolute velocity of the table motion. The pickup to be calibrated is rigidly mounted on the table, T.

The ideal exciter should produce pure axial motion free of transverse motions. The earlier use of flexural plates or suspension wires caused unwanted resonances and transverse motions.

More detailed discussions of the principles of operation and limitations of the electromechanical system are given in references [1, 2, and 3].

2.1. Air-Bearing Standard

The vibration exciter modified with an air-bearing suspension guidance system is shown in figure 1. The moving element is supported on two air bearings of the external pressure or hydrostatic type [4–7].

The only mechanical connections between the moving element and the stationary parts of the exciter are the flexible input wire to the driver coil and the thin output wire from the velocity sensing coil. The air bearings are located in the approximate position of the replaced flexure plates. Two different sizes of bearings are used. The front bearing is 2.187 in. in diameter and the back bearing 1.250 in. The lengths of the bearings are 1.000 in. The journal of the front bearing is also the vibration table of the exciter and was designed with a larger diameter to make it possible to mount large or small vibration pickups on it. The front bearing, shown in figure 2, has twelve orifices; the back bearing has six. The bearing sleeves have air distribution annuli 0.125 in. deep and 0.255 in. wide in their outer surface. Orifices of 0.02 in. diam. are drilled through these sleeves. The bearings have a radial clearance of 0.001 in. The bearings are made of brass and have aluminum journals.

The front bearing fixture, which is bolted down on three studs, is a 1 in. thick circular aluminum plate 14 in. in diameter. The back bearing is fixed in the same manner on the magnetic shield which is a circular steel plate ½ in. thick and 8 in. in diameter.

[1] Figures in brackets indicate the literature references at the end of this paper.

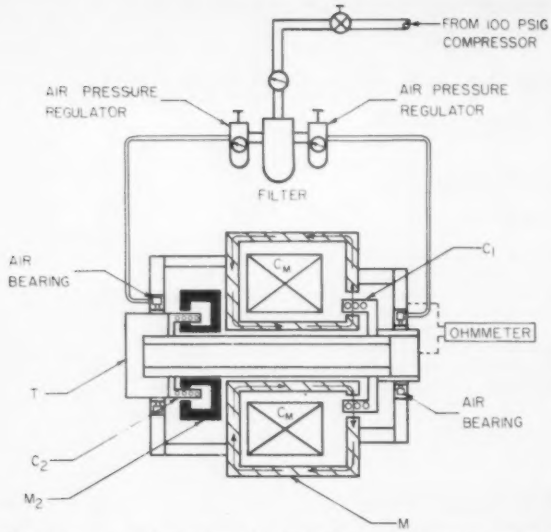

FIGURE 1. *Schematic of electrodynamic-vibration exciter equipped with air-bearing suspension-guidance system.*

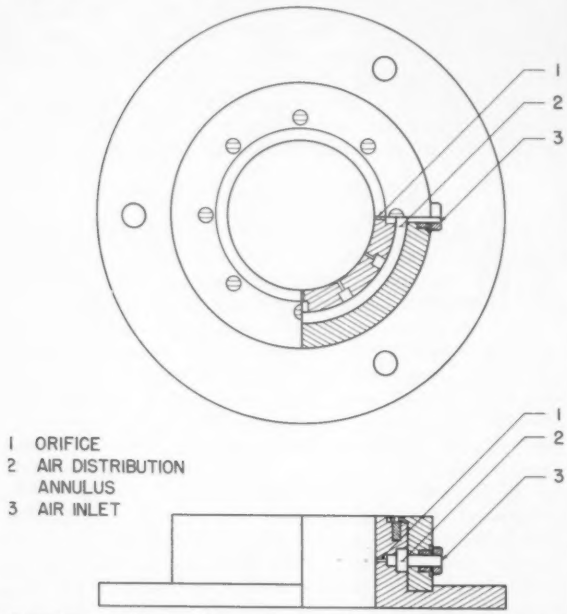

FIGURE 2. *Air bearing used to provide one degree of freedom in the electrodynamic exciter.*

The velocity coil was modified by cutting off the reduced diameter front part. It then was screwed and cemented rigidly to the table and the shaft.

The compressed air used is the building maintenance air supply. The air is filtered and each bearing has a separate air regulator (see fig. 1). The air is transmitted to the bearings by means of flexible tubing with an inside diameter of 0.125 in. During the calibration of the exciter and the pickups, the air pressure was maintained at 50 psig for both bearings

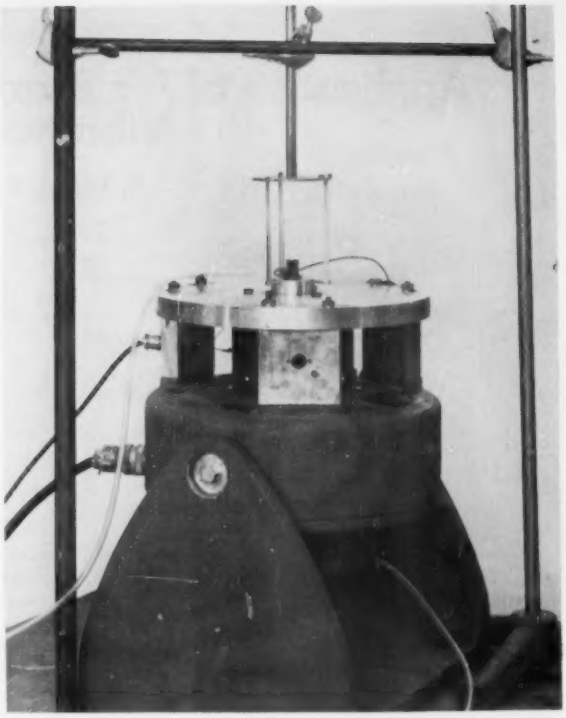

FIGURE 3. *Setup for calibration of a piezoelectric accelerometer.*

and the air temperature was about 65 °F. When varying the air pressure between 20 and 80 psig, no significant change is observed in the measured transverse motions.

When the exciter is used in a vertical position, the moving element is supported by three rubber bands 120° apart attached to the moving shaft by screws and to a circular plate positioned directly above the moving element as shown in figure 3. The circular plate can be rotated and the position of the moving element thus adjusted with respect to the stationary exciter. The equilibrium positions of the coils are held constant with respect to the magnets. With the exciter in a horizontal position, there is no need for any additional support. The leads from the driver coil provide sufficient support to keep the moving element from rotating and coming into physical contact with the stationary part of the exciter. An ohmmeter is connected between the moving element and the sleeve to indicate if metal to metal contact is made between the moving and nonmoving parts of the exciter. By careful alinement of the two bearings, this possibility is eliminated because the surfaces are always separated by a thin film of air. Having the exciter in a horizontal position with a 5 lb weight mounted on the table, and air pressure at 20 psig, no mechanical connection is observed. A 5 psig air pressure is adequate to support the moving element with no load attached. The performance data of the air bearing standard are given in table 1.

TABLE 1. *Performance data for air-bearing exciter*

Weight of moving element	2.20 lb.
Exciter table load	5 lb.
Force rating	50 to 50 lb to 500 c/s.
	50 to 25 lb to 1000 c/s.
Pounds per ampere	10.
Maximum table excursion	0.5 in.
Frequency of major resonance	2200 to 2300 c/s.
Frequency of magnet structure resonance	10 c/s approx.
D-c field resistance	50 to 55 ohms approx.
Driver coil resistance	2.0 ohms approx.
Stray magnetic field at table level	5 gauss approx

2.2. Transverse Motion Measurements

The transverse motions of the mounting table were measured using two piezoelectric accelerometers with their principal sensitive axes mutually perpendicular to each other as shown in figure 4 [2]. The one accelerometer, which measured vertical transverse motion, has its sensitive axis perpendicular to the axial motion of the table and measures motion up and down in the plane of the page. The second accelerometer, with a sensitive axis perpendicular to the axial motion and perpendicular to the plane of the page measured the transverse motion in the horizontal direction. A third accelerometer was mounted with its sensitive axis coaxial to the axial motion of the standard to measure the axial motion or axial acceleration. The three accelerometers were mounted on a small cube of stainless steel with two dummy accelerometers to balance the load of the vertical and horizontal accelerometers.

The transverse motions indicated with these devices should not be attributed entirely to the standard since the accelerometers themselves have a transverse response. The transverse motions of the air-bearing exciter depend to a great extent on the bearing alinement and bearing clearance.

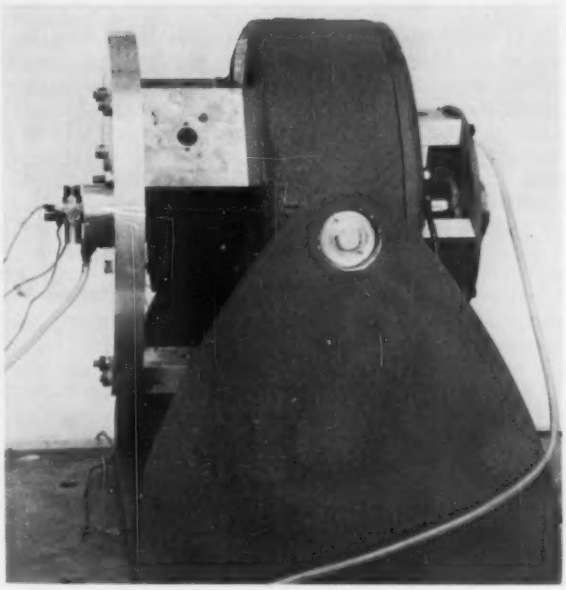

FIGURE 4. *Setup for measuring transverse motion with three piezoelectric accelerometers with their principle sensitive axes mutually perpendicular.*

Figure 5 shows the transverse motions of an air-bearing exciter using two experimental bearings with equal diameters but with closer radial clearances (less than 0.001 in.) than the bearings subsequently installed. Significant transverse motions in the vertical direction are observed in the regions of 750 and 2,190 c/s, and in the horizontal direction in the regions of 400 and 2,190 c/s. The transverse motions near 400 and 750 c/s are attributed to the

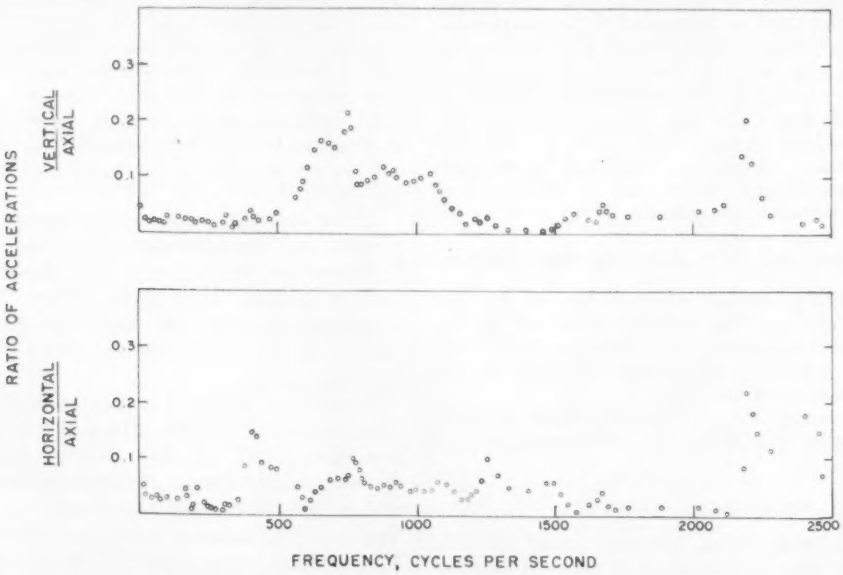

FIGURE 5. *Ratios of transverse to axial acceleration using experimental air bearings.*

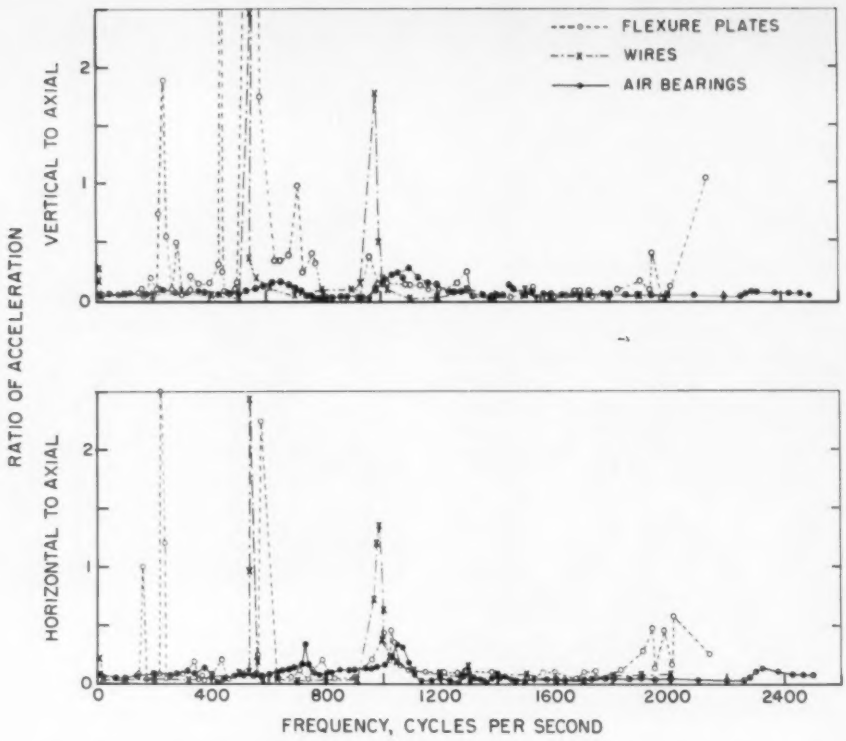

FIGURE 6. *Measured accelerations due to transverse motions using three types of suspension systems.*

fundamental and probably the second bending mode resonances of the moving element. In figure 6 the measured transverse motions of exciter No. 676 using air bearings (fig. 4) are compared with the transverse motions of exciter No. 619 using a flexure plate suspension and a tensioned wire suspension. Significant transverse motions of the air-bearing exciter in this case occur in the vertical direction at 650 and 1,100 c/s and in the horizontal direction at 730 and 1,050 c/s. The differences between the transverse motions plotted here (fig. 6) and the transverse motions in the experimental set of bearings (fig. 5) are thought to be due to differences in bearing clearance and alinement.

3. Calibration of the Air-Bearing Exciter

The air-bearing exciter was calibrated by the reciprocity method. The results obtained by the use of the interferometer fringe disappearance and optical target methods are compared with the results of the reciprocity method.

The exciter rests on a concrete block isolated from floor-borne vibrations by compression coil springs.

3.1. Reciprocity Calibration

The reciprocity theorem for mechanical systems states that if a force is impressed at point A and the velocity is measured at point B, the same velocity will be measured at point A if the force is impressed at point B. The reciprocity theorem as applied to electrodynamic vibration exciters is given in reference [1]. In order for the theorem to hold, the system must be linear, i.e., the displacement, velocity and current must increase linearly with force and voltage. The application of reciprocity to this system is limited to frequencies above and below the resonances of the moving element. At frequencies near each resonance there is a loss in precision due to changes in the electromechanical properties of the calibrator in that the relationships are no longer linear.

The reciprocity calibration consists of two experiments: (1) measurement of transfer admittance between the driving coil and the velocity-sensing coil; (2) measurement of the voltage ratio of the open circuited velocity coil and driving coil when the exciter to be calibrated is driven by an external exciter.

Transfer admittance measurements, $\overline{Y}_e$, were made with a series of weights attached one at a time to the mounting table of the exciter. Also a zero load transfer admittance measurement was made before and after each measurement with a weight attached. The zero load transfer admittance is denoted by $\overline{Y}_{e0}$. The weights were increment weights ranging from 0.1 lb to 2.0 lb.

Using the measured values of $\overline{Y}_e$ and $\overline{Y}_{e0}$, graphs of the real and imaginary values of the ratio $\frac{W_{(1,2,\ldots)}}{\overline{Y}_e - \overline{Y}_{e0}}$ are plotted versus $W_{(1,2,\ldots)}$ for each frequency, where $W_{(1,2,\ldots)}$ = increments of mass attached to the table. The zero intercepts, J and iJ, of the resulting straight lines and their slopes, Q and iQ, are computed by a weighted least square method.

Having determined the voltage ratio $\overline{R}$, $\overline{J}$, and $\overline{Q}$, the sensitivity of the exciter is given by

$$\overline{S} = 0.04288 + 0.04286 \frac{W\overline{Q}}{\overline{J}} (f\overline{R}\overline{J}\hat{j})^{1/2} \text{ v/in./sec}$$

where

f is the frequency in cycles per second and
$\hat{j}$ is the unit imaginary vector.

3.2. Interferometer Calibration

The air-bearing exciter was calibrated by the interferometric fringe disappearance method as given in reference [8]. Figure 7 shows the exciter and interferometer in position for calibration. The sensitivity of the exciter is given by

$$S = E\sqrt{2}/\pi f(2s)$$

where E is the rms voltage output of the velocity sensing coil corresponding to the first order fringe disappearance, s is the amplitude of displacement of the moving element (4.11×10^{-6} in. for the first order disappearance using mercury light and green filter), f is the frequency, and S is given in peak to peak v/in./sec. The voltage was read by an a-c transfer standard using a VTVM as a null. The data were taken with the exciter in a horizontal position. Readings for zero load and 1 lb load were taken over the range of 350 to 2,500 c/s.

Each value of voltage, E, is obtained from the average of two observations, one for the first fringe disappearance during slowly increasing displacement amplitude and the second for the fringe disappearance during slowly decreasing amplitude. For the zero load, the mean deviation from the mean of the voltage values ranged from 0.1 to 0.7 percent. The deviations were computed from sets of six or more values at each test frequency over the range of 350 to 2,500 c/s. The average deviation was 0.3 percent. The voltage values obtained by two observers differed from 0 to 0.8 percent for sets of three or more values per observer at each test frequency. The average repeatability was 0.3 percent.

For the 1 lb load readings the reflecting glass was attached to the center of the weight. The mean deviation for the 1 lb load readings ranged from 0.1 to 1.6 percent. The average deviation was 0.5 percent.

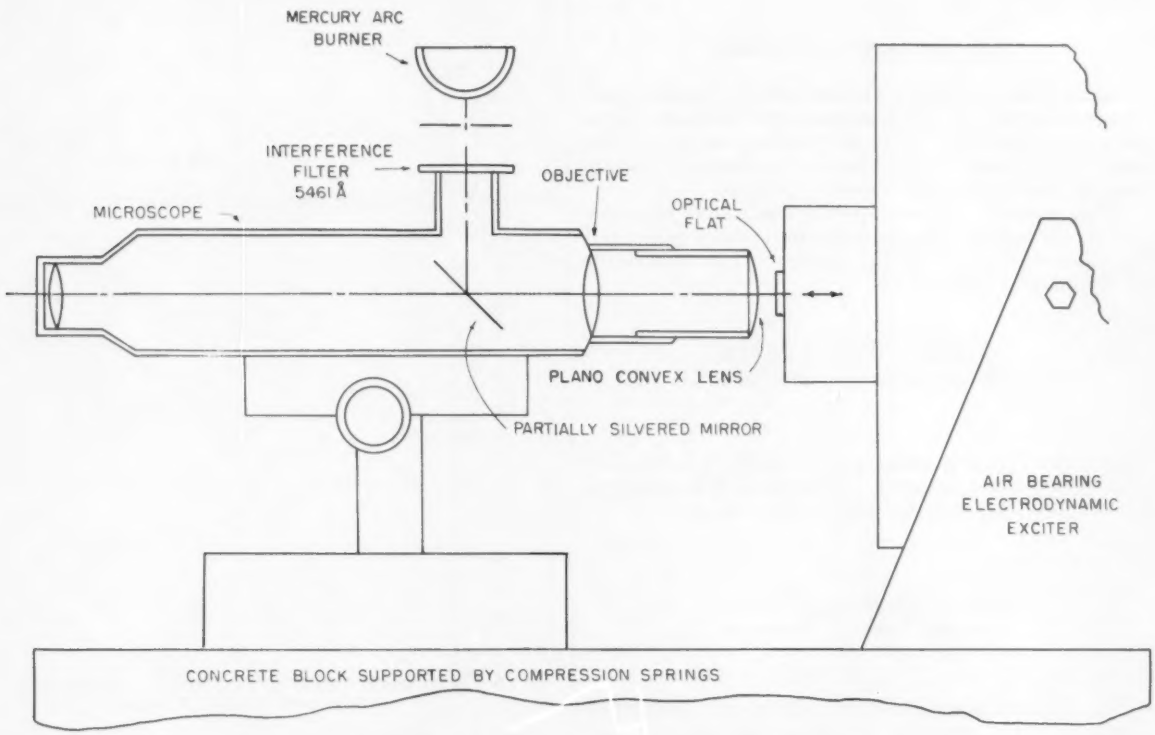

FIGURE 7. *Schematic arrangement for calibration of exciter with interferometer.*

The use of the interferometer fringe disappearance method is greatly facilitated on the air-bearing exciter as compared to the tensioned wire exciter because of the increased stability of the interference fringes.

3.3. Calibration With an Optical Target

The air-bearing exciter was calibrated optically by small wire targets mounted on the exciter table. The targets were coated with particles from camphor smoke and the diameters measured to ten-thousandths of a centimeter. Two diameters of wires were used. A 0.2042 cm wire was used to calibrate at 15, 17, 20, 30, and 45 c/s. A 0.1048 cm wire was used to calibrate at 55 and 70 c/s. The exciter was driven with increasing amplitude until the wire appeared to vanish. The output of the velocity coil was used as the output corresponding to the amplitude of vibration given by the diameter of the wire. Knowing the amplitude, frequency, and output of the velocity coil, the sensitivity of the exciter was determined. The average sensitivity for 13 observations at 7 frequencies was 0.1859 v/in./sec with a mean deviation of 0.0004. This compares with an average of 0.1857 v/in./sec for the reciprocity calibration from 10 to 400 c/s and 0.1857 volts/in./sec for the interferometer calibration from 350 to 750 c/s.

Figure 8 shows the calibration factors obtained for the air-bearing exciter by the three methods described above.

3.4. Calibration of Pickups

After calibrations by the reciprocity method and the interference fringe disappearance method, vibration standard 676 with air-bearing supports was used to calibrate a piezoelectric acceleration pickup and an electrodynamic velocity pickup.

The piezoelectric pickup was calibrated by comparing its voltage output with the voltage generated by the velocity coil of the exciter. The sensitivity of the pickup is given by

$$S_{\text{pickup}} = \frac{\text{voltage output of pickup}}{\text{voltage output of velocity coil}} S_{\text{exciter}}$$

where the S_{exciter} is corrected to read v/g instead of v/in./sec (g=386 in./sec^2). This ratio is determined by the following transfer admittance ratios:

$$\frac{I_{\text{driving coil}}/V_{\text{velocity coil}}}{I_{\text{driving coil}}/V_{\text{pickup}}} = \frac{V_{\text{pickup}}}{V_{\text{velocity coil}}}.$$

The electrodynamic velocity pickup was calibrated similarly. The results of these calibrations are given in figures 9 and 10.

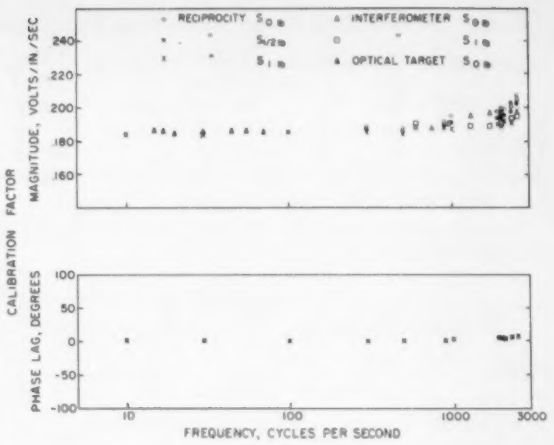

FIGURE 8. *Calibration factors of the exciter velocity sensing coil.*

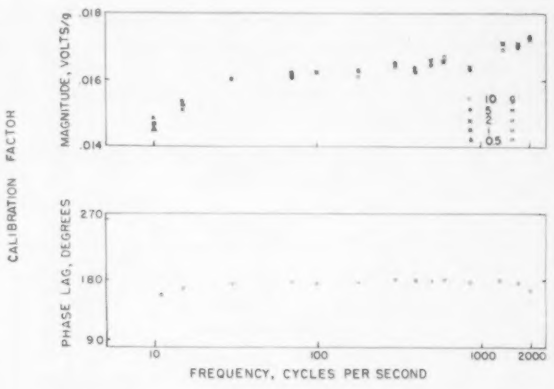

FIGURE 9. *Calibration factors of a piezoelectric acceleration pickup.*

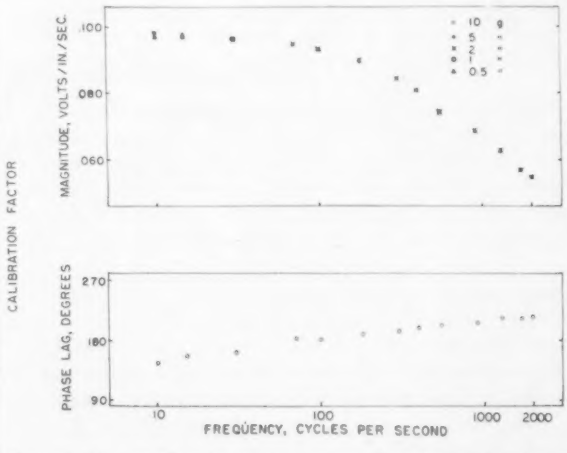

FIGURE 10. *Calibration factors of an electrodynamic velocity pickup.*

4. Discussion

Although the air-bearing suspension resulted in eliminating much of the transverse motion for exciter 676 (see fig. 6), there are still frequencies near 700 and 1,000 c/s which should be avoided during calibrations of vibration pickups.

It is extremely unlikely that five of the six degrees of freedom of the mounting table can be eliminated due to the geometrical configuration of the moving element as shown schematically in figure 1. Also, there are several materials with different moduli of elasticity incorporated into the moving element. Due to these factors, axial and flexural resonances may be excited in the moving element that interfere with its use as a pickup calibrator.

It is attractive to consider the possibility of constructing moving elements of uniform cross section and maximum axial and transverse stiffnesses. Such elements should be much better for use in vibration standards.

Certain advantages accrue from the substitution of the air-bearing suspension guidance system for flexure plates and tensioned wires. The air bearings allow larger axial motions than were possible with the mechanical suspension systems. The flexure plates and wires themselves were excited in resonance at certain frequencies which interfered with the utility of the exciter. With air bearings, the moving element is free to move axially but is prevented from moving laterally; this minimizes transverse motions at the mounting table.

Richard Harwell machined the bearings and supporting assembly. Ruth M. Woolley performed most of the computations. James A. Miller and L. R. Sweetman rendered valuable assistance and constructive criticism.

5. References

[1] Samuel Levy and Raymond R. Bouche, Calibration of vibration pickups by the reciprocity method, J. Research NBS **57**, 227–243 (1956) RP2714.

[2] R. R. Bouche, Improved standard for the calibration of vibration pickups, Proc. SESA, **XVIII** No. 1, 116–121 (1961).

[3] Anon., Calibration of shock and vibration pickups, ASA S2.2–1959.

[4] H. L. Wunsch, Design data for flat air bearing when operating under steady conditions of load, The Mechanical Engineering Research Laboratory, East Kilbride, Glasgow; reprint from Machinery, **93**, No. 2394, 765–775 (Oct. 1, 1958).

[5] S. K. Grinnel and H. H. Richardson, Design study of a hydrostatic gas bearing with inherent orifice compensation, Trans. ASME **79** (1957).

[6] J. H. Laub, Gas lubrication in instruments and control devices, National Aeronautics and Space Administration—Jet Propulsion Laboratory, Technical Release No. 34–169 (Nov. 10, 1960).

[7] P. H. Stahlhuth, Hydride gas bearings for better stability, Product Eng. (April 10, 1961).

[8] S. Edelman, E. Jones, and E. R. Smith, Some developments in vibration measurement, J. Acoust. Soc. Am. **27**, No. 4, 728–734 (July 1955).

[9] C. M. Harris and C. E. Crede, Shock and Vibration Handbook (McGraw-Hill Book Co., Inc., New York, 1961).

(Paper 67C4=144)

JOURNAL OF RESEARCH of the National Bureau of Standards—C. Engineering and Instrumentation
Vol. 67C, No. 4, October–December 1963

Leak-Resistant Rotation Seal for Vacuum Applications

Frank L. Howard

(June 6, 1963)

A leak-resistant rotation seal for application with vacuum systems is described. The packing comprises a system of Teflon cones with deformable ridges that act as bearing surfaces.

The seal described herein was designed to convert a rotary-tube stirrer used for measurement of freezing point at 1 atm to one that would allow measurements at reduced pressure, approaching triple point conditions.

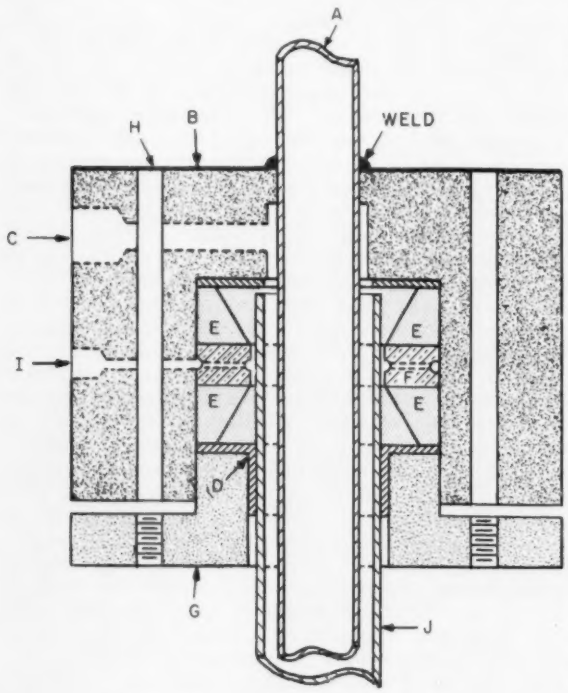

FIGURE 1. *Sectional view of seal.*

A. Thermometer well used in this application. The thermometer was attached through a standard packing gland.
B. Housing for the seal, made of stainless steel, o.d. = 2 in.
C. Connection to vacuum system.
D. Teflon spacer.
E, F. Packing shown in detail in figure 2.
G. Compression ring, tightened by six 5/32 machine screws passing through H.
I. Connection for guard vacuum.
J. Rotating tube with polished surface on bearing area.

For this application it was desired that the packing material be inert, provide low friction and effectively prevent leakage. Polytetrafluoroethylene (Teflon brand) was selected for this purpose, and the packing sections were designed to partially obviate the cold flow properties of this material and to reduce the

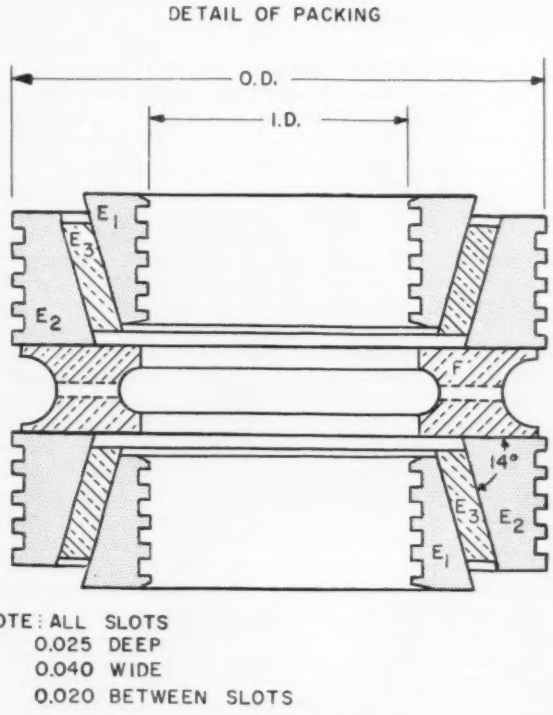

FIGURE 2. *Enlarged view of packing.*

E_1. Inner cones of Teflon, the internal diameter is 0.010 in. smaller than outside diameter of J (fig. 1).
E_2. Outer cones of teflon, similarly larger than inside diameter of housing B (fig. 1).
E_3. Brass cone, a taper of 14° was used.
F. Guard vacuum collecting ring.

friction inherent in large bearing surfaces. The parts of the seal are illustrated in figures 1 and 2. When the plastic packing cones are compressed vertically the small brass cones separating them cause them to tighten laterally against the rotating shaft and the outer housing. Some deformation of the protuberances between the grooves enables a tight fit.

The seal was tested with a helium mass spectrometer leak detector, while the shaft was rotated at 20 rpm. It was found that at about 5×10^{-5} mm Hg the leakage rate was less than 2×10^{-9} cm^3 (STP) of gas per minute. At this pressure, the guard vacuum was disconnected and no increase in pressure or in rate of leakage was noted. During 2 hr of operation the temperature of the housing increased about 10 °C.

The assistance of Herbert B. Lowey and Tully J. Pound, in making this apparatus is gratefully acknowledged. James L. Cross suggested use of the guard vacuum.

(Paper 67C4-145)

JOURNAL OF RESEARCH of the National Bureau of Standards—C. Engineering and Instrumentation
Vol. 67C, No. 4, October–December 1963

Studies on the Tungsten-Rhenium Thermocouple to 2000 °C

Douglas B. Thomas

(June 19, 1963)

Various lots of tungsten and rhenium wire were obtained from leading American manufacturers. Eleven tungsten-rhenium thermocouples were made up from these wire samples and tested at approximately 100 deg C intervals up to 2000 °C. A fourth order equation and a third order equation were selected to represent the emf of the tungsten-rhenium thermocouple in the range from 0 to 1000 °C and from 1000 to 2000 °C respectively. Using these two equations, reference tables were established and are presented in 5 deg C intervals from 0 to 2000 °C and in 10 deg F intervals from 32 to 3640 °F. Inverse tables giving temperature in °C and °F at 20 microvolt intervals are also included. Information is furnished on variations due to wire size and among different wire lots and different wire manufacturers. Spectrochemical analyses of the tungsten and rhenium elements that were used to represent the tables of temperature versus emf are listed. A graphic comparison is made between the NBS emf values and values from other investigators.

1. Introduction

In 1931 Goedicke [1] [1] investigated the possibility of using tungsten and rhenium as high temperature thermocouple elements. However, this early work was quite limited in scope and did not, for example, result in a precise relationship between temperature and emf for these thermocouple elements.

Between 1952 and 1956 the Battelle Memorial Institute conducted the first detailed investigation of various properties of rhenium [2, 3] and in 1957–58 their studies included the thermoelectric properties of rhenium, tungsten, and other high temperature thermocouple elements [4, 5]. In this latter work a power series was used to express the temperature-emf relationship of the tungsten-rhenium thermocouple between room temperature and 2200 °C. The workers at Battelle concluded that rhenium had several distinct advantages as a high temperature thermocouple element e.g., it was found to have excellent strength from room temperature to 2000 °C. was highly resistant to the water cycle and retained it ductility after thermal cycling above its recrystallization [2] temperature. Unfortunately, tungsten is affected by the water cycle and in addition becomes quite brittle upon reaching its recrystallization temperature. The recrystallization temperature of tungsten is not well defined. Smithells [6] reports that recrystallization can occur at any temperature from 1000 to 2000 °C depending upon the metallurgical properties of the tungsten, and Hall and Sikora [7] report partial recrystallization of commercially pure sintered tungsten at 1715 °C and complete recrystallization at 2090 °C. The brittleness of tungsten due to recrystallization can be somewhat inhibited by a process called "doping." This process involves the addition to the tungsten of small quantities of materials such as compounds of potassium, silicon, or aluminum. These "doping" compounds reduce grain growth and essentially raise the recrystallization temperature of the tungsten. In the case of pure tungsten, however, very little can be done to inhibit the brittleness resulting from recrystallization.

The water cycle effect which occurs at elevated temperatures alters the chemical and metallurgical properties of tungsten. In the case of tungsten thermocouple elements, this effect will eventually erode the metal to a point where the thermocouple fails. Langmuir [8] first demonstrated the water cycle effect with a tungsten filament lamp. A small amount of water vapor was released in a vacuum lamp and the filament was heated to incandescence. The water vapor coming into contact with the filament was decomposed, the oxygen combining with the tungsten and the hydrogen being evolved. The oxide distilled to the glass envelope where it was reduced to metallic tungsten by the atomic hydrogen given off by the filament. Reduction of the oxide resulted in the reconstitution of water vapor and the "water cycle" was able to repeat itself indefinitely. Thus, in applications where tungsten is used in a vacuum as a thermocouple element, care must be taken to keep the area surrounding the thermocouple free from water vapor at elevated temperatures.

Additional investigations concerning the tungsten-rhenium thermocouple were undertaken by Lachman and Kuether [9–11] and included useful information such as chemical analysis of the thermoelements, emf reproducibility of the thermocouple after prolonged temperature cycling and a table of temperature versus emf from 50 to 4000 °F.

The above workers concluded that the tungsten-rhenium thermocouple has the following advantages:

1. High thermoelectric potential.
2. High thermoelectric power.
3. Very high melting point of both elements of the thermocouple.

[1] Figures in brackets indicate the literature references at the end of this paper.
[2] Recrystallization is defined as the formation of a new, strain-free grain structure from that existing in the cold worked metal, usually accomplished by heating.

4. Chemical stability in vacuum, inert or reducing atmospheres up to 2200 °C.
5. Calibration accuracy of 0.1 mv up to 2200 °C.
6. Low cost of the tungsten element.
7. Good reproducibility after thermal cycling at 2200 °C.

Some of the disadvantages of the thermocouple are

1. Brittleness of the tungsten element after recrystallization.
2. Susceptibility of the tungsten element to destructive erosion due to the water cycle effect.
3. High cost of the rhenium element.
4. It cannot be used in an oxidizing atmosphere.

In view of the favorable advantages of the tungsten-rhenium thermocouple as a high temperature measuring instrument, a program was initiated at the National Bureau of Standards to carry out studies on this thermocouple. Although various studies were conducted on the tungsten-rhenium thermocouple by the authors mentioned, it was felt that an effort should be made at NBS to further evaluate this thermocouple using thermoelements that represent a variety of wire lots from various manufacturers. The results of this study could then be compared to the earlier reported results in order to ascertain the thermoelectric reproducibility of these materials.

2. Thermocouple Materials

2.1. Tungsten Elements

The tungsten elements that were used in this study were obtained from three major American tungsten wire manufacturers and represent a total of eight lots of wire. Although this tungsten wire was manufactured primarily for electronic applications, the chemical purity of the wire as determined by spectrochemical analysis (see table 1) was sufficiently high as to render it acceptable for this particular work. All of the tungsten elements consisted of two types of tungsten. One type of tungsten referred to by the manufacturers as "black as drawn" tungsten comprises five of the eight lots i.e., lots L–2, M–2, M–3, M–4, and N–1. The letters BL have been placed in parenthesis after each of these lot designations to denote the "black as drawn" wire type. The second type of tungsten is referred to as "chemically cleaned" tungsten and comprises three lots i.e., lots L–1, M–1, and N–2. The letters CL are used to denote this type of wire. According to the manufacturers, the "black as drawn" wire receives no additional treatment or processing after it has been drawn to the desired size. On the other hand, the chemically cleaned wire after having been drawn to the desired size is immersed into a hot caustic solution (usually KOH or NaOH), is rinsed and then dried. All of the tungsten elements contained "doping" compounds as reported by the manufacturers.

The prefixes L, M, and N designate the three manufacturers from whom the tungsten lots were obtained. One element was selected from each of the eight tungsten lots and labeled the same as the lot number followed by the letter "A." Five of these eight tungsten elements were used only once to represent the positive (+) leg of a particular tungsten-rhenium thermocouple and the other three elements viz, L–1(CL)A, M–4(BL)A and N–2(CL)A were used twice as a positive leg. For example, the element L–1(CL)A was paired with the two rhenium elements 219A and 228A, the combinations being designated thermocouple No. 1 and thermocouple No. 9 (see table 3). This arrangement resulted in a total of 11 thermocouples. This method of thermocouple selection was chosen rather than a method whereby all possible thermocouple combinations (each tungsten element versus each rhenium element) could be represented. All thermocouple combinations could be equally represented by averaging the data in figures 1 and 2, and then combining the averages via measurements of a

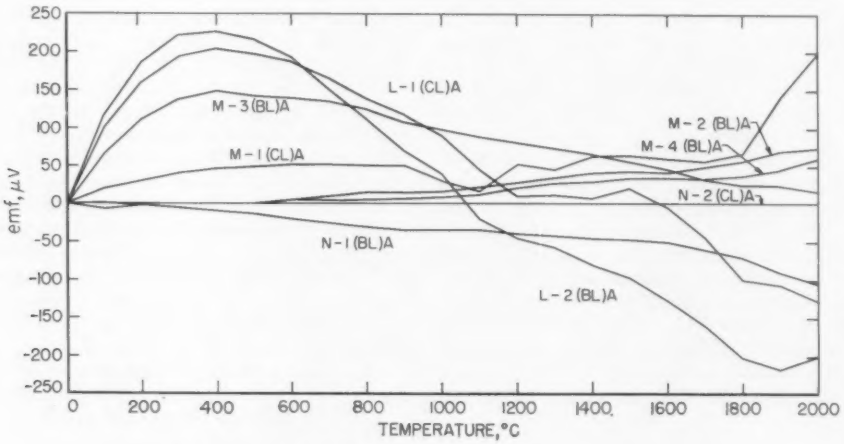

FIGURE 1. *Emf differences between eight tungsten elements.*
[With N-2(CL)A as the reference element]

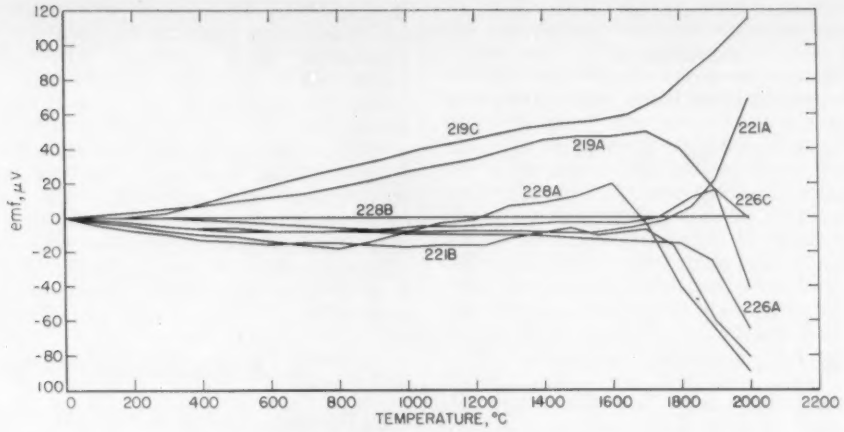

FIGURE 2. *Emf differences between eight rhenium elements.*
[With 228B as the reference element]

single tungsten-rhenium combination (see also in Experimental Procedure). However, in order to use this method effectively, the following must be realized.

(a) The tungsten and rhenium elements that are used as reference elements must be reproducible. Since all of the elements could not be tested in one furnace run, it was necessary to heat the reference elements several times. The tungsten and rhenium elements that were tested gave indications of not being reproducible from one furnace run to the next (Experimental Procedure).

(b) A considerable amount of weight would be placed on the single tungsten-rhenium combination measurement. If large errors were encountered in this measurement (poor optical pyrometer readings, for example), these errors would be grossly reflected in the final temperature—emf relationship.

Each of the eight tungsten elements was spectrochemically analyzed. A listing of the magnitude of the impurities is given in table 1.

2.2. Rhenium Elements

All of the rhenium elements associated with this study were obtained from the Chase Brass and Copper Company which is the sole American producer of rhenium wire in commercial quantities. Eight rhenium elements were paired with various tungsten elements as listed in table 3. These rhenium elements were taken from four lots of wire, numerically designated 219, 221, 226, and 228, with each element labeled A, B, or C of a particular lot [3]. All eight elements were 0.020 in. in diameter. As in the case of the tungsten elements, five of the eight rhenium elements were used only once to represent the negative leg of a particular tungsten-rhenium thermocouple and the three elements, 219A, 226C, and 228B, were used twice.

[3] Elements A, B, and C of a particular lot were remote from each other as far as the position of each element on a spool of wire is concerned.

TABLE 1. *Spectrochemical analysis of tungsten elements*

Chemical element	Tungsten element							
	L-1 (CL)A	L-2 (BL)A	M-1 (CL)A	M-2 (BL)A	M-3 (BL)A	M-4 (BL)A	N-1 (BL)A	N-2 (CL)A
Ag	—	—	—?	—	E	—?	—?	D
Al	—	—	—	—	—	—	—	—
B	—	—	—	—	—	—	—	—
Ba	—	—	—	—	—	—	—	—
Be	—	—	—	—	—	—	—	—
Bi	—	—	—	—	—	—	—	—
Ca	D	D	—	—	D	—	—?	—?
Cd	—	—	—	—	—	—	—	—
Co	—	—	—	—	—	—	—	—
Cr	D	D	D	—	C	D	—	—
Cu	D	D	E	—?	—?	E	E	E
Fe	D	D	D	D	D	D	D	C
Hf	—	—	—	—	—	—	—	—
Ir	—	—	—	—	—	—	—	—
Mg	D	D	D	D	D	D	D	C
Mn	—	—	—	—	—?	—	—	—
Mo	—?	—?	—?	—?	C	—	—?	—
Na	—	—	—	—	—	—	—	—
Ni	C	C	—	—	C	—	—	—
Os	—	—	—	—	—	—	—	—
Pt	—	—	—	—	—	—	—	—
Si	B	C	B	C	B	B	B	C
Sn	—	—	—	—	—	—	—	—
Sr	—	—	—	—	—	—	—	—
Ta	—?	—	—	—	—?	—	—	—
Th	—	—	—	—	—	—	—	—
Ti	—	—	—	—	—	—	—	—
Zn	—	—	—	—	—	—	—	—
Zr	—	—	—	—	—	—	—	—

A = 1.0%–0.1%.
B = 0.1%–0.01%.
C = 0.01%–0.001%.
D = 0.001%–0.0001%.
E = Less than 0.0001%.
— = Not detected.

The eight rhenium elements were spectrochemically analyzed by the same laboratory [4] that analyzed the tungsten elements and the results of the analysis are listed in table 2.

[4] Spectrochemistry Section of the National Bureau of Standards.

TABLE 2. *Spectrochemical analysis of rhenium elements*

Chemical element	Rhenium element							
	219A	219C	221A	221B	226A	226C	228A	228B
Ag	—	—	—	—	—	—	—	—
Al	D	D	D?	D?	D?	D?	D?	D?
B	—	—	—?	—?	—?	—?	—?	—?
Ba	—	—	—	—	—	—	—	—
Be	—	—	—	—	—	—	—	—
Bi	—	—	—	—	—	—	—	—
Ca	D	C	D	D	D	D	D	D
Cd	—	—	—	—	—	—	—	—
Co	—?	—?	—	—	—	—	—	—
Cr	—	—	—?	—?	—?	—?	—?	—?
Cu	C	C	A	B	A	C	C	D
Fe	C	C	A	C	B	C	B	C
Hf	—	—	—	—	—	—	—	—
Ir	—	—	—	—	—	—	—	—
K	B	B	—?	—?	—?	—?	—?	—?
Mg	D	C	C	D	B	A	C	C
Mn	—?	—?	—?	—?	—?	—?	—?	—
Mo	B	B	C	B	C	B	C	C
Ni	C	B	—	—	—	—	—	—
Os	—	—	—	—	—	—	—	—
Pb	—?	D	—	—	—	—	—	—
Pt	C	C	D	—	—	—	—	—
Si	C	B	D	D	C	C	C	C
Sn	—	—	—	—	—	—	—	—
Ta	—	—	—	—	—	—	—	—
Th	—	—	—	—	—	—	—	—
Ti	—	—	—	—	—	—	—	—
V	—	—	—	—	—	—	—	—
Zn	—	—	—	—	—	—	—	—
Zr	—	—	—	—	—	—	—	—

A=1.0%–0.1%.
B=0.1%–0.01%.
C=0.01%–0.001%.
D=0.001%–0.0001%.
E=Less than 0.0001%.
—=Not detected.

3. Apparatus

All of the thermocouple and thermoelement tests between 0 and 2000 °C were performed in one furnace. This furnace consists of a tantalum tube that serves as a heating element. The tantalum tube furnace is fully described elsewhere. [12] The thermocouples and thermoelements were vertically suspended inside the tantalum tube with the measuring junctions located in a molybdenum blackbody which was also suspended in the central region of the tantalum tube. All tests were conducted in a purified helium atmosphere, the pressure of which varied from 360 mm Hg at 20 °C to about 660 mm Hg at 2000 °C. The helium was purified by passing it through a titanium-zirconium purifying apparatus [12] before being released into the furnace chamber.

In the range from 100 to 1000 °C the instrument used for temperature determinations was a Pt 1 percent Rh versus Pt 30 percent Rh thermocouple. A modified commercial optical pyrometer was used in the 1000 to 2000 °C range. The "1 percent-30 percent" thermocouple was calibrated by direct comparison to a standard platinum versus platinum 10 percent rhodium thermocouple. The latter thermocouple received a fixed point calibration as described in the literature [13]. An estimate of the maximum uncertainty in the comparison calibration is ±0.5 °C. The optical pyrometer was calibrated and used on a basis of temperature versus optical pyrometer lamp current. The calibration was performed by sighting the pyrometer on a tungsten ribbon filament lamp, the temperature of which was determined by the Fairchild optical pyrometer [5] at NBS. An estimate of the maximum uncertainties in the optical pyrometer calibration is ±3.0° at 1000 °C and ±6.0° at 2000 °C. The lamp current was determined by measuring the voltage drop across a 1-ohm standard resistor in series with the lamp. The thermocouple emf measurements were made with a L & N K–3 type potentiometer having a limit of error of about 0.7 μv at 1000 μv and 10 μv at 50,000 μv.

4. Experimental Procedure

In the tests conducted in the 0 the 1000 °C range, the Pt 1 percent Rh versus Pt 30 percent Rh thermocouple and the tungsten and rhenium elements were placed in high purity aluminum oxide insulating tubes with the measuring junctions exposed at one end. The measuring junction of the 1 percent-30 percent thermocouple was mechanically and thermally bound to the measuring junction of the tungsten and rhenium elements by wrapping with platinum wire. Generally, a total of six thermoelements (two tungsten, two rhenium, and the two platinum-rhodium elements) were placed in the furnace at one time. The emfs of thermocouples No. 1 through No. 11 (table 3) were measured at approximately 100 deg intervals from 100 to 1000 °C with the reference junctions maintained at 0 °C. In addition to these measured values, an assumed emf of 0.000 mv at 0 °C for each thermocouple gave a total of 121 data points for the 0 to 1000 °C range. At each of the calibration points, the temperature in the hot zone of the furnace as determined by the 1 percent-30 percent thermocouple was allowed to stabilize before the emfs of the tungsten-rhenium thermocouples were measured.

[5] The NBS Fairchild optical pyrometer, also referred to in the literature [14] as "The NBS Optical Pyrometer" is a high precision instrument designed by C. O. Fairchild of NBS and is used at NBS for testing other optical pyrometers and pyrometer lamps submitted for calibration.

TABLE 3. *Thermocouple elements*

(All elements were 0.020 in. in diameter.)

Thermocouple number	Rhenium elements	Tungsten elements	
	Element number	Element number	Manufacturer
1	219A	L–1(CL)A	L
2	219A	M–4(BL)A	M
3	219C	N–1(BL)A	N
4	221A	M–3(BL)A	M
5	221B	N–2(CL)A	N
6	226A	M–2(BL)A	M
7	226C	L–2(BL)A	L
8	226C	M–4(BL)A	M
9	228A	L–1(CL)A	L
10	228B	M–1(CL)A	M
11	228B	N–2(CL)A	N

The eleven tungsten-rhenium thermocouples were also tested at approximately 100 deg intervals between 1000 and 2000 °C with the reference junctions at 0 °C. At each of the 100 deg intervals the emf of the thermocouple was read three times and an optical pyrometer observation was made three times but in an alternating sequence.[6] This resulted in a total of approximately 360 temperature-emf determinations. The data that were recorded for each thermocouple at each of the 100 deg intervals were averaged. This resulted in 101 averaged temperature-emf data points in the range from 1000 to 2000 °C. In most instances, and particularly at temperatures above 1700 °C, it was necessary to anneal the thermocouples at a slighty higher temperature than the temperature at which the data were taken. For example, in order to render the thermocouples stable at 1800 °C, it was necessary to raise the temperature of the furnace to about 1825 °C for a 5 to 10-min period and then lower the temperature to the initial 1800 °C. During the time that the thermocouple emf and optical pyrometer readings were recorded, the temperature in the hot zone of the furnace was not fluctuating by more than 0.05 percent per minute and in most cases the fluctuations were considerably less than this amount.

Since the tantalum tube furnace design allows the thermocouple to be freely suspended vertically, it was possible to avoid the use of ceramic supports, thereby eliminating two possible effects: (a) chemical contamination, and (b) electrical errors due to conduction in the ceramic material.

A d-c electric arc operating in a helium atmosphere was used to fuse the measuring junction of the tungsten and rhenium elements.

All of the emf measurements related to the tungsten and rhenium elements listed in table 3 were conducted in four separate test series. These four test series, in chronological order were as follows: (1) The emf's of the eleven thermocouples were measured between 1000 and 2000 °C, (2) the emf's of the eleven thermocouples were measured between 0 and 1000 °C, (3) the emf differences between the tungsten elements and between the rhenium elements were measured between 0 and 1000 °C, and (4) the emf differences between the tungsten elements and between the rhenium elements were measured between 1000 and 2000 °C. All readings were made with increasing temperature. After the first test series was completed, it was necessary to remove from 6 to 8 in. of wire from the measuring junction end of the tungsten elements since this portion of the wire had become brittle upon heating to 2000 °C. This removal of the embrittled portion of each tungsten element was necessary in order to reweld the elements for the succeeding parts of the test series.

Since short portions of the tungsten elements were removed after the first test series, it is apparent that the emf's that were measured in the second, third, and fourth test series would in some cases be inconsistent with those measured in the first series. If the emf's of the eleven thermocouples tested in the first and second series are compared with the calculated[7] emf's of the same thermocouples as derived from the differences measured between elements in the third and fourth series, it can be seen that the respective values are not consistent in all cases. These inconsistencies can be attributed to (a) the lack of emf reproducibility of the tungsten elements before and after the brittle portions of the elements were removed, (b) the lack of emf reproducibility of the rhenium elements, and (c) experimental errors encountered in each of the test series.

The long-term stability of the tungsten-rhenium thermocouples was not determined in this study. However, four test thermocouples were made up from the tungsten and rhenium wire lots pertinent to this study and were thermally cycled between 1100 and 2000 °C. The elements of these four thermocouples were none of the elements listed in table 3. The thermocouples were initially heated to 1100 °C (approx.) and their emf's were measured at that temperature. Then the thermocouples were heated to 2000 °C (approx.), the emf's again being measured, and then the temperature was lowered to 1100 °C. This heating cycle was repeated twice. The third and final measurement at 1100 °C showed that the emf's of the four thermocouples had increased (as compared to the initial measurement at 1100 °C) between 60 and 122 μv. This is equivalent to 3.5 and 7.2 °C, respectively. The total heating time during this cycling test was approximately 5 hr.

None of the tungsten and rhenium elements listed in table 3 were heat treated prior to testing except in the test series involving emf measurements between 1000 and 2000 °C. In this case, of course, the elements were heated to 1000 °C before emf measurements were begun.

5. Computations

In order to represent the raw data that were obtained in this study in a useful and concise form, several electronic computer programs were utilized. This data handling was performed with an IBM 7090 computer.

One of the first computation steps was to derive one or more polynomial equations that would represent the thermocouple data over the entire temperature range. For investigative purposes, the computer was programmed to derive by the least squares method (a) a single polynomial equation to represent the 0 to 2000 °C range and (b) one polynomial equation to represent the 0 to 1000 °C range and another polynomial equation to represent the 1000 to 2000 °C range. The function fitting was applied

[6] In a few cases four thermocouple emf readings and four optical pyrometer observations were made in alternating sequence.

[7] The emf was measured between the elements N-2 (CL)A and 228B as thermocouple No. 11 and also between each of these elements and the other 7 tungsten and 7 rhenium elements. From this relationship the other 10 thermocouple emf's can be determined.

to all of the thermocouple data in each of the temperature ranges, i.e., 121 data points in the low temperature range and 101 data points in the high temperature range. The results of this investigation showed that a sixth order equation would be needed to adequately represent the thermocouple data over the 0 to 2000 °C range. The same conclusion was reached by Sims, Gaines, et al. [5] over the temperature range of investigation. In the (b) part of the investigation it was determined that a fourth order equation and a third order equation would adequately represent the 0 to 1000 °C and the 1000 to 2000 °C ranges respectively. In practical applications, considerable time and effort is saved by using two equations. Hence, this method was selected to represent the temperature-emf relationship of the tungsten-rhenium thermocouple.

In examining these two equations it was found that the derivative dE/dt was not the same for both equations at 1000 °C and that the emfs at 1000 °C differed by about 19 μv. A computer operation was used to adjust the coefficients of the fourth order equation (for the 0 to 1000 °C range) such that the emf and slope of the two equations at 1000 °C were equal.

The equations for the average emf E in millivolts of the tungsten-rhenium thermocouples at a temperature t(°C) are

for the range 0 to 1000 °C

$$E=0.62893850\times10^{-2}t+0.20717363\times10^{-4}t^2 -0.15067280\times10^{-7}t^3+0.37778323\times10^{-11}t^4$$

for the range 1000 to 2000 °C

$$E=-3.3363162+0.18710331\times10^{-1}t +0.21067552\times10^{-5}t^2-0.17634201\times10^{-8}t^3.$$

The emf deviations of each of the eleven tungsten rhenium thermocouples from the above equations are shown graphically in figure 5 for the range 0 to 1000 °C and in figure 6 for the range 1000 to 2000 °C. The standard deviation of the form $S=\sqrt{\frac{\Sigma d^2}{n-N}}$ where d is the emf deviation of each data point from the respective polynomial equation, n is the number of data points [8] and N is the number of coefficients in the polynomial equation was determined for the two temperature ranges. For the 0 to 1000 °C range the standard deviation was 74.1 μv and for the 1000 to 2000 °C range it was 70.1 μv. An estimation of the maximum uncertainties in the temperature measurements made between 0 and 1000 °C is ±1.0 °C and between 1000 and 2000 °C is ±0.35 percent.

6. Results

Tables for the tungsten-rhenium thermocouple are presented giving emf at 5 °C and 10 °F intervals (tables 5 and 7). Inverse tables giving temperature in °C and °F at 20 μv intervals are also included (tables 4 and 6).

The emf differences were measured between each of the eight tungsten elements. N–2(CL)A was arbitrarily chosen as a reference element and the emfs developed between it and the other seven tungsten elements were measured between 0 and 2000 °C (fig. 1).[9]

Two of the eight tungsten lots were selected for studying the emf differences between elements of various diameters. The two lots selected were N–2(CL) and M–3(BL). From each lot three elements were obtained and designated with the suffixes B, C, and D. These were 0.020, 0.024, and 0.028 in. in diameter (nominal) respectively. N–2(CL)A[10] was again chosen as a reference element

[8] In the low temperature range, n was 121 data points and in the high temperature range n was the 101 averaged data points.

[9] The reference element, N–2(CL)A was connected to the negative post of the potentiometer.

[10] N–2(CL)A and N–2(CL)B were adjacent elements cut from one spool of wire. The same is true for the M–3(BL)A and M–3(BL)B elements.

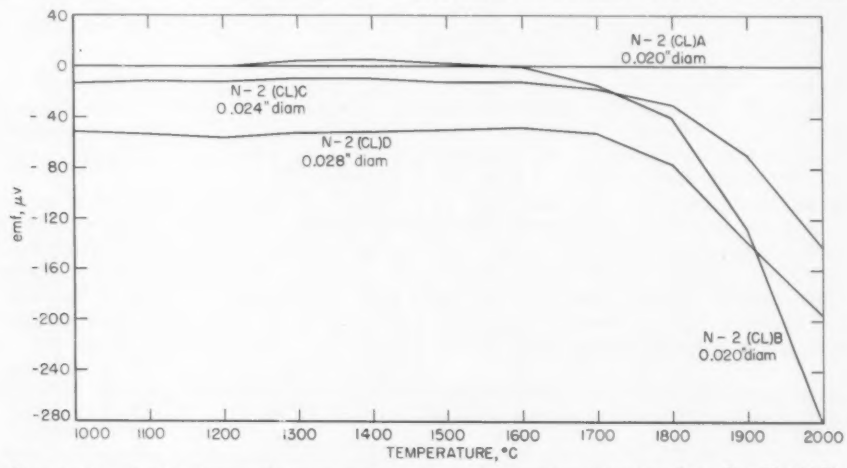

FIGURE 3. *Emf differences between tungsten elements of various diameters from Lot N–2(CL)*
[With N–2(CL)A as the reference element]

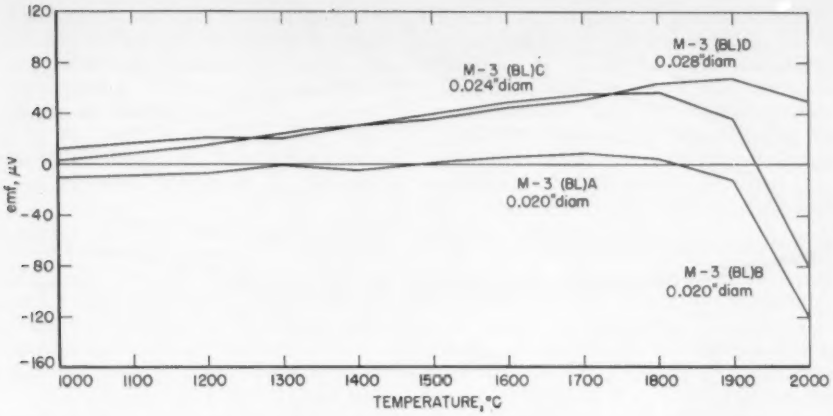

FIGURE 4. *Emf differences between tungsten elements of various diameters from Lot M–3 (BL).*
[With M-3(BL)A as the reference element]

and the emf's developed between it and elements N–2(CL)B, C, and D in the temperature range from 1000 to 2000 °C are shown graphically in figure 3. These measurements give an indication of the emf differences that can occur between two adjacent elements and also the differences that can occur between elements from the same lot but of varying diameters.

Similar measurements were conducted with the elements M–3(BL)A, B, C, and D, using M–3(BL)A as a reference element. Emf differences related to these elements are shown in figure 4. All of the measurements related to the tungsten elements of varying diameters were made after the four series of tests previously mentioned.

The emf differences between the eight rhenium elements were measured in the range 0 to 2000 °C by using 228B as a reference element.[11] These differences are shown in figure 2.

Since rhenium elements of diameters other than 0.020 in. were not available from the manufacturer for the four lots 219, 221, 226, and 228, no tests were conducted to denote emf differences between rhenium elements of various diameters.

The thermoelectric power of the tungsten-rhenium thermocouples included in this study average about 17.6, 17.6, 13.1, and 6.0 μv per deg C at 500, 1000, 1500, and 2000 °C, respectively. A maximum thermoelectric power of 18.33 μv per deg C occurs at 715 °C.

7. Discussion

In general it can be concluded that the total emf spread of the eleven tungsten-rhenium thermocouples included in this study is not exceedingly large if one considers that the thermocouple elements represent four wire manufacturers and twelve lots of wire. The greatest emf spread of the eleven thermocouples in the range 0 to 1000 °C was 246 μv at 370 °C (fig. 5). This corresponds to approximately 15.2 °C. Likewise, in the range 1000 to 2000 °C the greatest emf spread was 263 μv at 2000 °C corresponding to approximately 44.0 °C (fig. 6). The large emf spread of some of the thermocouples at 370 °C was rather surprising. It is interesting to note that all of the thermocouples (except No. 10) deviate a considerable amount from the table values in the 0 to 700 °C range. In the range 1000 to 2000 °C the deviations of all of the thermocouples from the table values are quite random.

Figures 1 and 2 definitely show that the large emf deviations of some of the thermocouples from the table values in the 0 to 700 °C range are, for the most part, due to the tungsten elements. The maximum emf spread of the eight tungsten elements at 400 °C is 237 μv and the maximum spread of the eight rhenium elements at that same temperature is 22 μv. The greatest emf spread between any two tungsten elements and any two rhenium elements occurred at 2000 °C in both cases. These maximum emf spreads at 2000 °C are 400 μv for the tungsten elements and 205 μv for the rhenium elements. It should be pointed out that the maximum emf spread of all of the tungsten elements should not be directly compared to that of all of the rhenium elements since the former represents three different manufacturers and the latter represents only one manufacturer. If the maximum emf spread of the elements produced by each of the four manufacturers are intercompared, it can be seen that these maximums are not significantly different i.e., the maximum spreads are all between 105 and 205 μv.

The tests that were conducted to determine the emf differences between tungsten elements of various diameters were limited in scope but gave a general

[11] The reference element 228B was connected to the negative post of the potentiometer.

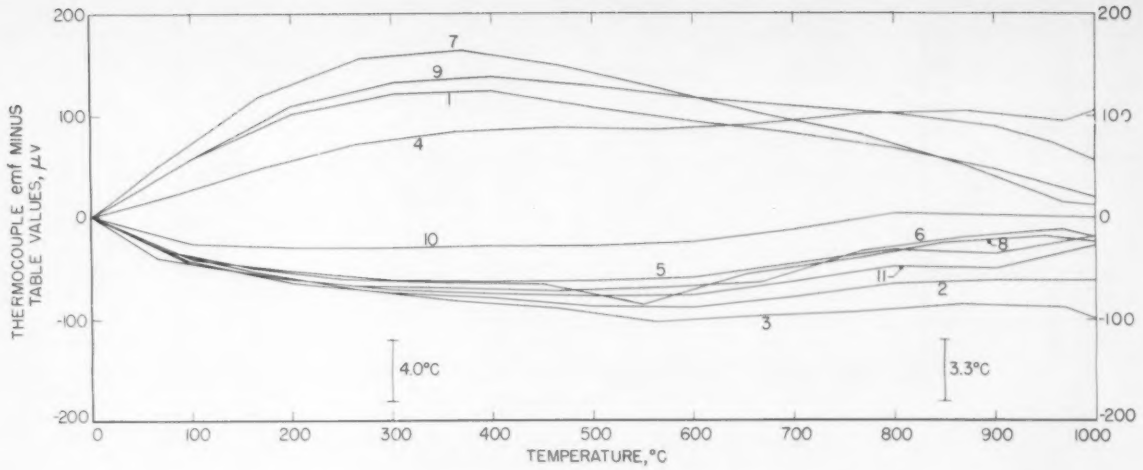

FIGURE 5. *Deviations of thermocouples No. 1 through No. 11 from the table values in the range 0 to 1000 °C.*

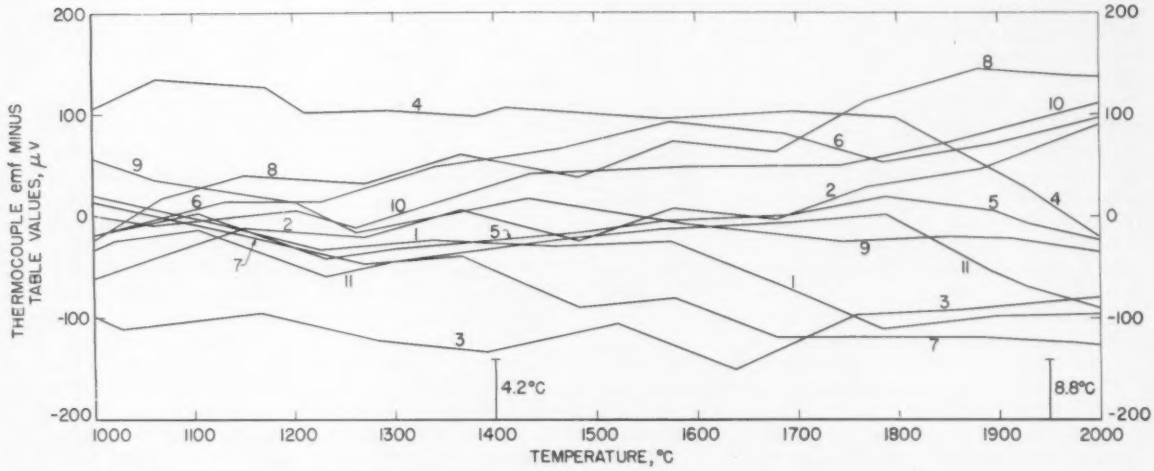

FIGURE 6. *Deviations of thermocouples No. 1 through No. 11 from the table values in the range 1000 to 2000 °C.*

indication of the magnitude of the differences that can occur. These tests show that the emf differences between tungsten elements of various diameters from one particular lot can be as large as the emf differences between elements from different lots and different manufacturers. At temperatures above 1800 °C the two elements N–2(CL) A and N–2(CL)B, which were adjacent samples on a spool of wire, developed a fairly large emf and at 2000 °C the emf was larger than that developed between the reference element and elements "C" and "D" (fig. 3). This same thing occurred between the two adjacent elements M–3(BL)A and M–3(BL)B at temperatures near 2000 °C (fig. 4). At temperatures between 1000 and 1800 °C the emf developed between elements of various diameters remained relatively small.

In general, the results of the spectrochemical analysis of the thermocouple elements show that the tungsten elements were of a higher purity than the rhenium elements. Of the eight tungsten elements that were analyzed, the element M–3(BL)A showed the greatest amount of impurities and M–2(BL)A showed the least impurities. If an average value is taken for the percentage range associated with each impurity listed (table 1), the total percent of im-

purities for M–3(BL)A would be 0.0665 percent. Likewise, the total impurities for M–2(BL)A would be 0.0060 percent. For comparison purposes, the impurities in reference grade thermocouple platinum reportedly [14, 15] are of the order of 0.001 percent. Thus, the purity of M–2(BL)A is approaching that of reference grade platinum and M–3(BL)A contains over 60 times the total impurities in reference platinum.

Of the eight rhenium elements that were analyzed, 221A showed the largest percentage of impurities with 1.012 percent and element 228B showed the least impurities with 0.0215 percent (table 2). Thus, element 221A contains more than a thousand times the impurities of reference grade platinum.

In view of the above analysis, it can be concluded that although termocouple elements of the same type are relatively pure, they may be appreciably different thermoelectrically. The opposite behavior, thermoelectric similarity in spite of differences of composition is shown by the two rhenium elements 221A and 228B. The emf developed between these two elements from 0 to 1900 °C was less than 20 μv (fig. 2) and yet element 221A contained nearly 50 times more impurities than element 228B. These results strongly indicate that rhenium possesses a thermoelectric uniqueness which manifests itself by the relatively small emfs produced between rhenium elements that contain significantly different quantities of impurities.

The emf differences that were recorded between the reference tungsten element N–2(CL)A and the other seven tungsten elements (fig. 1) show no unusual emf characteristics of the "chemically cleaned" wire as opposed to the "black as drawn" type of wire.

Figure 7 is a graphic presentation of the emf differences between the values for the tungsten-rhenium thermocouple as given in this paper and the values reported by Sims, Gaines, et al., [5] and Lachman [11]. The values from the three sources agree reasonably well between 1000 and 2000 °C but in the range 0 to 1000 °C the differences between the NBS values and the values from Sims, Gaines, et al., [5] are quite large. The largest emf difference over the entire range occurs at 340 °C with a 415 μv difference between the NBS values and the values from Sims, Gaines, et al., [5]. This corresponds to approximately 26.4 °C. The greater part of the differences that occur between the values from the three investigators is probably due to chemical and/or metallurgical differences between the thermocouple elements rather than errors arising from temperature measurement techniques.

The results of the various tests that were conducted in this study indicate that the thermoelectric quality of commercially available tungsten and rhenium wire could be improved. Causes of the large emf differences that may exist between tungsten elements from different lots and from different manufacturers might be identified by studying the individual effects of chemical and metallurgical variables on the thermal emf. Identification of the important variables could then lead to their control during the manufacturing process. Although some of the rhenium elements contained relatively large percentages of impurities, it was apparent that these impurities did not cause as large emf differences as in the tungsten elements. If the impurities in future lots of rhenium wire can be considerably reduced, perhaps the emf spread between elements would correspondingly be reduced.

It should be emphasized that the various tests indicate that the emf produced by a particular tungsten-rhenium thermocouple at a specific temperature is highly dependent on the lot of wire from which the thermocouple was fabricated and the degree of heat treatment (annealing) the thermocouple has received. In view of these factors, caution should be exercised in using the table values cited herein as the correct values for a specific tungsten-rhenium thermocouple.

It is anticipated that reference tables for the tungsten 3 percent rhenium versus tungsten 25 percent rhenium thermocouple and/or the tungsten 5 percent rhenium versus tungsten 25 percent rhenium thermocouple will be prepared at NBS in the near future.

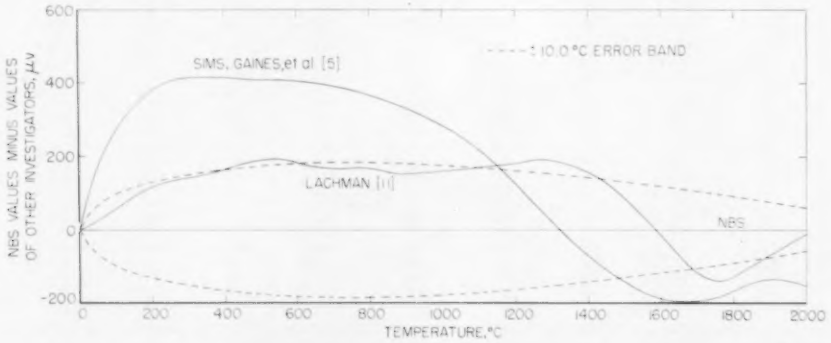

FIGURE 7. *Emf differences between NBS W-Re thermocouple tables and tables by other investigators.*

TABLE 4. *Tungsten versus rhenium thermocouples*

Electromotive force in absolute millivolts. Temperature in degrees C (Int. 1948). Reference junctions at 0 °C.

Millivolts	0.000	0.020	0.040	0.060	0.080	0.100	0.120	0.140	0.160	0.180	0.200	*Millivolts*
0.000	0.0	3.1	6.2	9.3	12.2	15.2	18.0	20.8	23.6	26.4	29.1	0.000
0.200	29.1	31.7	34.4	37.0	39.5	42.1	44.6	47.0	49.5	51.9	54.3	0.200
0.400	54.3	56.6	59.0	61.3	63.6	65.9	68.1	70.4	72.6	74.8	77.0	0.400
0.600	77.0	79.1	81.3	83.4	85.5	87.6	89.7	91.7	93.8	95.8	97.8	0.600
0.800	97.8	99.9	101.9	103.8	105.8	107.8	109.7	111.6	113.6	115.5	117.4	0.800
1.000	117.4	119.3	121.1	123.0	124.9	126.7	128.6	130.4	132.2	134.0	135.8	1.000
1.200	135.8	137.6	139.4	141.2	143.0	144.7	146.5	148.2	149.9	151.7	153.4	1.200
1.400	153.4	155.1	156.8	158.5	160.2	161.9	163.6	165.3	166.9	168.6	170.2	1.400
1.600	170.2	171.9	173.5	175.2	176.8	178.4	180.0	181.7	183.3	184.9	186.5	1.600
1.800	186.5	188.1	189.6	191.2	192.8	194.4	195.9	197.5	199.1	200.6	202.2	1.800
2.000	202.2	203.7	205.2	206.8	208.3	209.8	211.4	212.9	214.4	215.9	217.4	2.000
2.200	217.4	218.9	220.4	221.9	223.4	224.9	226.3	227.8	229.3	230.8	232.2	2.200
2.400	232.2	233.7	235.1	236.6	238.0	239.5	240.9	242.4	243.8	245.3	246.7	2.400
2.600	246.7	248.1	249.5	251.0	252.4	253.8	255.2	256.6	258.0	259.4	260.8	2.600
2.800	260.8	262.2	263.6	265.0	266.4	267.8	269.2	270.6	271.9	273.3	274.7	2.800
3.000	274.7	276.1	277.4	278.8	280.2	281.5	282.9	284.2	285.6	286.9	288.3	3.000
3.200	288.3	289.6	291.0	292.3	293.7	295.0	296.3	297.7	299.0	300.3	301.6	3.200
3.400	301.6	303.0	304.3	305.6	306.9	308.2	309.6	310.9	312.2	313.5	314.8	3.400
3.600	314.8	316.1	317.4	318.7	320.0	321.3	322.6	323.9	325.2	326.5	327.8	3.600
3.800	327.8	329.0	330.3	331.6	332.9	334.2	335.4	336.7	338.0	339.3	340.5	3.800
4.000	340.5	341.8	343.1	344.3	345.6	346.9	348.1	349.4	350.6	351.9	353.1	4.000
4.200	353.1	354.4	355.7	356.9	358.2	359.4	360.6	361.9	363.1	364.4	365.6	4.200
4.400	365.6	366.9	368.1	369.3	370.6	371.8	373.0	374.3	375.5	376.7	377.9	4.400
4.600	377.9	379.2	380.4	381.6	382.8	384.1	385.3	386.5	387.7	388.9	390.1	4.600
4.800	390.1	391.4	392.6	393.8	395.0	396.2	397.4	398.6	399.8	401.0	402.2	4.800
5.000	402.2	403.4	404.6	405.8	407.0	408.2	409.4	410.6	411.8	413.0	414.2	5.000
5.200	414.2	415.4	416.6	417.8	419.0	420.2	421.3	422.5	423.7	424.9	426.1	5.200
5.400	426.1	427.3	428.4	429.6	430.8	432.0	433.2	434.3	435.5	436.7	437.9	5.400
5.600	437.9	439.0	440.2	441.4	442.6	443.7	444.9	446.1	447.2	448.4	449.6	5.600
5.800	449.6	450.7	451.9	453.1	454.2	455.4	456.5	457.7	458.9	460.0	461.2	5.800
6.000	461.2	462.3	463.5	464.7	465.8	467.0	468.1	469.3	470.4	471.6	472.7	6.000
6.200	472.7	473.9	475.0	476.2	477.3	478.5	479.6	480.8	481.9	483.1	484.2	6.200
6.400	484.2	485.4	486.5	487.6	488.8	489.9	491.1	492.2	493.4	494.5	495.6	6.400
6.600	495.6	496.8	497.9	499.0	500.2	501.3	502.5	503.6	504.7	505.9	507.0	6.600
6.800	507.0	508.1	509.3	510.4	511.5	512.7	513.8	514.9	516.0	517.2	518.3	6.800
7.000	518.3	519.4	520.6	521.7	522.8	523.9	525.1	526.2	527.3	528.4	529.6	7.000
7.200	529.6	530.7	531.8	532.9	534.1	535.2	536.3	537.4	538.5	539.7	540.8	7.200
7.400	540.8	541.9	543.0	544.1	545.3	546.4	547.5	548.6	549.7	550.8	551.9	7.400
7.600	551.9	553.1	554.2	555.3	556.4	557.5	558.6	559.7	560.9	562.0	563.1	7.600
7.800	563.1	564.2	565.3	566.4	567.5	568.6	569.8	570.9	572.0	573.1	574.2	7.800
8.000	574.2	575.3	576.4	577.5	578.6	579.7	580.8	581.9	583.1	584.2	585.3	8.000
8.200	585.3	586.4	587.5	588.6	589.7	590.8	591.9	593.0	594.1	595.2	596.3	8.200
8.400	596.3	597.4	598.5	599.6	600.7	601.8	602.9	604.0	605.1	606.2	607.3	8.400
8.600	607.3	608.4	609.5	610.6	611.7	612.8	613.9	615.0	616.1	617.2	618.3	8.600
8.800	618.3	619.4	620.5	621.6	622.7	623.8	624.9	626.0	627.1	628.2	629.3	8.800
9.000	629.3	630.4	631.5	632.6	633.7	634.8	635.9	637.0	638.1	639.2	640.3	9.000
9.200	640.3	641.4	642.5	643.6	644.7	645.7	646.8	647.9	649.0	650.1	651.2	9.200
9.400	651.2	652.3	653.4	654.5	655.6	656.7	657.8	658.9	660.0	661.1	662.2	9.400
9.600	662.2	663.3	664.3	665.4	666.5	667.6	668.7	669.8	670.9	672.0	673.1	9.600
9.800	673.1	674.2	675.3	676.4	677.5	678.5	679.6	680.7	681.8	682.9	684.0	9.800
10.000	684.0	685.1	686.2	687.3	688.4	689.5	690.6	691.6	692.7	693.8	694.9	10.000
10.200	694.9	696.0	697.1	698.2	699.3	700.4	701.5	702.6	703.7	704.7	705.8	10.200
10.400	705.8	706.9	708.0	709.1	710.2	711.3	712.4	713.5	714.6	715.7	716.7	10.400
10.600	716.7	717.8	718.9	720.0	721.1	722.2	723.3	724.4	725.5	726.6	727.7	10.600
10.800	727.7	728.7	729.8	730.9	732.0	733.1	734.2	735.3	736.4	737.5	738.6	10.800
11.000	738.6	739.7	740.8	741.8	742.9	744.0	745.1	746.2	747.3	748.4	749.5	11.000
11.200	749.5	750.6	751.7	752.8	753.9	754.9	756.0	757.1	758.2	759.3	760.4	11.200
11.400	760.4	761.5	762.6	763.7	764.8	765.9	767.0	768.1	769.2	770.2	771.3	11.400
11.600	771.3	772.4	773.5	774.6	775.7	776.8	777.9	779.0	780.1	781.2	782.3	11.600
11.800	782.3	783.4	784.5	785.6	786.7	787.8	788.8	789.9	791.0	792.1	793.2	11.800
12.000	793.2	794.3	795.4	796.5	797.6	798.7	799.8	800.9	802.0	803.1	804.2	12.000
12.200	804.2	805.3	806.4	807.5	808.6	809.7	810.8	811.9	813.0	814.1	815.2	12.200
12.400	815.2	816.3	817.4	818.5	819.6	820.7	821.8	822.9	824.0	825.1	826.1	12.400
12.600	826.1	827.2	828.3	829.4	830.5	831.6	832.7	833.9	835.0	836.1	837.2	12.600
12.800	837.2	838.3	839.4	840.5	841.6	842.7	843.8	844.9	846.0	847.1	848.2	12.800

These tables are based on eleven thermocouples representing four manufacturers. The third decimal place in the emf values is given for interpolating purposes and does not represent table accuracy. Statements concerning accuracy are given in the text of this paper.

TABLE 4. *Tungsten versus rhenium thermocouples*—Continued

Millivolts	0.000	0.020	0.040	0.060	0.080	0.100	0.120	0.140	0.160	0.180	0.200	*Millivolts*
13.000	848.2	849.3	850.4	851.5	852.6	853.7	854.8	855.9	857.0	858.1	859.2	13.000
13.200	859.2	860.3	861.4	862.5	863.6	864.7	865.8	866.9	868.1	869.2	870.3	13.200
13.400	870.3	871.4	872.5	873.6	874.7	875.8	876.9	878.0	879.1	880.2	881.3	13.400
13.600	881.3	882.4	883.6	884.7	885.8	886.9	888.0	889.1	890.2	891.3	892.4	13.600
13.800	892.4	893.5	894.7	895.8	896.9	898.0	899.1	900.2	901.3	902.4	903.6	13.800
14.000	903.6	904.7	905.8	906.9	908.0	909.1	910.2	911.3	912.5	913.6	914.7	14.000
14.200	914.7	915.8	916.9	918.0	919.2	920.3	921.4	922.5	923.6	924.7	925.9	14.200
14.400	925.9	927.0	928.1	929.2	930.3	931.4	932.6	933.7	934.8	935.9	937.0	14.400
14.600	937.0	938.2	939.3	940.4	941.5	942.6	943.8	944.9	946.0	947.1	948.3	14.600
14.800	948.3	949.4	950.5	951.6	952.7	953.9	955.0	956.1	957.2	958.4	959.5	14.800
15.000	959.5	960.6	961.7	962.9	964.0	965.1	966.2	967.4	968.5	969.6	970.8	15.000
15.200	970.8	971.9	973.0	974.1	975.3	976.4	977.5	978.6	979.8	980.9	982.0	15.200
15.400	982.0	983.2	984.3	985.4	986.6	987.7	988.8	990.0	991.1	992.2	993.4	15.400
15.600	993.4	994.5	995.6	996.8	997.9	999.0	1000.2	1001.3	1002.4	1003.6	1004.7	15.600
15.800	1004.7	1005.8	1007.0	1008.1	1009.2	1010.4	1011.5	1012.6	1013.8	1014.9	1016.1	15.800
16.000	1016.1	1017.2	1018.4	1019.5	1020.6	1021.8	1022.9	1024.1	1025.2	1026.4	1027.5	16.000
16.200	1027.5	1028.7	1029.8	1030.9	1032.1	1033.2	1034.4	1035.5	1036.7	1037.8	1039.0	16.200
16.400	1039.0	1040.1	1041.3	1042.4	1043.6	1044.8	1045.9	1047.1	1048.2	1049.4	1050.5	16.400
16.600	1050.5	1051.7	1052.8	1054.0	1055.2	1056.3	1057.5	1058.6	1059.8	1061.0	1062.1	16.600
16.800	1062.1	1063.3	1064.4	1065.6	1066.8	1067.9	1069.1	1070.3	1071.4	1072.6	1073.8	16.800
17.000	1073.8	1074.9	1076.1	1077.3	1078.4	1079.6	1080.8	1081.9	1083.1	1084.3	1085.5	17.000
17.200	1085.5	1086.6	1087.8	1089.0	1090.2	1091.3	1092.5	1093.7	1094.9	1096.0	1097.2	17.200
17.400	1097.2	1098.4	1099.6	1100.8	1101.9	1103.1	1104.3	1105.5	1106.7	1107.9	1109.0	17.400
17.600	1109.0	1110.2	1111.4	1112.6	1113.8	1115.0	1116.2	1117.4	1118.5	1119.7	1120.9	17.600
17.800	1120.9	1122.1	1123.3	1124.5	1125.7	1126.9	1128.1	1129.3	1130.5	1131.7	1132.9	17.800
18.000	1132.9	1134.1	1135.3	1136.5	1137.7	1138.9	1140.1	1141.3	1142.5	1143.7	1144.9	18.000
18.200	1144.9	1146.1	1147.3	1148.5	1149.7	1150.9	1152.1	1153.3	1154.5	1155.8	1157.0	18.200
18.400	1157.0	1158.2	1159.4	1160.6	1161.8	1163.0	1164.3	1165.5	1166.7	1167.9	1169.1	18.400
18.600	1169.1	1170.3	1171.6	1172.8	1174.0	1175.2	1176.5	1177.7	1178.9	1180.1	1181.4	18.600
18.800	1181.4	1182.6	1183.8	1185.0	1186.3	1187.5	1188.7	1190.0	1191.2	1192.4	1193.7	18.800
19.000	1193.7	1194.9	1196.1	1197.4	1198.6	1199.8	1201.1	1202.3	1203.6	1204.8	1206.0	19.000
19.200	1206.0	1207.3	1208.5	1209.8	1211.0	1212.3	1213.5	1214.8	1216.0	1217.3	1218.5	19.200
19.400	1218.5	1219.8	1221.0	1222.3	1223.5	1224.8	1226.0	1227.3	1228.5	1229.8	1231.1	19.400
19.600	1231.1	1232.3	1233.6	1234.8	1236.1	1237.4	1238.6	1239.9	1241.2	1242.4	1243.7	19.600
19.800	1243.7	1245.0	1246.2	1247.5	1248.8	1250.0	1251.3	1252.6	1253.9	1255.1	1256.4	19.800
20.000	1256.4	1257.7	1259.0	1260.3	1261.5	1262.8	1264.1	1265.4	1266.7	1268.0	1269.3	20.000
20.200	1269.3	1270.5	1271.8	1273.1	1274.4	1275.7	1277.0	1278.3	1279.6	1280.9	1282.2	20.200
20.400	1282.2	1283.5	1284.8	1286.1	1287.4	1288.7	1290.0	1291.3	1292.6	1293.9	1295.2	20.400
20.600	1295.2	1296.5	1297.8	1299.1	1300.4	1301.8	1303.1	1304.4	1305.7	1307.0	1308.3	20.600
20.800	1308.3	1309.7	1311.0	1312.3	1313.6	1314.9	1316.3	1317.6	1318.9	1320.2	1321.6	20.800
21.000	1321.6	1322.9	1324.2	1325.6	1326.9	1328.2	1329.6	1330.9	1332.2	1333.6	1334.9	21.000
21.200	1334.9	1336.3	1337.6	1339.0	1340.3	1341.7	1343.0	1344.4	1345.7	1347.1	1348.4	21.200
21.400	1348.4	1349.8	1351.1	1352.5	1353.8	1355.2	1356.6	1357.9	1359.3	1360.6	1362.0	21.400
21.600	1362.0	1363.4	1364.7	1366.1	1367.5	1368.9	1370.2	1371.6	1373.0	1374.4	1375.7	21.600
21.800	1375.7	1377.1	1378.5	1379.9	1381.3	1382.7	1384.0	1385.4	1386.8	1388.2	1389.6	21.800
22.000	1389.6	1391.0	1392.4	1393.8	1395.2	1396.6	1398.0	1399.4	1400.8	1402.2	1403.6	22.000
22.200	1403.6	1405.0	1406.4	1407.8	1409.3	1410.7	1412.1	1413.5	1414.9	1416.4	1417.8	22.200
22.400	1417.8	1419.2	1420.6	1422.1	1423.5	1424.9	1426.3	1427.8	1429.2	1430.6	1432.1	22.400
22.600	1432.1	1433.5	1435.0	1436.4	1437.9	1439.3	1440.8	1442.2	1443.7	1445.1	1446.6	22.600
22.800	1446.6	1448.0	1449.5	1450.9	1452.4	1453.9	1455.3	1456.8	1458.3	1459.7	1461.2	22.800
23.000	1461.2	1462.7	1464.2	1465.6	1467.1	1468.6	1470.1	1471.6	1473.1	1474.5	1476.0	23.000
23.200	1476.0	1477.5	1479.0	1480.5	1482.0	1483.5	1485.0	1486.5	1488.0	1489.5	1491.1	23.200
23.400	1491.1	1492.6	1494.1	1495.6	1497.1	1498.6	1500.2	1501.7	1503.2	1504.7	1506.3	23.400
23.600	1506.3	1507.8	1509.3	1510.9	1512.4	1514.0	1515.5	1517.1	1518.6	1520.2	1521.7	23.600
23.800	1521.7	1523.3	1524.8	1526.4	1527.9	1529.5	1531.1	1532.6	1534.2	1535.8	1537.4	23.800
24.000	1537.4	1538.9	1540.5	1542.1	1543.7	1545.3	1546.9	1548.4	1550.0	1551.6	1553.2	24.000
24.200	1553.2	1554.8	1556.4	1558.1	1559.7	1561.3	1562.9	1564.5	1566.1	1567.8	1569.4	24.200
24.400	1569.4	1571.0	1572.6	1574.3	1575.9	1577.5	1579.2	1580.8	1582.5	1584.1	1585.8	24.400
24.600	1585.8	1587.4	1589.1	1590.8	1592.4	1594.1	1595.8	1597.4	1599.1	1600.8	1602.5	24.600
24.800	1602.5	1604.2	1605.8	1607.5	1609.2	1610.9	1612.6	1614.3	1616.0	1617.8	1619.5	24.800
25.000	1619.5	1621.2	1622.9	1624.6	1626.4	1628.1	1629.8	1631.6	1633.3	1635.0	1636.8	25.000
25.200	1636.8	1638.5	1640.3	1642.1	1643.8	1645.6	1647.3	1649.1	1650.9	1652.7	1654.5	25.200
25.400	1654.5	1656.2	1658.0	1659.8	1661.6	1663.4	1665.2	1667.1	1668.9	1670.7	1672.5	25.400
25.600	1672.5	1674.3	1676.2	1678.0	1679.8	1681.7	1683.5	1685.4	1687.2	1689.1	1691.0	25.600
25.800	1691.0	1692.8	1694.7	1696.6	1698.5	1700.4	1702.3	1704.2	1706.1	1708.0	1709.9	25.800
26.000	1709.9	1711.8	1713.7	1715.6	1717.6	1719.5	1721.5	1723.4	1725.4	1727.3	1729.3	26.000
26.200	1729.3	1731.2	1733.2	1735.2	1737.2	1739.2	1741.2	1743.2	1745.2	1747.2	1749.2	26.200
26.400	1749.2	1751.2	1753.3	1755.3	1757.3	1759.4	1761.4	1763.5	1765.6	1767.6	1769.7	26.400
26.600	1769.7	1771.8	1773.9	1776.0	1778.1	1780.2	1782.3	1784.5	1786.6	1788.7	1790.9	26.600
26.800	2790.9	1793.1	1795.2	1797.4	1799.6	1801.8	1804.0	1806.2	1808.4	1810.6	1812.8	26.800

TABLE 4. *Tungsten versus rhenium thermocouples*—Continued

Millivolts	0.000	0.020	0.040	0.060	0.080	0.100	0.120	0.140	0.160	0.180	0.200	*Millivolts*
27.000	1812.8	1815.0	1817.3	1819.5	1821.8	1824.1	1826.4	1828.6	1830.9	1833.2	1835.6	27.000
27.200	1835.6	1837.9	1840.2	1842.6	1844.9	1847.3	1849.7	1852.0	1854.4	1856.8	1859.3	27.200
27.400	1859.3	1861.7	1864.1	1866.6	1869.0	1871.5	1874.0	1876.5	1879.0	1881.5	1884.1	27.400
27.600	1884.1	1886.6	1889.2	1891.7	1894.3	1896.9	1899.6	1902.2	1904.8	1907.5	1910.2	27.600
27.800	1910.2	1912.8	1915.6	1918.3	1921.0	1923.8	1926.5	1929.3	1932.1	1935.0	1937.8	27.800
28.000	1937.8	1940.7	1943.6	1946.5	1949.4	1952.3	1955.3	1958.3	1961.3	1964.3	1967.4	28.000
28.200	1967.4	1970.4	1973.5	1976.7	1979.8	1983.0	1986.2	1989.4	1992.7	1996.0	1999.3	28.200
28.400	1999.3	2002.7										

TABLE 5. *Tungsten versus rhenium thermocouples*

Electromotive force in absolute millivolts. Temperature in degrees C (Int. 1948). Reference junctions at 0 °C.

Temp. ° *C*	0	5	10	15	20	25	30	35	40	45	50	Temp. ° *C*.
0	0.000	0.032	0.065	0.099	0.134	0.170	0.207	0.245	0.284	0.324	0.364	0
50	0.364	0.406	0.449	0.492	0.537	0.582	0.628	0.675	0.723	0.772	0.821	50
100	0.821	0.872	0.923	0.975	1.028	1.081	1.136	1.191	1.247	1.303	1.361	100
150	1.361	1.419	1.477	1.537	1.597	1.658	1.719	1.782	1.844	1.908	1.972	150
200	1.972	2.037	2.102	2.168	2.235	2.302	2.370	2.438	2.507	2.576	2.647	200
250	2.647	2.717	2.788	2.860	2.932	3.005	3.078	3.151	3.225	3.300	3.375	250
300	3.375	3.451	3.527	3.603	3.680	3.757	3.835	3.913	3.992	4.071	4.150	300
350	4.150	4.230	4.310	4.390	4.471	4.552	4.634	4.715	4.798	4.880	4.963	350
400	4.963	5.046	5.130	5.213	5.297	5.382	5.466	5.551	5.636	5.722	5.807	400
450	5.807	5.893	5.979	6.066	6.152	6.239	6.326	6.414	6.501	6.589	6.677	450
500	6.677	6.765	6.853	6.941	7.030	7.119	7.208	7.297	7.386	7.476	7.565	500
550	7.565	7.655	7.744	7.834	7.924	8.015	8.105	8.195	8.286	8.376	8.467	550
600	8.467	8.558	8.649	8.739	8.830	8.922	9.013	9.104	9.195	9.286	9.378	600
650	9.378	9.469	9.561	9.652	9.744	9.835	9.927	10.018	10.110	10.201	10.293	650
700	10.293	10.385	10.476	10.568	10.660	10.751	10.843	10.935	11.026	11.118	11.209	700
750	11.209	11.301	11.392	11.484	11.575	11.667	11.758	11.850	11.941	12.032	12.124	750
800	12.124	12.215	12.306	12.397	12.488	12.579	12.670	12.761	12.852	12.942	13.033	800
850	13.033	13.124	13.214	13.305	13.395	13.486	13.576	13.666	13.756	13.846	13.936	850
900	13.936	14.026	14.116	14.205	14.295	14.385	14.474	14.563	14.653	14.742	14.831	900
950	14.831	14.920	15.009	15.098	15.187	15.275	15.364	15.452	15.541	15.629	15.717	950
1000	15.717	15.805	15.893	15.981	16.069	16.156	16.243	16.331	16.417	16.504	16.591	1000
1050	16.591	16.677	16.764	16.850	16.935	17.021	17.107	17.192	17.277	17.362	17.447	1050
1100	17.447	17.532	17.616	17.700	17.784	17.868	17.952	18.036	18.119	18.202	18.285	1100
1150	18.285	18.368	18.450	18.532	18.614	18.696	18.778	18.859	18.941	19.022	19.103	1150
1200	19.103	19.183	19.264	19.344	19.424	19.504	19.583	19.663	19.742	19.821	19.899	1200
1250	19.899	19.978	20.056	20.134	20.212	20.289	20.366	20.444	20.520	20.597	20.673	1250
1300	20.673	20.749	20.825	20.901	20.976	21.051	21.126	21.201	21.275	21.350	21.424	1300
1350	21.424	21.497	21.571	21.644	21.717	21.789	21.862	21.934	22.006	22.077	22.149	1350
1400	22.149	22.220	22.290	22.361	22.431	22.501	22.571	22.640	32.710	22.778	22.847	1400
1450	22.847	22.915	22.984	23.051	23.119	23.186	23.253	23.320	23.386	23.452	23.518	1450
1500	23.518	23.583	23.649	23.713	23.778	23.842	23.906	23.970	24.033	24.097	24.159	1500
1550	24.159	24.222	24.284	24.346	24.408	24.469	24.530	24.590	24.651	24.711	24.771	1550
1600	24.771	24.830	24.889	24.948	25.006	25.064	25.122	25.179	25.237	25.293	25.350	1600
1650	25.350	25.406	25.462	25.517	25.572	25.627	25.682	25.736	25.790	25.843	25.896	1650
1700	25.896	25.949	26.001	26.053	26.105	26.156	26.207	26.258	26.308	26.358	26.408	1700
1750	26.408	26.457	26.506	26.554	26.603	26.650	26.698	26.745	26.792	26.838	26.884	1750
1800	26.884	26.929	26.975	27.020	27.064	27.108	27.152	27.195	27.238	27.281	27.323	1800
1850	27.323	27.365	27.406	27.447	27.488	27.528	27.568	27.607	27.646	27.685	27.723	1850
1900	17.723	27.761	27.799	27.836	27.873	27.909	27.945	27.980	28.015	28.050	28.084	1900
1950	28.084	28.118	28.152	28.185	28.217	28.249	28.281	28.312	28.343	28.374	28.404	1950
2000	28.404											2000

These tables are based on eleven thermocouples representing four manufacturers. The third decimal place in the emf values is given for interpolating purposes and does not represent table accuracy. Statements concerning accuracy are given in the text of this paper.

TABLE 6. *Tungsten versus rhenium thermocouples*

Electromotive force in absolute millivolts. Temperature in degrees F.* Reference junctions at 32 °F.

Millivolts	0.000	0.020	0.040	0.060	0.080	0.100	0.120	0.140	0.160	0.180	0.200	Millivolts
0.000	32.0	37.7	43.2	48.7	54.0	59.3	64.4	69.5	74.5	79.5	84.3	0.000
0.200	84.3	89.1	93.9	98.5	103.1	107.7	112.2	116.6	121.0	125.4	129.7	0.200
0.400	129.7	134.0	138.2	142.3	146.5	150.6	154.6	158.7	162.7	166.6	170.5	0.400
0.600	170.5	174.4	178.3	182.1	185.9	189.7	193.4	197.1	200.8	204.5	208.1	0.600
0.800	208.1	211.7	215.3	218.9	222.4	226.0	229.5	233.0	236.4	239.9	243.3	0.800
1.000	243.3	246.7	250.1	253.4	256.8	260.1	263.4	266.7	270.0	273.2	276.5	1.000
1.200	276.5	279.7	282.9	286.1	289.3	292.5	295.6	298.8	301.9	305.0	308.1	1.200
1.400	308.1	311.2	314.3	317.3	320.4	323.4	326.5	329.5	332.5	335.5	338.4	1.400
1.600	338.4	341.4	344.4	347.3	350.2	353.2	356.1	359.0	361.9	364.8	367.6	1.600
1.800	367.6	370.5	373.4	376.2	379.0	381.9	384.7	387.5	390.3	393.1	395.9	1.800
2.000	395.9	398.7	401.4	404.2	407.0	409.7	412.4	415.2	417.9	420.6	423.3	2.000
2.200	423.3	426.0	428.7	431.4	434.1	436.7	439.4	442.1	444.7	447.4	450.0	2.200
2.400	450.0	452.6	455.2	457.9	460.5	463.1	465.7	468.3	470.9	473.5	476.0	2.400
2.600	476.0	478.6	481.2	483.7	486.3	488.8	491.4	493.9	496.4	499.0	501.5	2.600
2.800	501.5	504.0	506.5	509.0	511.5	514.0	516.5	519.0	521.5	524.0	526.4	2.800
3.000	526.4	528.9	531.4	533.8	536.3	538.7	541.2	543.6	546.1	548.5	550.9	3.000
3.200	550.9	553.3	555.8	558.2	560.6	563.0	565.4	567.8	570.2	572.6	575.0	3.200
3.400	575.0	577.3	579.7	582.1	584.5	586.8	589.2	591.6	593.9	596.3	598.6	3.400
3.600	598.6	601.0	603.3	605.7	608.0	610.3	612.7	615.0	617.3	619.6	622.0	3.600
3.800	622.0	624.3	626.6	628.9	631.2	633.5	635.8	638.1	640.4	642.7	645.0	3.800
4.000	645.0	647.2	649.5	651.8	654.1	656.3	658.6	660.9	663.1	665.4	667.7	4.000
4.200	667.7	669.9	672.2	674.4	676.7	678.9	681.2	683.4	685.6	687.9	690.1	4.200
4.400	690.1	692.3	694.6	696.8	699.0	701.2	703.5	705.7	707.9	710.1	712.3	4.400
4.600	712.3	714.5	716.7	718.9	721.1	723.3	725.5	727.7	729.9	732.1	734.3	4.600
4.800	734.3	736.4	738.6	740.8	743.0	745.2	747.3	749.5	751.7	753.8	756.0	4.800
5.000	756.0	758.2	760.3	762.5	764.7	766.8	769.0	771.1	773.3	775.4	777.6	5.000
5.200	777.6	779.7	781.9	784.0	786.1	788.3	790.4	792.6	794.7	796.8	799.0	5.200
5.400	799.0	801.1	803.2	805.3	807.5	809.6	811.7	813.8	815.9	818.1	820.2	5.400
5.600	820.2	822.3	824.4	826.5	828.6	830.7	832.8	834.9	837.0	839.1	841.2	5.600
5.800	841.2	843.3	845.4	847.5	849.6	851.7	853.8	855.9	858.0	860.1	862.1	5.800
6.000	862.1	864.2	866.3	868.4	870.5	872.5	874.6	876.7	878.8	880.9	882.9	6.000
6.200	882.9	885.0	887.1	889.1	891.2	893.3	895.3	897.4	899.5	901.5	903.6	6.200
6.400	903.6	905.6	907.7	909.8	911.8	913.9	915.9	918.0	920.0	922.1	924.1	6.400
6.600	924.1	926.2	928.2	930.3	932.3	934.4	936.4	938.5	940.5	942.6	944.6	6.600
6.800	944.6	946.6	948.7	950.7	952.7	954.8	956.8	958.8	960.9	962.9	964.9	6.800
7.000	964.9	967.0	969.0	971.0	973.1	975.1	977.1	979.1	981.2	983.2	985.2	7.000
7.200	985.2	987.2	989.3	991.3	993.3	995.3	997.3	999.3	1001.4	1003.4	1005.4	7.200
7.400	1005.4	1007.4	1009.4	1011.4	1013.5	1015.5	1017.5	1019.5	1021.5	1023.5	1025.5	7.400
7.600	1025.5	1027.5	1029.5	1031.5	1033.5	1035.5	1037.5	1039.5	1041.6	1043.6	1045.6	7.600
7.800	1045.6	1047.6	1049.6	1051.6	1053.6	1055.6	1057.6	1059.6	1061.5	1063.5	1065.5	7.800
8.000	1065.5	1067.5	1069.5	1071.5	1073.5	1075.5	1077.5	1079.5	1081.5	1083.5	1085.5	8.000
8.200	1085.5	1087.5	1089.5	1091.4	1093.4	1095.4	1097.4	1099.4	1101.4	1103.4	1105.4	8.200
8.400	1105.4	1107.3	1109.3	1111.3	1113.3	1115.3	1117.3	1119.2	1121.2	1123.2	1125.2	8.400
8.600	1125.2	1127.2	1129.2	1131.1	1133.1	1135.1	1137.1	1139.1	1141.0	1143.0	1145.0	8.600
8.800	1145.0	1147.0	1148.9	1150.9	1152.9	1154.9	1156.9	1158.8	1160.8	1162.8	1164.8	8.800
9.000	1164.8	1166.7	1168.7	1170.7	1172.6	1174.6	1176.6	1178.6	1180.5	1182.5	1184.5	9.000
9.200	1184.5	1186.5	1188.4	1190.4	1192.4	1194.3	1196.3	1198.3	1200.3	1202.2	1204.2	9.200
9.400	1204.2	1206.2	1208.1	1210.1	1212.1	1214.0	1216.0	1218.0	1219.9	1221.9	1223.9	9.400
9.600	1223.9	1225.9	1227.8	1229.8	1231.8	1233.7	1235.7	1237.7	1239.6	1241.6	1243.6	9.600
9.800	1243.6	1245.5	1247.5	1249.5	1251.4	1253.4	1255.3	1257.3	1259.3	1261.2	1263.2	9.800
10.000	1263.2	1265.2	1267.1	1269.1	1271.1	1273.0	1275.0	1277.0	1278.9	1280.9	1282.9	10.000
10.200	1282.9	1284.8	1286.8	1288.8	1290.7	1292.7	1294.6	1296.6	1298.6	1300.5	1302.5	10.200
10.400	1302.5	1304.5	1306.4	1308.4	1310.4	1312.3	1314.3	1316.2	1318.2	1320.2	1322.1	10.400
10.600	1322.1	1324.1	1326.1	1328.0	1330.0	1332.0	1333.9	1335.9	1337.9	1339.8	1341.8	10.600
10.800	1341.8	1343.7	1345.7	1347.7	1349.6	1351.6	1353.6	1355.5	1357.5	1359.5	1361.4	10.800
11.000	1361.4	1363.4	1365.4	1367.3	1369.3	1371.3	1373.2	1375.2	1377.1	1379.1	1381.1	11.000
11.200	1381.1	1383.0	1385.0	1387.0	1388.9	1390.9	1392.9	1394.8	1396.8	1398.8	1400.7	11.200
11.400	1400.7	1402.7	1404.7	1406.6	1408.6	1410.6	1412.5	1414.5	1416.5	1418.4	1420.4	11.400
11.600	1420.4	1422.4	1424.3	1426.3	1428.3	1430.3	1432.2	1434.2	1436.2	1438.1	1440.1	11.600
11.800	1440.1	1442.1	1444.0	1446.0	1448.0	1450.0	1451.9	1453.9	1455.9	1457.8	1459.8	11.800
12.000	1459.8	1461.8	1463.8	1465.7	1467.7	1469.7	1471.6	1473.6	1475.6	1477.6	1479.5	12.000
12.200	1479.5	1481.5	1483.5	1485.5	1487.4	1489.4	1491.4	1493.4	1495.3	1497.3	1499.3	12.200
12.400	1499.3	1501.3	1503.2	1505.2	1507.2	1509.2	1511.2	1513.1	1515.1	1517.1	1519.1	12.400
12.600	1519.1	1521.0	1523.0	1525.0	1527.0	1529.0	1530.9	1532.9	1534.9	1536.9	1538.9	12.600
12.800	1538.9	1540.9	1542.8	1544.8	1546.8	1548.8	1550.8	1552.8	1554.7	1556.7	1558.7	12.800

*Based on the International Practical Temperature Scale of 1948.

These tables are based on eleven thermocouples representing four manufacturers. The third decimal place in the emf values is given for interpolating purposes and does not represent table accuracy. Statements concerning accuracy are given in the text of this paper.

TABLE 6. *Tungsten versus rhenium thermocouples*—Continued

Millivolts	0.000	0.020	0.040	0.060	0.080	0.100	0.120	0.140	0.160	0.180	0.200	*Millivolts*
13.000	1558.7	1560.7	1562.7	1564.7	1566.7	1568.6	1570.6	1572.6	1574.6	1576.6	1578.6	13.000
13.200	1578.6	1580.6	1582.6	1584.5	1586.5	1588.5	1590.5	1592.5	1594.5	1596.5	1598.5	13.200
13.400	1598.5	1600.5	1602.5	1604.5	1606.4	1608.4	1610.4	1612.4	1614.4	1616.4	1618.4	13.400
13.600	1618.4	1620.4	1622.4	1624.4	1626.4	1628.4	1630.4	1632.4	1634.4	1636.4	1638.4	13.600
13.800	1638.4	1640.4	1642.4	1644.4	1646.4	1648.4	1650.4	1652.4	1654.4	1656.4	1658.4	13.800
14.000	1658.4	1660.4	1662.4	1664.4	1666.4	1668.4	1670.4	1672.4	1674.4	1676.4	1678.4	14.000
14.200	1678.4	1680.5	1682.5	1684.5	1686.5	1688.5	1690.5	1692.5	1694.5	1696.5	1698.5	14.200
14.400	1698.5	1700.6	1702.6	1704.6	1706.6	1708.6	1710.6	1712.6	1714.6	1716.7	1718.7	14.400
14.600	1718.7	1720.7	1722.7	1724.7	1726.7	1728.8	1730.8	1732.8	1734.8	1736.8	1738.9	14.600
14.800	1738.9	1740.9	1742.9	1744.9	1746.9	1749.0	1751.0	1753.0	1755.0	1757.1	1759.1	14.800
15.000	1759.1	1761.1	1763.1	1765.2	1767.2	1769.2	1771.2	1773.3	1775.3	1777.3	1779.4	15.000
15.200	1779.4	1781.4	1783.4	1785.4	1787.5	1789.5	1791.5	1793.6	1795.6	1797.6	1799.7	15.200
15.400	1799.7	1801.7	1803.7	1805.8	1807.8	1809.8	1811.9	1813.9	1816.0	1818.0	1820.0	15.400
15.600	1820.0	1822.1	1824.1	1826.2	1828.2	1830.2	1832.3	1834.3	1836.4	1838.4	1840.4	15.600
15.800	1840.4	1842.5	1844.5	1846.6	1848.6	1850.7	1852.7	1854.8	1856.8	1858.9	1860.9	15.800
16.000	1860.9	1863.0	1865.0	1867.1	1869.2	1871.2	1873.3	1875.3	1877.4	1879.5	1881.5	16.000
16.200	1881.5	1883.6	1885.6	1887.7	1889.8	1891.8	1893.9	1896.0	1898.0	1900.1	1902.2	16.200
16.400	1902.2	1904.3	1906.3	1908.4	1910.5	1912.6	1914.6	1916.7	1918.8	1920.9	1923.0	16.400
16.600	1923.0	1925.0	1927.1	1929.2	1931.3	1933.4	1935.5	1937.5	1939.6	1941.7	1943.8	16.600
16.800	1943.8	1945.9	1948.0	1950.1	1952.2	1954.3	1956.4	1958.5	1960.6	1962.7	1964.8	16.800
17.000	1964.8	1966.9	1969.0	1971.1	1973.2	1975.3	1977.4	1979.5	1981.6	1983.7	1985.8	17.000
17.200	1985.8	1987.9	1990.1	1992.2	1994.3	1996.4	1998.5	2000.6	2002.8	2004.9	2007.0	17.200
17.400	2007.0	2009.1	2011.2	2013.4	2015.5	2017.6	2019.8	2021.9	2024.0	2026.1	2028.3	17.400
17.600	2028.3	2030.4	2032.5	2034.7	2036.8	2039.0	2041.1	2043.2	2045.4	2047.5	2049.7	17.600
17.800	2049.7	2051.8	2054.0	2056.1	2058.2	2060.4	2062.6	2064.7	2066.9	2069.0	2071.2	17.800
18.000	2071.2	2073.3	2075.5	2077.6	2079.8	2082.0	2084.1	2086.3	2088.5	2090.6	2092.8	18.000
18.200	2092.8	2095.0	2097.1	2099.3	2101.5	2103.7	2105.8	2108.0	2110.2	2112.4	2114.5	18.200
18.400	2114.5	2116.7	2118.9	2121.1	2123.3	2125.5	2127.7	2129.8	2132.0	2134.2	2136.4	18.400
18.600	2136.4	2138.6	2140.8	2143.0	2145.2	2147.4	2149.6	2151.8	2154.0	2156.2	2158.4	18.600
18.800	2158.4	2160.6	2162.8	2165.1	2167.3	2169.5	2171.7	2173.9	2176.1	2178.4	2180.6	18.800
19.000	2180.6	2182.8	2185.0	2187.3	2189.5	2191.7	2193.9	2196.2	2198.4	2200.6	2202.9	19.000
19.200	2202.9	2205.1	2207.3	2209.6	2211.8	2214.1	2216.3	2218.6	2220.8	2223.1	2225.3	19.200
19.400	2225.3	2227.6	2229.8	2232.1	2234.3	2236.6	2238.8	2241.1	2243.4	2245.6	2247.9	19.400
19.600	2247.9	2250.2	2252.4	2254.7	2257.0	2259.3	2261.5	2263.8	2266.1	2268.4	2270.7	19.600
19.800	2270.7	2272.9	2275.2	2277.5	2279.8	2282.1	2284.4	2286.7	2289.0	2291.3	2293.6	19.800
20.000	2293.6	2295.9	2298.2	2300.5	2302.8	2305.1	2307.4	2309.7	2312.0	2314.3	2316.7	20.000
20.200	2316.7	2319.0	2321.3	2323.6	2325.9	2328.3	2330.6	2332.9	2335.2	2237.6	2339.9	20.200
20.400	2339.9	2342.2	2344.6	2346.9	2349.3	2351.6	2354.0	2356.3	2358.7	3361.0	2363.4	20.400
20.600	2363.4	2365.7	2368.1	2370.4	2372.8	2375.2	2377.5	2379.9	2382.3	2384.6	2387.0	20.600
20.800	2387.0	2389.4	2391.7	2394.1	2396.5	2398.9	2401.3	2403.7	2406.0	2408.4	2410.8	20.800
21.000	2410.8	2413.2	2415.6	2418.0	2420.4	2422.8	2425.2	2427.6	2430.0	2432.5	2434.9	21.000
21.200	2434.9	2437.3	2439.7	2442.1	2444.6	2447.0	2449.4	2451.8	2454.3	2456.7	2459.1	21.200
21.400	2459.1	2461.6	2464.0	2466.5	2468.9	2471.3	2473.8	2476.2	2478.7	2481.2	2483.6	21.400
21.600	2483.6	2486.1	2488.5	2491.0	2493.5	2495.9	2498.4	2500.9	2503.4	2505.8	2508.3	21.600
21.800	2508.3	2510.8	2513.3	2515.8	2518.3	2520.8	2523.3	2525.8	2528.3	2530.8	2533.3	21.800
22.000	2533.3	2535.8	2538.3	2540.8	2543.3	2545.9	2548.4	2550.9	2553.4	2556.0	2558.5	22.000
22.200	2558.5	2561.0	2563.6	2566.1	2568.7	2571.2	2573.8	2576.3	2578.9	0 2581.4	2584.0	22.200
22.400	2584.0	2586.6	2589.1	2591.7	2594.3	2596.8	2599.4	2602.0	2604.6	2607.2	2609.8	22.400
22.600	2609.8	2612.3	2614.9	2617.5	2620.1	2622.7	2625.4	2628.0	2630.6	2632.2	2635.8	22.600
22.800	2635.8	2638.4	2641.1	2643.7	2646.3	2649.0	2651.6	2654.2	2656.9	2659.5	2662.2	22.800
23.000	2662.2	2664.8	2667.5	2670.2	2672.8	2675.5	2678.2	2680.8	2683.5	2686.2	2688.9	23.000
23.200	2688.9	2691.6	2694.3	2696.9	2699.6	2702.3	2705.0	2707.8	2710.5	2713.2	2715.9	23.200
23.400	2715.9	2718.6	2721.4	2724.1	2726.8	2729.6	2732.3	2735.0	2737.8	2740.5	2743.3	23.400
23.600	2743.3	2746.1	2748.8	2751.6	2754.4	2757.1	2759.9	2762.7	2765.5	2768.3	2771.1	23.600
23.800	2771.1	2773.9	2776.7	2779.5	2782.3	2785.1	2787.9	2790.7	2793.6	2796.4	2799.2	23.800
24.000	2799.2	2802.1	2804.9	2807.8	2810.6	2813.5	2816.3	2819.2	2822.1	2825.0	2827.8	24.000
24.200	2827.8	2830.7	2833.6	2836.5	2839.4	2842.3	2845.2	2848.1	2851.0	2854.0	2856.9	24.200
24.400	2856.9	2859.8	2862.8	2865.7	2868.6	2871.6	2874.5	2877.5	2880.5	2883.4	2886.4	24.400
24.600	2886.4	2889.4	2892.4	2895.4	2898.4	2901.4	2904.4	2907.4	2910.4	2913.4	2916.5	24.600
24.800	2916.5	2919.5	2922.5	2925.6	2928.6	2931.7	2934.7	2937.8	2940.9	2944.0	2947.0	24.800
25.000	2947.0	2950.1	2953.2	2956.3	2959.4	2962.6	2965.7	2968.8	2971.9	2975.1	2978.2	25.000
25.200	2978.2	2981.4	2984.5	2987.7	2990.9	2994.0	2997.2	3000.4	3003.6	3006.8	3010.0	25.200
25.400	3010.0	3013.2	3016.5	3019.7	3022.9	3026.2	3029.4	3032.7	3036.0	3039.2	3042.5	25.400
25.600	3042.5	3045.8	3049.1	3052.4	3055.7	3059.0	3062.4	3065.7	3069.0	3072.4	3075.8	25.600
25.800	3075.8	3079.1	3082.5	3085.9	3089.3	3092.7	3096.1	3099.5	3102.9	3106.3	3109.8	25.800

TABLE 6. *Tungsten versus rhenium thermocouples*—Continued

Millivolts	0.000	0.020	0.040	0.060	0.080	0.100	0.120	0.140	0.160	0.180	0.200	*Millivolts*
26.000	3109.8	3113.2	3116.7	3120.2	3123.6	3127.1	3130.6	3134.1	3137.6	3141.2	3144.7	26.000
26.200	3144.7	3148.2	3151.8	3155.3	3158.9	3162.5	3166.1	3169.7	3173.3	3176.9	3180.6	26.200
26.400	3180.6	3184.2	3187.9	3191.5	3195.2	3198.9	3202.6	3206.3	3210.0	3213.8	3217.5	26.400
26.600	3217.5	3221.3	3225.0	3228.8	3232.6	3236.4	3240.2	3244.1	3247.9	3251.7	3255.6	26.600
26.800	3255.6	3259.5	3263.4	3267.3	3271.2	3275.2	3279.1	3283.1	3287.1	3291.1	3295.1	26.800
27.000	3295.1	3299.1	3303.1	3307.2	3311.3	3315.3	3319.4	3323.6	3327.7	3331.8	3336.0	27.000
27.200	3336.0	3340.2	3344.4	3348.6	3352.9	3357.1	3361.4	3365.7	3370.0	3374.3	3378.7	27.200
27.400	3378.7	3383.0	3387.4	3391.8	3396.3	3400.7	3405.2	3409.7	3414.2	3418.7	3423.3	27.400
27.600	3423.3	3427.9	3432.5	3437.1	3441.8	3446.5	3451.2	3455.9	3460.7	3465.5	3470.3	27.600
27.800	3470.3	3475.1	3480.0	3484.9	3489.8	3494.8	3499.8	3504.8	3509.8	3514.9	3520.1	27.800
28.000	3520.1	3525.2	3530.4	3535.6	3540.9	3546.2	3551.5	3556.9	3562.3	3567.8	3573.2	28.000
28.200	3573.2	3578.8	3584.4	3590.0	3595.7	3601.4	3607.2	3613.0	3618.9	3624.8	3630.8	28.200
28.400	3630.8	3636.8										

TABLE 7. *Tungsten versus rhenium thermocouples*

Electromotive force in absolute millivolts. Temperature in degrees F.* Reference junctions at 32 ° F.

Temp. ° F	0	10	20	30	40	50	60	70	80	90	100	Temp. ° F
0					0.028	0.065	0.103	0.142	0.182	0.224	0.266	0
100	0.266	0.310	0.355	0.401	0.449	0.497	0.547	0.597	0.649	0.702	0.756	100
200	0.756	0.810	0.866	0.923	0.981	1.040	1.099	1.160	1.222	1.284	1.348	200
300	1.348	1.412	1.477	1.544	1.611	1.678	1.747	1.816	1.887	1.958	2.030	300
400	2.030	2.102	2.176	2.250	2.325	2.400	2.476	2.553	2.631	2.709	2.788	400
500	2.788	2.868	2.948	3.029	3.110	3.192	3.275	3.358	3.442	3.527	3.612	500
600	3.612	3.697	3.783	3.870	3.957	4.044	4.132	4.221	4.310	4.399	4.489	600
700	4.489	4.579	4.670	4.761	4.853	4.945	5.037	5.130	5.223	5.316	5.410	700
800	5.410	5.504	5.598	5.693	5.788	5.884	5.979	6.075	6.172	6.268	6.365	800
900	6.365	6.462	6.560	6.657	6.755	6.853	6.951	7.050	7.148	7.247	7.346	900
1000	7.346	7.446	7.545	7.645	7.744	7.844	7.944	8.045	8.145	8.245	8.346	1000
1100	8.346	8.447	8.548	8.649	8.750	8.851	8.952	9.053	9.154	9.256	9.357	1100
1200	9.357	9.459	9.561	9.662	9.764	9.866	9.967	10.069	10.171	10.273	10.375	1200
1300	10.375	10.476	10.578	10.680	10.782	10.884	10.985	11.087	11.189	11.291	11.392	1300
1400	11.392	11.494	11.596	11.697	11.799	11.900	12.002	12.103	12.205	12.306	12.407	1400
1500	12.407	12.508	12.609	12.710	12.811	12.912	13.013	13.114	13.214	13.315	13.415	1500
1600	13.415	13.516	13.616	13.716	13.816	13.916	14.016	14.116	14.215	14.315	14.414	1600
1700	14.414	14.514	14.613	14.712	14.811	14.910	15.009	15.108	15.206	15.305	15.403	1700
1800	15.403	15.502	15.600	15.698	15.796	15.893	15.991	16.088	16.185	16.282	16.379	1800
1900	16.379	16.475	16.572	16.668	16.764	16.859	16.955	17.050	17.145	17.239	17.334	1900
2000	17.334	17.428	17.522	17.616	17.710	17.803	17.896	17.989	18.082	18.174	18.266	2000
2100	18.266	18.358	18.450	18.541	18.633	18.724	18.814	18.905	18.995	19.085	19.174	2100
2200	19.174	19.264	19.353	19.442	19.530	19.618	19.707	19.794	19.882	19.969	20.056	2200
2300	20.056	20.143	20.229	20.315	20.401	20.486	20.571	20.656	20.741	20.825	20.909	2300
2400	20.909	20.993	21.076	21.160	21.242	21.325	21.407	21.489	21.571	21.652	21.733	2400
2500	21.733	21.813	21.894	21.974	22.053	22.133	22.212	22.290	22.369	22.447	22.525	2500
2600	22.525	22.602	22.679	22.756	22.832	22.908	22.984	23.059	23.134	23.208	23.283	2600
2700	23.283	23.357	23.430	23.503	23.576	23.649	23.721	23.792	23.864	23.935	24.005	2700
2800	24.005	24.076	24.145	24.215	24.284	24.353	24.421	24.489	24.557	24.624	24.691	2800
2900	24.691	24.757	24.823	24.889	24.954	25.019	25.084	25.148	25.211	25.275	25.337	2900
3000	25.337	25.400	25.462	25.523	25.585	25.645	25.706	25.766	25.825	25.884	25.943	3000
3100	25.943	26.001	26.059	26.116	26.173	26.230	26.286	26.342	26.397	26.452	26.506	3100
3200	26.506	26.560	26.613	26.666	26.719	26.771	26.823	26.874	26.924	26.975	27.024	3200
3300	27.024	27.074	27.123	27.171	27.219	27.267	27.314	27.360	27.406	27.452	27.497	3300
3400	27.497	27.541	27.585	27.629	27.672	27.715	27.757	27.799	27.840	27.881	27.921	3400
3500	27.921	27.961	28.000	28.038	28.077	28.114	28.152	28.188	28.224	28.260	28.295	3500
3600	28.295	28.330	28.364	28.397	28.430							3600

*Based on the International Practical Temperature Scale of 1948.

These tables are based on eleven thermocouples representing four manufacturers. The third decimal place in the emf is given for interpolating purposes and does not represent table accuracy. Statements concerning accuracy are given in the text of this paper.

The author acknowledges the contributions made by the following employees of the National Bureau of Standards in the computer program development and data handling that were utilized for the presentation of this paper: John S. Gallagher of the Temperature Physics Section, Daniel R. Flynn of the Heat Transfer Section, and Joseph Hilsenrath of the Equation of State Section.

8. References

[1] W. Goedicke, Thermocouples and the reproducibility of their data. Criteria for their usefulness in measuring high temperatures, Siebert Festschrift, pp. 72–99 (1931).
[2] C. T. Sims et al., Investigations of rhenium, WADC TR54–371 (June 1954).
[3] C. T. Sims et al., Investigations of rhenium, WADCTR-54–371 (September (1956).
[4] C. T. Sims and G. B. Gaines, Electrical resistivity and thermal electric potential of rhenium metal, ASTM Preprint No. 75 (1957).
[5] C. T. Sims et al., Investigations of rhenium for electron tube applications, AFCRC–TN–58–176 (June 1958).
[6] C. J. Smithells, Tungsten, Its Metallurgy, Properties, and Applications (Chemical Publishing Co., Inc., New York, 1953).
[7] R. W. Hall and P. F. Sikora, Tensile properties o molybdenum and tungsten from 2500° to 3700°F NASA Memo 3–9–59E, 1959.
[8] Irving Langmuir, Tungsten lamps of high efficiency, Trans. AIEE **32,** p. 1893 (1913).
[9] J. C. Lachman, Calibration of rhenium-molybdenum and rhenium-tungsten thermocouples to 4000 °F, GE-ANPD APEX–365 (April 1958).
[10] J. C. Lachman and F. W. Kuether, Stability of rhenium-tungsten thermocouples in hydrogen atmospheres, J. Inst. Soc. Am. (March 1960).
[11] J. C. Lachman, Refractory metal thrmocouples, Paper No. 59–HT–21, ASME–AIChE, Heat Transfer Conference, August 1959.
[12] D. B. Thomas, A furnace for thermocouple calibrations to 2200 °C, J. Res. NBS **66C** (Eng. and Instr.), No. 3 (July–Sept. 1962).
[13] Wm. F. Roeser and S. T. Lonberger, Methods of testing thermocouples and thermocouple materials; Circ. 590, NBS (Feb. 1958).
[14] H. J. Kostkowski and R. D. Lee, Theory and methods of optical pyrometry, NBS Mono. No. 41 (1962).
[15] Platinum vs. platinum-rhodium thermocouple specifications, Engelhard Industries, Inc., Newark, N.J.
[16] Precious metals as used in temperature measurements, Sigmund Cohn Corp., Mount Vernon, N.Y.

(Paper 67C4–146)

JOURNAL OF RESEARCH of the National Bureau of Standards—C. Engineering and Instrumentation
Vol. 67C, No. 4, October–December 1963

Publications of the National Bureau of Standards*

Selected Abstracts

Standard X-ray diffraction powder patterns, H. E. Swanson, M. C. Morris, R. P. Stinchfield, and E. H. Evans, *NBS Mono. 25, Section 2 (May 3, 1963), 35 cents.*

Standard X-ray diffraction powder patterns are presented for the following thirty-seven substances: Al $(PO_3)_3$, SbF_3*, $Ba_3(AsO_4)_2$*, $Ba(ClO_4)_2.3H_2O$, $Cd(CN)_2$*, $CdWO_4$, Cs_2OsBr_6*, Cs_2OsCl_6*, α-$CrPO_4$, $Co[Hg(CNS)_4]$*, β-$CoSO_4$, $Dy_3Ga_2(GaO_4)_3$*, $ErMnO_3$*, $Eu_3Ga_2(GaO_4)_3$*, $Gd_3Ga_2(GaO_4)_3$*, Li_3AsO_4*, $Li_3P_3O_{\sim}.3H_2O$*, $Li_2WO_4.\frac{1}{2}H_2O$*, $Lu_3Ga_2(GaO_4)_3$*, $LuMnO_3$*, $MnWO_4$ (huebnerite), HgF_2*, $NiSO_4$, $NiWO_4$*, K_2ReCl_6, K_2RuCl_5NO*, $RbClO_4$*, $RbIO_4$*, Ag_2SeO_4*, NaCNO*, $Na_2WO_4.2H_2O$, β-$Na_4P_4O_{12}.4H_2O$, $Sr_3(AsO_4)_2$*, Tl_3AsO_4*, $TlClO_4$*, $YAsO_4$, $ZnWO_4$*. Eleven are to replace patterns already given in the X-ray Powder Data File issued by the American Society for Testing and Materials, and twenty-six patterns indicated by asterisks are for substances not previously included. The X-ray Powder Data File is a compilation of diffraction patterns from many sources and is used for the identification of unknown crystalline materials by matching spacing and intensity measurements. The patterns were made with a Geiger counter X-ray diffractometer, using samples of high purity. When possible, the *d*-values were assigned Miller indices determined by comparison with calculated interplanar spacings and from space group extinctions. The densities and lattice constants were calculated, and the refractive indices were measured whenever possible.

Mechanical behavior of crystalline solids (*Proceedings of an American Ceramic Society Symposium, New York City, April 1962*), *NBS Mono. 59 (Mar. 25, 1963), $1.75.*

This Monograph represents the Proceedings of a Symposium on The Mechanical Behavior of Crystalline Solids, held under the auspices of the Ceramic Educational Council of the American Ceramic Society, with the cooperation of the National Bureau of Standards, and under the sponsorship of the Edward Orton Junior Ceramic Foundation, and the Office of Naval Research. The Symposium took place at the 64th Annual Meeting of the American Ceramic Society, in New York, on April 28 and 29, 1962.

Testing of metal volumetric standards, J. C. Hughes and B. C. Keysar, *NBS Mono. 62 (Apr. 1, 1963), 15 cents.*

The National Bureau of Standards has for many years calibrated and certified metal measures which are used as standards by weights and measures officials and others in the calibration of instruments for measuring the volumes of fluids. No complete specifications or tolerances for these standards have ever been published, however, nor have standardized procedures for the calibration and use of the liquid measures been available.

The information contained in this Monograph should assist in the purchase of quality instruments and the proper use of the standards in calibrating other measures for liquids and gases.

Reduction of data for piston gage pressure measurements, J. L. Cross, *NBS Mono. 65 (June 17, 1963), 15 cents.*

Pressure measurements made with piston gages are affected by gravity, temperature, pressure, and several other variables. For accurate determinations of pressure the calculations must take these variables into account. A general equation is developed and simplified procedures for calculating pressure are illustrated.

Tabulation of data on receiving tubes, C. P. Marsden and J. K. Moffitt, *NBS Handb. 83 (May 23, 1963), $1.25. (Supersedes Handb. 68.)*

A tabulation of Receiving-Type Electron Tubes with some characteristics of each type has been prepared in the form of two major listings, a Numerical Listing in which the tubes are arranged by type number, and a Characteristic Listing in which the tubes are arranged by tube type and further ordered on the basis of one or two important parameters. The tabulation is accompanied by a listing of similar tube types and basing connections for the listed tubes.

Transistorized building blocks for data instrumentation, R. L. Hill, *NBS Tech. Note 168 (Apr. 1, 1963), 55 cents.*

The National Bureau of Standards has developed a number of modular transistorized digital circuits that have been used in automatizing many data recording and preliminary processing tasks encountered in its scientific operations. These versitile building blocks can be connected together systematically to form digital circuits that accept raw data from experimental equipment and transpose these data into a form suitable for input to a high-speed electronic computer. Each assembly of packages can be tailored to fit the special requirements of the project and can be used at the site of the experiment. The output from the system can be: 1) fed directly to a computer, 2) recorded on a medium (paper tape, magnetic tape, etc.) suitable for computer input at a later date, or 3) used to drive display equipment that keeps the scientist informed of the progress of his experiment.

As a result of experience in the application of these units, some of the original packages have been modified and additional types developed. In addition to describing the modified and new package types, this report also includes a description of a new series of packages consisting of identical circuitry, but utilizing a different type of mating connector and a smaller circuit-board.

Phototypesetting of computer output, an example using tabular data, W. R. Bozman, *NBS Tech. Note 170 (June 25, 1963), 10 cents.*

A photocomposition machine controlled by the magnetic tape output from a computer was used to prepare a 559-page table of atomic transition probabilities at the National Bureau of Standards. This method makes possible the publication of computed data in high quality typography in a reasonable time and at a reasonable cost. Many styles of type are readily available to the programmer including Greek, italic, mathematical symbols, upper and lower case alphabets, etc.

Practical methods for calibration of potentiometers, D. Ramaley, *NBS Tech. Note 172 (Mar. 25, 1963), 30 cents.*

Potentiometer circuitry, particularly as related to calibration, is discussed with the primary consideration given to the required circuit measurements. The more feasible means of calibrating potentiometers are described in considerable detail. Emphasis is placed upon the use of the Universal Ratio Set as the basic implement for accomplishing the major portion of potentiometer calibrations.

Table of attenuation error as a function of vane-angle error for rotary vane attenuators, W. Larson, *NBS Tech. Note 177 (May 20, 1963), 75 cents.*

The table of attenuation error as a function of vane-angle error gives the error in decibels caused by vane misalinement which is common in the rotary vane attenuator. The attenuation errors corresponding to vane-angle errors ranging from zero to 0.499° (in increments of 0.001°) are presented for selected angles over the range of attenuation values from 0.01 to 70 db. The table is divided into the following intervals of attenuation value increments: 0.01–0.1 db in 0.01-db increments, 0.1–1.0 db in 0.1–db increments, 1–20 db in 1–db increments, and 20–70 db in 5–db increments.

With the aid of this table, the calibration data of a rotary vane attenuator can be analyzed for numerous characteristics, in-

cluding the following: misalinement between rotor and stator sections, realinement techniques, resettability, and backlash.

Tabulation of published data on Soviet electron devices, C. P. Marsden, *NBS Tech. Note 186 (June 3, 1963), 45 cents.*
This tabulation includes published data on Soviet electron devices as collected from various publications, mostly handbooks published by the various ministries and institutes of the USSR. Information is given on all active devices ranging from receiving to microwave devices, semiconductor devices, and various miscellaneous devices such as, for example, photographic flash tubes and thermistors.

Calibration of volt-ampere converters, E. S. Williams, *NBS Tech. Note 188 (Apr. 25, 1963), 20 cents.*
These notes have been prepared to describe the National Bureau of Standards calibration services for volt-ampere converters (or transfer volt-ammeters), to suggest procedures for d–c standardization in the user's laboratory, and to describe a voltage comparator which can be used to make such calibrations quickly and easily.

Tables describing small-sample properties of the mean, median, standard deviation, and other statistics in sampling from various distributions, C. Eisenhart, L. S. Deming, and C. S. Martin, *NBS Tech. Note 191 (June 14, 1963), 20 cents.*
This note includes a collection of tables useful for study of the sampling distributions of some frequently-used statistics, with brief discussions of their construction and use. (1) The probability level $P(\epsilon,n)$ of any continuous parent distribution corresponding to level ϵ of the distribution of the median. (2) Probability points of certain sample statistics for samples from six distributions: normal and double-exponential (mean, median), rectangular (mean, median, midrange), Cauchy, Sech, Sech^2 (median). In all the above tables, the sample size $n=3(2)15(10)95$ and the probability levels are $\epsilon=.001, .005, .01, .025, .05, .10, .20, .25$. Together with the tables listed under (2) are given the values of certain ratios useful for comparing the various statistics. (3) Probability that the standard deviation of a normal distribution will be underestimated by the sample standard deviation s and by unbiased estimators of σ based on s, on the mean deviation, and on the sample range. Divisors are given for obtaining the corresponding "median unbiased" estimators.

National standard reference data program, background information, *NBS Tech. Note 194 (June 1963), 25 cents.*
Plans are proposed for a National Standard Reference Data System that will provide critically evaluated data in the physical sciences on a national basis. It will be conducted as a decentralized operation across the country, with central coordination and administration by NBS. Data will be centrally stored at NBS and disseminated through a series of services tailored to user needs in science and industry.

New absolute null method for the measurement of magnetic susceptibilities in weak low-frequency fields, C. T. Zahn, *Rev. Sci. Instr.* **34;** *No. 3, 285–291 (Mar. 1963).*
Use is made of the magnetic equivalence of a uniformly polarized volume of paramagnetic material and a solenoid carrying electric current, to design a permanent variable standard of magnetic susceptibility. Such a standard is incorporated into a magnetic susceptibility bridge in a simple manner, surrounding the specimen; and the bridge is thereby transformed into an absolute null instrument of high accuracy and sensitivity, and of great ease and low cost of construction and operation. By this method numerous particular advantages of other methods are combined; and some of their notable limitations are overcome. A preliminary application was made showing that the bridge performs as expected. Important features in the design of this bridge are discussed. A detailed consideration of sources of error suggests that it may eventually be possible by this method to obtain greater absolute accuracy than by other known methods.

A method for measuring the instability of resistance strain gages at elevated temperatures, R. L. Bloss and J. T. Trumbo, *ISA Trans.* **2;** *No. 2, 112–116 (Apr. 1963).*
The usefulness of resistance strain gages at elevated temperatures is frequently limited by the instability of gage resistance with time. Methods and equipment that have been developed to measure this effect are described.

Maximum efficiency of a two-arm waveguide junction, R. W. Beatty, *IEEE Trans. Microwave Theory and Tech.* **MTT–11,** *94 (Jan. 1963).*
Given the scattering coefficients of a 2-arm waveguide junction, an equation is presented to calculate Γ_M, the reflection coefficient of the load for which the efficiency of a 2-arm waveguide junction is η_M, the maximum efficiency. Once Γ_M has been calculated, an equation is given to determine η_M and the relationship between η_M and A_I, the intrinsic attenuation of the waveguide junction, is given.

Applications of a semiconductor-surface-state charge-storage device, L. J. Swartzendruber, *Solid-State Elec.* **6,** *59–61 (Pergamon Press, Inc., New York, N.Y. 1963).*
Several possible applications of a new two terminal semiconductor device which utilizes surface phenomena to produce a charge storage effect are described. The major advantage of the device lies in the magnitude of the charges which can be stored and the ease with which it can be controlled by small bias currents.

Audio-frequency compliances of prestressed quartz, fused silica, and aluminum, M. Greenspan and C. Tschiegg, *Proc. Fourth Intern. Congr. on Acoustics, Part I, Paper P12 (Copenhagen, Denmark, Aug. 21–28, 1962).*
An attempt was made to find the excess compliances associated with dispersions found by Fitzgerald. Compliances were obtained from resonant frequencies of fixed-free composite reeds. Prestress was either piezoelectrically or thermally induced. No excess compliances were observed.

Ten-kilocycle pound-type kylstron stabilizer, H. E. Radford, *Rev. Sci. Instr.* **34,** *No. 3, 304–305 (Mar. 1963).*
Through a simple circuit modification, commercial klystron frequency stabilizers of the FM type can be made to function alternatively as CW Pound-type stabilizers, with greater spectral purity of the klystron output. The performance of such a stabilizer is discussed.

Kihara parameters and second viral coefficients for cryogenic fluids and their mixtures, J. M. Prausnitz and A. L. Myers, *A. I. Ch. E. Journal* **9,** *No. 1, 5–11 (Jan. 1963).*
The volumetric properties of sixteen fluids of interest in cryogenic engineering have been used to calculate second viral coefficients over as large a temperature range as possible. These coefficients were then fitted to theoretical expressions based on the Kihara potential function. For helium, hydrogen, and neon quantum corrections were applied. For nitrogen, carbon dioxide, and acetylene corrections for quadrupole interactions were made. It was found that the theoretical expressions give an extremely good fit of all reliable experimental data. The theoretical expressions may therefore be used with confidence to predict volumetric behavior at very low temperatures where data are frequently unavailable.
With the aid of semiempirical mixing rules the theoretical expressions may be used to predict second viral coefficients for mixtures. Agreement with the very limited amount of experimental mixture data is satisfactory. Finally it is shown that calculations based on the Kihara potential may be employed to make useful predictions of phase equilibria such as the solubility of a solid in a compressed gas.

Transparent rigid mount for vacuum stopcock, M. M. Anderson, *Rev. Sci. Instr.* **34,** *No. 2, 178 (Feb. 1963).*
A transparent block of plastic, moulded around a glass stopcock, then drilled and tapped for mounting, reduces vacuum system breakage and allows visual inspection of the grease seal.

Design of low voltage electron guns, J. A. Simpson and C. E. Kuyatt, *Rev. Sci. Instr.* **34,** *No. 3, 265–268 (Mar. 1963).*
It is shown that by use of a multistage technique in which electrons are drawn from a cathode by a high potential and

decelerated to the required final energy, guns can be designed capable of forming beams in which the current is limited only by space charge in the beam itself. The design principles and procedures are given and illustrated by two examples of electron guns giving highly collimated beams and operating at energies of 30 and 500 eV. The measured currents obtained are somewhat greater than the space charge limited beam maximum because of ion neutralization.

Thermometry, low temperature, R. P. Hudson, *Encyclopaedic Dictionary of Physics* **7,** *323–325 (1962).*
A discussion is given of apparatus and methods for thermometry in the range 1°–100°K in a style and brevity suited to an entry in a scientific encyclopaedia.

Effect of outdoor exposure on some properties of chrome-retanned leather, T. J. Carter, *J. Am. Leather Chemists Assoc.* **LVIII,** *No. 3, 155–160 (Mar. 1963).*
Two groups of specimens of chrome-retanned leather were subjected to outdoor exposure and the changes in physical and chemical properties were determined. One group was subjected to all weather conditions while the other group was shielded from the sun. The effect of the exposure was determined by measurements of physical properties, such as flex tension and impact resistance, elongation, stitch tearing strength, tensile strength, change in area, relative stiffness, and shrinkage temperature, and of chemical properties, such as grease content and *p*H.
Results show that specimens shielded from the sun changed little in impact resistance, stitch tear strength, elongation of tensile strength specimens, and stiffness, but changed significantly in flex tension resistance, elongation (due to flexing), area, and shrinkage temperature. Specimens exposed to the sun showed deleterious changes in all the physical properties studied. Shrinkage temperature declined significantly under both conditions, the decrease being somewhat greater for specimens exposed to direct sunlight. The chemical properties, grease content and *p*H values, showed only slight changes under either condition of exposure.

APPA-TAPPI reference material program. II. Effectiveness of a reference material in reducing the between-laboratory variability of TAPPI standard T 414 m-49 for internal tearing resistance of paper, T. W. Lashof, *Tappi* **46,** *No. 3, 145–150 (Mar. 1963).*
The effectiveness of a reference material was predicted on the basis of the results of the first round robin which was reported in Part I. The analysis was modified for the second round robin so as to provide corrections in terms of measurements on the reference material. If the current TAPPI procedure is followed (5 replications, no standard reference material), the total coefficient of variation, including both within- and between-laboratory variability, is about 4½ to 5%, as shown in both round robins. As shown in this second part, a standard reference material and increased replication may be used to reduce the total coefficient of variation to about 3%. It is also shown that the correction curve or nomograph based on the measurements on the reference material may be used for at least four to five months, provided that there are no changes in observer, instrument, or conditions.
The limitation to further reduction in the total coefficient of variation is $V(\lambda)$, the random interaction between interfering properties of the materials being tested and laboratory conditions or instrument peculiarities. It is shown that a portion of this is probably due to insufficient control of relative humidity. Since $V(\lambda)$ is higher for laboratories using new-type instruments than for those using old-type instruments, further work must be done to determine whether this is due to the instruments or to laboratory conditions.

Some characteristics of a simple cryopump, L. O. Mullen and R. B. Jacobs, *1962 Trans. Ninth Natl. Vacuum Symp., Am. Vacuum Soc., pp. 220–226 (1962).*
A simple and easily definable cryopump was constructed as a stage in a pumping system, and data were obtained to permit the computation of pumping speeds, performance decay and capture coefficients. Information on the pumping of CO_2 and N_2 as well as outgassing vapors, by surfaces at 77°K and 20°K is presented. The pressure range of the tests is $5(10)^{-10}$ torr to $5(10)^{-3}$ torr and the gas flow range is 3.6×10^{-7} torr liters cm.$^{-2}$ sec.$^{-1}$ to $3.6(10)^{-2}$ torr liters cm.$^{-2}$ sec.$^{-1}$. Pumping speeds higher than those previously reported and higher than theory predicts were obtained, the results are discussed in detail.

Experimental investigation of Fabry-Perot interferometer, R. W. Zimmerer, *Proc. IEEE* **51,** *475-476 (Mar. 1963).*
Preliminary measurements of the microwave performance of Fabry-Perot interferometers with spherical mirrors is presented and compared with theory. Of particular interest is the evidence of the stop band recently predicted by Boyd and Kogelnik.

The measurement of moisture boundary layers and leaf transpiration with a microwave refractometer, D. M. Gates, M. J. Vetter, and M. C. Thompson, Jr., Nature **197,** 1070–1072 (Mar. 16, 1963).
A microwave refractometer has been used as a hygrometer to measure the moisture gradient found near a free water surface and near the surface of a leaf. Interesting transpiration effects were observed for begonia and bean leaves when the leaves were stimulated with light. The instrument samples the air through a small orifice and thereby produces very little disturbance to the moisture boundary layer under investigation.

New scale of nuclidic masses and atomic weights, E. Wichers, *Nature* **194,** *No. 4829, 621–624 (May 10, 1962).*
This is an article written at the request of the Editor of "NATURE."
It reviews the considerations that led to the adoption by the International Unions of Physics and Chemistry of a new scale of nuclidic masses and atomic weights based on $C^{12}=12$.

Calibration of photogrammetric lenses and cameras at the National Bureau of Standards, F. E. Washer, *Photogrammetric Eng.* **XXIX,** *No. 1, 113–119 (Jan. 1963).*
A summary of calibrations performed at the National Bureau of Standards on lenses and cameras that are used in precise photogrammetric work is given. Brief description of the photographic and visual calibrations most frequently required are given. This paper includes a list of publications by members of the NBS staff that pertain to problems of lens and camera calibration.

Building a simple transistor tester, G. F. Montgomery, *Electronics* **36,** *No. 16, 56 (Apr. 19, 1963).*
A simple instrument is described for measuring two dc transistor parameters: leakage current and common-emitter current amplification.

A magnetic amplifier for use with diode logic, E. W. Hogue, *Proc. IEEE 1963 Intern. Conf. Nonlinear Magnetics No. T–149, 8.6–1 to 8.6–6 (Apr. 1963).*
A digital amplifier of simple noncritical design incorporating an emitter-follower and a small magnetic amplifier is described. Timing and some of the operating power are provided by a 300-kc 2-phase 7-volt sine-wave source. In structure and mode of operation, the amplifier is particularly suited for use with two-level diode gating to provide the AND and OR logical operations. A NOT-amplifier provides negation with amplification. The volt-second transfer characteristic of the stage critically determines the stability of propagation of binary signals. Factors governing the required shape of this transfer characteristic are discussed.

The speed of light, A. G. McNish, *IRE. Trans. Instr.* **I–11,** *Nos. 3 and 4, 138–148 (Dec. 1962).*
Numerous measurements of the speed of light published during the last 30 years lead to widely divergent results as compared with the assigned experimental uncertainties. Because of wide diversity in the methods employed in the measurements, all of the data may not be combined effectively in a grand average. Sufficient data had been obtained by the geodimeter method to group them and derive a statistical estimate of the uncertainty in the speed of light by this method. This result, and conclusions reached from careful examination of several experiments, leads to the conclusion

that the value 299,792.5 km per sec which has been internationally adopted for use in radio propagation and geodetic work is very close to the best value and not likely to be in error by as much as one part in one million.

Performance characteristics of split-type residential air-to-air heat pumps, J. C. Davis and P. R. Achenbach, *Suppl. Bull. Inst. Intern. Refrigeration, p. 1–7 (1961–1962).*
This paper presents test results obtained during a laboratory study of six split-type residential air-to-air heat pumps, a type more widely used than others for residential application in the United States in the last few years. For residential use, these systems are currently selected to satisfy the cooling requirements of the house under design summer conditions, and, if necessary, the heating capacity of the compression-cycle is supplemented with electric resistance heaters. The investigation showed that the compression-cycle heating capacity of the heat pumps equipped with expansion valves increased linearly with increasing outdoor temperature at constant indoor temperature and humidity, whereas the capacity of the heat pumps equipped with capillary tubes also increased but tended toward constant values at higher temperatures. It was shown that the cooling capacity of the heat pumps decreased linearly with outdoor temperature, when indoor temperature and relative humidity were held constant. At constant outdoor temperatures, cooling capacity increased linearly either with increasing indoor temperature or indoor relative humidity. The changes in the latent and sensible fractions of the total cooling capacity caused by change in indoor relative humidity, and the effect of outdoor temperature on coefficient of performance under heating and cooling conditions, are also reported.

Millimeter wavelength resonant structures, R. W. Zimmerer, M. V. Anderson, G. L. Strine, and Y. Beers, *IEEE Trans. Microwave Theory Tech.* **MMT–11,** *142–149 (Mar. 1963).*
This paper discusses the construction of millimeter wave Fabry-Perot resonators, using both planar and spherical reflectors. It also discusses the equivalent circuits of planar reflectors and the method of obtaining efficient power transfer into the resonators.

A simple environmental chamber for rotating beam fatigue testing machines, J. A. Bennett, *Mater. Res. Std.* **3,** *No. 6, 480–482 (June 1963).*
A gas-tight sleeve, made from transparent plastic, permits fatigue testing under controlled atmosphere conditions. Tests of magnesium and aluminum alloys have shown that changes in humidity may change the fatigue strength by more than 10%.

Evidence regarding the mechanism of fatigue from studies of environmental effects, J. A. Bennett, *Acta Met.* **11,** *No. 7, 799–800 (July 1963).*
Fatigue tests of aluminum alloy specimens are being conducted under controlled humidity conditions. Results of tests in which the environment is changed during the test show that there is an initial period during which the humidity has no effect. This is interpreted to indicate that the deformation during that period is not localized.

Calorimetric calibration of the electrical energy measurement in an exploding wire experiment, D. H. Tsai and J. H. Park, *Exploding Wires* **2,** *27–107 (Plenum Press, Inc., New York, N.Y., 1962).*
A discussion is presented on the requirements and the methods for measuring the current and voltage during the transient discharge of a capacitor bank employed in an exploding wire experiment. A method is described for accurately calibrating the measured current, voltage, and electrical energy by comparing the calorimetric heating of a fixed resistance element with the electrical energy dissipated in the element. Results show that the accuracy of the energy measurement is about 1–2%

Oil baths for saturated standard cells, P. H. Lowrie, Jr., *ISA J.* **9,** *No. 12, 47–50 (Dec. 1962).*
The increasing use of saturated standard cells in industry has caused a growing need for information on equipment associated with tneir use. This paper discusses oil baths suitable for the close temperature control of these cells and describes the oil baths in use at NBS Boulder Laboratories. In these baths, the temperature is controlled by a modified on-off system that limits cyclic variations to less than $\pm 0.001°C$ from the mean temperature. The mean does not change more than 0.002°C per day in an environment in which the ambient temperature may change by as much as 2°C during the day.

Performance of the barium fluoride film hygrometer element on radiosonde flights, F. E. Jones, *J. Geophys. Res.* **68,** *No. 9, 2735–2751 (May 1, 1963).*
Ten flights of the barium fluoride film electric hygrometer element in a modified radiosonde on the same train with a conventional ithium chloride element in an AN/AMT–11 radiosonde were made from the grounds of the National Bureau of Standards (Wash., D.C.) during the period January 16 through July 21 of 1961. The flights were intended to provide information on the performance of the barium fluoride element under conditions encountered in routine radiosonde flights and to provide information to be used in assessing the value of the element as a research tool.
The results for the flights verified results of laboratory tests in several areas. The element responded to changes in humidity over a range of indicated relative humidity, RH, of 1.5 to 100% in the temperature range 33.1 to −58.7° C, preflight room temperature calibrations indicated that the ten elements flown were typical, in this respect, of elements tested under laboratory conditions, exposure to high humidity and passage through precipitation had no apparent effect on the functioning of the element, the rapid response of the element and its ability to resolve fine humidity structure were demonstrated, indications of saturation or near-saturation were correlated with U.S. Weather Bureau surface observations of clouds and radar weather observations.
In several of the flights, a strong correlation exists between changes in indicated RH and ambient temperature lapse rates. A sharp drop in indicated RH within the first several hundred feet above the surface in at least five of the flights is possibly related to boundary layer phenomena at or near the surface. In two of the flights the element detected supersaturation with respect to ice.
Although the instability with time of the barium fluoride element, in its present state of development, precludes its use in routine radiosonde flights, the ten flights indicated the value of the element for experimental use and as a research tool.
In addition to the flights of the barium fluoride element, one flight was made of a lead iodide film hydrometer element.

Intererfence fringes with long path difference using He-Ne laser, T. Morokuma, K. F. Nefflen, T. R. Lawrence, and T. M. Klucher, *J. Opt. Soc. Am.* **53,** *No. 3, 394–395 (Mar. 1963).*
Interference fringes have been obtained in a Michelson interferometer with path length differences up to 9 meters using a helium neo laser as lignt source.

Hyrdogen retention system for pressure calibration of microphones in small couplers, W. Koidan, *J. Acoust, Soc. Am.* **35,** *No. 4, 614 (Apr. 1963).*
The pressure calibration of microphones using small hydrogen-filled couplers can be facilitated by connecting relatively large containers of hydrogen to the capillary tubes of the coupler and using additional capillary tubes to vent the large containers to the atmosphere.

Other NBS Publication

Journal of Research 67A (Phys. and Chem.), No. 4 (July–Aug. 1963), 70 cents.
Symmetry splitting of equivalent sites in oxide crystals and related mechanical effects. J. B. Wachtman, Jr., H. S. Peiser, and E. P. Levine.
Relaxation modes for trapped crystal point defects. A. D. Franklin.
A note on the galvanomagnetic and thermoelectric coefficients of tetragonal crystalline materials. W. C. Hernandez, Jr., and A. H. Kahn.

Photolytic behavior of silver iodide. G. Burley.
Correlation of muscovite sheet mica on the basis of color, apparent optic angle, and absorption spectrum. St. Ruthberg, M. W. Barnes, and R. H. Noyce.
Thermodynamic properties of magnesium oxide and beryllium oxide from 298 to 1,200 °K. A. C. Victor and T. B. Douglas.
Heat exchange in adiabatic calorimeters. E. D. West.
Preparation of anhydrous single crystals of rare-earth halides. N. H. Kiess.
A phase study of the system: oxalic acid/acetic acid/water; its significance in oxalic acid crystal growth. J. Strassburger and J. L. Torgesen.
Wavelength calibrations in the far infrared (30 to 1000 microns). K. N. Rao, R. V. de Vore, and E. K. Plyler.
On the fourth order Hamiltonian of an asymmetric rotor molecule of orthorhombic symmetry. Wm. B. Olson and H. C. Allen, Jr.
Measurement of the thickness and refractive index of very thin films and the optical properties of surfaces by ellipsometry. F. L. McCrackin, E. Passaglia, R. R. Stromberg, and H. L. Steinberg.
Color phenomena associated with energy transfer in afterglows and atomic flames. A. M. Bass and H. P. Broida.

Journal of Research 67A (Phys. and chem.), No. 5 (Sept.–Oct. 1963), 70 cents.

Reduction of space groups to subgroups by homogeneous strain. H. S. Peiser, J. B. Wachtman, Jr., and R. W. Dickson.
High-temperature thermodynamic functions for zirconium and unsaturated zirconium hydrides. T. B. Douglas.
Heat of oxidation of aqueous sulfur dioxide with gaseous chlorine. W. H. Johnson and J. R. Ambrose.
Thickness of adsorbed polystyrene layers by ellipsometry. R. R. Stromberg, E. Passaglia, and D. J. Tutas.
Melting temperature and change of lamellar thickness with time for bulk polyethylene. J. J. Weeks.
Precise coulometric titrations of potassium dichromate. G. Marinenko and J. K. Taylor.
Resolution limits of analyzers and oscillatory systems. Edith L. R. Corliss.
Synthesis, purification, and physical properties of seven twelve-carbon hydrocarbons. T. W. Mears, C. L. Stanley, E. L. Compere, Jr., and F. L. Howard.
Reactions of polyfluorobenzenes with nucleophilic reagents. L. A. Wall, W. J. Pummer, J. E. Fearn, and J. M. Antonucci.

Journal of Research 67B (Math. and Math. PHys.), No. 3 (July–Sept. 1963), 75 cents.

Remarks on hypo-elasticity. C. Truesdell.
Error bounds in the pointwise approximation of solutions of elastic plate problems. J. H. Bramble and L. E. Payne.
Effect of error in measurement of elastic constants on the solutions of problems in classical elasticity. J. H. Bramble and L. E. Payne.
Eigenfunctions of the f^3 configuration. J. C. Eisenstein.
Zeros of first derivatives of Bessel functions of the first kind, $J_n'(x)$, $21 \leq n \leq 51$, $0 \leq x \leq 100$. G. W. Morgenthaler and H. Reismann.

Journal of Research 67D (Radio Prop.), No. 5 (Sept.–Oct. 1963), 70 cents.

Ionospheric VHF scattering near the magnetic equator during the International Geophysical Year. R. Cohen and K. L. Bowles.
Radio pulse propagation by a reflection process at the lower ionosphere. J. R. Johler.
Field of a horizontal magnetic dipole in the presence of a magnetoplasma halfspace. G. Tyras, A. Ishimaru, and H. M. Swarm.
Reflection of VLF radio waves from an inhomogeneous ionosphere. Part II. Perturbed exponential model. J. R. Wait and L. C. Walters.
Collisional detachment and the formation of an ionospheric C region. E. T. Pierce.
Magnetic torques and Coriolis effects on a magnetically suspended rotating sphere. J. C. Keith.
Radiation field characteristics of lightning discharges in the band 1 kc/s to 100 kc/s. W. L. Taylor.
Low-frequency radio propagation into a moderately rough sea. D. F. Winter.
VLF superdirective loop arrays. E. W. Seeley.
Curves of ground proximity loss for dipole antennas (a digest). L. E. Vogler and J. L. Noble.
Observations and results from the "hiss recorder" an instrument to continuously observe the VLF emissions. J. M. Watts, J. A. Koch, and R. M. Gallet.

Influence of a sector ground screen on the field of a vertical antenna, J. R. Wait and L. C. Walters, NBS Mono. 60 (Apr. 15, 1963), 25 cents.
Refractive indices and densities of aqueous solutions of invert sugar, C. F. Snyder and A. T. Hattenburg, NBS Mono. 64 (June 7, 1963), 15 cents.
Radiobiological dosimetry. Recommendations of the International Commission on radiological units and measurements, NBS Handb. 88 (Apr. 30, 1963), Supersedes parts of Handb. 78. Handbooks 84 through 89 will completely replace H78, 25 cents.
Quarterly radio noise data, June, July, August 1962, W. Q. Crichlow, R. T. Disney, and M. A. Jenkins, NBS Tech. Note 18–15 (Mar. 1, 1963), 45 cents.
Quarterly radio noise data, September, October, November 1962, W. Q. Crichlow, R. T. Disney and M. A. Jenkins, NBS Tech. Note 18–16 (June 10, 1963), 60 cents.
Mean electron density variations of the quiet ionosphere, November 1959, J. W. Wright, L. R. Wescott, and D. J. Brown, NBS Tech. Note 40–9 (Apr. 22, 1963), 35 cents.
Mean electron density variations of the quiet ionosphere, December 1959, J. W. Wright, L. R. Wescott, and D. J. Brown, NBS Tech. Note 40–10 (Mar. 24, 1963), 35 cents.
The error rates in multiple FSK systems and the signal-to-noise characteristics of FM and PCM-FS systems, H. Akima, NBS Tech. Note 167 (Mar. 25, 1963), 40 cents.
Bibliography on atmospheric aspects of radio astronomy, including selected references to related fields, W. Nupen, NBS Tech. Note 171 (May 1, 1963), $2.00.
Tables to facilitate the determination of the ferrimagnetic resonance linewidth of non-metallic magnetic materials, C. C. Preston and W. E. Case, NBS Tech. Note 173 (Apr. 15, 1963), 25 cents.
Curves of ground proximity loss for dipole antennas, L. E. Vogler and J. L. Noble, NBS Tech. Note 175 (May 20, 1963), 30 cents.
An interpolation procedure for calculating atmospheric band absorptions from laboratory data, L. Doppleman, L. R. Megill, and R. F. Calfee, NBS Tech. Note 178 (June 3, 1963), 20 cents.
Relative power transmission characteristics of the ear and skull from hearing threshold data, E. L. Smith, Proc. Fourth Intern. Congr. on Acoustics, Part I, Paper H48 (Copenhagen, Denmark, Aug. 21–28, 1962).
Polymer research at the U.S. National Bureau of Standards, Part I, G. M. Kline, SPE J. **19,** No. 3, 278–283 (Mar. 1963).
Polymer research at the U.S. National Bureau of Standards, Part 2, G. M. Kline, SPE J. **19,** No. 4, 403–408 (Apr. 1963).
Radiation and the world we live in, L. S. Taylor, Radiology **80,** No. 3, 358–368 (Mar. 1963).
Natural and synthetic rubbers, E. J. Parks and F. J. Linnig, Anal. Chem. **35,** No. 5, 160R–178R (Apr. 1963).
Degradation of polymers, L. A. Wall and J. H. Flynn, Rubber Chem. Technol. **XXXV,** No. 5, 1157–1221 (Dec. 1962).
Chemical and magnetic enhancement of perturbed lines in the violet spectrum of CN, H. E. Radford and H. P. Broida, J. Chem. Phys. **38,**, No. 3, 644–657 (Feb. 1, 1963).
Profiles of Stark-broadened Blamer lines in a hydrogen plasma, W. L. Wiese, D. R. Paquette, and J. E. Solarski, Phys. Rev. **129,** No. 3, 1225–1232 (Feb. 1, 1963).
Low-temperature thermometry, K. D. Timmerhaus, Book, Applied Cryogenic Engineering, ed. R. W. Vance, ch. 4, 60–103 (John Wiley & Sons, Inc., New York, N.Y., 1962).
Magnetic susceptibilities and dilution effects in low-spin d^4 complexes: Osmium (IV), R. B. Johannesen and G. A.

Candela, Inorg. Chem. **2,** 67–72 (1963).

Standards and the microwave profession, J. M. Richardson, IRE Trans. Microwave Theory and Tech. **MTT–10,** No. 6, 413–415 (Nov. 1962).

Delay time of polar-cap blackout and its relation to decay time of geomagnetic disturbance, C. S. Warwick, J. Geophys. Res. **68,** No. 5, 1561–1562 (Mar. 1, 1963).

Electrolytic conductance of ammonium dihydrogen phosphate solutions in the saturation region, J. L. Torgesen and A. T. Horton, J. Phys. Chem. **67,** 376–381 (1963).

Determination of source self-absorption in the standardization of electron.capturing radionuclides, S. B. Garfinkel and J. M. R. Hutchinson, Intern. J. Appl. Radiation and Isotopes **13,** 629–639 (1962).

Standards for the 70s, W. A. Wildhack, Ind. Res. **5,** No. 3, 15–20 (Mar. 1963).

Nuclear orientation, E. Ambler, Book, Methods of Experimental Physics **5,** sect. 2.4.2.3, 196–214 (Academic Press Inc., New York, N.Y., 1963).

The ionosphere over Antarctica, W. R. Piggott and A. H. Shapley, Antarctic Research, Geophysical Mono. **7,** p. 111–126 (1962).

Mean first-passage times and the dissociation of diatomic molecules, K. E. Shuler and G. H. Weiss, J. Chem. Phys. **38,** No. 2, 505–509 (Jan. 15, 1963).

The personal side of a research project, A. T. McPherson, J. Wash. Acad. Sci. **53,** No. 3, 63–66 (Mar. 1963).

Wavelengths, energy levels, and pressure shifts in mercury 198, V. Kaufman, J. Opt. Soc. Am. **52,** No. 8, 866–870 (Aug. 1962).

On the isomerization of isobutyl radicals, J. R. McNesby and W. M. Jackson, J. Chem. Phys. **38,** No. 3, 692–693 (Feb. 1, 1963).

The electrophoretic mobility of asphaltenes in nitromethane, J. R. Wright and R. R. Minesinger, J. Colloid Sci. **18,** 223–236 (Mar. 1963).

A suggestion for improving forecasts of geomagnetic storms, Y. Hakura and J. V. Lincoln, J. Geophys. Res. **68,** No. 5, 1563–1564 (Mar. 1, 1963).

Observation of a 6300 A arc in France, America, and Australia, F. E. Roach, D. Barbier, and R. A. Duncan, Ann. Geophys. **18,** 390–391 (Oct.–Dec. 1962).

Intercomparison of national roentgen and gamma ray exposure-dose standards, H. O. Wyckoff, A. Allisy, G. H. Aston, G. P. Barnard, W. Hübner, T. Loftus, and G. Taupin, Acata Radiol. **1,** No. 1, 57–58 (Feb. 1963).

X-ray microscopy of polymers by point projection, S. B. Newman, Mod. Plastics **40,** No. 7, 165–179 (Mar. 1963).

Electric fields in the ionosphere and the excitation of the red lines of atomic oxygen, L. R. Megill, M. H. Rees, and L. K. Droppleman, Planetary Space Sci. **11,** 45–56 (Jan. 1963).

Microwave spectrum and structure of difluoramine, D. R. Lide, Jr., J. Chem. Phys. **38,** No. 2, 456–460 (Jan. 15, 1963).

International geophysical calendar for 1963, A. H. Shapley and J. V. Lincoln, J. Geophys. Res. **68,** No. 4, 1157–1159 (Feb. 15, 1963).

Infrared absorption spectra of carbon suboxide and malonotitrile in solid argon matrices, L. L. Ames, D. White, and D. E. Mann, J. Chem. Phys. **38,** No. 4, 910–917 (Feb. 15, 1963).

Interactions matrix element in a shell model, U. Fano, F. Prats, and Z. Goldsmith, Phys. Rev. **129,** No. 9, 2643–2652 (Mar. 16, 1963).

Electron impact ionization of atomic hydrogen, S. Geltman, M. R. H. Rudge, and M. J. Seaton, Proc. Phys. Soc. **81,** Pt. 2, No. 520, 375–378 (1963).

U.S. participation in international standardization, A. T. McPherson, ASTM Mater. Res. Stds. **3,** No. 4, 310–311 (Apr. 1963).

Effective diffusion constant in a polyelectrolyte solution, J. L. Jackson and S. R. Coriell, J. Chem. Phys. **38,** No. 4, 959–968 (Feb. 15, 1962).

Electron attachment coefficients of some hydrocarbon flame inhibitors, T. G. Lee, J. Phys. Chem. **67,** 360–366 (1963).

The measurement of moisture boundary layers and leaf transpiration with a microwave refractometer, D. M. Gates, M. J. Vetter, and M. C. Thompson, Jr., Nature **197,** 1070–1072 (Mar. 16, 1963).

Nuclear resonance and the hyperfine field in dilute alloys of nickel in iron, R. L. Streever, L. H. Bennett, R. C. La Force, and G. F. Day, J. Appl. Phys. **34,** No. 4, pt. 2, 1050–1051 (Apr. 1963).

The history of Pt 27, E. Wichers, Book, Temperature, Its Measurement and Control in Science and Industry **3,** pt. 1, 259–262 (Reinhold Publ. Corp., New York, N.Y., 1962).

Some causes of resonant frequency shifts in atomic beam machines. I. Shifts due to other frequencies of excitation, J. H. Shirley, J. Appl. Phys. **34,** 783–788 (Apr. 1963).

Some causes of resonant frequency shifts in atomic beam machines. II. The effect of slow frequency modulation on the Ramsey line shape, J. H. Shirley, J. Appl. Phys. **34,** 789–791 (Apr. 1963).

On the dependence of absorption coefficients upon the area of the absorbent material, E. D. Daniel, J. Acoust. Soc. Am. **35,** No. 4, 571–573 (Apr. 1963).

The role of the International Union of pure and applied chemistry, E. Wichers, J. Chem. Doc. **3,** No. 7, 7–11 (1963).

Note on a subgroup of the modular group, M. Newman and J. R. Smart, Proc. Am. Math. Soc. **14,** No. 1, 102–104 (Feb. 1963).

The orthobaric densities of parahydrogen, derived heats of vaporization and critical constants, H. M. Roder, D. E. Diller, L. A. Weber, and R. D. Goodwin, Cryogenics **3,** 16–22 (Mar. 1963).

Melting pressure equation for the hydrogens, R. D. Goodwin, Cryogenics **2,** No. 6, 1–3 (Dec. 1962).

Isotopic fractionation of uranium in sandstone, J. N. Rosholt, W. R. Shields, and E. L. Garner, Science **139,** 224–226 (Jan. 18, 1963).

The total electron content of the ionosphere at middle latitudes near the peak of the solar cycle, R. S. Lawrence, D. J. Posakony, O. K. Garriott, and S. C. Hall, J. Geophys. Res. **68,** 1889–1898 (Apr. 1, 1963).

Present status of our knowledge of atomic transition probabilities, W. L. Wiese, Proc. Tenth Colloquium Spectroscopic Intern., pp. 37–56 (Univ. of Maryland, College Park, Md., 1962).

Rubber and rubber products, W. P. Tyler and M. Tryon, Book, Industrial and Natural Products and Noninstrumental Methods, 6th ed., Standard Methods of Chemical Analysis IIB, ch. 43, 2146–2226 (D. Van Nostrand Co., Inc., New York, N. Y., 1963).

The information and oxidation of high-area carbon films, V. R. Deitz and E. F. McFarlane, Proc. Fifth Carbon Conference II, 219–232 (Pergamon Press, Inc., London, England, 1963).

Pure substance and measurement, E. Wichers, Mater. Res. Stds. **1,** No. 4, 314–315 (Apr. 1961).

The specific heat at constant volume of parahydrogen at temperatures from 15 to 90 °K and pressures to 340 atm, B. A. Younglove and D. E. Diller, Cryogenics **2,** No. 6, 1–5 (Dec. 1962).

Radiation detectors, L. Costrell, Science **139,** No. 3558, 899 (Mar. 8, 1963).

Electron spin resonance of gamma-irradiated cellulose, R. E. Florin and L. A. Wall, J. Polymer Sci. **1,** Pt. A, 1163–1173 (1963).

Fundamentals of measurement, A. G. McNish, Electro-Technol. **53,** 113–128 (May 1963).

Optimum estimators of the parameters of negative exponential distributions from one or two order statistics, M. M. Siddiqui, Ann. Math. Stat. **34,** 117–121 (Mar. 1963).

Electron microscopy studies of the surfaces of magnetic recording media, F. Nesh and D. B. Ballard, IEEE Trans. Audio **AU–11,** No. 1, 15–18 (Jan. 2, 1963).

Kinetics of the acid-catalyzed hydrolysis of acetal in water-acetone solvents at 15, 25, and 35°, R. K. Wolford, J. Phys. Chem. **67,** 632–636 (1963).

Crystallographic changes with the substitution of aluminum for iron in dicalcium ferrite, D. K. Smith, Acta Cryst. **15,** 1146–1152 (Jan. 1963).

Methods for the analysis of rubber and related products, M. Tryon and E. Horowitz, Handb. Analytical Chemistry,

sect. 13, pp. 233–256 (McGraw-Hill Book Co., Inc., New York, N.Y., 1963).

Pressure-density-temperature relations of freezing liquid parahydrogen to 350 atmospheres, R. D. Goodwin, Cryogenics **3,** 12–15 (Mar. 1963).

Nuclear magnetic resonance in metal powders at low temperatures, R. J. Snodgrass and L. H. Bennett, J. Appl. Spectry. **17,** No. 2, 53–54 (1963).

Lunar point-to-point communication, L. E. Vogler, Book, Technology of Lunar Exploration, Progress in Astronautics and Aeronautics **9,** 533–559 (Academic Press Inc., New York, N.Y., 1963).

Comment on "Parametric behavior of an ideal two-frequency varactor," G. F. Montgomery, Proc. IEEE **51,** No. 3, 491 (Mar. 1963).

Distribution of latitude of red arcs, E. Marovich and F. E. Roach, J. Geophys. Res. **68,** No. 7, 1885–1888 (Apr. 1, 1963).

The following papers were published in the Proc. Intern. Conf. Ionosphere, London, 1962 (The Institute of Physics and The Physical Society, London, England):

A model of the atmosphere and the ionosphere in the *E* and *F*1 regions, R. B. Norton, T. E. VanZandt, and J. S. Denison, pp. 26–34.

Doppler studies of the ionospheric effects of solar flares, K. Davies, pp. 76–83.

Ionospheric variations during geomagnetic storms, S. Matsushita, pp. 120–127.

The location of the irregularities responsible for ionospheric scintillation of a radio source, H. J. A. Chivers, pp. 258–266.

Equatorial spread-*F* motions, W. Calvert, K. Davies, E. Stiltner, and J. T. Brown, pp. 316–322.

Evidence for field-aligned ionization irregularities between 400 and 1000 km above the earth's surface, W Calvert, T. E. VanZandt, R. W. Knecht, and G. B. Goe, pp. 324–329

Experimental observations and theoretical calculations leading to a model for the lower ionosphere, R. H. Doherty, pp. 428–434.

Radio wave reflections at a continuously stratified plasma with electron collision frequency proportional to energy and arbitrary magnetic induction, J. R. Johler, pp. 436–445.

Very low frequency propagation in the earth-ionosphere waveguide of non-uniform width, J. R. Wait, pp. 446–451.

United States participation in international standardization, A. T. McPherson, Mater. Res. Std. 3, No. 4, 310–311 (Apr. 1963).

Instability of the equatorial *F* layer after sunset, W. Calvert, J. Geophys. Res. **68,** 2591–2593 (May 1, 1963).

Standard potential of the silver-silver chloride electrode and activity coefficients of hydrochloric acid in aqueous methanol (33.4 Wt %) with and without added sodium chloride at 25°, R. G. Bates and D. Rosenthal, J. Phys. Chem. **67,** 1088–1090 (1963).

International standardization. A new responsibility of the engineer, A. T. McPherson, Natl. Acad. Sci.-Natl. Res. Council Div. of Eng. and Ind. Res. Newsletter, No. 26, 2–4 (June 1, 1963).

Path antenna gain and comments on "properties of 400 Mc/s long-distance tropospheric circuits," W. J. Hartman, Proc., IEEE **51,** 847–848 (May 1963).

Absorption and scattering of photons by deformed nuclei, E. G. Fuller, Proc. Second All-Union Conf. Nuclear Reactions at Low and Intermediate Energies, p. 419, 1960 (Russian Academy of Science, U.S.S.R., 1962).

Microwave spectrum of tertiary butyl chloride, A. Comparison of tertiary butyl structures, D. R. Lide, Jr., and M. Jen, J. Chem. Phys. **38,** No. 7, 1504–1507 (Apr. 1, 1963).

Search for a slow component in alpha ionozation, Z. Bay and R. M. Pearlstein, Phys. Rev. **130,** No. 1, 223–227 (Apr. 1963).

Dielectric friction on a rotating dipole, R. Zwanzig, J. Chem. Phys. **38,** No. 7, 1605–1606 (Apr. 1, 1963).

Field-aligned *E*-region irregularities identified with acoustic plasma waves, K. L. Bowles, B. B. Balsley, and R. Cohen, J. Geophys. Res. **68,** 2485–2501 (May 1, 1963).

The association of plane-wave electron-density irregularities with the equatorial electrojet, R. Cohen and K. L. Bowles, J. Geophys, Res. **68,** 2603–2611 (May 1, 1963).

Quasi-equilibrium theory of mass spectra, H. M. Rosenstock and M. Krauss, Book, Mass Spectrometry of Organic Ions, pp. 1–64 (Academic Press, Inc., New York, N.Y., 1963).

Determination of differential X-ray photon flux and total beam energy, J. S. Pruitt and H. W. Koch, Book, Nuclear Physics **5,** ch. 2.8.2, pt. B, 508–553, ed. L. C. L. Yuan and C. Wu (Academic Press, Inc., New York, N.Y., 1963).

Index to the communication sof the ACM, 1958–1962, W. W Youden, Comm. ACM **6,** No. 3, 1–32 (Mar. 1963).

Electrode potentials in fused systems. VI. Membrane potentials, K. H. Stern, Phys. Chem. **67,** 893–895 (1963).

Electron spin resonance spectra of aged, γ-irradiated polystyrenes, R. E. Florin, L. A. Wall, and D. W. Brown, J. Polymer Sci. pt. A. **1,** 1521–1529 (1963).

Magnetic properties of acetinide element alloys and compounds, J. C. Eisenstein, Book, Landolt-Bornstein, 6 Ed. **2,** pt. 9, p. 3.236 (Springer-Verlag, Berlin, Germany 1962).

Planar twin boundary in aluminum, T. H. Orem, Trans Met. Soc. AIME **227,** 786–788 (June 1963).

Radio noise anomalies in August 1958, C. A. Samson, J. Geophys. Res. **68,** 2719–2726 (May 1, 1963).

Optical studies of the formation and breakdown of passive films formed on iron single crystal surfaces in inorganic inhibitor solutions, J. Kruger, J. Electrochem. Soc. **110,** No. 6, 654–663 (June 1963).

The importance of environment in fatigue failure of metals, J. A. Bennett, W. L. Holshouser and H. P. Utech, Book, Fatigue of Aircraft Structures, pp. 1–18 (Pergamon Press, Inc., London, England, 1963).

Production of Lyman alpha radiation in ion-atom collisions, G. H. Dunn, R. Geballe, and D. Pretzer, Phys. Rev. **128,** No. 5, 2200–2206 (Dec. 1, 1962).

Microwave spectrum of aluminum monofluoride, D. R. Lide, Jr., J. Chem. Phys. **38,** No. 8, 2027 (Apr. 15, 1963).

Some limits on the effect of coronal self-emission upon the excitation state of coronal ions, R. N. Thomas and C. Pecker, Astrophys. J. **137,** No. 3, 967–980 (1962).

Two-stream plasma instability as a source of irregularities in the ionosphere, D. T. Farley, Jr., Phys. Rev. Letters **10,** No. 7, 279–282 (Apr. 1, 1963).

Radiation induced polymerization of propylene at high pressure, D. W. Brown and L. A. Wall, J. Phys. Chem. **67,** 1016–1019 (1963).

Dielectric friction on a moving ion, R. Zwanzig, J. Chem. Phys. **38,** No. 7, 1603–1605 (Apr. 1, 1963).

Survey of Rb^{85}/Rb^{87} ratios in minerals, W. R. Shields, E. L. Garner, C. E. Hedge, and S. S. Goldich, J. Geophys. Res. **68,** No. 8, 2331–2334 (Apr. 15, 1963).

Dissociation constant of pyrrolidinium ion and related thermodynamic quantities from 0 to 50°, H. B. Hetzer, R. G. Bates, and R. A. Robinson, J. Phys. Chem. **67,** 1124–1127 (1963).

Introduction to the International Symposium on Equatorial Aeronomy, R. Cohen and K. L. Bowles, J. Geophys. Res. **68,** 2359–2361 (May 1, 1963).

Numerical computation of time-dependent properties of isotopically disordered one-dimensional harmonic crystal lattices, R. J. Rubin, J. Phys. Soc. Japan **18,** Suppl. II, 63–69 (1963).

The National Bureau of Standards: Where measurement is the central theme, C. S. McCamy, Ind. Phot. **11,** No. 8, 28 (Aug. 1962).

Statistical computation of configuration and free volume of a polymer molecule with solvent interaction, J. Mazur and L. Joseph, J. Chem. Phys. **38,** No. 6, 1292–1300 (Mar. 15, 1963).

**Publications for which a price is indicated are available by purchase from the Superintendent of Documents, U.S. Government Printing Office, Washington, D.C., 20402 (foreign postage, one-fourth additional). Reprints from outside journals and the NBS Journal of Research may often be obtained directly from the authors.*

INDEX TO VOLUME 67C

January to December 1963

A

Page

A power-series buildup factor formulation. Application to rectangular and off-axis disk source problems ... 291
Air bearings, application of, to an electrodynamic vibration standard ... 327
Almer, H. W., H. A. Bowman, Minimization of the arrestment error in one-pan two-knife balance systems ... 227
An alinement interferometer ... 307
Analysis of a microwave radiometer for precise standardization of noise sources ... 139
Apparatus for the detection of piezoelectric coupling ... 197
Application to air bearings to an electrodynamic vibration standard ... 327
Aqueous solution, equipment for single crystal growth ... 25
Arrestment error in one-pan two-knife balance systems, minimization ... 227
Automatic multichannel correlator ... 33

B

Balance systems, one-pan two-knife, minimization of the arrestment error ... 227
Blaine, L. R., A far-infrared vacuum grating spectrometer ... 207
Bowman, H. A., H. E. Almer, Minimization of the arrestment error in one-pan two-knife balance systems ... 227
Brown, R. F., Jr., Automatic multichannel correlator ... 33
Buildup source, a power-series buildup factor formulation, application ... 291

C

Calibrating method, a standard volt box ... 1
Calibration systems, instrument, realistic evaluation of the precision and accuracy ... 161
Cassidy, E. C., D. H. Tsai, New fast-opening, large-aperture shutter for high-speed photography ... 65
Cellulosic materials exposed to thermal radiation, surface flame propagation ... 251
Colorimeter, thermoelectric, development of filters ... 319
Compensation and measurement, drag with manned satellites: feasibility study ... 247
Conduction, steady state heat, in cylinders with multiple continuous line heat sources ... 119
Correlator, multichannel, automatic ... 33
Crystal growth, single, from aqueous solution, equipment ... 25
Cylinders with multiple continuous line heat sources, steady state heat conduction ... 119

D

Darling, W. F., F. E. Washer, Determination of optical path difference for a photographic objective ... 311
Determination of optical path difference for a photographic objective ... 311
Determination of residual thiosulfate in processed film ... 237
Development of filters for a thermoelectric colorimeter ... 319
Dimoff, T., B. F. Payne, Application of air bearings to an electrodynamic vibration standard ... 327
Disk source, a power-series buildup factor formulation, application ... 291
Drag compensation and measurement with manned satellites: feasibility study ... 247
Dunfee, B. L., Method for calibrating a standard volt box ... 1

E

Eisenhart, C., Realistic evaluation of the precision and accuracy of instrument calibration systems ... 161
Elastic constant—porosity relations for polycrystalline thoria ... 39
Elastic constants of thoria specimens of varying porosity, temperature dependence ... 93
Electrolytic hydrogen and deuterium through iron, permeation rates ... 111
Electron beam density of unipotential electron guns at low voltages ... 279
Electron guns, unipotential, at low voltages, limitations on electron beam density ... 279
Emara, S. H., R. P. Teele, Development of filters for a thermoelectric Colorimeter ... 319
Emittance, relation of, to other optical properties ... 217
Equations for the radiofrequency magnetic permeameter ... 69
Equipment for a single crystal growth from aqueous solution ... 25

F

Far-infrared vacuum grating spectrometer ... 207
Flame propagation, surface, on cellulosic materials exposed to thermal radiation ... 251
Film, processed, determination of residual thiosulfate ... 237
Filters for a thermoelectric colorimeter, development ... 319
Flynn, D. R., Radial-flow apparatus for determining the thermal conductivity of loose-fill insulations to high temperatures ... 129
Frenkel, L., Apparatus for the detection of piezoelectric coupling ... 197

G

Greenspan, L., Oxygen partial pressure warning instrument ... 47
Gross, D., J. J. Loftus, Surface flame propagation on cellulosic materials exposed to thermal radiation ... 251
Guns, unipotential electron, at low voltages, limitations on electron beam density ... 279

H

Page

Harrington, R. D., C. A. Hoer, Parallel reversible permeability measurement techniques from 50 kc/s to 3 Gc/s ... 259
High-speed photography, new fast-opening, large-aperture shutter ... 65
Hoer, C. A., R. D. Harrington, Parallel reversible permeability measurement techniques from 50 kc/s to 3 Gc/s ... 259
—, *A. L. Rasmussen*, Equations for the radiofrequency magnetic permeameter ... 69
Horton, A. T., J. L. Torgesen, C. P. Saylor, Equipment for single crystal growth from aqueous solution ... 25
Howard, F. L., Leak-resistant rotation seal for vacuum applications ... 335
Hubbell, J. H., A power-series buildup factor formulation. Application to rectangular and off-axis disk source problems ... 291
Hydrogen and deuterium, electrolytic through iron permeation rates ... 111

I

Infrared, far, vacuum grating ... 207
Instrument calibration systems, realistic evaluation of the precision and accuracy ... 161
Insulations, thermal conductivity of loose-fill, high temperature, radial-flow apparatus for determining ... 129
Interferometer, alinement ... 307
Interferometers, large aperture with small beam dividers ... 201

K

Knudsen, F. P., S. Spinner, L. Stone, Elastic constant—porosity relations for polycrystalline thoria ... 39
—, —, —, Temperature dependence of the elastic constants of thoria specimens of varying porosity ... 93
Kuyatt, C. E., J. A. Simpson, Limitations on electron beam density of unipotential electron guns at low voltages ... 279

L

Langer, R. M., J. P. Vinti, Drag compensation and measurement with manned satellites: feasibility study ... 247
Large aperture interferometers with small beam dividers ... 201
Leak-resistant rotation seal for vacuum applications ... 335
Limitations on electron beam density of unipotential electron guns at low voltages ... 279
Loftus, J. J., D. Gross, Surface flame propagation on cellulosic materials exposed to thermal radiation ... 251

M

Magnetic permeameter, equations for the radiofrequency ... 69
Manned satellites, drag compensation and measurement with: feasibility study ... 247
Measurement and compensation, drag, with manned satellites: feasibility study ... 247
Method for calibrating a standard bolt box ... 1
Microfilm, processed, stability of residual thiosulfate ... 15
Microwave noise sources, radiometer for precise standardization ... 139
Mills, R. M., New radiofrequency mass spectrometer having high duty cycle ... 283
Minimization of the arrestment error in one-pan two-knife balance systems ... 227
Multichannel correlator, automatic ... 33

N

New fast-opening, large-aperture shutter for high-speed photography ... 65
New radiofrequency mass spectrometer having high duty cycle ... 283
Newton, C. J., Residual stresses and their relaxation on the surfaces of sections cut from plastically deformed steel specimens ... 101
Noise, electrical, analysis of a microwave radiometer for precise standardization ... 139

O

One-pan two-knife balance systems, minimization of the arrestment error ... 227
Optical path difference, for a photographic objective ... 311
Optical properties, relation of emittance ... 217
Oxygen partial pressure warning instrument ... 47

P

Parallel reversible permeability measurement techniques from 50 kc/s to 3 Gc/s ... 259
Partial pressure warning instrument, oxygen ... 47
Payne, B. F., T. Dimoff, Application of air bearings to an electrodynamic vibration standard ... 327
Peary, B. A., Steady state heat conduction in cylinders with multiple continuous line heat sources ... 119
Permeability measurement techniques from 50 kc/s to 3 Gc/s ... 259
Permeameter, magnetic, equations for radiofrequency ... 69
Permeation rates of electrolytic hydrogen and deuterium through iron ... 111
Photography, high-speed, new fast-opening, large-aperture shutter ... 65
Piezoelectric coupling, apparatus for the detection of ... 197
Pitts, J. W., Permeation rates of electrolytic hydrogen and deuterium through iron ... 111
Pointing interferometer ... 307
Polycrystalline thoria, elastic constant—porosity relations ... 39
Pope, C. J., Determination of residual thiosulfate in processed film ... 237
—, Stability of residual thiosulfate in processed microfilm ... 15
Porosity relations for polycrystalline thoria ... 39

Page

Pressure warning instrument, partial, oxygen 47
Properties, optical, relation of emittance 217

R

Radial-flow apparatus for determining the thermal conductivity of loose-fill insulations to high temperatures 129
Radiation, thermal, surface flame propagation on cellulosic materials exposed 251
Radiofrequency magnetic permeameter, equations 69
Radiofrequency, new, mass spectrometer having high duty cycle 283
Radiometers, microwave, for precise standardization of noise sources, analysis 137
Rasmussen, A. L., C. A. Hoer, Equations for the radiofrequency magnetic permeameter 69
Rectangular source, a power-series buildup factor formulation, application 291
Realistic evaluation of the precision and accuracy of instrument calibration systems 161
Relation of emittance to other optical properties 217
Residual stresses and their relaxation on the surfaces of sections cut from plastically deformed steel specimens 101
Residual thiosulfate, stability of, in processed microfilm 15
Richardson, J. M., G. D. Ward, Analysis of a microwave radiometer for precise standardization of noise sources 139
Richmond, J. C., Relation of emittance to other optical properties 217

S

Satellites, manned, drag compensation and measurement with: feasibility study 247
Saunders, J. B., An alinement interferometer 307
—, Large aperture interferometers with small beam dividers 201
Saylor, C. P., J. L. Torgesen, A. T. Horton, Equipment for a single crystal growth from aqueous solution 25
Seal, leak-resistant rotation, for vacuum applications 335
Shutter, new fast-opening, large-aperture, for high-speed photography 65
Simpson, J. A., C. E. Kuyatt, Limitations on electron beam density of unipotential electron guns at low voltages 279
Spectrometer, a far-infrared vacuum grating 207
Spectrometer, mass, new radiofrequency, having high duty cycle 283
Spinner, S., F. P. Knudsen, L. Stone, Elastic constant—porosity relations for polycrystalline thoria 39
—, —, —, Temperature dependence of the elastic constants of thoria specimens of varying porosity 93
Stability of residual thiosulfate in processed microfilm 15
Standard volt box, method for calibrating 1
Standards, noise sources, analysis of a microwave radiometer 139
Steady state heat conduction in cylinders with multiple continuous line heat sources 119

Page

Steel specimens, plastically deformed, surfaces of sections cut from, residual stresses and their relaxation 101
Stone, L., S. Spinner, F. P. Knudsen, Elastic constant—porosity relations for polycrystalline thoria 39
—, —, —, Temperature dependence of the elastic constants of thoria specimens of varying porosity 93
Studies on the tungsten-rhenium thermocouple to 2000 °C 337
Surface flame propagation on cellulosic materials exposed to thermal radiation 251

T

Teele, P. P., S. H. Emara, Development of filters for a thermoelectric colorimeter 319
Temperature dependence of the elastic constants of thoria specimens of varying porosity 93
Thermal conductivity of loose-fill insulations to high temperatures, radial-flow apparatus for determining 129
Thermal radiation, surface flame propagation on cellulosic materials exposed 251
Thermocouple, tungsten-rhenium, to 2000 °C, studies on 337
Thermoelectric colorimeter, development of filters for 319
Thiosulfate, residual, in processed film, determination 237
Thiosulfate, stability of residual, in processed microfilm 15
Thomas, D. B., Studies on the tungsten-rhenium thermocouple 337
Thoria, polycrystalline, elastic constant—porosity relations 39
Thoria specimens of varying porosity, temperature dependence of the elastic constants 93
Torgesen, J., L., A. T. Horton, C. P. Saylor, Equipment for single crystal growth from aqueous solution 25
Tsai, D. H., E. C. Cassidy, New fast-opening, large-aperture shutter for high-speed photography 65
Tungsten-rhenium thermocouple to 2000 °C, studies on 337

V

Vacuum applications, leak-resistant rotation seal 335
Vibration, electrodynamic exciter, application of air bearings 327
Vinti, J. P., P. M. Langer, Drag compensation and measurement with manned satellites: feasibility study 247
Volt box, standard, method for calibrating 1

W

Ward, G. D., J. M. Richardson, Analysis of a microwave radiometer for precise standardization of noise sources 139
Washer, F. E., W. P. Darling, Determination of optical path difference for a photographic objective 311

U.S. GOVERNMENT PRINTING OFFICE:1963

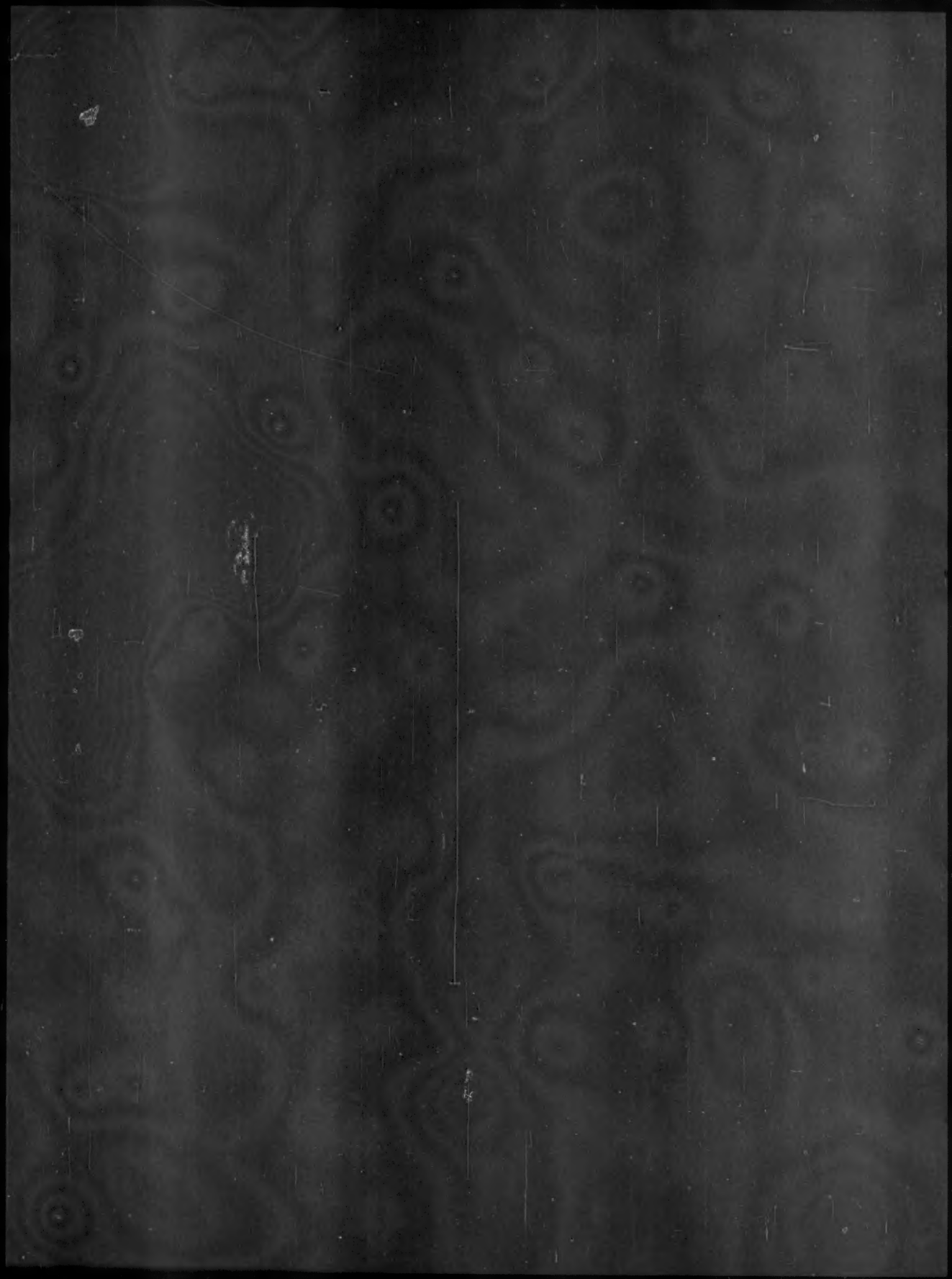

UNIVERSITY MICROFILMS INC
EDITORIAL DEPARTMENT
313 NORTH FIRST ST
ANN ARBOR MICH

UNITED STATES
GOVERNMENT PRINTING OFFICE
DIVISION OF PUBLIC DOCUMENTS
WASHINGTON, D.C. 20402

OFFICIAL BUSINESS

PENALTY FOR PRIVATE USE TO AVOID PAYMENT OF POSTAGE, $300 (GPO)

JOURNAL OF RESEARCH of the National Bureau of Standards Vol. 67C, No. 4 October–December 1963
C. Engineering and Instrumentation

Contents

	Page
Limitations on electron beam density of unipotential electron guns at low voltages. J. Arol Simpson and C. E. Kuyatt.	279
New radiofrequency mass spectrometer having high duty cycle. Robert M. Mills.	283
A power-series buildup factor formulation. Application to rectangular and off-axis disk source problems. J. H. Hubbell.	291
An alinement interferometer. J. B. Saunders.	307
Determination of optical path difference for a photographic objective. Francis E. Washer and Walter R. Darling.	311
Development of filters for a thermoelectric colorimeter. Sayeda H. Emara and Ray P. Teele.	319
Application of air bearings to an electrodynamic vibration standard. T. Dimoff and B. F. Payne.	327
Leak-resistant rotation seal for vacuum applications. Frank L. Howard.	335
Studies on the tungsten-rhenium thermocouple to 2000 °C. Douglas B. Thomas.	337
Publications of the National Bureau of Standards.	353
Index to volume 67C, January to December 1963.	361

Library of Congress Catalog Card Number: 62-3900

For sale by the Superintendent of Documents, U.S. Government Printing Office, Washington, D.C., 20402. Price 75 cents (single copy). Subscription price: $2.25 a year; 50 cents additional for foreign mailing.
UNITED STATES GOVERNMENT PRINTING OFFICE, WASHINGTON : 1963